The thermal evolution of subduction zone lithosphere: Evidence from the chemical development of Mt. Ruapehu and surrounding vents, New Zealand.

TIMOTHY R LEE

The thermal evolution of subduction zone lithosphere: Evidence from the chemical development of Mt. Ruapehu and surrounding vents, New Zealand.

Timothy R. Lee

Mt. Ruapehu is an andesite volcano located at the southwest termination of the Taupo Volcanic Zone (TVZ) in the North Island of New Zealand where the Pacific Plate subducts beneath the Australian Plate. Volcanism has migrated south with time as rifting from the Kermadec arc has propagated into the North Island lithosphere making Ruapehu the most recent addition to the TVZ. A detailed study of volcanic rocks and crustal xenoliths collected from Mt. Ruapehu and nearby satellite vents was conducted to establish how differentiation processes in arc magmas change with time in response to tectonic movements in the arc lithosphere.

The thickness and composition of the arc crust in the southern TVZ directly controls the differentiation histories of magmas from Mt. Ruapehu and satellite vents. The crustal column beneath Ruapehu is composed of two main lithologies; a localised 5-10 km thick lower crustal meta-igneous granulite overlain by 20-25 km of meta-sediment. While fractional crystallisation is an important process in modifying the major and trace element concentrations, crustal assimilation plays a major role in modifying the isotopic composition of magmas from the southern TVZ. New trace element and isotope data for lavas and crustal xenoliths confirm a distinct change in assimilants between the oldest (Te Herenga - TH) and younger formations (Post Te Herenga - PTH) at Ruapehu. TH lavas are a product of lower crustal differentiation involving assimilation of meta-igneous granulite. PTH lavas display evidence for interaction with the same meta-igneous granulite followed by contamination with meta-sedimentary crust. This change in assimilant coincides with increased rates of extension at the southern tip of the Taupo Volcanic Zone (TVZ). We propose that the change in melt-crust interaction reflected in major geochemical changes from TH to PTH lavas is a response to adjustments in differentiation depth.

Peripheral satellite vents near Ruapehu have produced some of the most primitive lavas in the southern TVZ with compositions resembling high-Mg andesite. This contrasts with the central-northern TVZ where the most primitive lavas are high-alumina basalt. The spatial distribution of these two magma series has developed as a result of the evolution of TVZ lithosphere. High-Mg andesites appear to be generated from depleted mantle during the very earliest stages of arc development when the lithosphere is thicker causing fractionation at relatively deep levels. High-alumina basalts however, represent a more mature phase of arc development and are derived from relatively fertile mantle following lithospheric thinning causing fractionation at relatively shallow levels.

Finally, new osmium isotope data from meta-igneous xenoliths indicate the lower crust beneath Ruapehu is not formed of altered Jurassic oceanic crust. The relatively unradiogenic $^{187}Os/^{188}Os$ ratios of the xenoliths instead suggest they represent localised underplated material, which has only developed beneath the graben axis where the magma flux is greatest.

The thermal evolution of subduction zone lithosphere: Evidence from the chemical development of Mt. Ruapehu and surrounding vents, New Zealand.

A thesis presented for the degree of

Doctor of Philosophy

By

Timothy. R. Lee

Department of Earth Sciences

Durham University

May 2008

Declaration

This thesis is entirely the work of the author, except were reference has been made to previously published/unpublished work. No section of this thesis has previously been submitted for a degree at this or any other university.

Timothy. R. Lee

Department of Earth Sciences
University of Durham

May 2008

Acknowledgements

I would like to thank my supervisors Colin Macpherson and Jon Davidson for giving me the opportunity to conduct research in arc magmatism and providing considerable support, time and advice throughout my PhD. I am also extremely grateful to NERC for funding this project and the VMSG and Ustinov College for financing travel to national and international conferences.

I am indebted to Richard Price, Ian Graham and Joel Baker for providing rock samples and field assistance in New Zealand. Thanks also go to John Gamble, Ian Wright and Harry Keys (DOC) for considerable assistance in obtaining sample collection permits for Mt. Ruapehu and providing valuable insight into Taupo Volcanic Zone magmatism. I would also like to thank the Ngati Tuwharetoa band for permitting me to conduct research in the Tongariro National Park.

Special thanks go to Geoff Nowell, Chris Ottley and Graham Pearson without whom the generation of most of the geochemical analyses presented in this thesis would not have been possible. Thanks also go to Goddfrey Fitton and Nic Odling at Edinburgh University for training in XRF preparation, Eric Condliffe for electron microprobe assistance at Leeds University, and Dave Lowry and Nathalie Grassineau for supervision during oxygen isotope analysis at Royal Holloway. Dave Sales at Durham University is also thanked for excellent preparations of thin sections.

Thanks also go to Ambre Luguet, Victoria Martin, Laura Font and Chris Dale for valuable discussion concerning igneous geochemistry.

I am ever grateful to my Mum, Dad, Naomi and Keni for continued support during my geological escapades and providing welcome breaks in Scotland.

Last but not least, I am eternally grateful to Christa for supporting me in pursuing a life-long passion in studying arc volcanoes, accompanying me to Durham and becoming acquainted with the north-east, and continuing to provide encouragement in finishing the writing process on our return to Calgary.

Contents

List of Figures

Chapter 1

Chapter 2

Chapter 3

Chapter 4

Chapter 5

Chapter 6

List of Tables

Chapter 2

Chapter 3

Chapter 4

Chapter 5

Chapter 6

Chapter 1

Introduction

1.1. General Introduction

Striking compositional similarities exist between typical arc andesite and bulk continental crust (e.g. trace element patterns). On this basis, it is believed arc magmatism has played an important role in the formation of the continental crust through geological time (Davidson and Arculus, 2006; Ringwood, 1974; Rudnick, 1995; Rudnick and Gao, 2005; Taylor, 1967). However, primary partial melts derived from the mantle wedge are generally basaltic in composition (Arculus, 1981; Gill, 1981) suggesting crustal additions from the mantle are too mafic to account for the andesitic nature of the continental crust. On the other hand, differentiation processes within the over-riding plate (Fig. 1.1) at subduction zones can easily generate andesite magmas and in doing so explain the compositional discrepancy between mantle-derived basalt and bulk continental crust. Therefore discerning the origin and evolution of magmas generated at volcanic arcs is fundamental for evaluating the origin and growth of continents.

The effects of differentiation such as fractional crystallisation, crustal contamination or magma mixing are frequently identified in arc magmas (e.g. Davidson et al., 1987; Handley et al., 2007; Hildreth and Moorbath, 1988; Gamble et al., 1999). Differentiation in arc systems is often modelled as occurring at fixed depths without variation in the availability or composition of contaminants during the lifetime of the system (Fig. 1.1). However, volcanic arcs represent a particularly dynamic environment where differentiation depths are likely to adjust with time in response to the tectonic evolution of the arc crust.

The Taupo Volcanic Zone (TVZ) forms the southern extremity of the Tonga-Kermadec arc where the Pacific plate subducts beneath the Australian plate (Fig. 1.2). The transition between the southern Kemadec arc and TVZ is marked by an

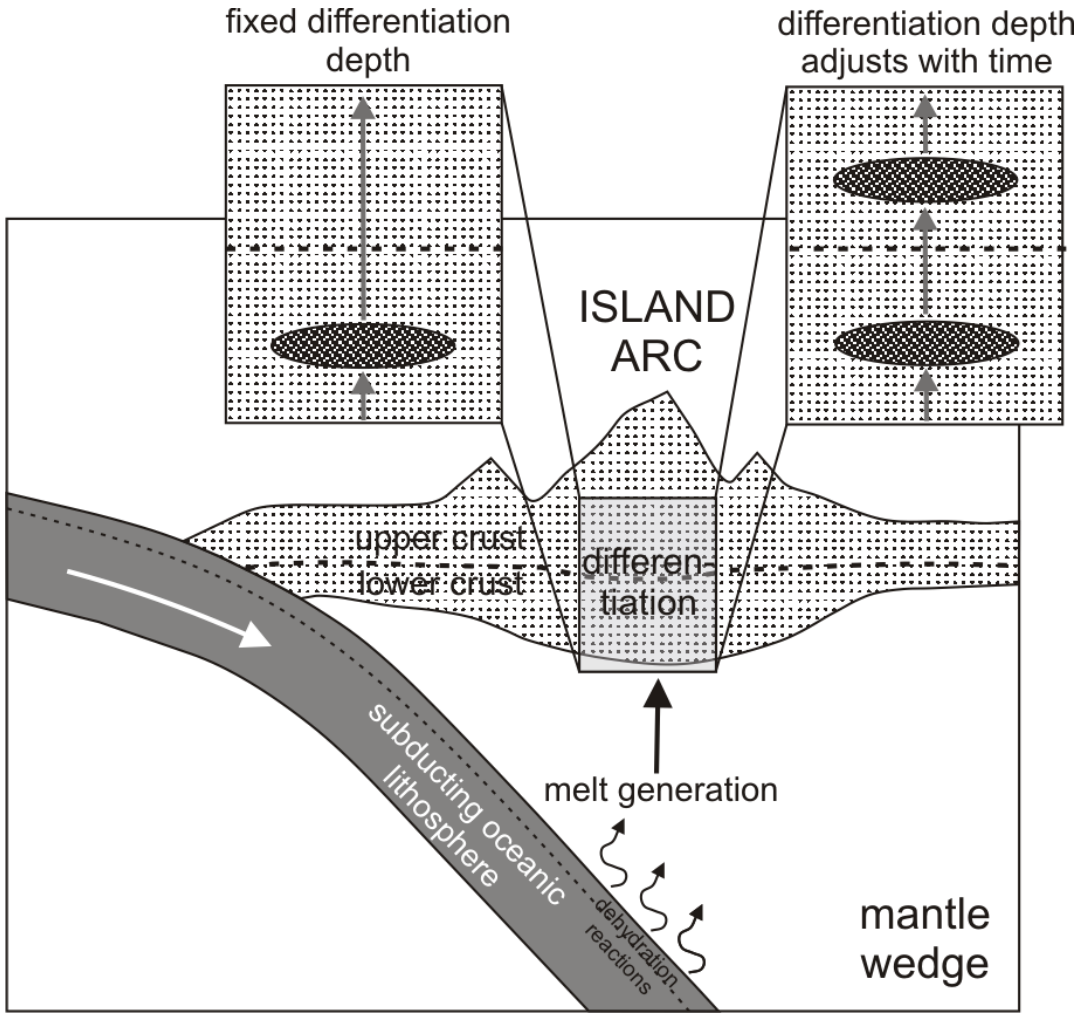

Fig. 1.1. Schematic diagram illustrating magma generation and differentiation at a volcanic arc. Hydrous melting within the mantle wedge is induced by dehydration reactions within the upper part of the subducting plate (McCulloch and Gamble, 1991). Buoyant mantle-wedge melts rise and stall within the crust where they undergo differentiation processes, e.g. fractional crystallisation, crustal contamination or magma mixing.

abrupt change from oceanic to continental lithosphere in the over-riding plate. This change in lithospheric composition is reflected in the type of lava erupted, with basalt-andesite dominating in the Kermadec arc while rhyolites accompanied by minor andesite prevail in the TVZ to the south. As the southern extremity of the Tonga-Kermadec arc impinges on the North Island of New Zealand, the petrology of rhyolites in the TVZ have been studied in considerable detail (e.g. Graham et al.,

1995; McCulloch et al., 1994; Sutton et al., 1995; Wilson et al., 2006). Andesites on the other hand have until recently received relatively little attention because of their minor volumetric abundance compared to rhyolite. However, growing evidence suggests andesites may in fact represent precursors to rhyolites in the TVZ (Price et al., 2005) and therefore represent an important stage in the evolution of the TVZ.

This study will build upon previous work on TVZ andesites (Gamble et al, 1999; Graham and Hackett, 1987; Price et al., 2005; Waight et al., 1999) by improving constraints on differentiation processes involved in the generation of andesites in the southern TVZ and how these change in response to the tectonic evolution of the arc crust.

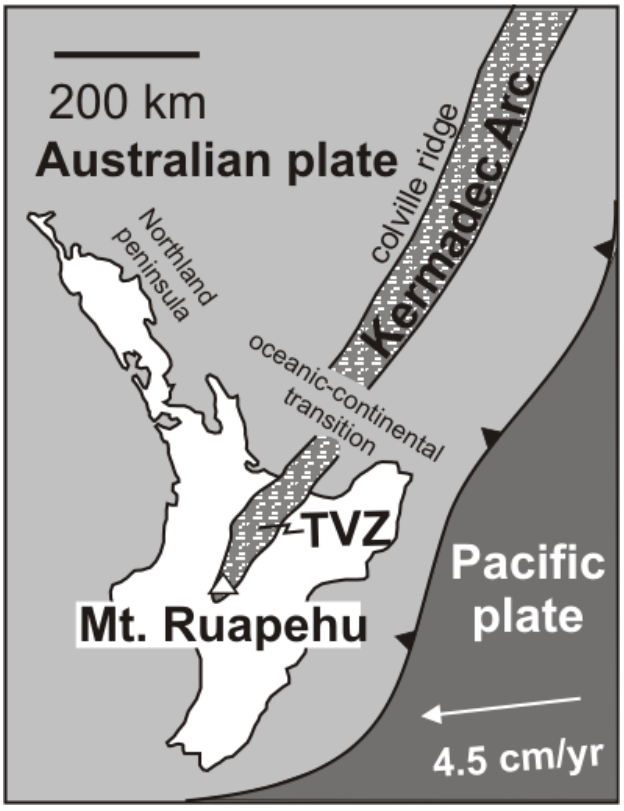

Fig. 1.2. Tectonic setting of the Taupo Volcanic Zone (TVZ) located at the southern end of the Tonga-Kermadec Arc. Pacific plate convergence rate from Acocella et al. (2003). Kermadec-TVZ junction marks the transition from oceanic to continental lithosphere in the over-riding plate.

1.2. General Setting

1.2.1. Tectonic History

The tectonic history that led to the development of the TVZ began more than 25 Ma with the initial convergence of the Pacific Plate beneath the Australian Plate (Malpas et al., 1992). This resulted in the growth of a volcanic arc within the Northland Peninsula of the North Island. Subduction terminated in the Northland ~ 5 Ma due to the clockwise rotation of the arc caused by the southward extension of the Kermadec arc (Malpas et al., 1992). ~4Ma plate rotation enhanced back arc extension in the Kermadec system (Malahoff, 1982), which culminated in the arc splitting into the Colville ridge and the modern Kermadec ridge. ~2Ma the arc extended southwards into the continental crust of New Zealand leading to the development of the TVZ (Hochstein, 1995). At present the Pacific lithosphere (~100Myr old) dipping at ~50-60º, subducts beneath the TVZ at an oblique angle (mean convergence vector ~263^0 with a velocity of 4.5cm/yr^{-1} (Acocella et al. 2003)) relative to the Australian Plate. The median of the TVZ is located 80–120 km above the Benioff zone (Reyners et al., 2006).

1.2.2. Taupo Volcanic Zone (TVZ)

The 250-300 km long TVZ (Fig. 1.3) is characterised by thin extended continental crust with exceptionally high heat flow (~700 mW/m^2; Bibby et al., 1995). The central region of the TVZ is dominated by rhyolites (15,000-20,000 km^3), comprising >80% of total erupted material. The remaining volcanism has been erupted from andesite centres at the southern and northern margins of the TVZ. Volcanism has migrated south with time as rifting from the Kermadec arc has propagated into the

North Island lithosphere making Mt. Ruapehu the most recent addition to the TVZ. The composition of the arc crust in the southern TVZ is composed of two main lithologies; a localised 5-10 km thick lower crustal meta-igneous granulite overlain by 20-25 km of meta-sediment. Furthermore crustal thickness increases by ~ 10km moving from the central to southern TVZ (Stern et al., 2006). Therefore, Mt. Ruapehu and surrounding satellite vents provide a unique opportunity to investigate how intra-crustal differentiation processes are influenced by the thermal and structural evolution of arc crust.

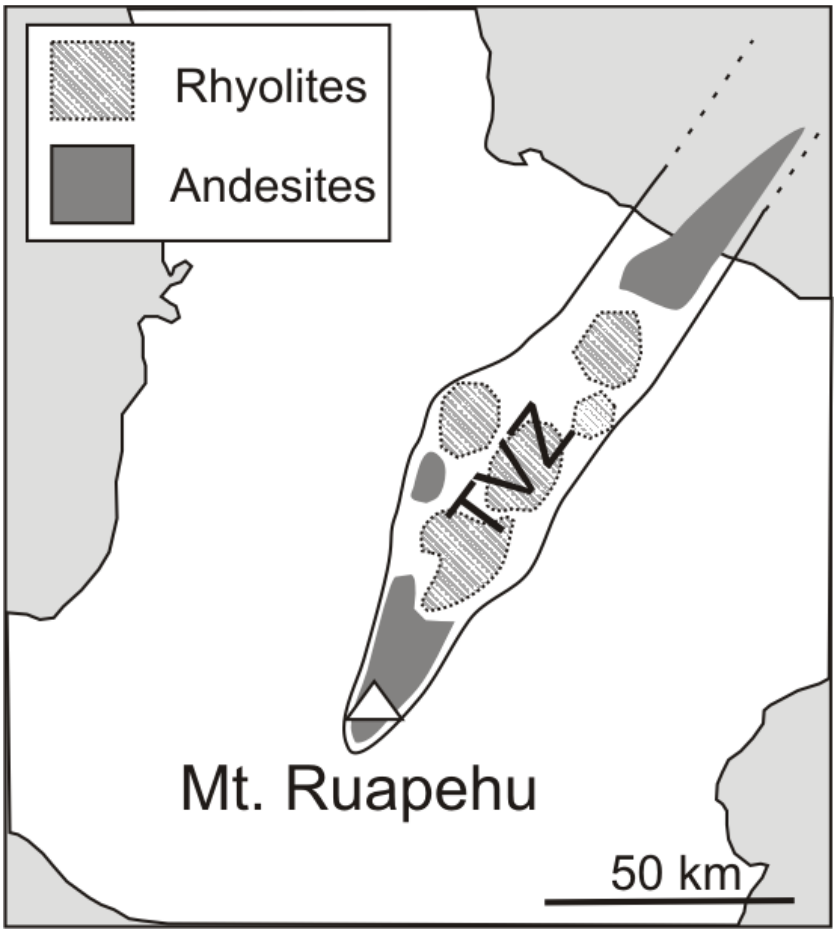

Fig. 1.3. Distribution of rhyolite and andesite centres within the TVZ. Extension within the North Island has spread south with time making Mt. Ruapehu the most recent volcanic addition to the TVZ.

1.3. Thesis aims

The main aims of this thesis are:

1. Summarize the composition of the arc crust in the southern TVZ by examining the composition and origin of crustal xenoliths within Ruapehu lavas.
2. Investigate the magmatic evolutionary trends at Mt. Ruapehu by establishing temporal variations in fractional crystallisation and melt-crust interactions throughout the lifetime of the volcano.
3. Address why satellite vents near Mt. Ruapehu produce high-Mg andesites and explain why these compositions appear restricted to the southern TVZ.
4. Relate temporal geochemical variations in Ruapehu and satellite vent lavas to the structural and thermal evolution of the southern TVZ arc lithosphere.

Chapter 2 focuses on the geochemistry of Ruapehu crustal xenoliths and addresses aim 1. The geochemistry of Ruapehu and satellite vent lavas are examined in Chapters 3 and 4 and address aims 2 and 3. Chapter 5 then addresses aim 4 by examining the structural evolution of the southern TVZ crust. Chapter 6 presents new Os isotope data for lower crustal meta-igneous granulite and summarises the main conclusions of the thesis.

Chapter 2

The geochemistry and stratigraphy of the Ruapehu crustal column: evidence from crustal xenoliths

2.1 Introduction

Arc magmatism is believed to have played an important role in the formation of the continental crust (Davidson and Arculus, 2006; Ringwood, 1974; Rudnick, 1995; Rudnick and Gao, 2005; Taylor, 1967). This is illustrated by the striking similarities in trace element patterns of typical arc andesites and bulk continental crust (Fig. 2.1), e.g LILE enriched, Nb - Ta anomalies and other HFSE depletions. Major element data also support a similar generation process between volcanic rocks at arcs and average continental crust, both displaying an andesitic composition with high SiO_2 and low Mg-numbers.

However most partial melts produced by hydrous melting of mantle wedge peridotite are basaltic in composition (Arculus, 1981; Gill, 1981). Consequently, although typical arc andesites have major and trace element trends similar to bulk continental crust, crustal additions from the mantle are too mafic to explain bulk continental crust compositions. Intra-crustal reprocessing of mantle derived basalt however can resolve this compositional discrepancy (e.g. Davidson and Arculus, 2006; Hildreth and Moorbath, 1988; Rudnick, 1995), producing an evolved andesite differentiate in addition to a mafic cumulate/restite. The latter component is assumed to either delaminate back into the mantle or reside beneath the seismic Moho.

A further inspection of the continental crust reveals it is often chemically and lithologically stratified into lower (mafic) and upper (felsic) layers (Levander et al., 2006; Rudnick and Fountain, 1995). Intra-crustal recycling again provides a mechanism for generating the vertically differentiated profile of the continental crust with an emphasis on partial melting of pre-existing crust (Annen et al., 2006; Davidson and Arculus, 2006). It is generally agreed that most crustal derived melts are formed by fluid-absent melting reactions with major melt production occurring at

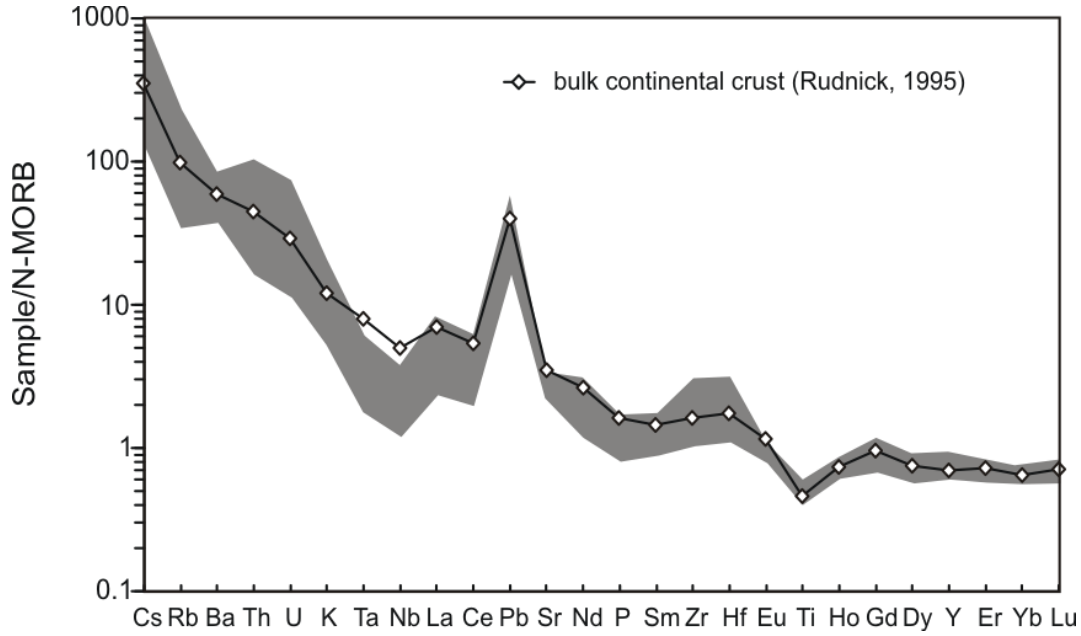

Fig. 2.1. N-MORB normalised trace element diagram displaying the close similarity between Ruapehu andesite compositions (shaded field) and bulk continental crust values. Data sources: bulk continental crust from Rudnick (1995); N-MORB normalisation values from Sun and McDonough (1989).

≥800 °C (Clemens, 2006). These temperatures equate to specific metamorphic reactions between upper amphibolite and granulite facies. However, these grades of metamorphism are only achieved by crustal thickening or the addition of heat from magmatism (e.g. underplating). Consequently much of the lower crust in arcs is believed to consist of a residual mafic granulite which formed as a result of granitic melt extraction. Intra-crustal recycling is recorded in exposed granulite terrains by the regular occurrence of segregated quartzo-feldspathic leucosomes. These granulites provide field evidence that the lower crust plays an integral role in the reprocessing of basaltic magma, resulting in the bulk andesitic composition of the continental crust and its differentiated profile.

The isotopic composition of continental arc volcanics is commonly displaced towards crustal values suggesting intra-crustal recycling is typically open system within this tectonic setting. Therefore, constraining intra-crustal recycling processes

in the lower crust is a fundamental requirement to understand andesite generation at arc volcanoes. Much of our current understanding of partial melting within the lower-middle continental crust has been derived from studying mineral reactions and textural information in exhumed deep crustal terrains (e.g. Schnetger, 1994; Solar and Brown, 2001). Unfortunately these studies can be limited by melt extraction and re-equilibration processes during exhumation (e.g. Cesare, 2000 and references therein). Crustal xenoliths within volcanics however, have often been brought to the surface over relatively short timescales and consequently do not suffer from the same limitations associated with exhumed terrains. Therefore, they are more likely to record both the processes and products resulting from partial melting in the middle-lower crust enabling an assessment of their significance to arc magmatism and crustal differentiation.

With the collection of a new trace element and isotopic data set for Ruapehu crustal xenoliths, the aims of this chapter are to further evaluate the issues addressed by Graham (1985a);

1) Characterise the composition and geochemistry of crustal xenoliths in Ruapehu lavas.
2) Establish a basement stratigraphy for the Ruapehu crustal column.
3) Examine the geochemical changes induced through partial melting of crustal xenoliths.

2.2 Sampling

Micro-xenoliths (< 10 mm width) are common in Ruapehu lavas however they tend to increase in abundance in younger formations. Owing to the rarity of any sizable xenoliths (> 20 mm width) found within this study, geochemical analyses were

performed on a selection of samples originally collected over a two year period by Graham (1985a). The existing whole rock geochemical database for these specimens comprised of major elements with limited trace element, $^{87}Sr/^{86}Sr$, $^{143}Nd/^{144}Nd$ and oxygen isotope analyses (Graham, 1987; Graham et al., 1988, 1990). Our study builds upon this previous work by extending the whole rock database to include full REE (rare earth element) and Sr, Nd, Hf and Pb isotope analyses (see Appendix C for comparison of Sr and Nd isotopes from each study). Where possible, xenoliths were also characterised using petrography and mineral analysis.

All xenoliths analysed for whole rock geochemistry had previously been classified as either meta-sedimentary or meta-igneous based on mineralogy and chemical composition (Graham, 1987; Graham et al., 1990). These two types comprise ~70% of all xenoliths in Ruapehu lavas with the remaining 30% consisting of recycled cumulates or volcanics genetically related to current Ruapehu magmatism (Graham et al., 1990). Meta-sedimentary xenoliths are the metamorphosed equivalents of the inter-bedded argillite and greywacke Torlesse sediments that outcrop to the east of the TVZ (Graham, 1985b, 1987; Graham et al., 1988). These sediments were derived from two distinct granite terrains ~240 Ma and ~420 Ma (Adams et al., 1998). The meta-igneous xenoliths are assumed to have formed by granulite metamorphism of basaltic material. Graham et al. (1990) suggested that the original basaltic protolith was either fragments of altered Jurassic oceanic crust (i.e. Pacific plate) underthrust beneath the Ruapehu crustal column, or recent underplated material.

2.3 Petrography

2.3.1 Meta-igneous xenoliths

The mineral assemblage in meta-igneous xenoliths consists of plagioclase (andesine-bytownite), clinopyroxene (mainly augite), orthopyroxene (bronzite-hypersthene) and ilmenite with minor quantities of titanomagnetite and chrome-spinel (Graham et al., 1990). Olivine, biotite, apatite and sulphides have also been reported in a few specimens (Price et al., 2005). Limited plagioclase analyses from xenoliths in this study are uniformly calcic ranging from bytownite to anorthite while pyroxene compositions are relatively Fe-rich - augite/ferroaugite and pigeonite (Fig. 2.2a and b). Quartz becomes more prominent as bulk-rock silica increases. Chemical zonation in crystals is weak or absent and xenolith-lava contacts are either sharp or display thin recrystallised margins consisting of fine grained plagioclase. Samples usually exhibit a directional fabric (Fig. 2.3a; from lava WX22) identifiable from mineral layering (1-5 mm width), resulting from either a relic cumulate texture or a schistose metamorphic overprint. Based on the absence of garnet, and pyroxene thermometry values between 800-930°C, meta-igneous xenoliths probably represent lower crustal material derived from near the Moho at pressures between 7-10 kbars (Graham et al., 1990).

2.3.2 Meta-sedimentary xenoliths

Graham (1987) subdivided meta-sedimentary xenoliths into four types; quartz, feldspar, spinel and buchitic meta-sedimentary xenoliths. A summary of each type is given below after Graham (1985a). Plagioclase and orthopyroxene compositions from meta-sedimentary xenoliths in this study are illustrated in Figure 2.2a and b.

Quartz-rich xenoliths generally include quartz + plagioclase + clinopyroxene/orthopyroxene ± titanite ± ilmenite ± titanomagnetite ± biotite ± glass.

Some rare examples include garnet and/or cordierite. These xenoliths generally contain > 80% quartz and can be strongly foliated often exhibiting granoblastic textures.

Feldspar-rich varieties commonly occur as pyroxene-hornfels composed of 60-80% unzoned plagioclase (andesine-labradorite) accompanied by hypersthene, pleonaste, titanomagnetite, ilmenite and biotite (Fig. 2.3b; 17425). Brown glass within cavities and vesicles is common in some samples. Textures vary from hypidiomorphic granular to granoblastic.

Spinel-rich xenoliths are rare but have been documented throughout most formations at Ruapehu. They contain high abundances of titanomagnetite, ilmenite and pleonaste. Millimetre wide foliations are common segregating mafic (titanoferous biotite, aluminous hypersthene, spinel) and felsic (calcic plagioclase, An_{74}-An_{96}) mineralogies. Olivine only occurs as a minor phase.

Buchitic xenoliths are distinct from the other meta-sedimentary types due to a high percentage of glass (up to 80%). Their bulk mineralogy consists of quartz and calcic plagioclase although a diverse range of minerals coexist within the quenched glass: cordierite, orthopyroxene, spinel (pleonaste), ilmenite, rutile and pyrrhotite.

Thermometry calculations for quartz, feldspar and spinel rich meta-sedimentary xenoliths using garnet-biotite and titanomagnetite-ilmenite pairs suggest equilibration temperatures between 808-979°C (Graham, 1987). Few of these xenoliths contain an appropriate mineral assemblage for barometry calculations; however the presence of cordierite and almandine garnet in a feldspar rich sample may suggest pressure limits between 4-7 kbar (Graham, 1987). In buchitic xenoliths, a comparison between glass chemistry and phase relations from melting experiments

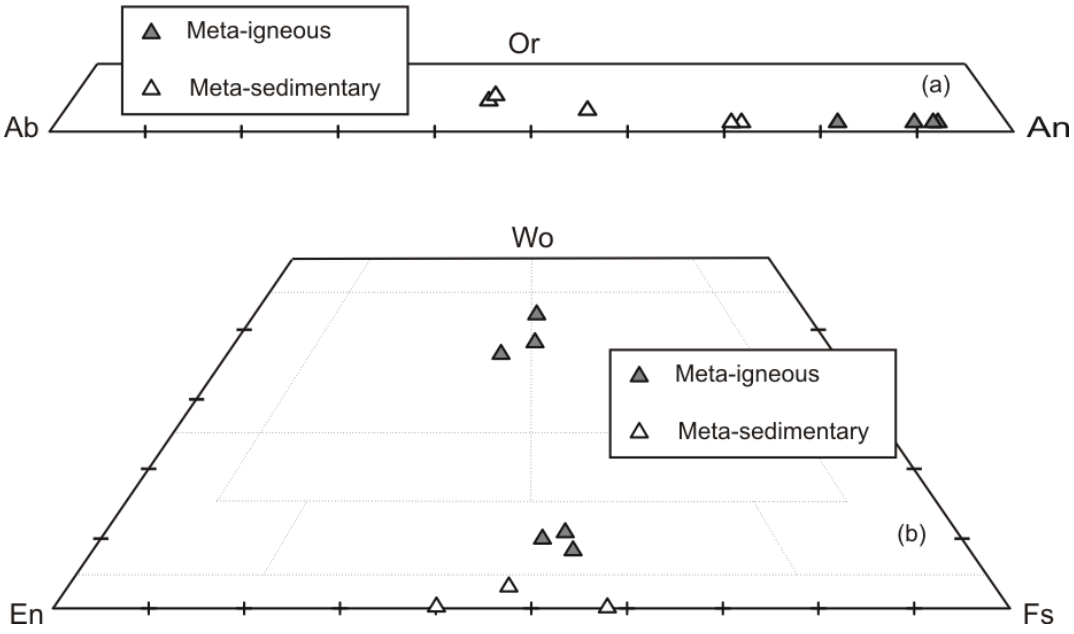

Fig. 2.2. a) Plagioclase and b) pyroxene compositions in meta-igneous and meta-sedimentary xenoliths.

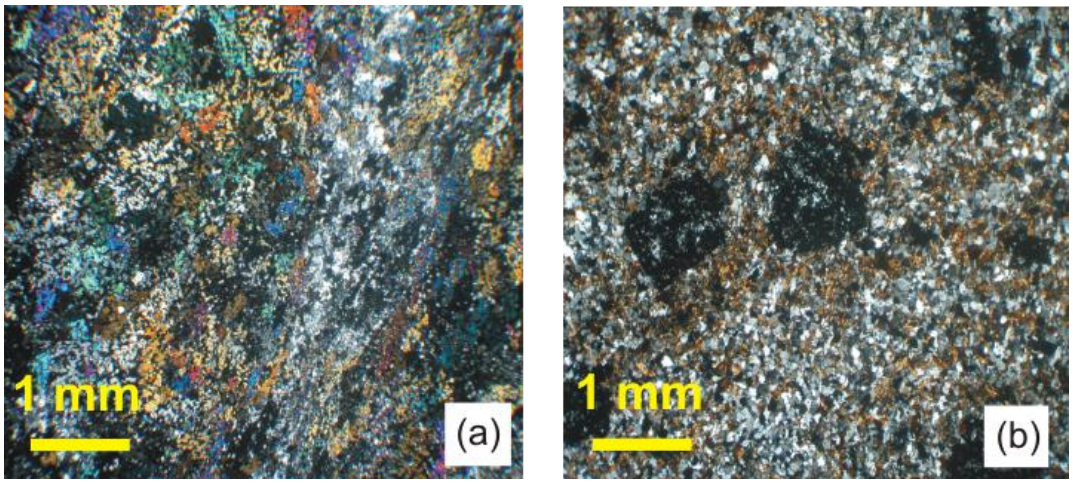

Fig 2.3. Photographs of mineralogy and textures present in a) meta-igneous xenolith (from lava WX22) and b) meta-sedimentary xenolith (sample 17425). Meta-igneous xenolith displays N-S directional fabric defined by mineral layering (clinopyroxene, orthopyroxene, plagioclase and ilmenite). The meta-sedimentary xenolith displays spinel porphyroblasts (~1 mm width) with a biotite, feldspar and quartz granoblastic groundmass.

suggest a much shallower origin for this type (~1.5 kbar) at temperatures ≥ 775°C (Graham et al., 1988).

The predominance of meta-igneous and meta-sedimentary xenoliths suggests the Ruapehu crustal column is largely composed of these two lithologies. Based on the barometry estimates from each crustal lithology and assuming a lithostatic stress gradient of 1 kbar ≈ 3 km depth, the basement stratigraphy can be subdivided into a 10 km thick lower crustal meta-igneous granulite, overlain by 20-25 km of Torlesse meta-sediment (Fig. 2.4a). Poor resolution in seismic refraction/reflection studies has hampered recent efforts to resolve the internal crustal structure of the TVZ due to the thick superficial volcanic sequence (e.g. Rowlands et al., 2005). However, seismic attenuation studies (*Qp*) approximately 50-100 km south of Ruapehu (Eberhart-Philips et al., 2005) have identified a high-*Qp* (>600) lower crustal region interpreted as basaltic material, overlain by Torlesse meta-sediment (*Qp* = 300-400) (Fig. 2.4b). This provides geophysical evidence in support of the two-layered crustal structure proposed in this study.

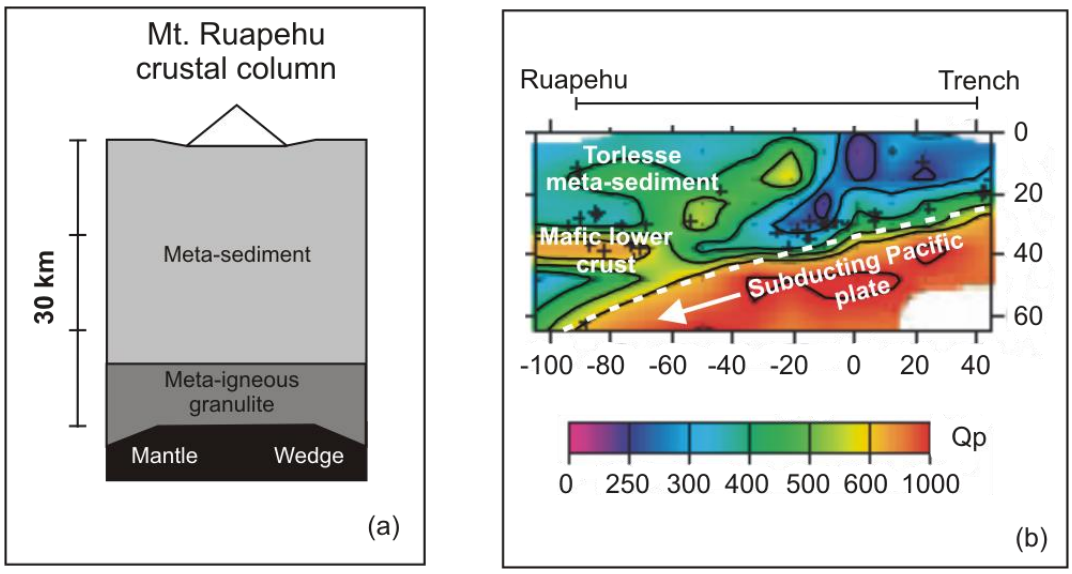

Fig. 2.4. a) Diagram illustrating the stratigraphy and composition of the crustal column at Mt. Ruapehu, deciphered from barometry estimates (Graham, 1987; Graham et al., 1990) from crustal xenoliths. b) Modified seismic attenuation image (Eberhart-Philips et al., 2005). Geophysical evidence for a two layered crustal structure at the southern termination of the TVZ.

2.4 Geochemistry

2.4.1 Major Element Data

Major element data for both crustal xenoliths are presented in full by Graham (1985a). Most elements are controlled by modal abundance of certain phases. Modal percentage of quartz and feldspar greatly influence SiO_2 (41-98 wt %) and Al_2O_3 (0.8-26 wt %) in both xenolith types, while biotite and K-feldspar determine wt % K_2O in meta-sediments. High abundances of MgO (3.5-14.2 wt %) are characteristic of the meta-igneous xenoliths and may support a restite/cumulate origin.

2.4.2 Trace Element Geochemistry

Trace element data for crustal xenoliths are listed in Appendix B. To examine trace element characteristics of the crustal xenoliths and illustrate differences between meta-igneous and meta-sedimentary varieties, samples have been normalised to N-MORB on multi element and rare earth element plots. These normalising values were chosen for consistency throughout the study and aid direct comparison with lavas presented in later chapters.

2.4.2.1 Meta-Igneous Xenoliths

Meta-igneous xenoliths have high but variable concentrations of compatible elements such as Ni (10-465 ppm), Cr (17-1073 ppm) and Sc (22-50 ppm); lower values tend to correspond to higher SiO_2 contents. They display characteristics of subduction zone lavas such as moderate LILE/LREE enrichment (La/Yb_n=2.4-6.6) and HFSE/HREE depletions relative to N-MORB, (Fig. 2.5a). Most samples also display small depletions in Rb and K. Nb-Ta fractionation relative to N-MORB is probably a result of contamination while using a tungsten carbide disc mill during sample preparation

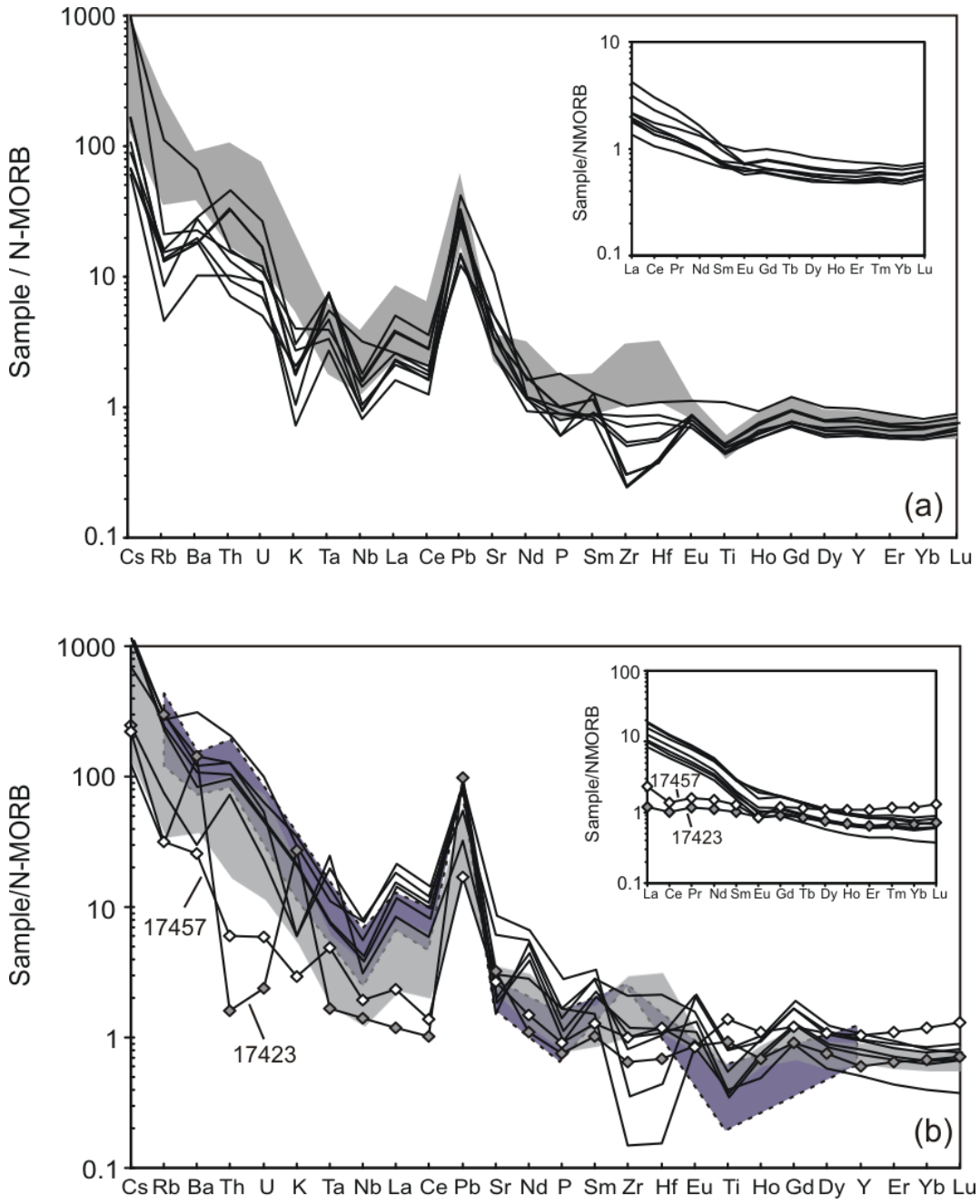

Fig. 2.5. N-MORB normalised trace element diagrams for a) meta-igneous and b) meta-sedimentary xenoliths. Grey field represents Ruapehu andesites; blue field is Torlesse sediment. Inset diagrams are REE profiles for each xenolith type. Samples 17457 and 17423 are meta-sedimentary xenoliths with unusual trace element patterns. N-MORB normalisation values are from Sun and McDonough (1989). Torlesse sediment from Graham (1985b).

at the Victoria University of Wellington. Trace element patterns are similar to average andesites from Ruapehu but are generally displaced to lower concentrations. The REE

plot highlights that samples either have no or small negative Eu anomalies (Eu/Eu* = 0.8-1.04).

The arc-like trace element pattern of the meta-igneous xenoliths has been explained by the addition of trench sediment to the under-thrusted oceanic crust basalt (Graham et al., 1990). Alternatively if the meta-igneous xenoliths represent recent underplated material related to current Ruapehu magmatism (lower crustal cumulates) the arc-like trace element pattern can be accounted for by the slab-derived component which induced partial melting within the mantle wedge.

2.4.2.2 Meta-sedimentary Xenoliths

Meta-sedimentary xenoliths contain much higher concentrations of incompatible elements than their meta-igneous counterparts. In particular LILE and LREE are usually an order of magnitude greater than meta-igneous granulites (e.g. Rb $\leq$ 168 ppm) and consequently display strong LILE/LREE enrichment (La/Yb_n = 16-26) and moderate HFSE/HREE depletions relative to N-MORB (Fig. 2.5b). Trace element patterns of meta-sedimentary xenoliths are similar to the Ruapehu lavas although many xenoliths extend to higher concentrations in LILE, LREE and some HFSE. The Torlesse sediment (Graham, 1985b) also displays a similar pattern to the meta-sediments, however, some xenoliths extend to lower concentrations of Rb, Ba and K and higher concentrations of Sr. Two xenoliths that are low in SiO_2 (41-42 wt%) and strongly aluminous (Al_2O_3 = 22-26 wt %) have very different trace element compositions compared to other meta-sedimentary examples; 17423 is feldspar bearing while 17457 is a spinel rich variety (Graham, 1985a). Both samples have unusually high Cr (187 and 858 ppm), Ni (117 and 97 ppm) and Cu (134 and 437 ppm) concentrations indicating they may have an igneous origin rather sedimentary. 17423 is unique due to depletions in LREE, HFSE, Th and U, yet remains enriched in

most LILE (Cs, Rb, Ba and K) while sample 17457 is depleted in most incompatible elements. Both samples display flat REE profiles very similar to N-MORB however the spinel-rich sample (17457) appears moderately enriched in MREE-HREE.

2.4.3 Radiogenic Isotopes

Sr, Nd, Hf and Pb isotope data for both xenolith types is listed in Appendix C.

2.4.3.1 Meta-Igneous Xenoliths

Meta-igneous xenoliths define a field with more radiogenic Sr than the Ruapehu lavas with $^{87}Sr/^{86}Sr$ composition ranging from 0.705770-0.708698 and εNd values of 2.8 - 6.3 (Fig. 2.6a). εHf values (6.6-13.4) are also widespread overlapping with the more primitive lava compositions at Ruapehu (Fig. 2.6b). $^{206}Pb/^{204}Pb$ (18.530-18.826) values are indistinguishable from Ruapehu lavas; however, $^{208}Pb/^{204}Pb$ (38.432-38.766) and more so $^{207}Pb/^{204}Pb$ (15.624-15.655) extends to more radiogenic compositions than the Ruapehu array at equivalent $^{206}Pb/^{204}Pb$ values (Fig. 2.6c & d).

Meta-igneous xenoliths display a large departure from MORB in Sr and O isotopes which could result from sea-water alteration of basaltic material (Graham et al., 1990) Low temperature alteration (< 50°C) in addition to a high water/rock ratio present on a sea-floor (> 50/1; Stakes and O'Neil, 1982) can increase $\delta^{18}O$ in basalt to values of 8-10‰ within a few million years. The insoluble behaviour of Nd and Hf make these elements less susceptible to the effects of sea-water alteration; nevertheless, both are displaced from typical MORB values. The shift to less radiogenic εNd has been attributed to the addition of sediment to the basalt during subduction/underthrusting of the Pacific plate (Graham et al., 1990) which can also explain the similar behaviour in εHf. Previous studies investigating changes in Pb isotopes of basalt during sea-water alteration have proved inconclusive (Spooner and

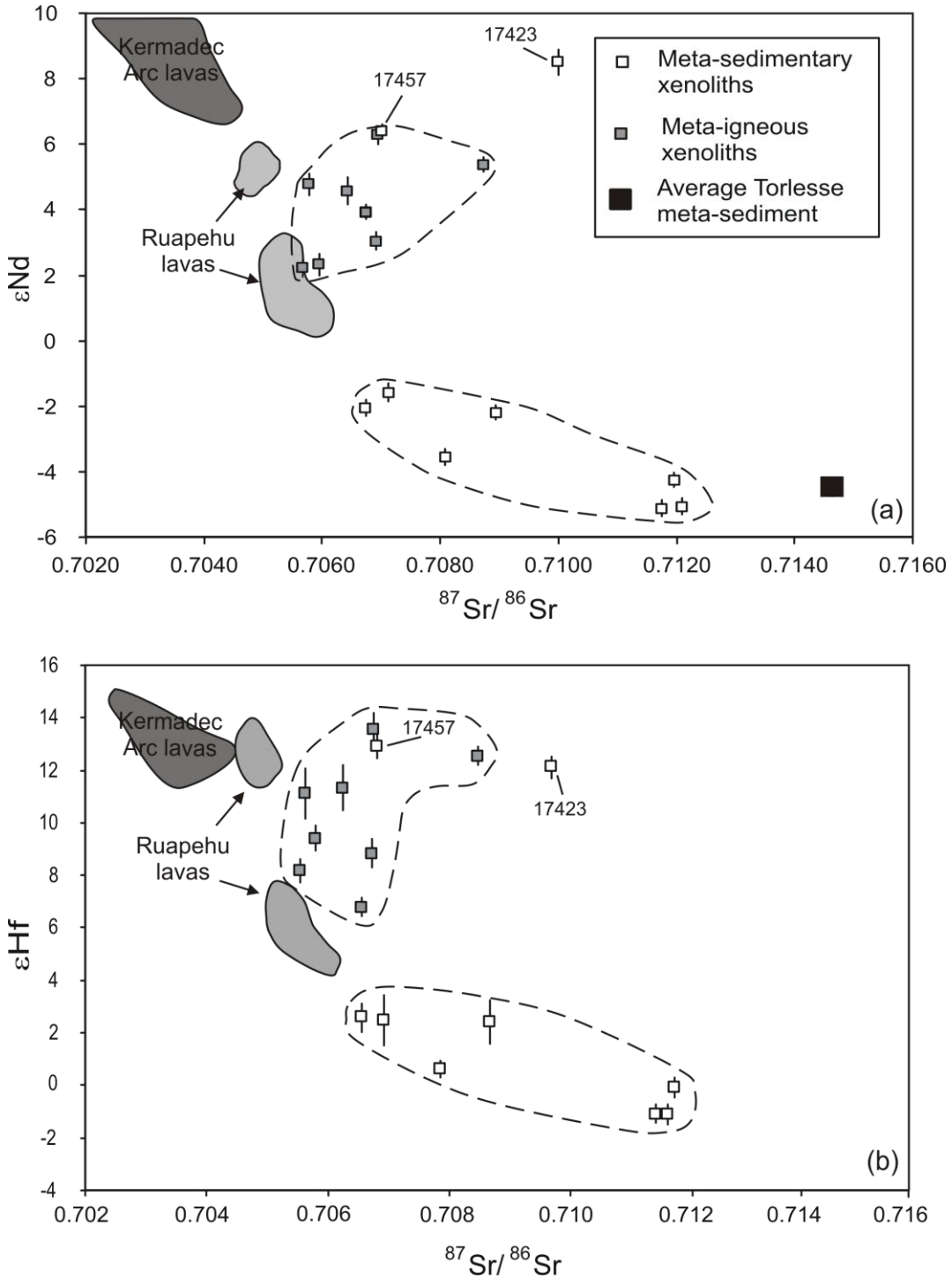

Fig. 2.6. Variation of a) εNd with $^{87}Sr/^{86}Sr$ and b) εHf with $^{87}Sr/^{86}Sr$ for Ruapehu crustal xenoliths. Note the clearest distinction between meta-igneous and meta-sedimentary xenoliths is in εHf values. Data sources: Kermadec Arc field from Gamble et al. (1996; $^{87}Sr/^{86}Sr$, εNd) and Woodhead et al. (2001; εHf); Average Torlesse meta-sediment from Graham et al. (1992); Torlesse trench sediment from Woodhead et al. (2001). External errors (2σ) are shown for each data point however they are often smaller than symbol.

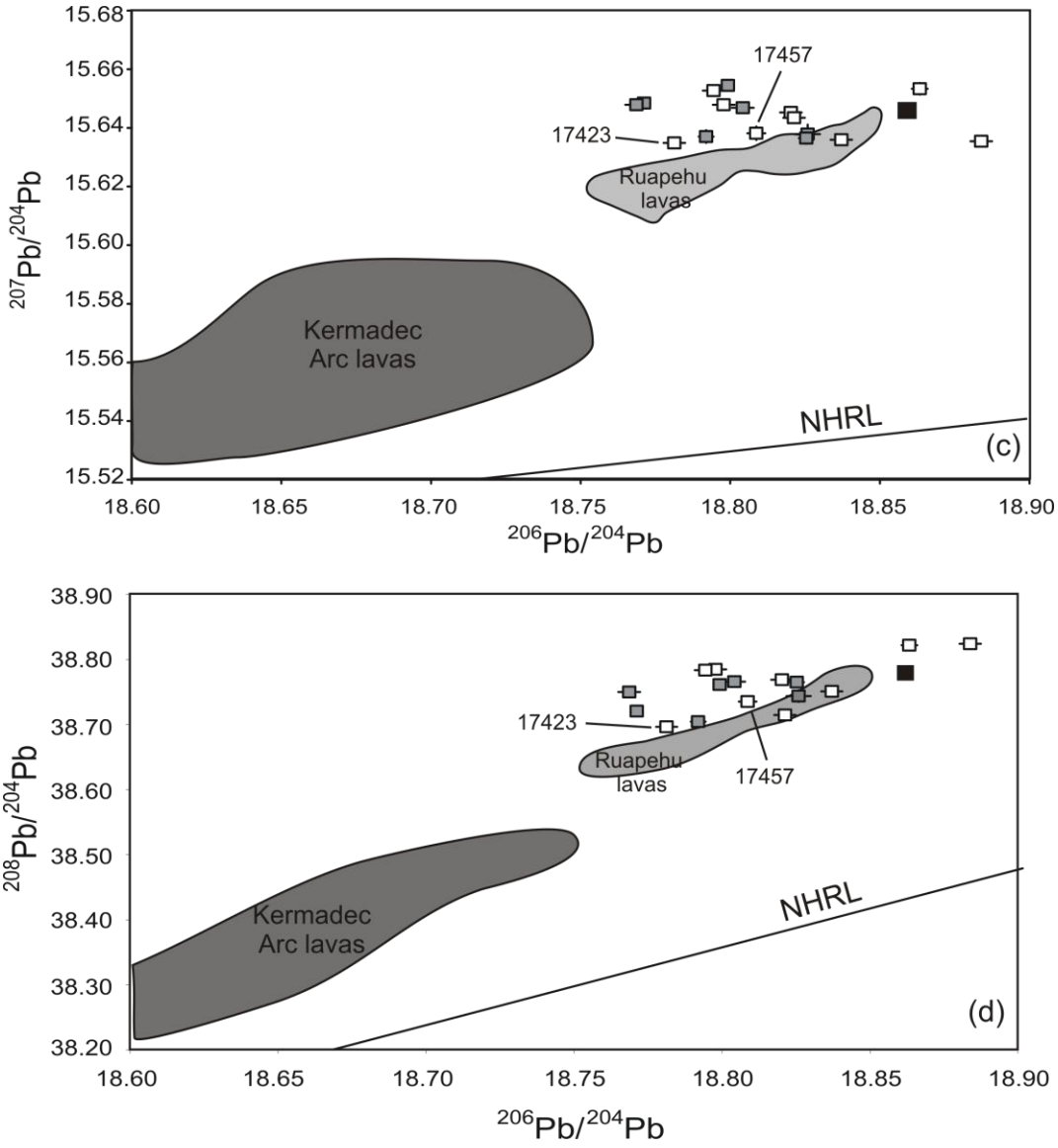

Fig. 2.6 cont. Variation of c) $^{207}Pb/^{204}Pb$ with $^{206}Pb/^{204}Pb$ and d) $^{208}Pb/^{204}Pb$ with $^{206}Pb/^{204}Pb$ for Ruapehu crustal xenoliths. Data sources: Kermadec Arc field from Gamble et al. (1995 & 1996; Pb isotopes); Average Torlesse meta-sediment from Graham et al. (1992); NHRL (Northern Hemisphere Reference Line) from Hart (1984). External errors (2σ) are shown for each data point however they are often smaller than symbol.

Gale, 1982; Vidal and Clauer, 1981). However the relatively immobile behaviour of Pb suggests a sedimentary component would also account for the radiogenic Pb in the meta-igneous xenoliths.

Alternatively the isotopic composition of the meta-igneous xenoliths could be a result of two stages of contamination on early underplated basalt (Fig. 2.7). During

the initial stages of magmatism beneath Ruapehu it is likely that the earliest melts would have stalled and slowly crystallised at the base of the crust, possibly assimilating small quantities of pre-existing crust (stage 1). Figure 2.7 displays Energy Constrained - Assimilation Fractional Crystallisation (EC-AFC (see Appendix G for details); Bohrson and Spera, 2001) modelling where mantle wedge basalt is contaminated by 1-5% of overlying Torlesse meta-sediment (Table 2.1; modelling parameters). Primitive wedge derived basalt compositions is assumed to equal a mean value from Rumble IV volcano (samples 161, 162 and 168/1B; Gamble et al., 1996; see Chapter 3 for further details). Modelled compositions would have lower εHf values (~ +13 to +8) due to the low Sr/Hf ratio in the assimilant. During assimilation, solidifying magmas will gradually release their volatiles and slowly convert to meta-basalts developing the granoblastic and schistose textures observed in the meta-igneous xenoliths. Fluids derived from freezing magmas have been shown to be a key part of lower crustal metamorphism (Newton, 1989) where cation exchange between fluids and minerals can significantly change the composition of lower crustal lithologies (e.g. transport of LILE and REE). Recent seismic studies in the North Island of New Zealand (Bannister et al., 2007; Reyners et al., 2007) provide significant evidence for fluids within the lower crust of the TVZ. These fluids could provide a mechanism for generating the radiogenic $^{87}Sr/^{86}Sr$ composition of the meta-igneous xenoliths by isotopic exchange between Torlesse meta-sediment and cumulate underplate whereby migrating fluids act as a medium of transport (stage 2). Although the exact composition of these lower crustal fluids is unknown, it is likely the fluid would have an elevated Sr/Hf ratio after interacting with Torlesse meta-sediment due to the higher solubility of Sr relative to HFSE. This ratio could be increased further as plagioclase is known to be particularly soluble in geothermal

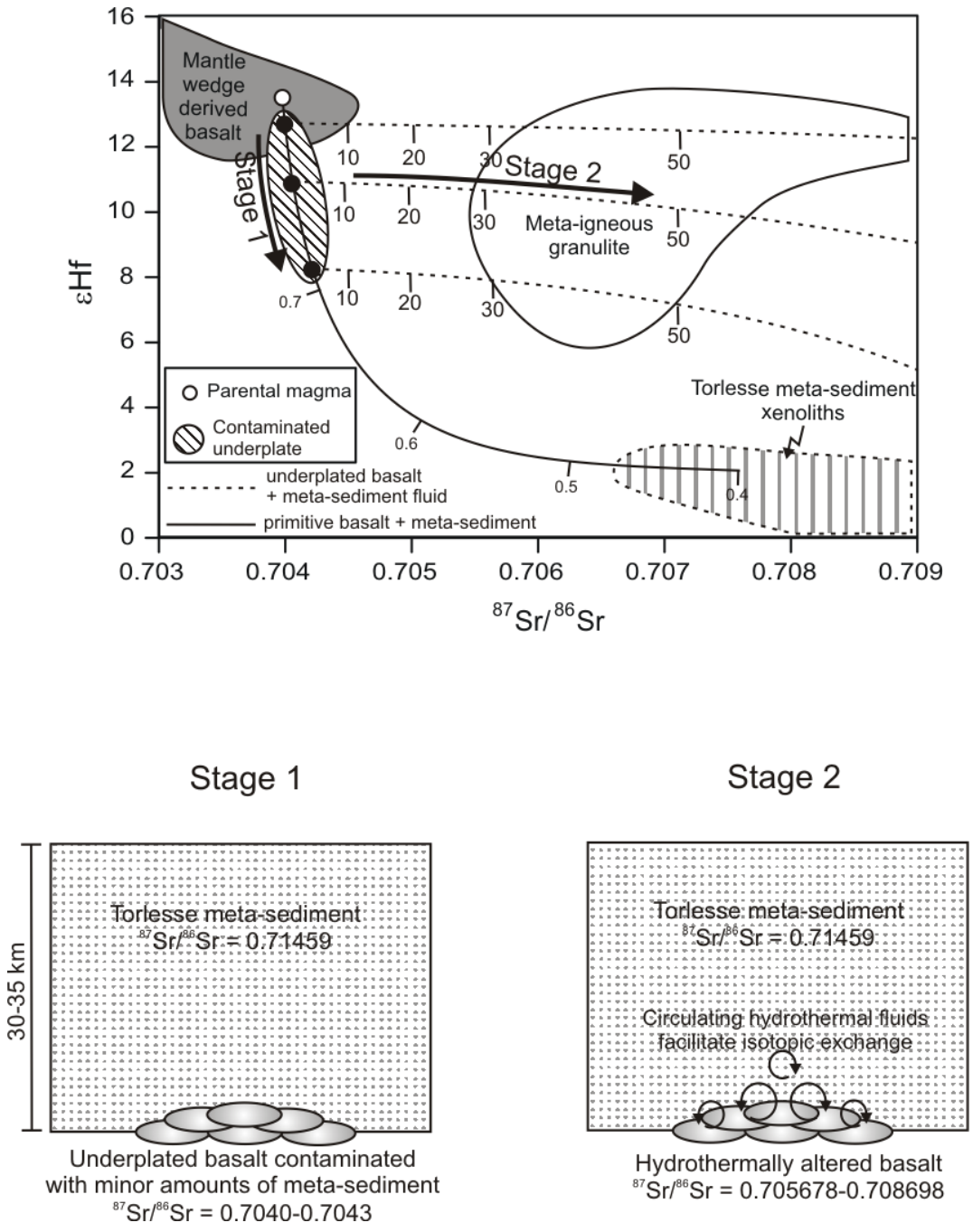

Fig. 2.7. Two stage modelling of meta-igneous granulite generation. Stage 1: EC-AFC (Spera and Bohrson, 2001) models using $^{87}Sr/^{86}Sr$ vs εHf for a mantle wedge basalt contaminated by Torlesse meta-sediment (1, 2 and 5% contamination). Modelling parameters listed in Table 2.1. Tick marks represent fraction of liquid remaining (F) in 0.1 increments. Mantle wedge derived basalt field from Kermadec Arc lavas (Gamble et al., 1996; Woodhead et al., 2001; Handler, M. pers comm). Stage 2: Mixing curves between contaminated basalts and hydrothermal fluid. Tick marks represent fraction of fluid involved in mixing. Modelling parameters listed in Table 2.2.

Table 2.1. End member compositions and parameters used in EC-AFC modelling

	Sr ppm (D)	Hf ppm (D)	$^{87}Sr/^{86}Sr$	εHf
Mantle wedge basalt	243 (0.5-1)	1.3 (0.2)	0.704	+13.4
Meta-sediment	217 (2)	7 (0.3)	0.71459	-1
	Initial Temp (°C)	Liquidus (°C)	Solidus (°C)	
Mantle Wedge basalt	1200	1150	-	
Meta-sediment	450	1000	800	

Bulk distribution coefficients (D) in brackets. Crustal lithology D values from Chapter 2. Melt D values calculated from observed phase proportions in samples and Kd values in Appendix F. Mantle wedge basalt εHf from Woodhead et al. (2001) and Handler, M. pers comm. Mantle wedge basalt trace element concentrations from Gamble et al. (1996). Initial temperature and liquidus values of parental magma determined by comparison of experimental estimates of primitive mantle wedge melts (Baker et al., 1994; Pichavant et al., 2002; Tatsumi, 1982; Ulmer, 2001). Initial temperature of meta-sediment are based on conservative estimates of a typical continental geotherm - 20°C/km (Brown and Musset, 1993), and relative depths of this lithology. This is intended to represent a meta-sediment temperature during the very initial stages of underplating/intrusion beneath Ruapehu and would increase with time as the TVZ crust thermally evolves. Solidus values of meta-sediment are based on experimental studies (Stevens and Clemens, 1993 and references therein).

Table 2.2. End member compositions used in mixing calculations

	Sr ppm	Hf ppm	$^{87}Sr/^{86}Sr$	εHf
Basalt	243	1.3	0.704-0.7043	+13 - +8
Fluid	100	0.000007	0.71459	-1

Basalt compositions represents varying degrees of Torlesse meta-sediment assimilation (1-5%). Fluid $^{87}Sr/^{86}Sr$ assumed to equal Torlesse meta-sediment. Fluid Sr concentration estimated from studies where geothermal fluid concentrations have been influenced by plagioclase feldspar dissolution (e.g. Cook and Herczeq, 2002). Hf concentrations are not availbale for geothermal fluids, hence sea-water concentrations are assumed to be an approximation of rock-fluid partitioning for this element (Environmental Chemistry: http://environmentalchemistry.com)

fluids (e.g. Cook and Herczeq, 1999; Ishikawa et al., 2007), although uncertainty exists if this is also the case within the lower crust. Modelling with a high Sr/Hf fluid composition illustrates meta-igneous xenolith isotopic compositions can be achieved by mixing 30-50% of lower crustal fluid with solidified meta-basalt (Table 2.2; modelling parameters). Lower crustal hydrothermal exchange was also suggested by Graham et al. (1990) and emphasised that meta-igneous granulite can be generated from recent underplated material as oppose to requiring underthrusting of altered Pacific oceanic crust.

2.4.3.2 Meta-Sedimentary Xenoliths

Although meta-sedimentary $^{87}Sr/^{86}Sr$ (0.706723-0.712072) values overlap with meta-igneous granulite, they extend to considerably more radiogenic compositions similar to average Torlesse sediment ($^{87}Sr/^{86}Sr$ = 0.71459; Graham et al., 1992) (Fig. 2.6a). εNd ((-1.6) – (-5.1)) values also encompass Torlesse sediment (εNd = -4.5; Graham et

al., 1992). No Hf isotope data has been published from the Torlesse terrain; however, there is good agreement between εHf values for xenoliths ((-1.2)-(+2.5)) and reworked Torlesse meta-sediment (Fig. 2.6b) derived from the Hikurangi Trough (εHf = -0.5; Woodhead et al., 2001). The Pb isotope fields for meta-sedimentary xenoliths encompass average values of the Torlesse terrain ($^{206}Pb/^{204}Pb$ = 18.859, $^{207}Pb/^{204}Pb$ = 15.646, $^{208}Pb/^{204}Pb$ = 38.787; Graham et al., 1992). However Pb isotopes provide a poor discriminatory tool for distinguishing meta-sediment and meta-igneous xenoliths (Fig 2.6c and d).

In addition to samples 17423 and 17457 exhibiting unusual trace element patterns, these xenoliths also possess different isotopic compositions. This is most notable in εNd and εHf values with 17457 (εNd = 6.4; εHf = 12.7) located in the meta-igneous field and 17423 (εNd = 8.5; εHf = 11.9) coinciding with primitive lavas from the Kermadec Arc (Fig. 2.5b). Similarly Pb isotopic compositions for both xenoliths are less radiogenic than other meta-sediment types with similarities to meta-igneous granulite. High concentrations of compatible elements (Ni, Cr and Cu) and distinctive radiogenic isotope values indicate samples 17457 and 17423 may have an igneous origin. Radiogenic Sr and Pb values however suggest they must have experienced similar alteration processes (lower crust hydrothermal fluids) to the meta-igneous xenoliths.

2.6 Melting reactions and textures; evidence from thin section

Partial melting of both crustal lithologies is evident from xenoliths in thin section. Figures 2.8a-c are photographs of a fine grained, silica-rich meta-igneous xenolith. Well developed foliation is defined by layers of quartz-feldspar and pyroxene. Parallel

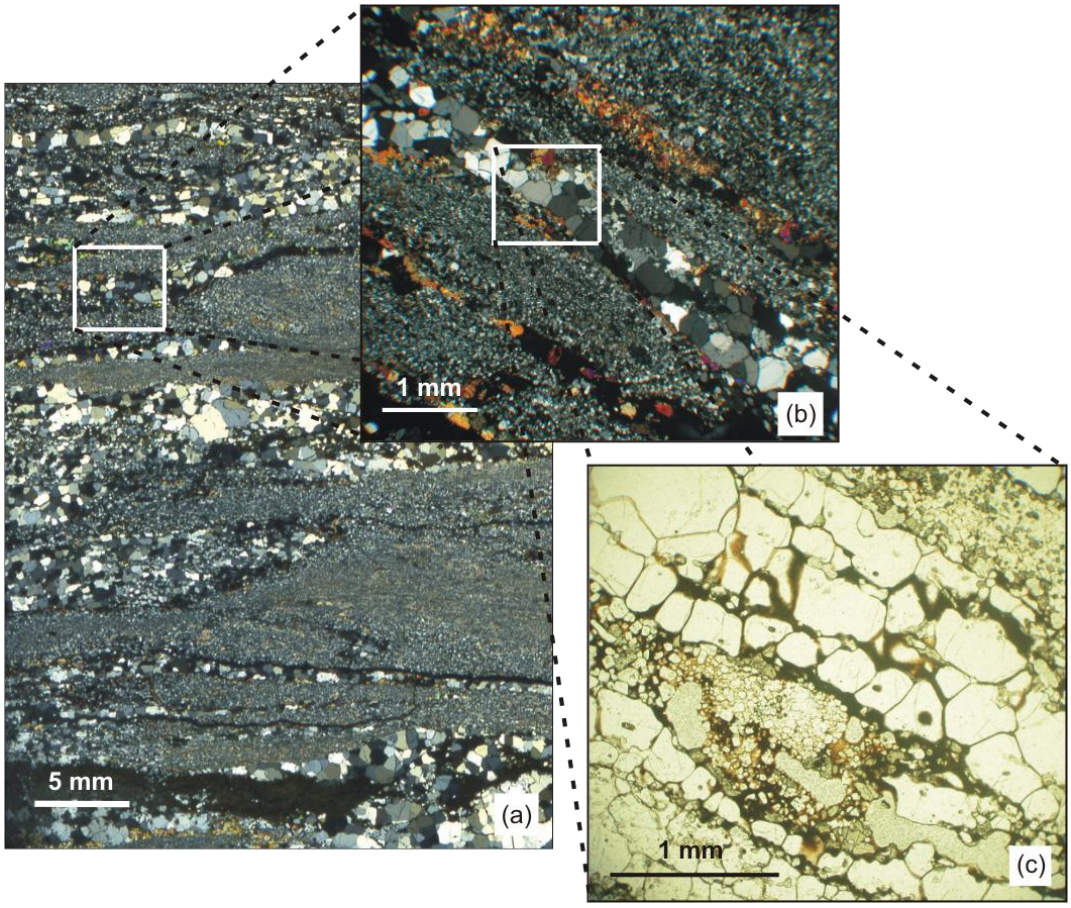

Fig. 2.8. Photographs of melting textures within meta-igneous xenoliths: a-b) leucosomes in meta-igneous granulite defined by quartz and pyroxene (high birefringence) foliations (XPL), c) detailed image of micro-leucosome illustrating melt films around quartz crystals and high relief mafic (pyroxene) selvedges (PPL).

to the foliation are quartz rich layers ~ 1-2 mm wide, interpreted as micro-leucosomes displaying a granoblastic texture (Fig. 2.8c). The leucosomes have thin mafic selvedges at the margins composed of pigeonite and augite-ferroaugite. Silica-rich glass (73-75 wt% SiO_2) occurs as melt films along grain boundaries and junctions between quartz crystals resulting in a rounded/corroded appearance. Similar textures reported elsewhere (e.g. Brown, 2006) have been interpreted as melt extraction by grain boundary flow. The leucosomes probably mark dilational sites forming parallel to foliation due to anisotropy within the protolith (Sawyer, 2001). The pyroxene is probably a residual product (melanosome) from the breakdown of a hydrous phase.

Crustal melting is particularly evident in thin sections of meta-sedimentary xenoliths, with melt preserved along foliation planes or in small vugs. An example of pervasive melting is illustrated in R96/26 (Fig. 2.9a-b); a quartz-plagioclase-spinel xenolith with > 60% glass. Glass compositions are rhyolitic (SiO_2 = 72-74 wt%) and metaluminous (molecular A/CNK = 0.94-0.99). The high degree of interconnectivity between glass pockets suggests the xenolith had reached its percolation threshold and was probably close to complete digestion within the host magma. In other meta-sedimentary xenoliths melting appears to have been less destructive with one example still preserving original sedimentary laminations (Fig. 2.8c; WX9). WX9 is a fine grained plagioclase-quartz-orthopyroxene-biotite-spinel-cordierite bearing meta-sediment. Glass occurs at the margins of the xenolith and within extensional shear bands perpendicular to sedimentary laminations. Within the shear bands orthopyroxene, oxides, spinel and biotite coexist with glass and represent either residual melting products or meta-stable peritectic phases. Two distinct dacitic glass compositions can be identified on the basis of silica and alumina content (Fig. 2.10a-b) and contrasting molecular A/CNK values. Alkali enrichment in the glass phase suggests that the orthoclase component of decomposing biotite enters the melt while partitioning of Fe, Mg and Ti into peritectic phases (oxides, spinel and orthopyroxene) prevents enrichment of these elements in the melt (Vielzeuf and Montel, 1994). The bimodal glass compositions probably reflect fine interbedding in the original Torlesse sediment with lower SiO_2-peraluminous glasses associated with argillite layers while higher SiO_2 compositions relate to greywacke laminations. High volumes of glass within the shear bands also suggest they acted as small scale melt conduits. Presumably deep in the crust these would have been part of a complex drainage network leading to progressively larger melt pathways, e.g. leuocosome stromata and

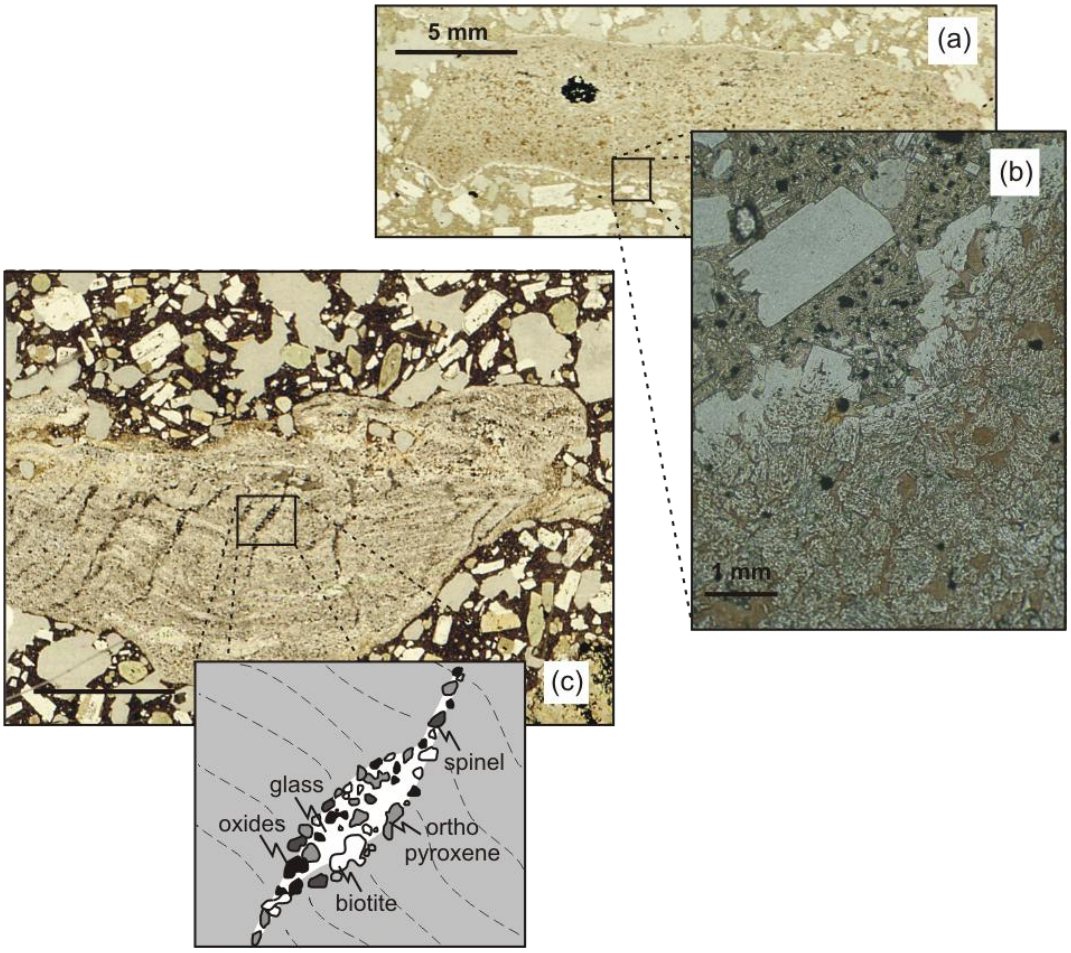

Fig. 2.9. Photographs (PPL) of melting textures within meta-sedimentary xenoliths: a) elongate meta-sedimentary xenolith (R96/26) with quartz-feldspar-spinel assemblage. Dark porphyroblast is spinel, b) detailed image of the xenolith rim illustrating the glasses (brown) pervasive nature and high degree of interconnectivity (PPL), c) preservation of original sedimentary laminations within meta-sediment (from lava WX9; PPL). Drawing illustrates melt filled shear bands (micro-melt conduits) perpendicular to sedimentary laminations. Spinel, orthopyroxene and biotite occur within the glass.

dike feeder systems. Previous studies have suggested that if melt is allowed to accumulate in the matrix of a rock to > 20-30% volume, magma-like flow occurs and original internal features such as sedimentary laminations are destroyed (Vigneresse et al., 1996). Therefore, preservation of sedimentary laminations in WX9 may suggest the Torlesse meta-sediment has well developed permeability networks during crustal melting.

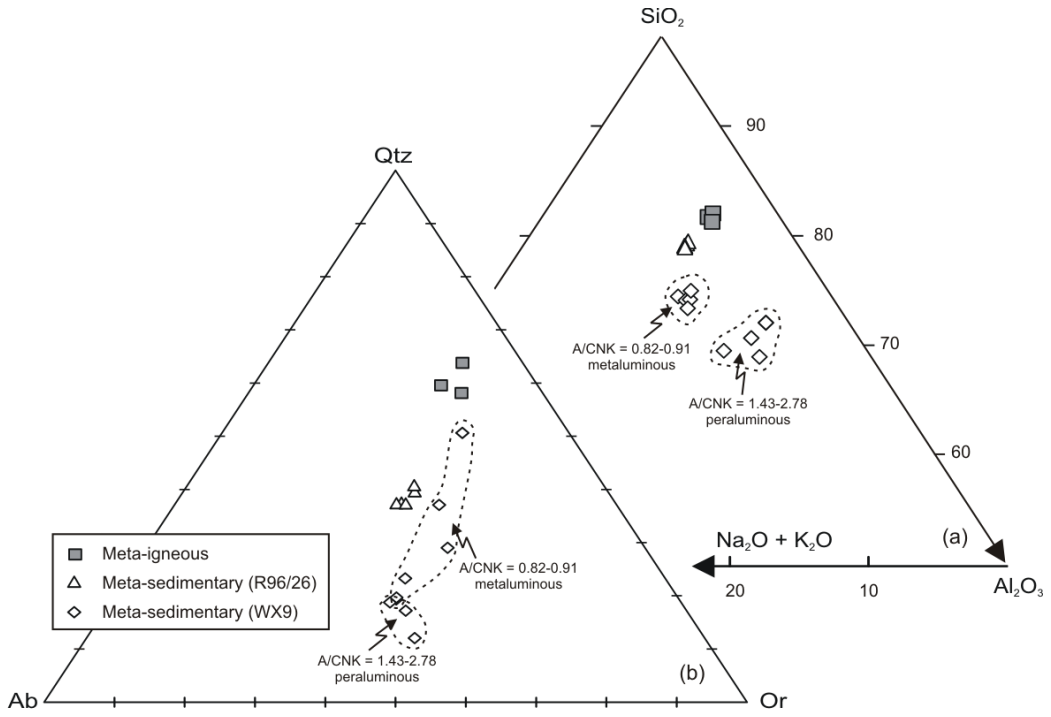

Fig. 2.10. Glass compositions from meta-igneous and meta-sedimentary xenoliths in terms of a) weight percent SiO_2-Al_2O_3-(Na_2O + K_2O) and b) CIPW normative Qtz-Ab-Or.

Figure 2.10 also illustrates that glass compositions in meta-sediments differ to those in meta-igneous xenoliths; glass compositions within the meta-sediments are generally more alkaline and contain less silica relative to meta-igneous samples.

2.6 Partial melting reactions

Most crustal-derived melts are formed by fluid absent melting reactions, usually at temperatures ≥ 800 °C (Clemens, 2006). Combining geochemical and petrographic evidence from crustal xenoliths with each respective protolith composition allows a detailed inspection of specific metamorphic reactions responsible for partial melting in each lithology.

The mafic mineralogy in meta-igneous xenoliths indicates they formed by granulite metamorphism of a basaltic material. Crustal melting in mafic lithologies is usually a result of amphibole dehydration reactions (Clemens, 2006):

$$hbl \pm qz \pm plag = opx + cpx + plag + melt$$

Experimental evidence indicates amphibole becomes unstable between ~ 850-925°C at 7-10 kbar (Beard and Lofgren, 1991; Rushmer, 1991; Wolf and Wyllie, 1994). Although petrographic evidence for amphibole is lacking, its involvement in melting of the lower crust is illustrated in REE data. Figure 2.11a illustrates that amphibole preferentially incorporates MREE over HREE compared to clinopyroxene. Consequently partial melting in the presence of residual amphibole will produce a restite and melt with a higher and lower MREE/HREE ratio, respectively when compared to the original source composition. This relationship is observed in the meta-igneous xenoliths although the absence of amphibole from the mineral assemblage indicates the samples represent the melt dominated end members with lower Dy/Yb ratios than the original source (Fig. 2.11b). This suggests the source rock has a mafic/ultramafic composition (~45 wt% SiO_2) indicative of a cumulate underplate. However an alternative explanation for the absence of amphibole is that dehydration reactions were taken to completion, exhausting this phase from the xenoliths mineralogy.

Phase changes during partial melting of metapelites and metagreywackes have been studied by many authors (e.g. Montel and Vielzeuf, 1997; Patino-Douce and Beard, 1995; Patino-Douce and Johnston, 1991; Stevens et al., 1997; Vielzeuf and Holloway, 1988). The mineralogy of the meta-sedimentary xenoliths indicates melting of this lithology is induced by mica breakdown (Stevens and Clemens, 1993 and references therein):

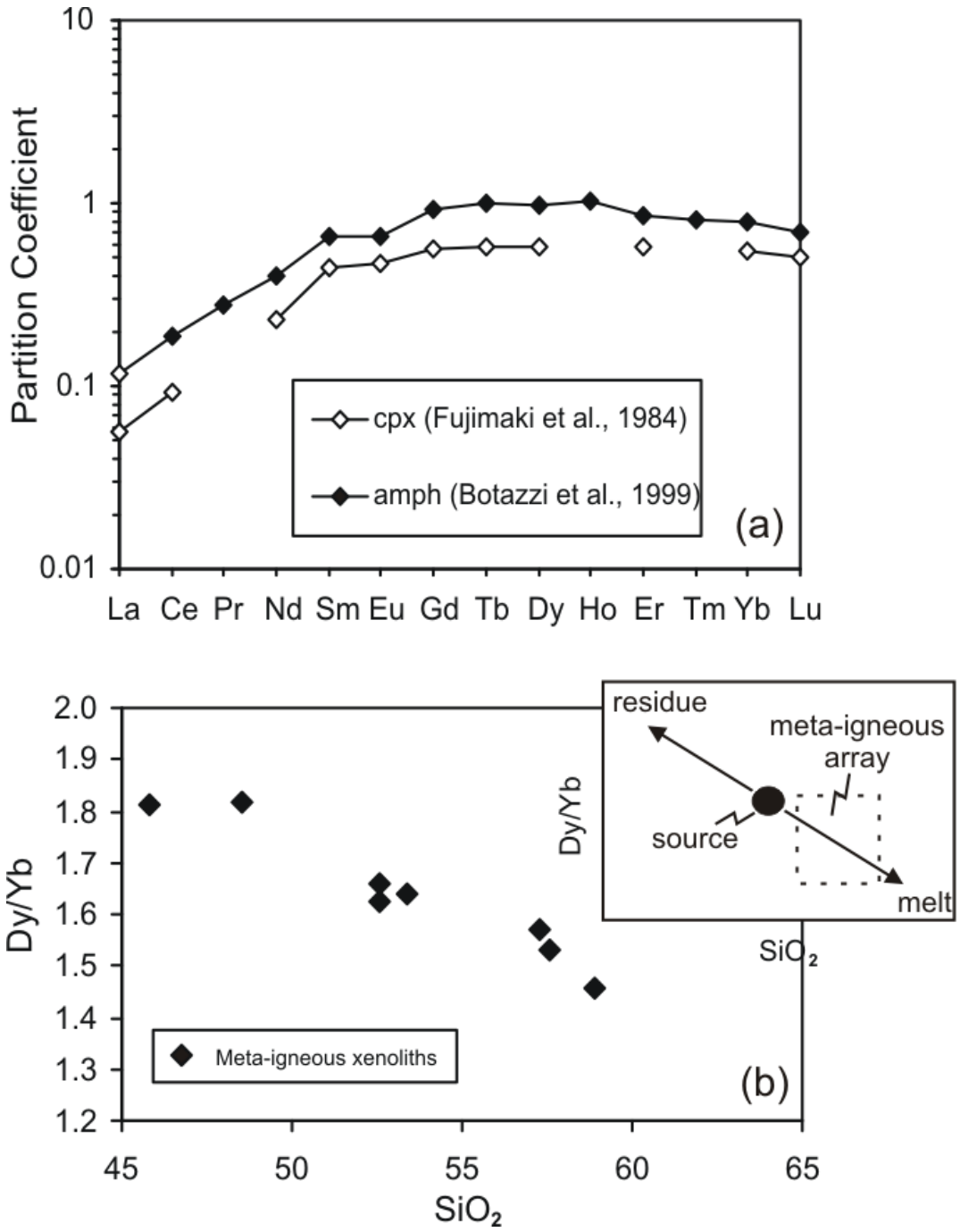

Fig. 2.11. a) REE diagram illustrating partition coefficients for clinopyroxene and amphibole with a basaltic liquid. Note amphibole preferentially incorporates MREE over HREE. b) Variation of Dy/Yb with SiO_2 for meta-igneous xenoliths. The negative correlation suggests partial melting in the presence of amphibole. Data sources: Clinopyroxene from Fujimaki et al. (1984); Amphibole from Botazzi et al. (1999).

muscovite + qz + plag = melt + sillimanite ± kspr (740°C, 7kbar)

biotite + aluminosilicate + qz + plag = melt + grt/crd ± kspr + melt (850°C, 10 kbar)

biotite + qz + plag = melt + opx ± cpx ± kspr (900°C, 10 kbar)

biotite + plag + sill = melt + ilm + biotite + spl + plag (900°C, 500 MPa)

Although experimental evidence indicates that K-feldspar is a product in many of these reactions it is generally absent in outcrop examples (Clemens, 2006), suggesting the melt phase is often enriched in K_2O, as seems to be the case in meta-sedimentary xenolith glasses from this study (K_2O = 4.7-6.2 wt %; Appendix D).

2.7 Partial melting of xenoliths and composition of melts; clues from trace elements.

It is desirable to constrain the geochemical effects partial melting has had on the crustal xenoliths. Furthermore assessing if there is any distinct compositional difference in melts produced from meta-igneous and meta-sedimentary xenoliths is particularly useful when examining reasons for differences in trace element compositions in Ruapehu lavas (see Te Herenga and Post Te Herenga lava compositions in Chapter 3).

Based on thermometry calculations for meta-igneous and meta-sedimentary xenoliths (900-1000 °C; Graham, 1987; Graham et al., 1990) many, if not all, samples have experienced granulite metamorphism. Restite rocks at granulite facies within the lower crust should be characterised by: depletions in K, Rb, Th and U; increases in K/Rb and Th/U, and exhibit positive Eu anomalies (Heier and Thoresen, 1971; Rudnick et al., 1985; Rudnick, 1992). These features are necessary to mass balance the enrichment of LILE and negative Eu anomalies in the upper crust. Studies of granulites from surface outcrops however rarely exhibit these restite features

(Rudnick, 1992). Two reasons have been proposed to explain why this might be the case: a) the parent of the granulite also had a negative Eu anomaly, and/or b) melt must still remain in the residue (Rudnick, 1992). LILE concentrations are usually an order of magnitude higher in melt relative to its residue; consequently, any retention of melt results in this phase dominating the LILE signature of the rock. The lower crustal meta-igneous xenoliths in this study do exhibit characteristic LILE depletions relative to the upper crust (see Fig. 2.5 for comparison); however, they do not display positive Eu anomalies. Therefore, considering the anhydrous mineralogy and general lack of melt observed in most thin sections (Graham et al., 1990), the meta-igneous protolith must also have had a negative Eu anomaly.

Previous studies have recognised that relative element depletions in granulites resulting from lower crustal metamorphism are particularly evident in LILE ratios (e.g. K/Rb and Th/U) of granulites (Rudnick et al, 1985). K_2O versus K/Rb (Fig. 2.12a) indicate that the K/Rb ratios for the whole xenolith dataset can generally correlated to absolute K_2O concentration. The data can be sub-divided into K_2O contents > 0.5 % that have K/Rb between 200-300, and K_2O contents < 0.5 % that have K/Rb = 300-500. The majority of the meta-igneous xenoliths occupy the group with higher K/Rb values; implying granulites with lower K_2O contents have experienced greater degrees of Rb depletion. Similar features have been reported in other granulite terrains (Rudnick et al., 1985; Rudnick, 1992) where greater Rb depletions in lower K_2O rocks have been explained by the mineralogy and composition of the protolith. Rocks with low K_2O contents usually require potassium to be preferentially accommodated within plagioclase due to the absence of any K-bearing minerals. However large cations like Rb are excluded from most anhydrous mineral lattice sites, resulting in Rb behaving as a mobile element. This may account

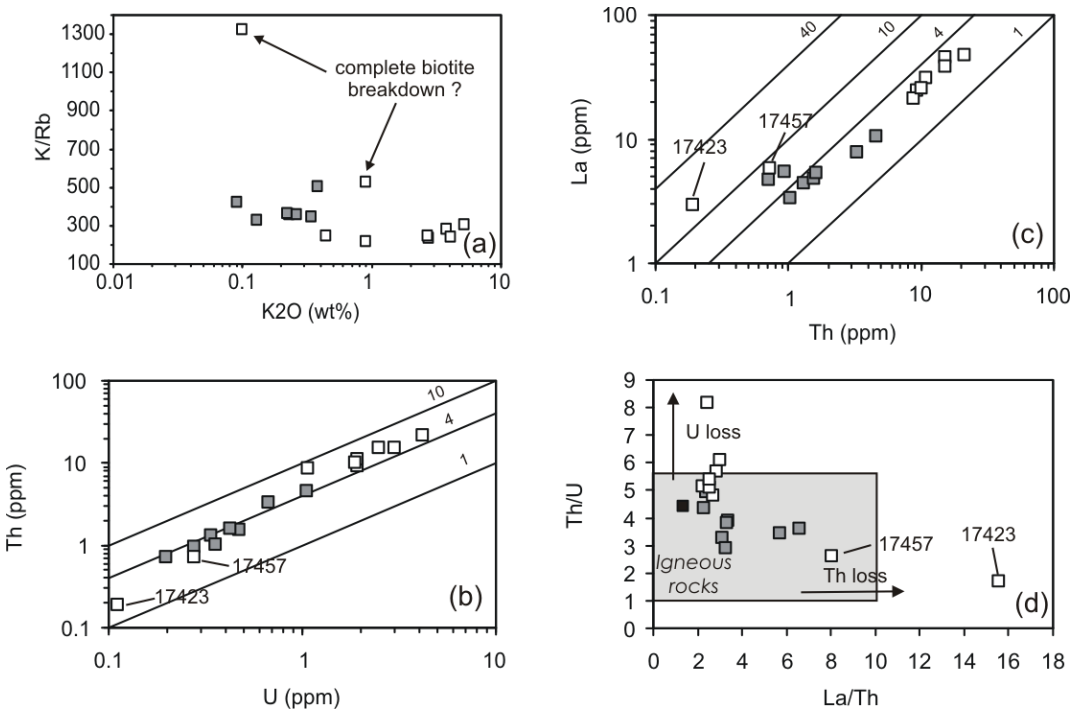

Fig. 2.12. Variation of a) K_2O versus K/Rb b) Th with U, c) La with Th and d) Th/U with La/Th for Ruapehu crustal xenoliths. Note xenoliths with < 0.5 wt% have greater degrees of Rb depletion and most meta-sedimentary xenoliths display U depletion relative to Th. Igneous rock field from Roger and Adams, (1978).

for its notable depletions in the meta-igneous granulite. The two meta-sedimentary xenoliths also exhibiting Rb depletion may be a result of complete biotite breakdown (e.g. biotite + quartz = enstatite, k-feldspar + vapour; Cesare, 2000). Biotite contains proportionally more Rb than K-feldspar; hence this reaction will result in a rapid increase of K/Rb within the restite assemblage. However the majority of the meta-sedimentary xenoliths have higher K_2O contents. Many of these samples contain residual biotite and/or have retained melt, both of which can account for their higher Rb concentrations.

Th and U depletions are also characteristic of some granulites (Rudnick et al., 1985). Most igneous rocks have Th/U ratios of 3.5-4.0 (Roger and Adams, 1978); consequently, this ratio can be used to assess relative depletions in the meta-igneous xenoliths. Similarly depletions in Th and U for the meta-sedimentary xenoliths can be

made by comparing its Th/U ratio with a value from average Torlesse sediment (~ 4.5; Graham, 1985b). Based on their very low abundances, U and Th are probably depleted in meta-igneous xenoliths; however, the Th/U ratio has remained constant ~ 4 (Fig. 2.12b). On the other hand, most of the meta-sedimentary xenoliths seem to exhibit moderate U depletions, as indicated by Th/U ratios > 4.5. Two anomalous meta-sedimentary xenoliths (17423 and 17457) appear to display Th depletions relative to U, however both these samples have very low absolute concentrations of U and Th and radiogenic isotopes which indicate an igneous protolith. Determining relative Th depletions within the xenoliths can be assessed by comparison with an immobile element like La, using La/Th ratios from each protolith (La/Th = 1-10 for igneous rocks (Rudnick et al., 1985); La/Th = 1.5 for average Torlesse sediment) (Fig. 2.12c). It is unclear if Th is depleted in the meta-igneous xenoliths as all samples have La/Th < 10. Most of the meta-sedimentary xenoliths may have small degrees of Th depletion compared to the Torlesse sediment although this is only definitive for the two samples with very low absolute La and Th concentrations (La/Th = 8.1 and 15.6). The behaviour of Th and U in the xenoliths is summarised in La/Th versus Th/U (Fig. 2.12d), illustrating there is no comparative loss in U or Th within the meta-igneous xenoliths based on their similar La/Th and Th/U ratios to unmetamorphosed igneous rocks. In contrast, most of the meta-sedimentary xenoliths display relative loss in U, apart from two samples which also are depleted in Th. U depletion in the meta-sedimentary xenoliths has been explained by this element preferentially concentrating along mineral grain boundaries (Dostal and Capedri, 1978), opposed to Th which only occupies mineral lattices. Grain boundary U concentrations have a strong tendency to mobilise when hydrous fluids are released between amphibolite and granulite facies metamorphism, resulting in a residue depleted in this element.

Crustal melting can also be examined by comparing the compositions of xenoliths with their respective partial melts (LA-ICP-MS; Price et al., 2005). Unfortunately it is difficult to determine if trapped melt within crustal xenoliths represent the original partial melt composition since many only preserve melt residuum, i.e. the immobile portion of the melt (Guernina and Sawyer, 2003). Therefore in this study an assessment of geochemical changes during crustal melting is based on trace element trends in xenoliths and melts, normalised to an approximated protolith composition (Fig. 2.13). Accordingly if an accurate protolith is used, relative trace element depletion patterns in restite xenoliths will be reflected by subsequent enrichment patterns in the partial melt. For this reason, meta-igneous xenoliths are not included here due to poor constraints on the protolith composition. Figure 2.13 illustrates that meta-sedimentary xenolith melt is enriched in incompatible elements with the only notable exception being the compatible behaviour of Sr and Eu which can be explained by residual feldspar. The greater incompatible trace element abundances within the meta-sediments compared to meta-igneous xenoliths (Fig. 2.5) is similarly reflected in the composition of each respective melt. This is apparent in U and Th, with nearly an order of magnitude difference between melt derived from meta-sediment and meta-igneous granulite which is particularly significant in the generation of younger lavas at Ruapehu (see Post Te Herenga lavas in Chapter 3). Furthermore as U and Th are strongly partitioned into refractory phases like zircon, the strong enrichment of these elements in the meta-sedimentary melt suggests this mineral is not a significant residual phase. In the absence of garnet, HREE are also partitioned into accessory phases like zircon; consequently, the enrichment of Dy-Yb in the meta-sedimentary melt also indicates that zircon is not present in the residue. The depletion of Rb and Ba in the meta-sedimentary melt phase is probably a result of

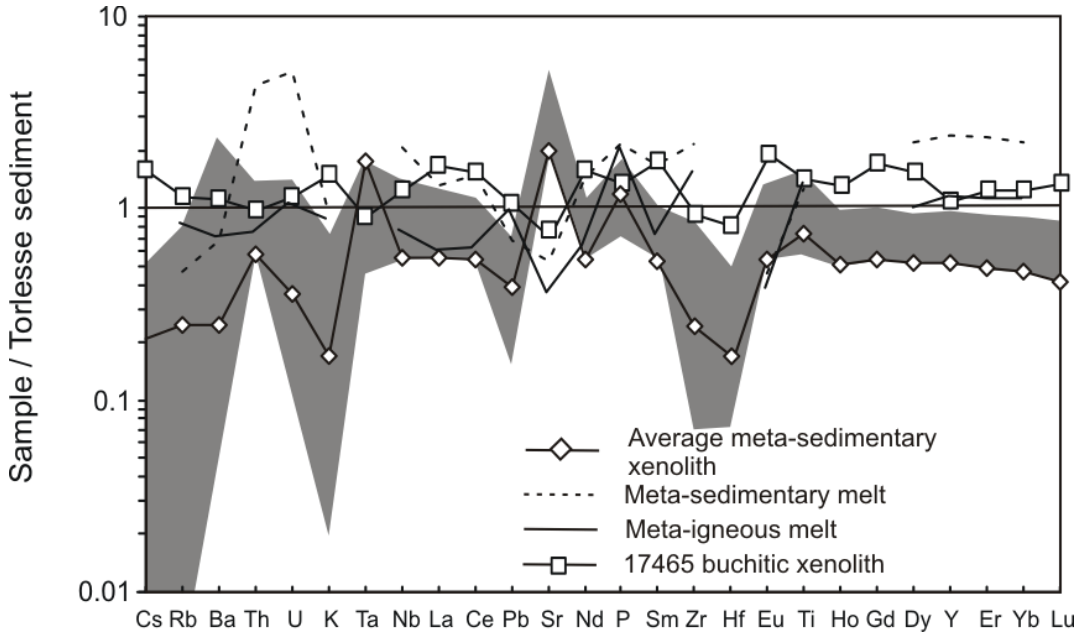

Fig 2.13. Torlesse sediment normalised trace element diagram for meta-sedimentary xenoliths (grey shaded field) and meta-sedimentary melt data. Meta-igneous melt data shown for comparison. Note: enrichment in most incompatible elements within the melt except depletion in Sr and Eu; depleted restite patterns of xenoliths; strong enrichment in U and Th in melt phase reflected in depletions of these elements in the average meta-sedimentary xenolith data. Data sources: Torlesse sediment normalisation values from Graham (1987); Meta-igneous and meta-sedimentary melt data from Price et al. (2005).

residual biotite and K-feldspar within the xenolith assemblage. However enrichment in Rb and Ba in the meta-igneous melt can be explained by the inability of the anhydrous restite assemblage to accommodate these elements. The minimal trace element depletions in the buchitic meta-sedimentary xenoliths (e.g. 17465) have been attributed to a shallow origin (~ 1.5 kbar) which has inhibited significant melt extraction by the host lava (Graham et al., 1988).

*D*s (bulk partition coefficient = conc^n trace element solid (*Cs*) / conc^n trace element liquid (*Cl*)) can be calculated by using bulk chemical analyses of xenoliths (*Cs*) with glass data (*Cl*) (Price et al., 2005) to estimate the behaviour of trace elements during partial melting (Fig. 2.14). These will be particularly useful for Sr, Nd and Hf which are used in crustal contamination modelling in later chapters. For

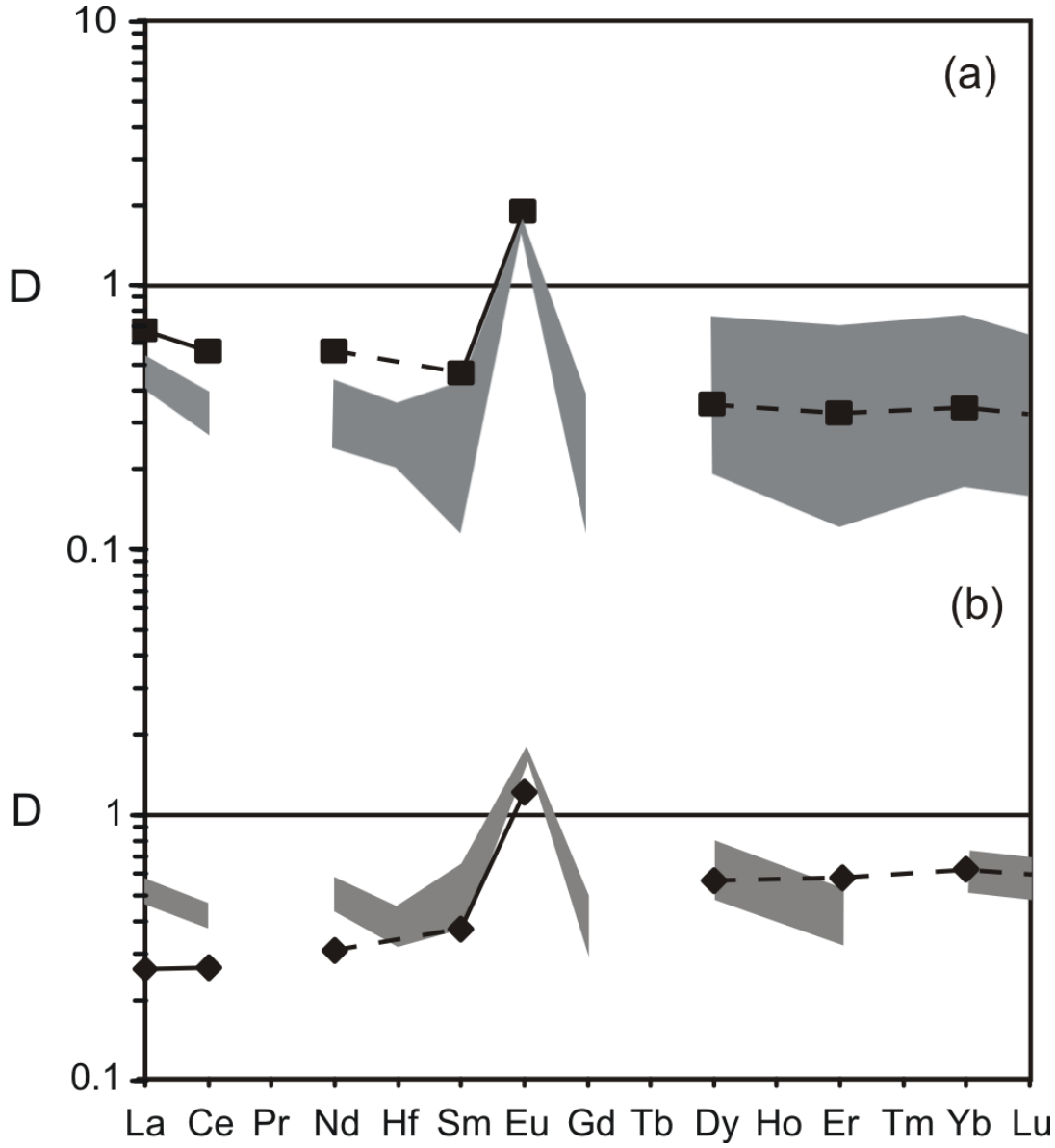

Fig. 2.14. *D* (bulk partition coefficient) estimates for REE in, a) meta-sedimentary xenoliths and b) meta-igneous xenoliths. Calculated using bulk chemical analyses of xenoliths and glass data (Price et al., 2005). Grey shaded fields are theoretical bulk partition coefficients calculated using a range of xenolith mineral abundances and rhyolite partition coefficients from Rollinson (1993).

comparison theoretical *D*s have also been calculated for a range of xenolith modal abundances and silica rich liquids for each crustal lithology (Table 2.3 and 2.4). Both methods compare favourably and suggest most REE behave incompatibly during partial melting of meta-igneous and meta-sedimentary xenoliths. Average Nd *D* values of 0.3 were chosen for meta-igneous granulite and 0.4 for meta-sediment.

Table 2.3. Meta-igneous xenolith mineral abundances used for calculating theoretical D values during partial melting using rhyolite trace element partition coefficients

Plag	Opx	Cpx	Ilm
0.5	0.3	0.1	0.1
0.7	0.1	0.1	0.1
0.5	0.2	0.1	0.2
0.4	0.2	0.2	0.2
0.5	0.3	0.15	0.05
0.5	0.3	0.03	0.17
0.6	0.3	0.05	0.05

Table 2.4. Meta-sedimentary xenolith modal abundances used for calculating theoretical D values during partial melting using rhyolite trace element partition coefficients

Plag	Kspr	Opx	Cpx	Bio	Ilm	Mag	Grt
0.7	0.1	0.1	0	0.05	0	0.05	0
0.65	0.1	0.1	0	0.05	0.05	0.05	0
0.6	0.1	0.1	0.05	0.05	0.05	0.05	0
0.6	0.1	0.1	0.1	0	0.05	0.05	0
0.6	0.1	0.1	0.09	0	0.05	0.05	0.01
0.6	0.1	0.1	0.09	0.02	0.03	0.05	0.01
0.6	0.1	0.1	0.09	0.02	0.03	0.06	0

Unfortunately Hf glass data was not available although the theoretical comparison field suggests a *D* value 0.3 and 0.4 are also reasonable for meta-igneous granulite and meta-sediment respectively. Although not illustrated, the same methods were used for Sr *D* values. Sr appears to be compatible (D = 1.5-3.0) during partial melting in meta-igneous and meta-sedimentary xenoliths. This can be explained from petrography, with a residual feldspar assemblage present in both xenolith types which also accounts for the similar behaviour in Eu.

2.8 Summary and Conclusions

The two most abundant crustal xenoliths found at Ruapehu are meta-igneous and meta-sedimentary xenoliths. The anhydrous mineralogy of the meta-igneous xenoliths consists of plagioclase, orthopyroxene, clinopyroxene and ilmentite. The meta-sedimentary mineralogy is more variable but is generally quartz, feldspar or spinel rich with micas and other minor phases.

The stratigraphy of the crustal column beneath Ruapehu based on xenoliths and geophysical studies consists of a 5-10 km thick meta-igneous lower crust, overlain by 20-25 km of Torlesse meta-sediment. The source of the meta-igneous xenoliths remains contentious, however the LILE-LREE enrichment and HFSE depletion relative to N-MORB suggests the mafic protolith maybe underplated material (cumulates) related to current magmatism at Ruapehu. However radiogenic $^{87}Sr/^{86}Sr$ values indicate this cumulate material must have underwent isotopic hydrothermal exchange with overlying Torlesse meta-sediment during or after conversion to meta-basalt.

Sr and Pb isotopes display overlap between meta-igneous and meta-sedimentary xenoliths whereas εNd and εHf values efficiently distinguish between each lithology. Both xenolith types are distinct from MORB and Ruapehu compositions indicating contamination of lavas from crustal lithologies will be discernible in isotope space.

Partial melting in xenoliths is probably induced by the breakdown of hydrous phases during the transition from amphibolite to granulite facies. Although no hydrous phases are present in the meta-igneous assemblage REE data indicates that partial melting involves amphibole. Partial melting within the meta-sediments is controlled by biotite and/or muscovite. The greater abundance of glass in meta-

sedimentary xenoliths indicates it is more fertile than lower crustal meta-igneous granulite. Similarly this is reflected in the meta-sedimentary glass compositions which tend to be richer in alkalis and alumina than glass within meta-igneous xenoliths.

Trace element patterns of meta-sedimentary xenoliths normalised to an estimated protolith composition (Torlesse) highlight that these xenoliths tend to have refractory/restite characteristics. Furthermore, specific trace element depletions within the restite xenoliths are often complimented by subsequent enrichment patterns in crustal melt data.

A simple relationship exists between K_2O content and degrees of Rb depletion within the xenolith dataset. The greatest Rb depletion occurs within the meta-igneous samples (K_2O < 0.5 wt %), while the group with K_2O > 0.5% is composed largely of meta-sedimentary xenoliths. The K_2O-Rb relationship is controlled by mineralogy and is largely dependent on the presence of K-bearing minerals, e.g. K-feldspar and biotite.

U and Th depletions are also common and display differing behaviour between meta-sedimentary and meta-igneous xenoliths. Although these elements are depleted in both xenolith types, the meta-sedimentary samples show greater degrees of relative U loss due to this element concentrating along grain boundaries. Meta-igneous samples do not illustrate relative U depletion because of its location in mineral lattice sites.

Finally the anomalous trace elements concentrations (e.g. high Cr, Ni and Cu) and primitive εNd-εHf values in samples 17423 and 17457 are very different to other meta-sedimentary xenoliths indicating they formed from an igneous protolith.

Chapter 3

Characterising temporally distinct geochemical evolutionary pathways at Mt. Ruapehu

3.1. Introduction

Arc magmatism has played a crucial role in continental crustal growth throughout the Phanerozoic (Davidson and Arculus, 2006; Rudnick, 1995). Petrogenetic models of crustal generation in arcs generally involve intrusion of the crust with primary melts derived from hydrous partial melting of mantle peridotite. However the evolved composition of many arc magmas indicates that primary melts rarely reach the Earth's surface as a result of the large density contrast between mantle melts and the continental crust. Consequently it is envisaged that many primary magmas stall in the lower crust near the Moho (under/intraplating), where they differentiate to produce the andesitic compositions commonly associated with convergent margins (e.g. Annen et al., 2006; Hildreth and Moorbath, 1988).

It is not surprising therefore that intra-crustal differentiation is frequently recognised in arc lavas, with fractional crystallisation (Handley et al., 2007), crustal assimilation (Davidson et al., 1987; Hildreth and Moorbath, 1988; Macpherson et al., 1998) and magma mixing (Gamble et al., 1999; Nakagawa et al., 2002) identified as common processes that modify primary magmas. Consequently, resolving differentiation histories in arcs can be challenging particularly as the degree and/or type of differentiation rarely remains constant throughout the lifetime of a magmatic system. However, using stratigraphically controlled sample suites from individual volcanoes has proved particularly useful in this regard as additional constraints can be placed on; a) individual fractionation trends and b) local crustal contaminants.

Mt. Ruapehu volcano is located at the southwest termination of the Taupo Volcanic Zone (TVZ) in New Zealand. The TVZ forms the southern extremity of the 3000 km long Tonga-Kermadec arc where the upper plate of the subduction zone changes from oceanic to continental lithosphere. The arc has developed by the

continued subduction of the Pacific plate beneath the Australian plate, with current convergence rates displaying a systematic decrease with latitude from 17.8 cm/year near Tonga (Smith and Price, 2006) to 4.5 cm/year (Acocella et al., 2003) offshore New Zealand (Hikurangi Trough). The 250-300 km long TVZ has been active for ~ 2 Myrs and is characterised by thin extended continental crust with exceptionally high heat flow (~700 mW/m^2; Bibby et al., 1995). The central region of the TVZ is dominated by rhyolites (15,000-20,000 km^3) which comprise > 80% of the total erupted material. The remaining volcanism has been erupted from andesite centres at the southern and northern margins of the TVZ. Volcanism has migrated south with time as rifting from the Kermadec arc has propagated into the North Island lithosphere making Ruapehu the most recent addition to the TVZ. It therefore provides a unique opportunity to investigate intra-crustal differentiation processes during early stage magmatism in a continental arc.

Ruapehu has been studied extensively over the past two decades, with detailed mapping (Graham and Hackett, 1987; Waight et al., 1999) and Ar-Ar dating (Gamble et al., 2003) producing a well constrained lava flow stratigraphy. This has enabled differentiation processes to be investigated over varying timescales, with initial studies recognising that crustal assimilation has been an important process throughout the lifetime of Ruapehu (Graham and Hackett, 1987). However, more recent detailed studies have identified smaller scale geochemical changes within separate packages which have been interpreted as magma recharge/mixing events operating over the timescales of individual eruptions (Gamble et al., 1999; Price et al., 1997; Waight et al., 1999). Therefore, Ruapehu, like many other arc volcanoes, appears to have a complex magmatic plumbing system where temporal changes in the geochemistry of

lavas is a consequence of varying degrees/styles of differentiation operating in the subvolcanic basement.

This study builds upon previous work by examining temporal changes in Ruapehu lavas with particular emphasis on melt-crust interaction. Using constraints on crustal compositions (chapter 2) and a new geochemical database (Appendix A-D) including the first Hf and O (laser fluorination) isotope data for Ruapehu lavas, the aims of this chapter are;

1) to investigate magmatic evolutionary trends of the volcano.
2) characterise the effects of crustal assimilation on magma compositions.
3) establish if there is a temporal variation in melt-crust interactions as a result of the thermal evolution of the crustal column.

3.3. Overview of Mt. Ruapehu and sampling details

Mt. Ruapehu is a large composite andesite volcano (2797 m) which has been active since ~ 300 ka (Gamble et al., 2003). Current volcanism at Ruapehu has been limited to the crater lake at the volcano's summit with the most recent activity producing a lahar in March 2007, and a phreatomagmatic eruption in September 1995. The latter event appears to be part of a 20-30 year eruptive periodicity at the volcano with historic eruptions recorded in the 1860s, 1895-1906, 1925, 1945-1946 and 1966-1967 (Cole and Nairn, 1975; Gamble et al., 1999; Houghton et al., 1987). The volcano is situated within the Mt. Ruapehu graben, bound to the east and west by the Raurimu and Rangipo faults (Fig. 3.1). Graham and Hackett (1987) identified four main stratigraphic formations at Ruapehu each representative of a major cone building episode; Te Herenga (250-180 ka), Waihianoa (160-115 ka), Mangawhero (55-15 ka) and Whakapapa (<15 ka; K-Ar dates from Gamble et al., 2003). More recent studies

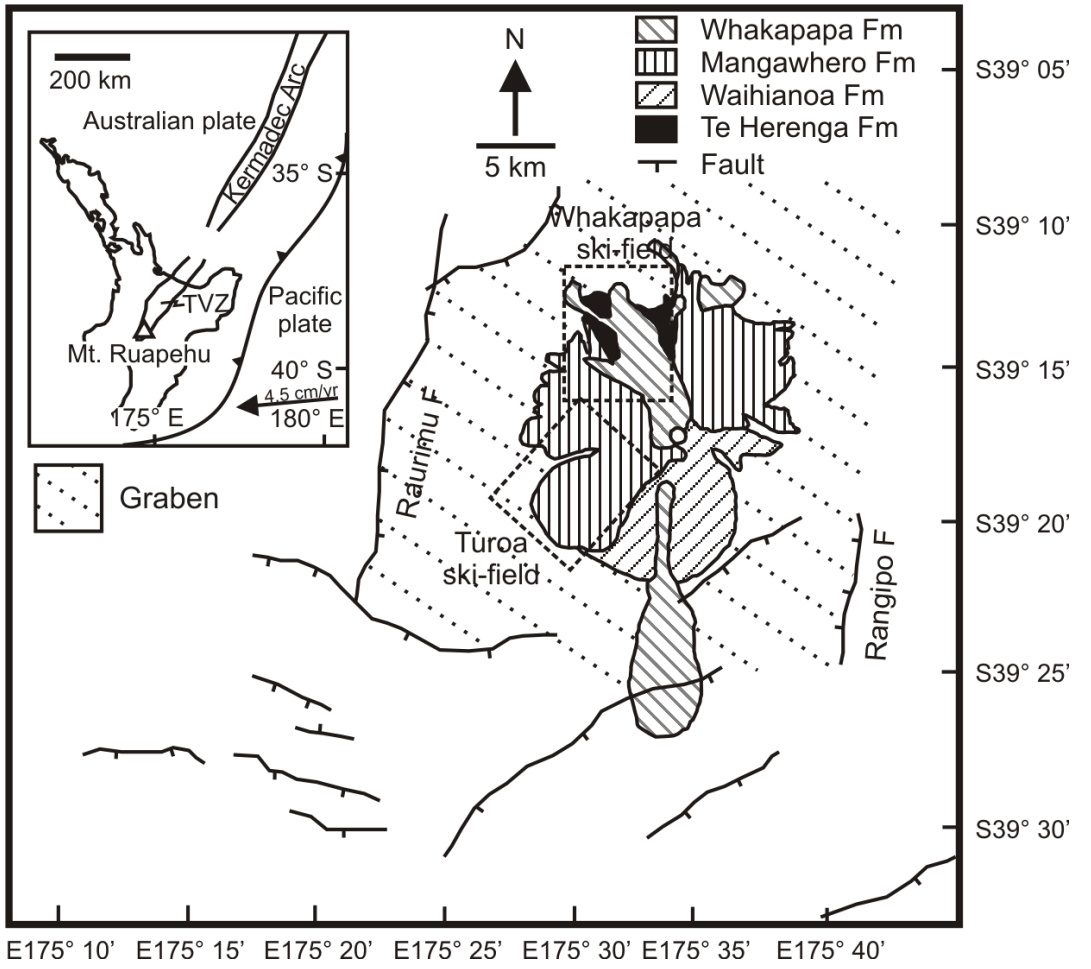

Fig. 3.1. Location map (adapted from Gamble et al., 2003) showing Mt. Ruapehu positioned within the faults of the Mt. Ruapehu Graben (Villamor and Berryman, 2006b). Inset displays the location of the Taupo Volcanic Zone (TVZ) in the North Island of New Zealand at the southern end of the Tonga-Kermadec Arc.

on the southern (Turoa ski-field) and northern (Whakapapa ski-field) flanks of the volcano have produced detailed stratigraphic maps identifying individual flow units within the Mangawhero (Waight et al., 1999) and Whakapapa (Price et al., 2000) formations (Fig. 3.2; illustrated with sample locations from this study). Sampling in this study focussed on each ski-field where reasonable age constraints could be placed on lavas from the Te Herenga, Mangawhero and Whakapapa formations. Waihianoa lavas are best exposed on the south eastern flank in the Whangaehu gorge. Due to the relatively inaccessible nature of this locality, samples and geochemical data from the Waihianoa formation were provided by R. Price.

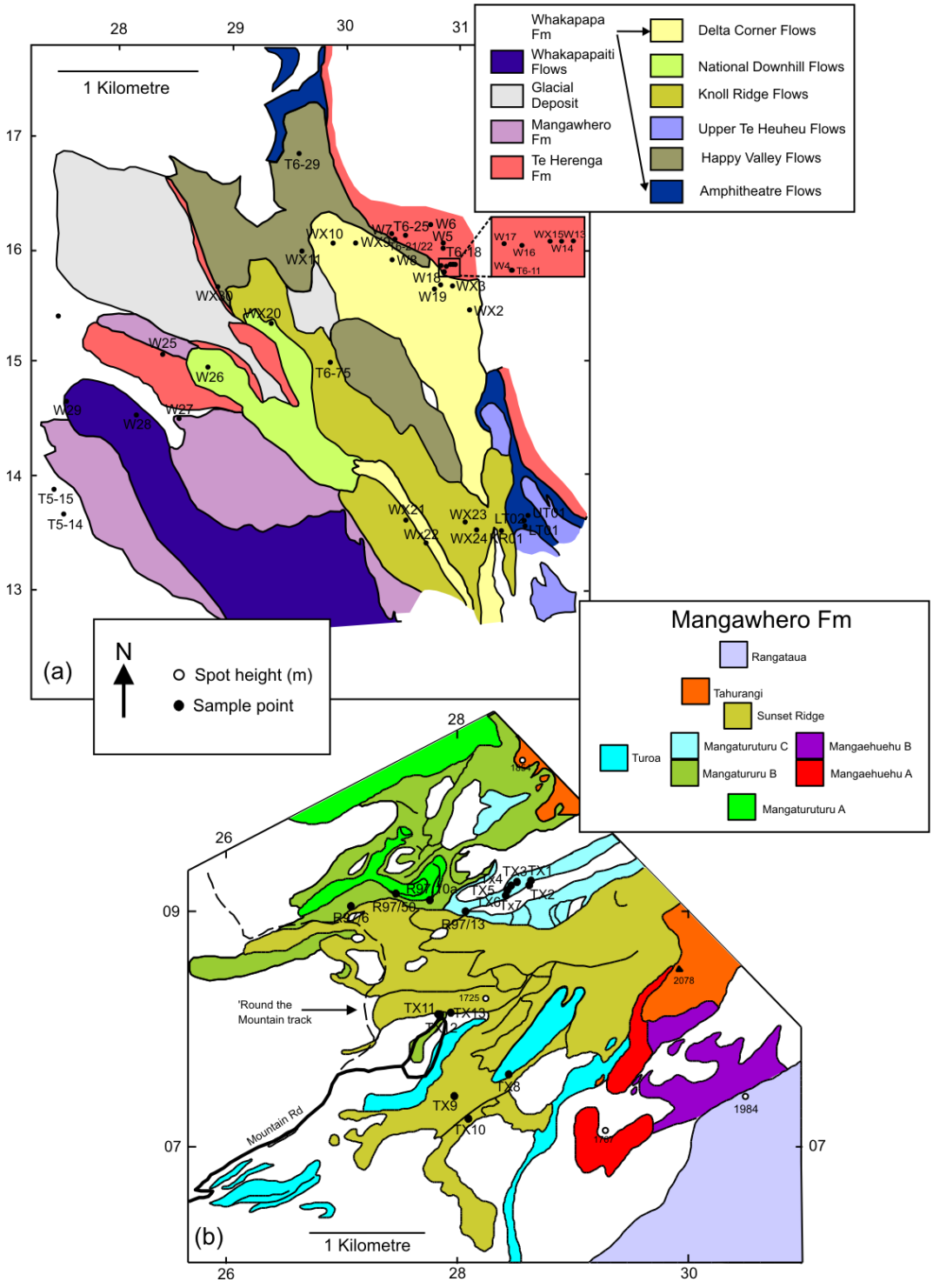

Fig. 3.2. a) Whakapapa ski-field (modified from Price et al., 2000) and b) Turoa ski-field (modified from Waight et al., 1999). Sample points are displayed. Note Waihianoa samples are not displayed as they were collected from the eastern flank of the edifice.

3.3. Petrography and Mineral Chemistry

Detailed petrographical descriptions of Ruapehu lavas have previously been documented (Hackett, 1985; Gamble et al., 1999; Graham, 1985a; Graham and Hackett, 1987; Waight et al., 1999; Price et al., 2005). A mineralogical and petrographical summary of lavas in this study is reported below with modal analyses and mineral compositions available in Appendix A and D. The most common mineral assemblage in lavas from each formation is a two pyroxene, plagioclase andesite. However, textural variability is common with phenocryst contents ranging from 7-51% with plagioclase > clinpyroxene ≤ ≥ orthopyroxene. Few petrographic distinctions can be made between each formation; however, the Te Herenga (TH) lavas tend to exhibit higher and less variable phenocryst abundances (~40-60%) than younger formations (7-40%). Groundmass assemblages comprising of fine-grained plagioclase-pyroxene microlites are particularly common in TH lavas. In contrast, brown vesicular glass is more typical of the Whakapapa formation.

Plagioclase phenocrysts are ubiquitous in all Ruapehu lavas but tend to be in greatest abundance in TH lavas (~30%); younger formations commonly have ~10-20% plagioclase phenocrysts. Compositions in this study vary from An_{81-53} (An_{89-40} reported in Graham and Hackett, 1987), with the most primitive anorthite contents occurring in the Ruapehu basalt (RB) from the Mangawhero formation (Fig. 3.3a). Crystals are subhedral to euhedral and often display complex normal and reverse oscillatory zoning. Other disequilibrium textures such as sieved plagioclase cores and/or rims are common in lavas of all ages. Small pyroxene and apatite inclusions frequently occur in larger phenocrysts.

Variable clinopyroxene-orthopyroxene ratios exist in Ruapehu lavas (cpx/cpx+opx = 24-86%). Clinopyroxene phenocrysts comprise between 1-12%

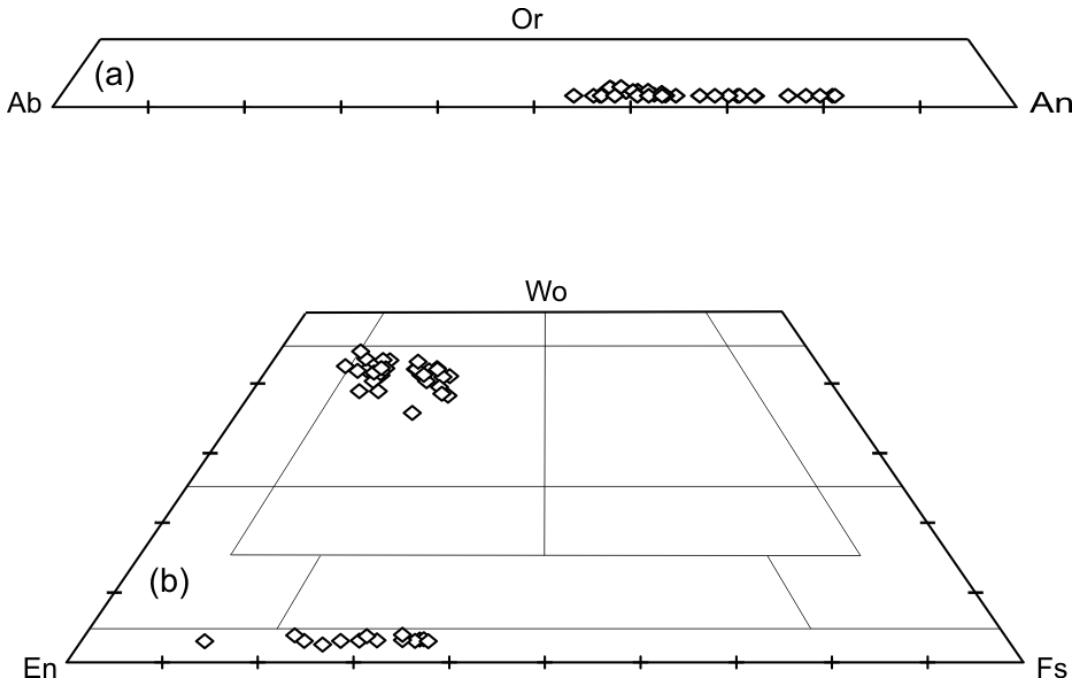

Fig. 3.3. a) Plagioclase and b) pyroxene compositions in Ruapehu lavas.

modal volume in Ruapehu lavas and are usually subhedral-euhedral. Compositions range between $Ca_{45}Mg_{47}Fe_8$ - $Ca_{35}Mg_{46}Fe_{18}$ lying in the augite field on the pyroxene quadrilateral (Fig. 3.3b). Normal and reverse zoning is common in many clinopyroxene phenocrysts with some rims displaying orthopyroxene overgrowths or resorbed reaction rims embayed by groundmass. Clinopyroxene also occurs as coarser grained monomineralic glomerocrysts or in gabbroic inclusions. Orthopyroxene becomes more abundant at higher SiO_2 compositions and therefore tends to be more abundant in the Mangawhero and Whakapapa lavas. Phenocrysts are typically subhedral-euhedral and comprise 1-10% modal volume. Compositions range from $Ca_3Mg_{84}Fe_{12}$ - $Ca_3Mg_{61}Fe_{36}$ and display both normal and reverse zoning.

Oxides occur in all lavas and are typically titanomagnetite in composition. They occur as phenocrysts, inclusions in pyroxenes and microlites in the groundmass.

Olivine was only observed in one sample in this study (RB), although it has been reported as a rare phenocryst phase in the Waihianoa, Mangawhero and

Whakapapa formations (Hackett, 1985; Graham, 1985a; Graham and Hackett, 1987). In the Ruapehu basalt (RB) olivine phenocrysts occur as anhedral-euhedral crystals and comprise ~7% modal volume. Compositions range between Fo_{90}-Fo_{73} and display normal zoning. Crystal margins are often resorbed and occasionally exhibit thin orthopyroxene overgrowths.

Rare amphibole crystals have been reported in the Waihianoa and Mangawhero formations (Hackett, 1985; Waight et al., 1999), however this phase was not observed in any samples in this study.

3.4. Sample Groupings - K_2O vs SiO_2

Previous work at Ruapehu produced a lava classification based on mineralogical and geochemical criteria (types 1-6; Graham and Hackett, 1987). In this study geochemical analysis of samples from the Te Herenga, Waihianoa, Mangawhero and Whakapapa formations are used to investigate temporal magmatic evolutionary trends at Ruapehu, e.g. variations in K_2O with time (Fig. 3.4). Compositional heterogeneity and mean K_2O values increase with time at Ruapehu with the greatest change occurring between the Te Herenga and Waihianoa formation. Each formation also defines a positive linear array between K_2O and SiO_2 in addition to a systematic shift to higher K_2O values in younger formations (at a given SiO_2 content). Geochemically, however, there is little distinction in the K_2O trajectories for the three younger formations, a feature replicated in many other major and trace elements when plotted against indices of differentiation. Therefore, as a result of the geochemical similarity in Waihianoa, Mangawhero and Whakapapa formations the Ruapehu lavas can be subdivided into the Te Herenga (TH; >180ka) and Post Te Herenga (PTH; <160 ka)

series. The Ruapehu basalt is identified separately as a result of its relatively primitive composition.

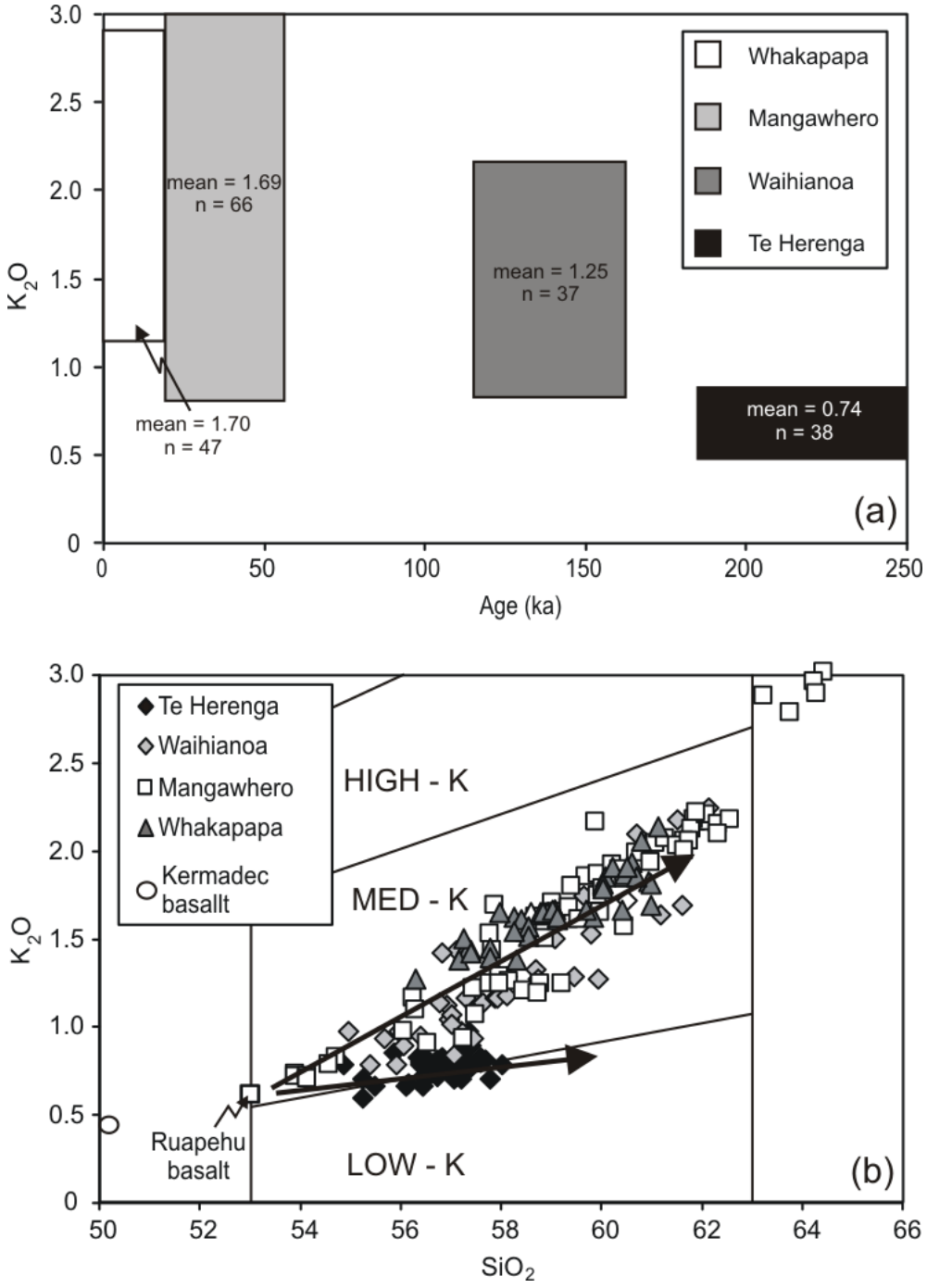

Fig. 3.4. a) Variations in K_2O with time and b) SiO_2 vs K_2O diagram for Ruapehu volcanics (primitive Kermadec basalt illustrated for comparison). Note the differing evolutionary pathways for Te Herenga and Post Te Herenga lavas. Additional data from Graham and Hackett (1987), Hackett (1985) and Gamble et al. (1993a).

3.5. Geochemistry

3.5.1. Major element data

Major element data are listed in Appendix B. Ruapehu lavas possess a moderate range in SiO_2 values (52.9-64.4 wt %) covering basaltic andesite to dacite compositions. Major element variations are presented using silica variation diagrams (Fig. 3.5a-g). CaO and Fe_2O_{3tot} abundances decrease linearly with increasing SiO_2 while MgO decreases rapidly between 52-57 wt% SiO_2 followed by a gradual decrease at >57 wt% SiO_2. Al_2O_3 however increases rapidly between 52-57 wt% SiO_2 followed by a gradual decrease in values at higher silica. Na_2O displays a positive correlation against silica but with increased scatter. P_2O_5 behaves similarly to K_2O defining a positive correlation with the TH series possessing lower P_2O_5 values than PTH at comparable SiO_2 contents. No discernible trend is present in TiO_2 however the highest values are recorded in samples with SiO_2 > 60 wt%. The TH series (55.2-57.9 wt % SiO_2) defines a relatively distinct group at the high and low ends of negative (MgO, CaO, Al_2O_3, Fe_2O_3) and positive (Na_2O, P_2O_5) correlations, respectively. The Ruapehu basalt lies outside of the TH and PTH array as a consequence of its relatively primitive composition, lower SiO_2 content, and its higher compatible (MgO, Fe_2O_3) and lower incompatible (K_2O, P_2O_5, Na_2O) major element concentration.

3.5.2. Trace element geochemistry

As a result of Ruapehu lavas having evolved compositions, Ni concentrations are generally low (<50 ppm) showing no discernible variation with SiO_2 (Fig. 3.6a). However the TH lavas display considerably less scatter in Ni concentrations than the PTH series. Ni content in the Ruapehu basalt (146 ppm) resembles MgO (Fig. 3.5d), possessing a considerably higher concentration than other Ruapehu lavas. Large ion

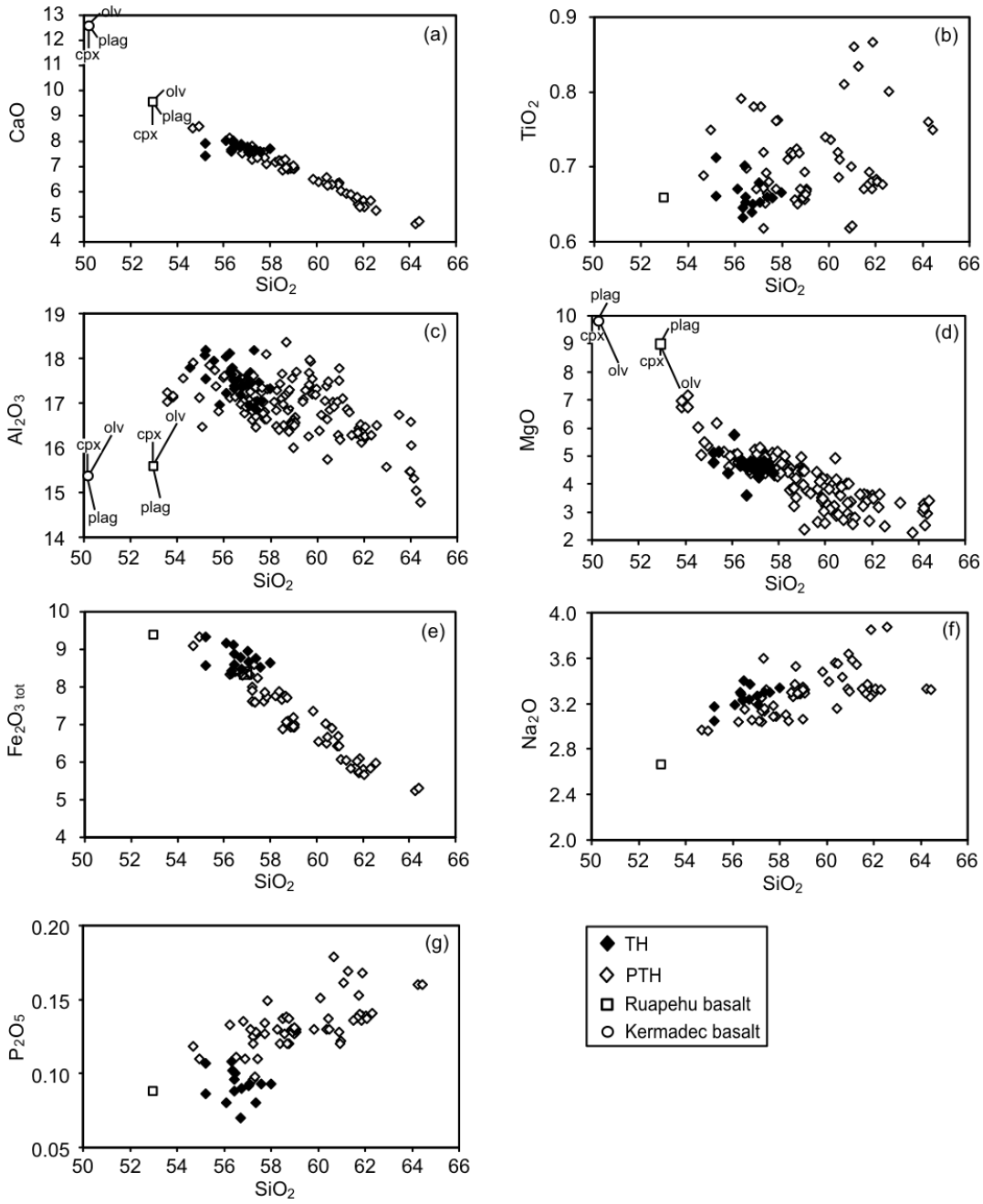

Fig. 3.5. Major element variation for Ruapehu rocks separated into TH and PTH lavas. Crystallisation vectors (Graham and Hackett, 1987) in Figs. a, c and d represent 5% fractionation of each respective phase from the Ruapehu basalt and Kermadec basalt.

lithophile element variations (LILE; Rb, Cs, Ba, U and Th) within the TH and PTH lavas (Fig. 3.6b-c) mirror that of K_2O, with higher concentrations in the PTH series at

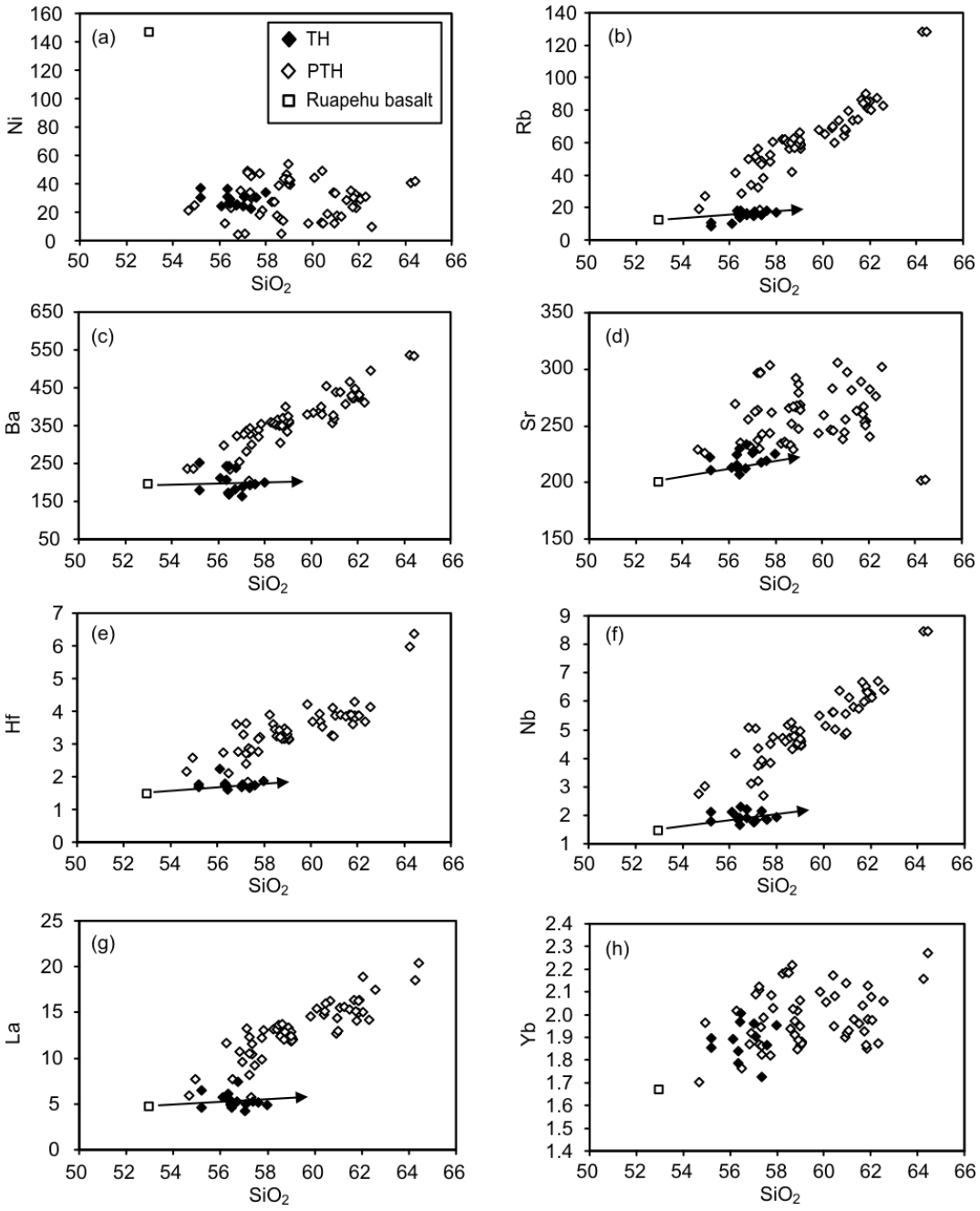

Fig. 3.6. Trace element variation diagrams for TH and PTH lavas. Arrows (Figs. b, c, d, e, g) represent the evolution of the Ruapehu basalt by fractionation crystallisation of its phenocryst assemblage (olv+cpx+opx+mag).

similar SiO_2 values. The TH lavas generally display small or no increases in LILE with increasing silica. Sr displays very little systematic variation with SiO_2 although there is considerably more scatter in the PTH series at higher silica (Fig. 3.6d). Variation in high field strength elements (HFSE; Hf, Zr, Nb and Ta) also have similarities to K_2O variations with positive correlations in the PTH lavas and

relatively constant values throughout the TH (Fig. 3.6e-f). Rare earth element (REE) variations with SiO_2 are displayed in Figure 3.6g and h. Light REE (LREE; La) variations in Ruapehu lavas mirror K_2O, with a systematic increase to higher concentrations in PTH lavas and constant values in the TH series. However, heavy REE (HREE; Yb) concentrations lack any significant correlation with increased scatter at elevated SiO_2 values.

Ruapehu lavas exhibit typical N-MORB normalised trace element abundance patterns of subduction related rocks, with enrichment of LILE and LREE relative to HFSE and HREE. The highly to moderately incompatible elements are all enriched, while many of the HFSE and MREE-HREE are depleted relative to N-MORB. The Ruapehu basalt has a comparable pattern to the TH series with very similar levels of enrichment and depletion (Fig. 3.7). PTH lavas are enriched in the most incompatible elements relative to the TH series as illustrated on the inset diagram of Fig. 3.7. LILE display the greatest enrichment in PTH lavas relative to TH while Sr and the MREE-HREE only display very minor increases in abundance (e.g. Lu displays ~2% increase in PTH). There are also significant enrichments in Th-U and Nb-Zr-Hf in the PTH series.

3.5.3. Radiogenic isotopes

Sr, Pb, Nd and Hf isotope data for Ruapehu lavas are listed in Appendix C and plotted in Fig. 3.8a-d. The differences recognised between the TH and PTH series in major and trace element variations is also evident in isotopic compositions. TH lavas form a distinct group isolated from the PTH series with a small range of values midway between local primitive basalt (Kermadec arc lavas) and meta-igneous granulite compositions. They are the most primitive isotope compositions measured at the

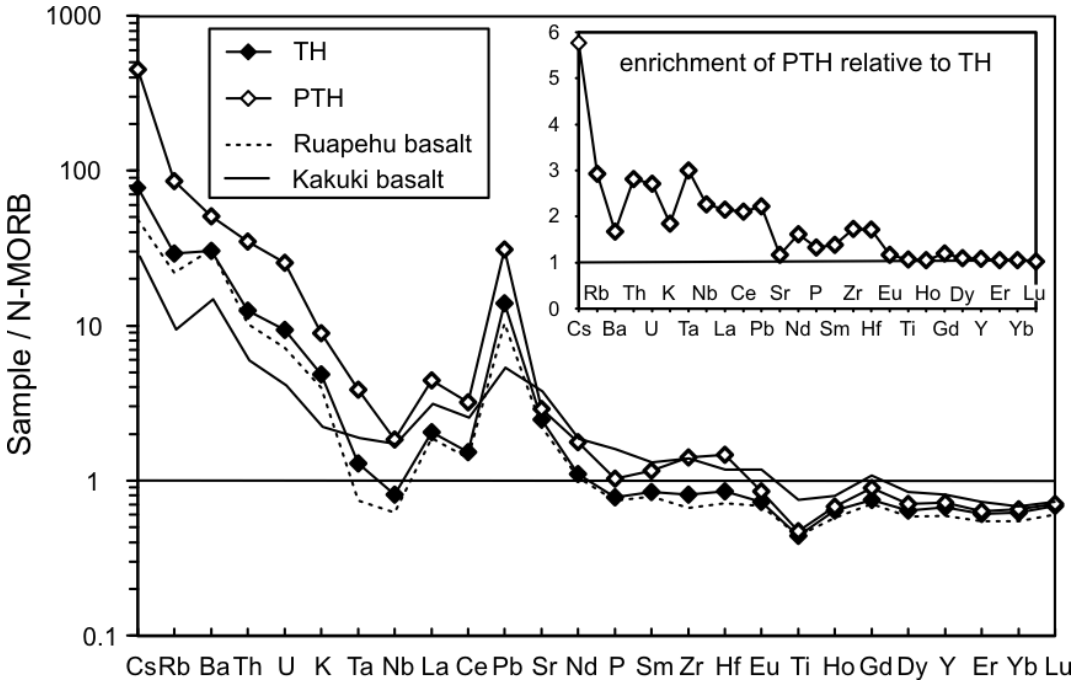

Fig. 3.7. N-MORB normalised trace element diagram for mean TH and PTH lava (at 57 wt% SiO_2). Also illustrated are the Ruapehu basalt and the Kakuki basalt (primitive TVZ basalt). Inset diagram displays the average enrichment of the PTH lavas relative to the TH series. N-MORB normalisation values from Sun and McDonough, 1989.

volcano ($^{87}Sr/^{86}Sr$ = 0.704706-0.705046; εNd = 4.7-5.6; εHf = 11.9-13.6). The Ruapehu basalt also has a relatively primitive isotope composition ($^{87}Sr/^{86}Sr$ = 0.704774; εNd = 5.3; εHf = 13.0) lying within the range of TH lavas. The PTH series display more heterogeneous isotopic compositions ($^{87}Sr/^{86}Sr$ = 0.705115-0.705910; εNd = 0.5-2.8; εHf = 4.9-7.4) consistent with their greater range in major and trace element abundances. They form an array that is tangential to the meta-igneous granulite field and trend towards the lower εNd values of the meta-sedimentary xenoliths. Pb isotope compositions for Ruapehu lavas define a linear array above and tangential to the Northern Hemisphere Reference Line (NHRL; Δ7/4 = 10.1; Δ8/4 = 34.7) and also distinguish between TH and PTH lavas. TH lavas possess moderately primitive compositions ($^{206}Pb/^{204}Pb$ = 18.757-18.818; $^{207}Pb/^{204}Pb$ = 15.612-15.635; $^{208}Pb/^{204}Pb$ = 38.640-38.721) trending towards the primitive lavas from the Kermadec

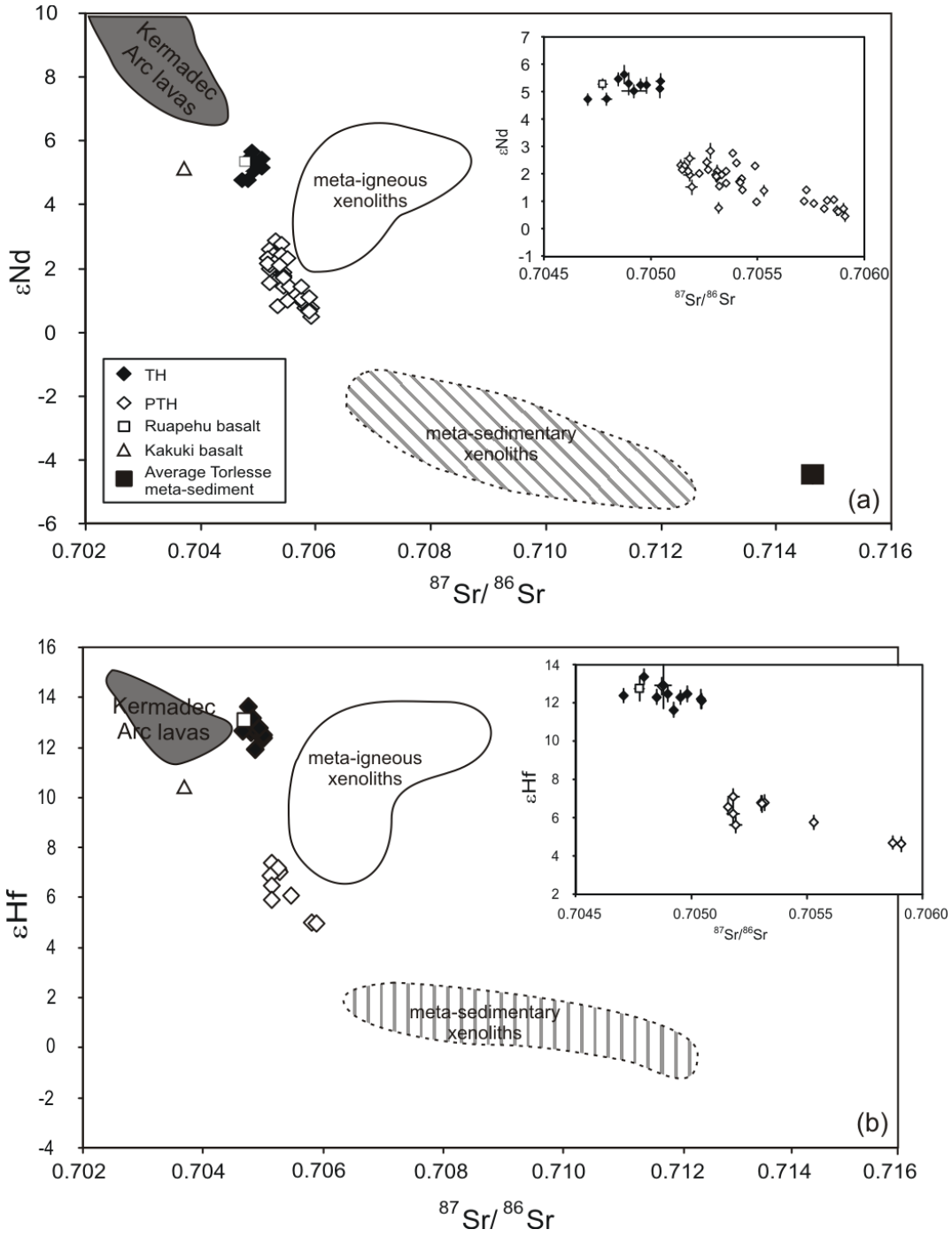

Fig. 3.8. Variation of (a) εNd vs $^{87}Sr/^{86}Sr$ and (b) εHf vs $^{87}Sr/^{86}Sr$ for TH and PTH lavas. Also illustrated are the Ruapehu basalt and the Kakuki basalt (primitive TVZ composition). Average Torlesse meta-sediment from Graham et al. (1992). Inset displays external errors (2σ) for each data point however they are often smaller than the symbol.

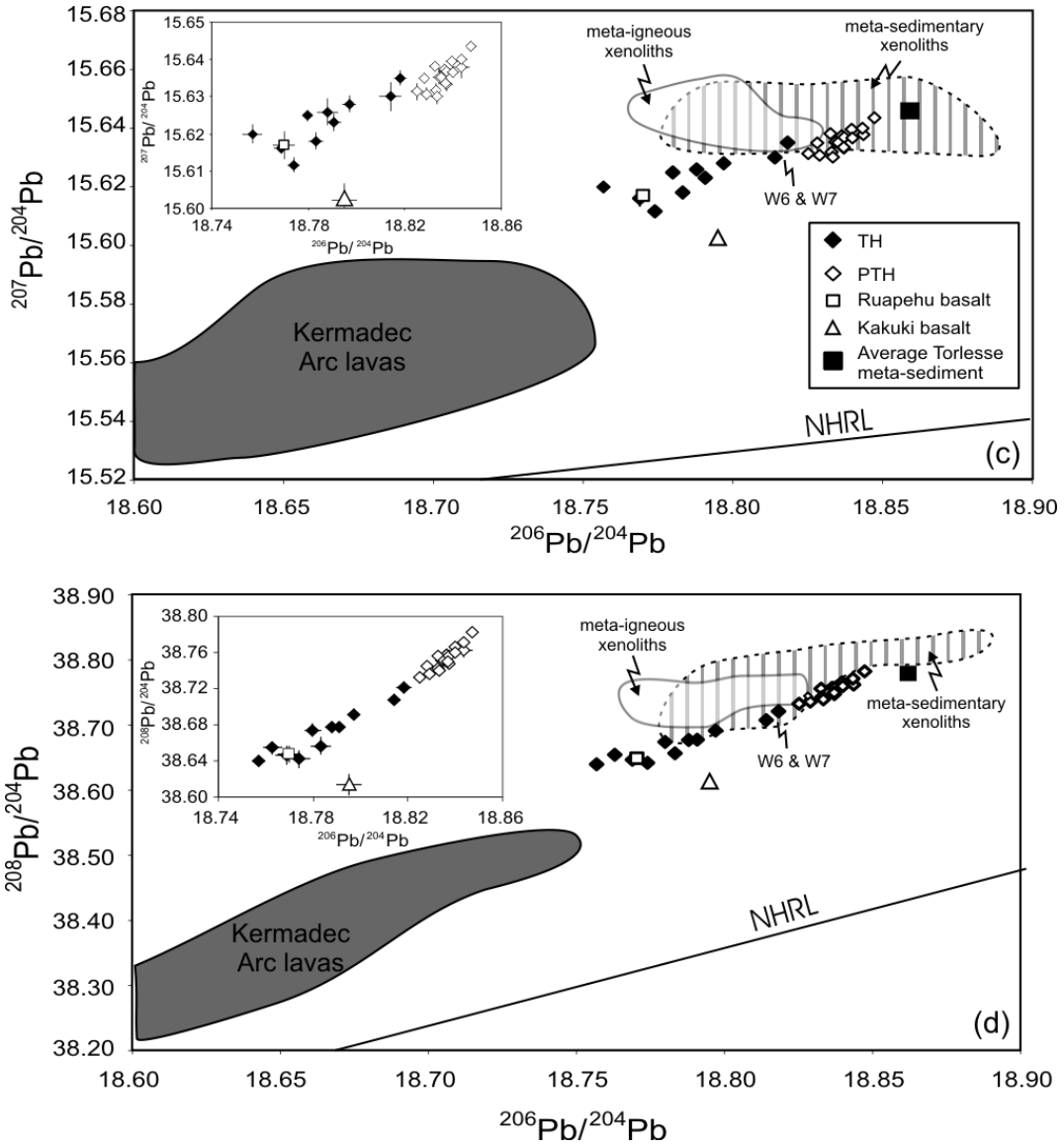

Fig. 3.8 cont. Variation of (c) $^{207}Pb/^{204}Pb$ vs $^{206}Pb/^{204}Pb$, (d) $^{208}Pb/^{204}Pb$ vs $^{206}Pb/^{204}Pb$, for TH and PTH lavas. Also illustrated are the Ruapehu basalt and the Kakuki basalt (primitive TVZ composition). Average Torlesse meta-sediment from Graham et al. (1992). NHRL (Northern Hemisphere Reference Line) from Hart (1984). Inset displays external errors (2σ) for each data point however they are often smaller than the symbol.

arc. Two samples, however, (W6 and W7) have intermediate Pb isotope compositions between the rest of the TH lavas and the PTH fields. In addition these samples possess relatively high U and Th concentrations. Similarly with Sr, Nd and Hf isotopes, the Ruapehu basalt ($^{206}Pb/^{204}Pb$ = 18.770; $^{207}Pb/^{204}Pb$ = 15.617; $^{208}Pb/^{204}Pb$ = 38.648) has a Pb isotope composition comparable to the most primitive TH lavas. PTH lavas

possess more radiogenic Pb compositions ($^{206}Pb/^{204}Pb$ = 18.825-18.847; $^{207}Pb/^{204}Pb$ = 15.630-15.644; $^{208}Pb/^{204}Pb$ = 38.721-38.783) overlapping with the meta-sedimentary xenolith field.

3.5.4. Oxygen isotope data

Oxygen isotope data for Ruapehu lavas are listed in Appendix C and presented in Figure 3.9. Clinopyroxene is a common ferromagnesian phenocryst phase in Ruapehu lavas and consequently was analysed in all selected samples. Additional oxygen isotope ratios were also measured in five samples with abundant orthopyroxene and one sample with minor olivine (RB). The range in $\delta^{18}O$ values for clinopyroxene and orthopyroxene is +5.82 to +6.59 (n = 20) and +6.58 to +7.19 (n = 5) respectively. The geochemical distinction between TH and PTH lavas recognised in trace elements and radiogenic isotopes, is also reflected in a bimodal distribution in $\delta^{18}O_{cpx}$ (TH $\delta^{18}O_{cpx}$ = +5.82 – +6.05 ‰; PTH $\delta^{18}O_{cpx}$ = +6.23 – +6.60 ‰). Orthopyroxene also exhibits a bimodal distribution; however, it is less well defined than the clinopyroxene trend due to fewer data points. 85% of the $\delta^{18}O$ values for clinopyroxene are enriched in ^{18}O, lying outside of the typical $\delta^{18}O_{cpx}$ range for the upper mantle (+5.35 – 5.89 ‰, Mattey et al., 1994; Ionov et al., 1994). The remaining 15% of clinopyroxene samples that correspond to upper mantle values belong to the TH formation (+5.82, +5.84, +5.89). The solitary olivine oxygen isotope ratio, from the Ruapehu basalt (+5.50 ‰), corresponds to the upper limit of mantle olivine (+4.8 – +5.5 ‰, Mattey et al., 1994). A comparison with $\delta^{18}O_{cpx}$ values from the southern Kermadec arc lavas which represent local source contaminated upper mantle (Macpherson et al., 1998) illustrate that all of the Ruapehu clinopyroxene phenocrysts show significant ^{18}O enrichment; a mean $\delta^{18}O_{cpx}$ value from each study reveals 0.71‰ enrichment at Ruapehu. ^{18}O

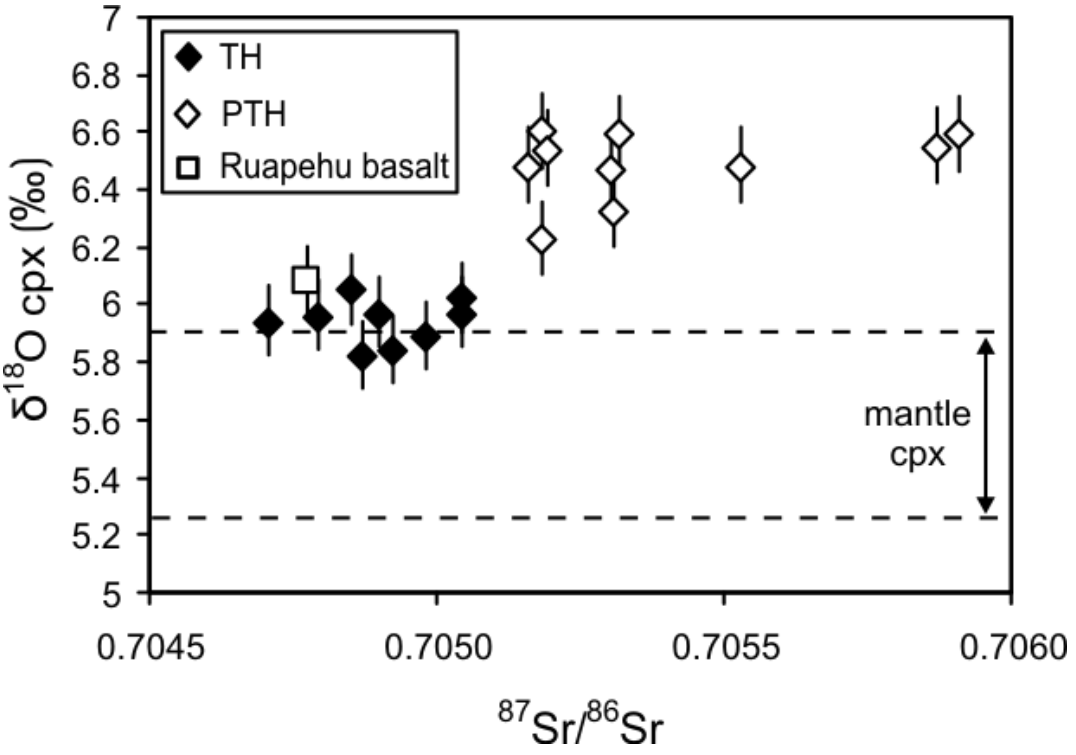

Fig. 3.9. $\delta^{18}O_{cpx}$ versus $^{87}Sr/^{86}Sr$ (whole-rock) for Ruapehu lavas. Error bars for $\delta^{18}O$ are ±1σ of replicate analysis or ±2% where replicate analyses were not performed. $\delta^{18}O_{cpx}$ mantle range (5.35 - 5.89 ‰) from Mattey et al. (1994) and Ionov et al. (1994).

enrichment (0.55‰) is also present in olivine from the Ruapehu basalt. $\Delta_{cpx\text{-}opx}$ (0.46–0.87; n = 5) and $\Delta_{cpx\text{-}olv}$ (0.58; n = 1) values from coexisting mineral pairs are higher than mantle peridotite values (Mattey et al., 1994), suggesting isotopic disequilibrium at typical magmatic temperatures for andesite liquids (Macpherson and Mattey, 1998; Macpherson et al., 1998). This provides additional evidence that open system behaviour is an important process in the evolution of magmas at Mt. Ruapehu.

3.6. Discussion

3.6.1. Magmatic differentiation

Differentiation processes can strongly influence the composition of magma resulting in the notable absence of primary lavas (e.g. high MgO, Ni and Cr abundances) at

continental arcs. The elevated SiO_2 contents and rarity of olivine phenocrysts in samples from Ruapehu indicate many, if not all, lavas have experienced some degree of differentiation prior to eruption. Even the olivine-bearing Ruapehu basalt with > 8 wt% MgO is unlikely to be a true primary mantle melt due to its relatively elevated SiO_2 content (52.9 wt% - basaltic andesite; Le Maitre et al., 1989).

The large variation in phenocryst abundance throughout the Ruapehu lavas (7-60%) suggests fractional crystallisation exerts some control on magma composition and may be responsible for correlations of various major and trace elements with indices of differentiation (e.g. SiO_2). Although the different isotopic composition of TH and PTH lavas preclude that each series is directly related through fractional crystallisation the divergence in differentiation trajectories on major and trace element variation diagrams (e.g. SiO_2 vs K_2O) may result from different fractionating mineral assemblages operating on a similar parental magma. Although CaO and Al_2O_3 versus silica (Fig. 3.5a&c) display a continuous trend throughout the Ruapehu data set, the TH formation can be distinguished by its relatively high CaO contents and notable clustering around the inflection in Al_2O_3 at 17-18 wt%. Crystallization vectors (from Graham and Hackett, 1987) predicting magmatic evolution from the Ruapehu basalt or local primitive basalt (Kermadec arc basalt; 168/1B from Gamble et al., 1995) suggest these differentiation trends may result from a different fractionating mineral assemblage in each series (Fig. 3.5a, c and d). Fractionating an assemblage of clinopyroxene + olivine ± plagioclase can replicate TH lavas, while PTH compositions require a similar assemblage but with more plagioclase fractionation relative to clinopyroxene and olivine/orthopyroxene. TH lavas have notably higher modal plagioclase abundances than PTH lavas (~10%) which in addition to CaO and

Al_2O_3 variations suggest the TH series has lost less plagioclase during fractional crystallisation.

3.6.2. Fractional Crystallisation

The major element variations in TH and PTH lavas can be investigated using XLFRAC least-squares modelling (see Stormer and Nicholls, 1978) to ascertain if separate differentiation trends are the result of varying plagioclase fraction. The Ruapehu basalt and a primitive Kermadec arc lava (168/1B; from Gamble et al., 1995) are both used as potential parental compositions for modelling the TH series. Models 1-7 in Table 3.1 suggest that TH lavas can be produced from the either parental composition by fractionation of olivine, clinopyroxene, plagioclase and magnetite (Σr^2 = 0.02-0.12). A mean TH daughter composition (model 8) also yields similar results (Σr^2 = 0.07). Modelling between the least and most evolved TH lavas requires low levels of plagioclase fractionation (Models 9 and 10). Models 1-8 indicate that plagioclase comprises ~25-44% of the total assemblage and is invariably less than clinopyroxene fractionation (37-55%). Orthopyroxene was substituted for olivine in PTH modelling to account for increased whole-rock SiO_2 contents. Modelling of PTH lavas used least evolved samples as parents which can produce daughter compositions by fractionation of orthopyroxene, clinopyroxene, plagioclase and magnetite. A higher sum of residuals (Σr^2 = 0.3) indicate a slightly poorer agreement in PTH models as a consequence of large negative K_2O residuals in calculated compositions. Nevertheless it is evident that PTH lavas require greater plagioclase and lower clinopyroxene fractionation (56-87% and 8-22% respectively) compared to the TH series. Therefore, it is suggested that plagioclase abundance is the primary difference in the fractionating assemblages of TH and PTH lavas with the TH array reproduced

Table 3.1. Results of major element least squares modelling

Series	Model No.	Parent	Daughter	ΔSiO_2 (wt%)	Σr^2	% removed					% Crystals	Modal abundance in thin section				
						olv	opx	cpx	plag	mag		olv	opx	cpx	plag	mag
TH	1	RB	WX2	2.23	0.03	7.2 (24)	-	12.7 (43)	8.8 (30)	1 (3)	29.7	-	4.2	8.1	27.4	0.6
	2	RB	W6	3.36	0.05	7.6 (23)	-	13.7 (42)	9.8 (30)	1.8 (5)	32.9	-	11.2	7.1	31.8	1.3
	3	RB	W7	2.22	0.05	6.9 (22)	-	15.6 (48)	8.2 (25)	1.5 (5)	32.2	-	6.9	7.2	33.4	1.8
	4	RB	W5	3.37	0.06	7.7 (23)	-	13.8 (40)	10.8 (31)	2 (6)	34.3	-	-	-	-	-
	5	RB	WX3	4.33	0.02	8.6 (24)	-	12.3 (34)	13.6 (37)	2.1 (5)	36.6	-	-	-	-	-
	6	168/1B	RB	2.73	0.04	0.1 (0.2)	-	20.5 (51)	17.6 (44)	2.2 (4)	40	7.2	3.5	8.7	25.4	0.4
	7	168/1B	W7	4.95	0.12	2.5 (5)	-	28.2 (55)	17 (34)	3.3 (6)	51	-	6.9	7.2	33.4	1.8
	8	RB	Avg TH	3.66	0.07	8.1 (24)	-	12.7 (37)	11.7 (34)	1.9 (5)	34.4	-	-	-	-	-
	9	WX2	W17	1.22	0.01	-	3.4 (31)	**0.2 (1)**	6.7 (61)	0.8 (7)	10.9	-	8.9	4.8	32.4	0.8
	10	WX2	W14	1.88	0.01	-	4.7 (22)	1 (4)	14.2 (65)	2.1 (9)	22	-	7.9	5.5	33.8	1.6
PTH	11	R04-03	WX9	2.69	0.24	-	4.8 (15)	2.5 (8)	22.6 (68)	3.1 (9)	33	-	7.5	2.9	18.1	0.1
	12	WX9	R96-26	0.89	0.02	-	3.2 (26)	2.2 (17)	7 (56)	0.01 (1)	12.4	-	6.4	2.2	22.7	0.6
	13	R96-26	W27	3.62	0.34	-	5.3 (17)	7 (22)	15.9 (52)	2.6 (52)	30.8	-	-	-	-	-
	14	W27	T5-14	2.56	0.37	-	**0.2 (1)**	**1.6 (11)**	13.1 (87)	1.9 (13)	15	-	3.2	3.8	17.8	0.4
	15	Avg TH	Avg PTH	2.94	0.56	-	4.2 (16)	2.8 (11)	16.5 (62)	3 (11)	26.8	-	-	-	-	-
	16	RB	Avg PTH	6.91	0.36	9.3 (21)	-	14.1 (31)	18.1 (40)	3.5 (7.8)	45	-	-	-	-	-

XLFRAC least-squares modelling based on eight oxides. Minerals compositions taken from parental lava (see Appendix D) or in the case of 168/1B, Gamble et al. (1993b). ΔSiO_2 refers to the difference calculated between parent and daughter compositions. olv, olivine; opx, orthopyroxene; cpx, cliinopyroxene; plag, plagioclase; mag, magnetite. Number in brackets refers to the phase percentage of the total assemblage. Bold font infers the addition of a phase.

through clinopyroxene > plagioclase fractionation, while PTH compositions require a plagioclase > clinopyroxene assemblage (Fig. 3.10). As TH lavas precede the PTH formation their major element composition may also provide a suitable parental magma for producing younger lavas. Modelling between a mean TH and mean PTH daughter also requires a plagioclase > clinopyroxene fractionating assemblage, however the high Σr^2 (0.56) and isotopic disparity between each group suggests additional differentiation processes to fractional crystallisation are required. Similar results are obtained when modelling a mean PTH composition from the Ruapehu basalt (model 16).

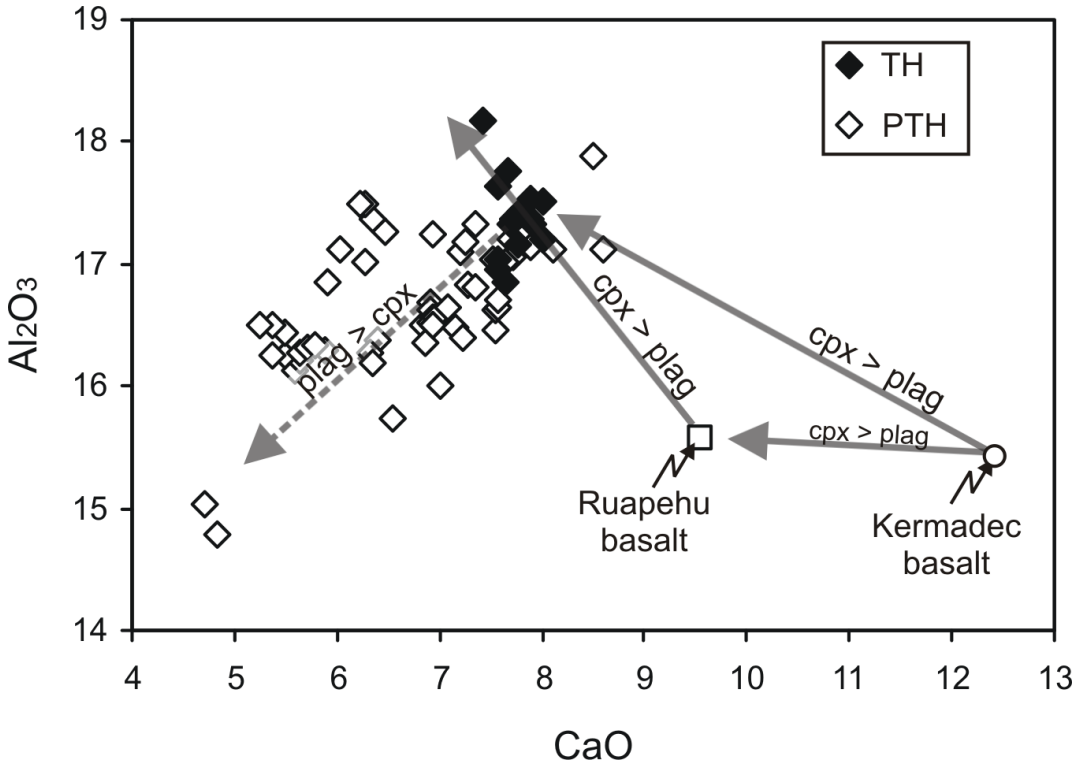

Fig. 3.10. Variation of CaO vs Al_2O_3 illustrating different evolutionary pathways for TH and PTH lavas. Arrows illustrate results of least squares major element modelling from parental magma. Additional data from Graham and Hackett (1987) and Hackett (1985).

Many trace element trends are similar to major element variations indicating their concentrations are also influenced by fractional crystallisation. With the results from major element modelling (i.e. phase proportions and degree of crystallisation) it is possible to examine the accuracy of least-squares analysis using the Rayleigh fractionation equation, $C_l = C_o F^{(D-1)}$: C_o = concentration of element in parental liquid, C_l = concentration of element in daughter liquid, F = fraction of liquid remaining, D = bulk distribution coefficient (given in Appendix F). The results of modelling for TH (including the Ruapehu basalt) and PTH compositions are shown in Table 3.2 with differences between calculated and measured trace element concentrations illustrated in Fig. 3.11a&b. In general TH data (models 1, 2, 8 & 9) normalise relatively close to 1, with calculated values usually lying within 20-30% of measured concentrations. However, each model consistently over-estimates most trace element concentrations with model 1 in particular displaying a large discrepancy with calculated Rb abundance. This feature is probably a consequence of the Ruapehu basalt itself having experienced small degrees of differentiation resulting in its trace element composition being slightly high for modelling TH lavas. Modelling the Ruapehu basalt from the Kermadec basalt (Model 6) produces good results for Rb, Sr, Zr and Hf concentrations but poor correlation in Ba and Th abundances. The relatively high Σr^2 values from PTH least-squares analysis is also reflected in poor results for trace element modelling. Calculated concentrations are frequently under-estimated with LILE (including Th and U) and HFSE concentrations up to 60% less than measured abundances (Fig. 3.11b) suggesting the addition of an incompatible element enriched component is necessary to satisfy PTH compositions.

In summary, trace element modelling for TH lavas supports least-squares analysis suggesting the variation in this series can be produced by fractionation of a

Table 3.2. Results of trace element fractional crystallisation modelling

Model no:	1	2	6	8	9	11	12	14	15
Parent	RB	RB	168/1B	RB	WX2	R04-03	WX9	W27	Avg TH
Daughter	WX2	W6	RB	Avg TH	W17	WX9	R96-26	T5-14	Avg PTH
Series	TH	TH	-	TH	TH	PTH	PTH	PTH	PTH
Σr^2	0.03	0.05	0.04	0.07	0.01	0.24	0.02	0.37	0.56
olv	7.2	7.6	0.1 (0.2)	8.1	-	-	-	-	-
opx	-	-	-	-	3.4	4.8	3.2	-	4.2
cpx	12.7	13.7	20.5 (51)	12.7	-	2.5	2.2	-	2.8
plag	8.8	9.8	17.6 (44)	11.7	6.7	22.6	7	13.1	16.5
mag	1.0	1.8	2.2 (4)	1.9	0.8	3.1	0.01	1.9	3
total	29.7	32.9	40	34.4	10.9	33	12.4	15	26.8
F	0.7	0.67	0.6	0.66	0.89	0.67	0.88	0.85	0.73
Calculated (ppm)									
Rb	17.3	18.0	13.0	18.3	10.8	27.4	55.1	98.3	19.2
Ba	271	282	369	269	223	309	360	493	243
Th	1.75	1.82	0.92	1.85	1.72	2.86	5.03	8.80	1.89
U	0.48	0.50	-	0.51	0.49	0.76	1.31	2.32	0.57
Ta	0.14	0.14	-	0.14	0.15	-	-	-	0.16
Nb	2.06	2.14	-	2.17	2.26	3.66	4.21	7.04	2.34
Sr	232	236	256	231	202	171	281	205	189
Zr	69	72	64	73	74	105	111	182	74
Hf	1.93	1.95	1.65	1.98	2.00	2.86	3.06	4.77	2.07
Measured (ppm)									
Rb	8.5	17.9	15.1	15.1	16.9	49.0	61.9	128.3	63.6
Ba	180	242	203	203	200	328	359	534	371
Th	1.34	1.94	1.48	1.48	1.50	4.45	5.12	12.32	5.78
U	0.38	0.57	-	0.45	0.46	1.16	1.55	3.36	1.55
Ta	0.13	0.14	-	0.13	0.13	-	-	-	0.40
Nb	1.80	1.95	-	1.95	1.93	3.81	4.71	8.46	5.11
Sr	211	225	220	220	226	298	235	202	260
Zr	58	59	59	59	64	99	124	225	123
Hf	1.70	1.79	1.74	1.74	1.87	2.73	3.91	6.37	3.47

Σr^2 values and phase proportions for each model taken from Table 3.1.
Note Ta concentrations in R04-03, R96-26 and T5-14 are unreliable and were therefore not included in modelling
Th, U and Nb concentrations are not available for 168/1B

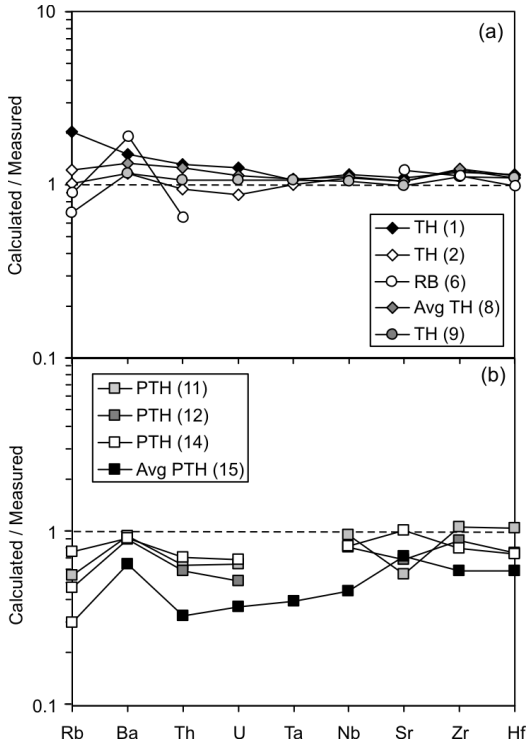

Fig. 3.11. Comparison of trace element concentrations measured in samples with results from forward modelling for (a) TH lavas and (b) PTH lavas. Model numbers in brackets correspond to Table 3.2. Table 3.1 (major element least squares modelling) displays the degree of crystallisation, mineral phases and abundances used in trace element modelling. Mineral-melt distribution coefficients are listed in Appendix F. Note poor agreement between calculated and measured trace element concentrations in PTH samples.

clinopyroxene > plagioclase assemblage from a parental composition similar to the Ruapehu basalt. PTH lavas require fractionation of a plagioclase > clinopyroxene assemblage, however this process alone is unable to account for many incompatible trace element abundances.

On the basis of the modelling and phenocryst assemblages in each series, it is possible to infer the relative fractionation depths. Lower pressures and/or lower water contents in basaltic/andesitic magma tends to induce a higher degree of plagioclase crystallisation (Grove et al., 2002), hence we interpret the relative proportion of this mineral in fractionation models as reflecting a shallower mean differentiation depth for PTH relative to TH. However, large discrepancies in PTH trace element modelling indicate crystal fractionation cannot be the only process operating during differentiation. Furthermore TH and PTH isotopic compositions trend towards crustal values (Fig. 3.8) suggesting contamination by local crust.

3.6.3 Crustal Contamination of Ruapehu lavas

Evolved isotope ratios in arc magmas are often attributed to contamination of primary mantle-wedge derived melts by isotopically distinct crust (Davidson, 1987, 1996; Hildreth and Moorbath, 1988; Macpherson et al., 1998). Crustal material can be added to magma in the source region of the mantle wedge (source contamination) and/or during ascent through the arc lithosphere (crustal contamination). These different contamination processes can be distinguished by examining how isotope ratios vary with indices of differentiation (e.g. SiO_2). If the crustal isotopic signature was imparted on the magma during differentiation in the arc crust (ie. crustal contamination) isotopes would be expected to correlate with SiO_2. This is the case

with the Ruapehu data-set where correlations of $^{87}Sr/^{86}Sr$, $^{206}Pb/^{204}Pb$, εHf and $\delta^{18}O$ with SiO_2 (Fig. 3.12) are consistent with assimilation within the arc crust.

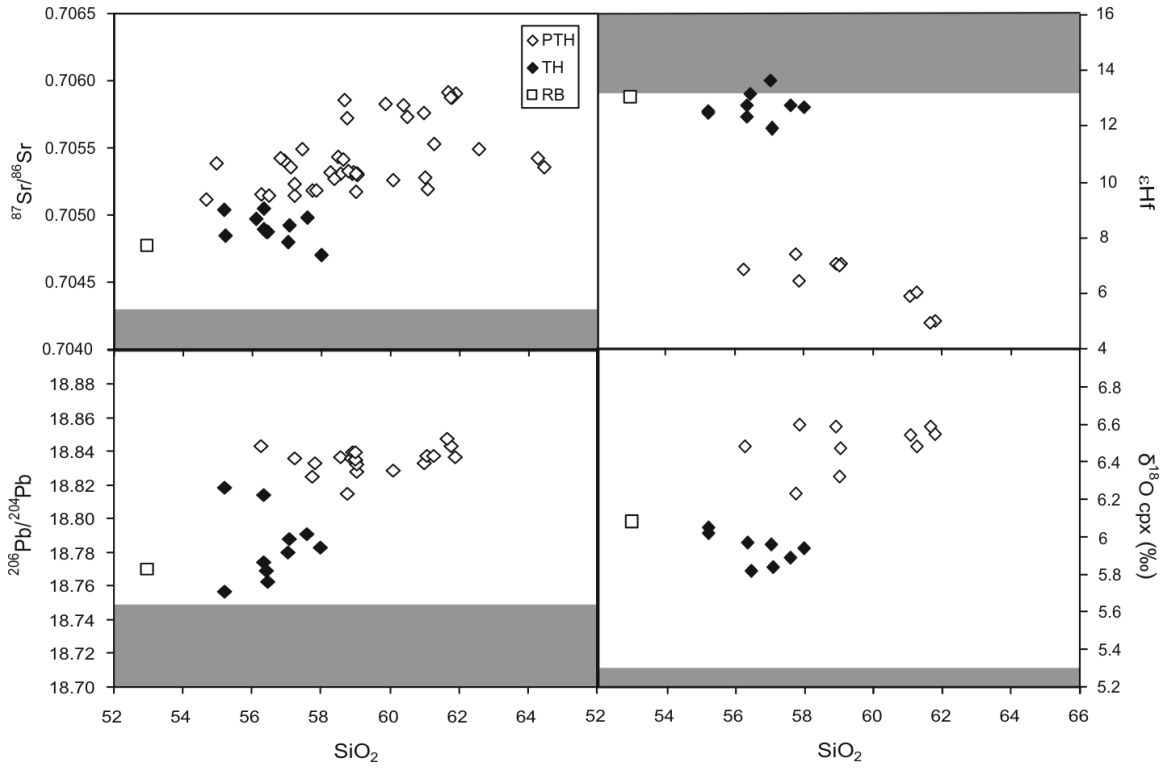

Fig. 3.12. $^{87}Sr/^{86}Sr$, $^{206}Pb/^{204}Pb$, εHf, and $\delta^{18}O$ versus SiO_2 for Ruapehu lavas. Grey field represents primitive Kermadec arc lavas (Gamble et al., 1996; Macpherson et al., 1998; Woodhead et al., 2001; Handler, M. pers comm).

3.6.3.1 Identification of end-member components

The composition of the basement beneath Mt. Ruapehu was determined from crustal xenoliths in Chapter 2. These suggest that the basement is composed of two lithologies; meta-igneous granulite, and meta-sediments resembling the Torlesse formation. Geobarometry suggests that these comprise a 5-10 km thick meta-igneous lower crust overlain by 20-25 km of meta-sediment (Graham, 1987; Graham et al., 1990).

Establishing a mantle source composition is equally important when evaluating the effects of contamination on primary magmas. Differentiation trends in volcanic suites can be used to project back to source compositions. Unfortunately however, even the least differentiated samples in continental arcs have often been modified en route to the surface and are unlikely to represent true primary mantle melts (ie. high Mg#, Ni). The Kakuki basalt is a high-alumina basalt from the central TVZ with relatively primitive major (see Gamble et al., 1990) and trace element characteristics (Fig. 3.7). Consequently this sample has frequently been used to represent a mantle wedge composition when modelling crustal contamination in lavas throughout the TVZ (Gamble et al., 1993a; Graham et al., 1992; 1995; Waight et al., 1999). However, the relatively enriched HFSE and REE composition of the Kakuki basalt renders it an unsuitable parental magma for generating primitive Ruapehu lavas (TH series) by fractionation. Furthermore, new Hf isotope data for the Kakuki basalt illustrate that its εHf composition is too low to generate any of the TH series by crustal contamination (Fig. 3.8b).

250 km north of Ruapehu the upper plate of the Hikurangi margin changes from continental to oceanic lithosphere at the Ngatoro Basin/southern Kermadec Arc. Previous modelling of primitive lavas from this region has reconciled their isotopic composition with < 1% source contamination of mantle wedge derived melt (Macpherson et al., 1998). The rate and angle of subduction of the Pacific plate and composition of sediment within the trench remain constant along from the Ngatoro Basin to the southern extent of the TVZ. Therefore, it is possible to suggest that primitive melts derived from the mantle wedge beneath the Ngatoro Basin and southern Kermadec Arc are likely to possess similar compositions to parental melts which have produced the differentiated lavas within the TVZ. Pb isotopes support this

to be the case as TH lavas clearly trend towards the Kermadec Arc field (Fig. 3.8c&d) suggesting these lavas are a suitable parental composition for modelling crustal contamination at Ruapehu.

3.6.3.2. TH series: constraints from isotopes

Two component model: primitive basalt + meta-igneous granulite

Homogenous isotopic compositions in the TH formation contrast with heterogeneous isotopic ratios of the PTH lavas (Fig. 3.13a; see also Price et al., 2001 and 2005). In Nd/Sr and Hf/Sr isotopic space, both suites are displaced from the range of primary Kermadec Arc lavas and trend towards different crustal compositions (Fig. 3.13a and b). Figure 3.13 displays Energy Constrained - Assimilation Fractional Crystallisation (EC-AFC (see Appendix G for details); Bohrson and Spera, 2001) modelling between a primitive Kermadec Arc composition and meta-igneous and meta-sedimentary crust (Table 3.3; modelling parameters). Radiogenic isotope ratios and trace element concentrations for the primitive Kermadec Arc composition are assumed to equal a mean value from Rumble IV volcano (samples 161, 162 and 168/1B; Gamble et al., 1996). Mixing arrays indicate that contamination of primitive Kermadec magma by ~ 30-50 % mass of meta-igneous granulite is the only means of reproducing the isotopic compositions of the TH suite (and the Ruapehu basalt).

3.6.3.3. PTH series: constraints from isotopes and trace elements

Two component model: primitive basalt + meta-sediment

Higher $^{87}Sr/^{86}Sr$ and lower εNd - εHf values in the PTH lavas strongly suggests involvement of Torlesse meta-sediment. Previous modelling of Ruapehu lavas has explained their isotopic composition by contamination of primitive basalt with meta-

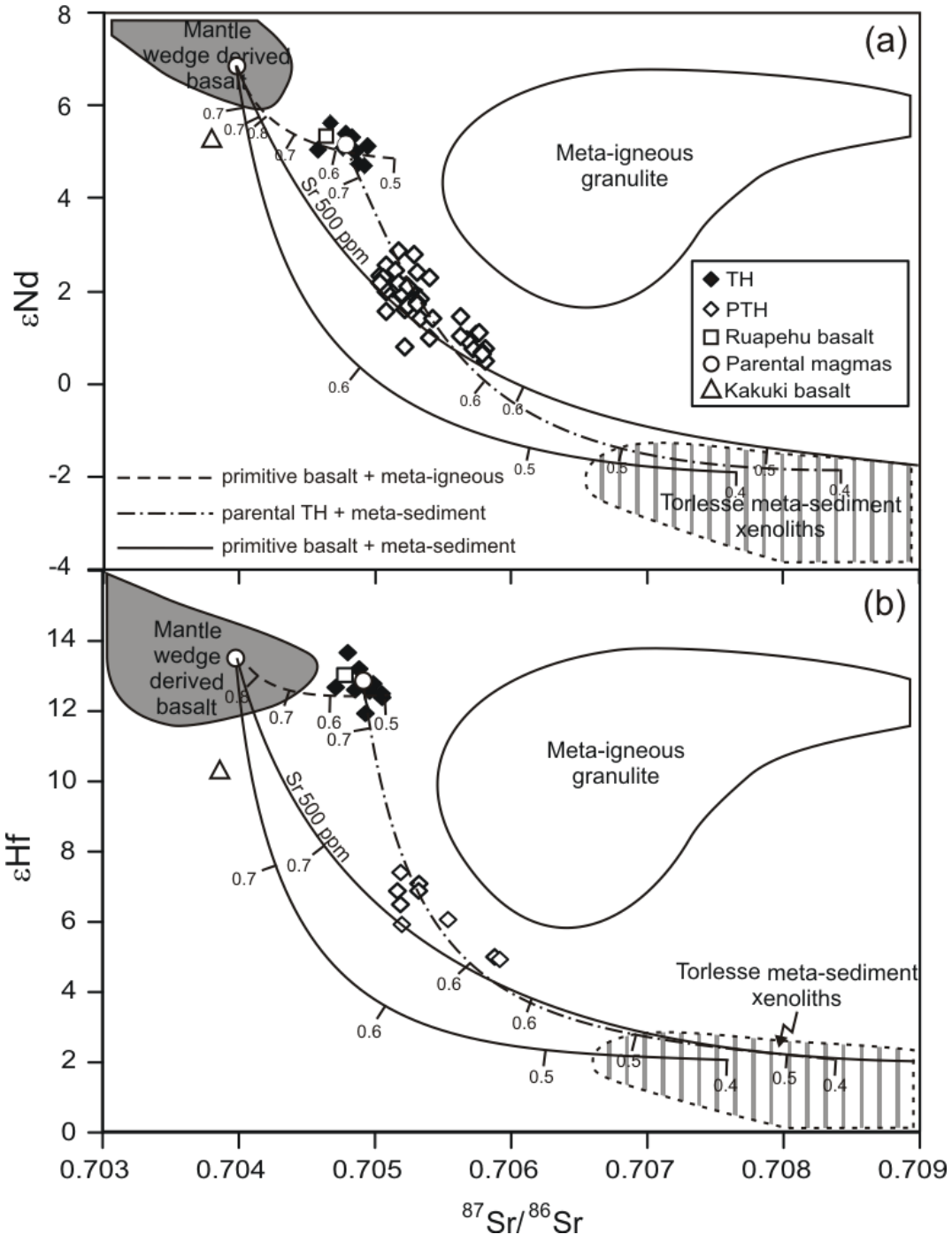

Fig. 3.13. EC-AFC (Spera and Bohrson, 2001) models using (a) $^{87}Sr/^{86}Sr$ vs εNd and (b) $^{87}Sr/^{86}Sr$ vs εHf, for a mantle wedge basalt and average TH lava contaminated with meta-igneous granulite and Torlesse meta-sediment. Modelling parameters listed in Table 3.3. Tick marks represent fraction of liquid remaining (F) in 0.1 increments. Mantle wedge derived basalt field from Kermadec Arc lavas (Gamble et al., 1996; Woodhead et al., 2001; Handler, M. pers comm).

Table 3.3. End member compositions and parameters used in EC-AFC modelling

	Sr ppm (D)	Nd ppm (D)	Hf ppm (D)	$^{87}Sr/^{86}Sr$	εNd
Mantle Wedge basalt	243 (0.5-1)	5.4 (0.2)	1.3 (0.2)	0.704	+7.1
Average TH	220 (1)	8.2 (0.2)	1.74 (0.2)	0.704909	+5.2
Meta-igneous granulite	323 (2)	12 (0.3)	1.25 (0.3)	0.707	+3.5
Meta-sediment	217 (2)	30 (0.4)	7 (0.4)	0.71459	-5.0

	εHf	Initial Temp (°C)	Liquidus (°C)	Solidus (°C)
Mantle Wedge basalt	+13.4	1200	1150	-
Average TH	+13	1200	1150	-
Meta-igneous granulite	+10	650	1050	850
Meta-sediment	-1	450	1000	800

Bulk distribution coefficients (D) in brackets. Crustal lithology D values from Chapter 2. Melt D values calculated from observed phase proportions in samples and Kd values in Appendix F. Mantle wedge basalt εHf from Woodhead et al. (2001) and Handler, M. pers comm. Mantle wedge basalt trace element concentrations from Gamble et al. (1996). Initial temperature and liquidus values of parental magmas determined by comparison of experimental estimates of primitive mantle wedge melts (Baker et al., 1994; Pichavant et al., 2002; Tatsumi, 1982; Ulmer, 2001). Initial temperature of meta-igneous granulite and meta-sediment are based on conservative estimates of a typical continental geotherm - 20°C/km (Brown and Musset, 1993), and relative depths of each lithology. This is intended to represent a meta-igneous and meta-sediment temperature during the very initial stages of underplating/intrusion beneath Ruapehu and would increase with time as the TVZ crust thermally evolves. Solidus values of meta-igneous granulite and meta-sediment based on experimental studies of meta-basalts (Beard and Lofgren, 1991; Rushmer, 1991; Wolf and Wyllie, 1994) and meta-sediments (Stevens and Clemens, 1993 and references therein).

sediment (Gamble et al., 1993a; Graham and Hackett, 1987; Graham et al., 1995 Waight et al., 1999). However, mixing arrays between primitive Kermadec magma and meta-sediment in Nd/Sr and Hf/Sr isotopic space fail to explain any of the PTH compositions due to the low Sr/Nd and Sr/Hf of the assimilant. Nevertheless many meta-sedimentary xenoliths have a refractory assemblage rich in plagioclase feldspar (see Chapter 2) which suggest the Sr/Nd - Sr/Hf ratio could increase after an extended period of partial melting. Increasing the Sr concentration in the meta-sediment to 500 ppm improves the fit, but EC-AFC curves tend to pass across rather than along the array of PTH compositions and fail to account for the relatively heterogeneous range in data.

Two stage, three component model: primitive basalt + meta-igneous granulite + meta-sediment

Although primitive Kermadec basalt is an adequate parental composition in TH modelling, it is an inappropriate end-member for generating PTH compositions by two-component mixing with meta-sediment. The trajectory of PTH data lies to the right or cross-cuts mixing between mantle wedge basalt and meta-sediment

suggesting that a two stage model maybe more appropriate. TH compositions generated in the lower crust may therefore provide an intermediate stage from which further crustal contamination by meta-sediment can generate PTH lavas. Mixing curves indicate assimilation of ~ 6-12 % mass of meta-sediment by an average TH magma can account for the relatively wide PTH isotopic array. The ability to produce PTH lavas by contaminating TH magma with meta-sediment can also be demonstrated with trace elements. Fig. 3.14 displays PTH normalised trace element patterns of a TH lava (relatively depleted; <1) and a typical crustal melt (enriched; >1) derived from a meta-sedimentary xenolith (LA-ICP-MS data; Price et al., 2005). Results from trace element modelling are also displayed to illustrate that enrichments required to produce PTH compositions from TH magma are far greater than can be achieved by fractional crystallisation, i.e. many LILE, LREE and HFSE normalised concentrations <1 after 40% fractionation. However as a result of the almost mirror-opposite trace element patterns of the TH lava and Torlesse melt, any mixing between these components would produce a composition near or close to 1 on Fig. 3.14. Results of simple mixing between Torlesse melt and fractionated TH lava for depleted elements are shown in Table 3.3. Indeed, many PTH lava trace element concentrations can be attained by mixing a fractionated TH lava with a similar mass of Torlesse melt (5-13%) predicted from isotopic modelling. However, the much larger mass of melt required in mixing to achieve K, Rb, and Ba PTH abundances indicates trapped meta-sediment melt may only preserve residuum concentrations for these elements due to their strongly incompatible behaviour during crustal anatexis (see Chapter 2). Nevertheless, in general, contamination of TH magma by meta-sediment can produce the evolved isotopic compositions of PTH lavas and also account for the increased LILE, LREE and HFSE abundances observed throughout the series.

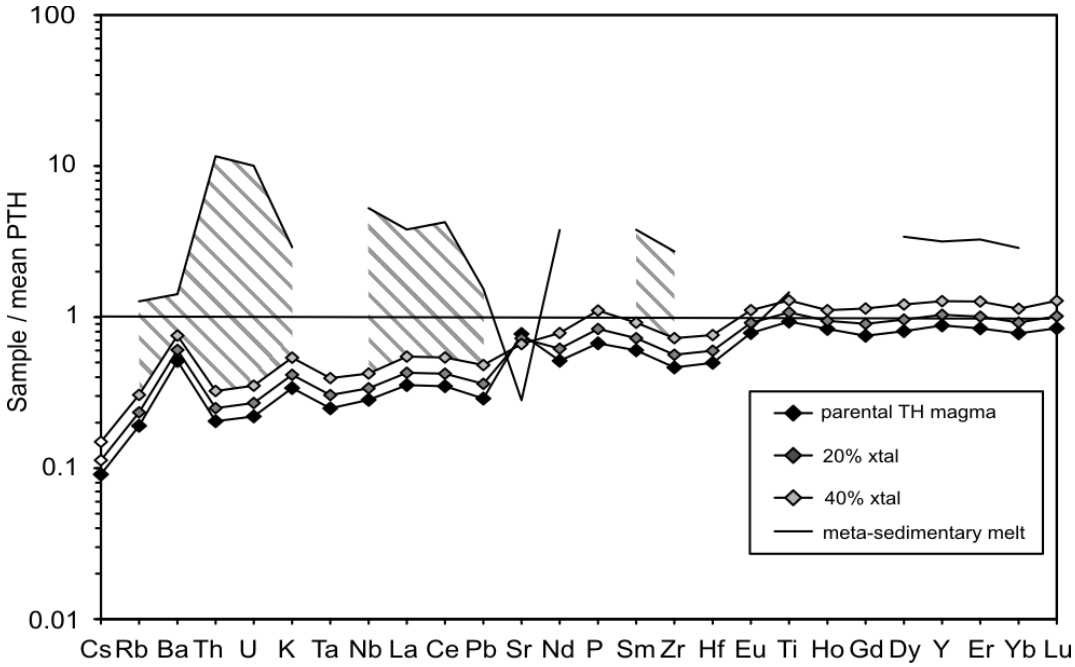

Fig. 3.14. Trace element variation diagram for a fractionated TH magma and meta-sedimentary melt normalised to evolved PTH sample. Phase assemblage used in TH fractionation modelling: 20% olivine, 50% plagioclase, 25% clinopyroxene, 2.5% orthopyroxene, 2.5% magnetite. Mineral-melt distribution coefficients are listed in Appendix F. Meta-sediment melt data (LA-ICP-MS) from Price et al. (2005).

Table 3.3. Results of mixing between fractionated TH lava and meta-sediment melt

	Meta-sediment melt (ppm)	Fractionated TH lava* (ppm)	Mass of meta-sediment melt required in mixing (%)**	Mean PTH lava (ppm)
Rb	80	19	0.5	52
Ba	526	280	0.38	371
Th	67	1.87	0.06	5.78
U	15.52	0.54	0.07	1.55
K	4.9	0.9	0.2	1.7
Nb	26.9	2.2	0.11	5.1
La	50.3	7.3	0.13	13.2
Ce	122	15.5	0.12	28.7
Nd	56.1	11.7	0.07	14.9
Zr	334	89	0.13	123

* 40% crystal fractionation

** Mass of meta-sediment required to achieve mean PTH trace element concentrations from fractionated TH lava

Meta-sediment melt data (LA-ICP-MS) from Price et al. (2005)

In summary isotopic data point towards involvement of primitive Kermadec arc lava and meta-igneous granulite during all stages of magmatism at Mt. Ruapehu. Meta-sedimentary rocks only became involved during the PTH phase of the volcano.

3.6.3.4 Temporal melt evolution: constraints from oxygen isotopes

Crustal contamination modelling using $^{87}Sr/^{86}Sr$, εNd and εHf values has shown that compositional differences between TH and PTH lavas may be a consequence of an adjustment from isobaric to polybaric differentiation. Previous studies of oxygen isotope ratios in arc lavas have calculated the $\delta^{18}O$ of the melt from phenocryst values using predefined coefficients to aid comparison with whole-rock data (e.g. Vroon et al., 2001). This calculation assumes that minerals and melt were in equilibrium at magmatic temperatures. Comparing coexisting mineral fractionations in Ruapehu lavas with corresponding phases in peridotites (Mattey et al., 1994) provides a test for equilibrium conditions. Figure 3.15 shows mineral pair Δ values of cpx-opx and cpx-olv in relation to mantle values ($\Delta_{i\text{-}j} = \delta^{18}O_i - \delta^{18}O_j$). $\Delta_{cpx\text{-}opx}$ range from 0.46–0.87 (n = 5) which is clearly higher than values from the mantle while the $\Delta_{cpx\text{-}olv}$ value from the Ruapehu basalt (0.58) is also out of equilibrium. Oxygen isotope ratios of phenocrysts are primarily controlled by the $\delta^{18}O_{melt}$, therefore disequilibrium in coexisting mineral pairs indicates that each phase crystallised from magma of differing isotopic composition. Evolving isotopic compositions within a batch of magma result from open system processes such as crustal contamination or magma mixing. At Ruapehu radiogenic isotopes provide unequivocal evidence for crustal contamination. Therefore $\delta^{18}O$ values from phenocrysts can be used to trace the evolution of the TH and PTH series as they ascend through the lithosphere (Fig. 3.16).

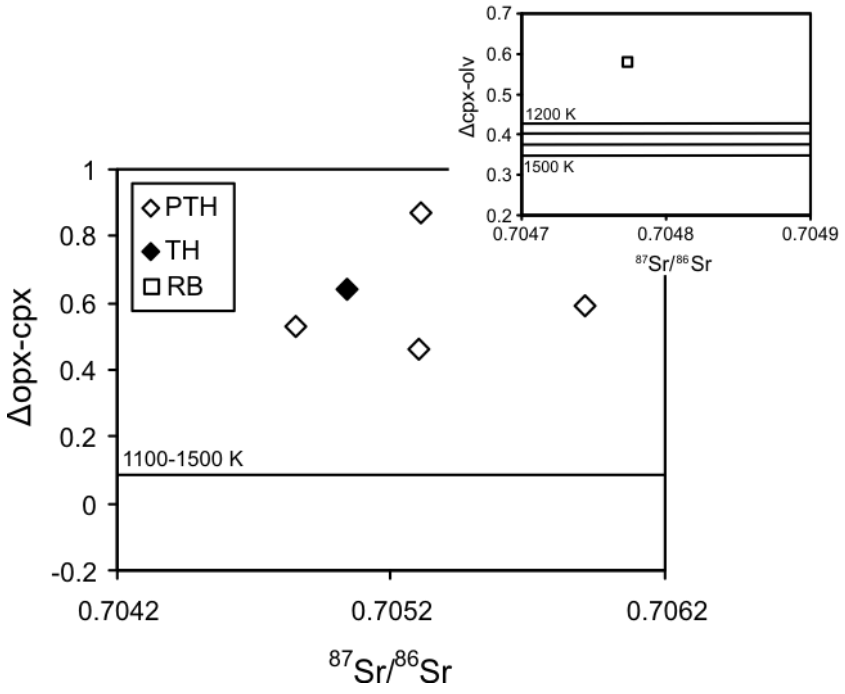

Fig. 3.15. $\Delta_{opx\text{-}cpx}$ and $\Delta_{cpx\text{-}olv}$ vs $^{87}Sr/^{86}Sr$. Theoretical $\Delta_{opx\text{-}cpx}$ values from Zheng (1993a). Experimental $\Delta_{cpx\text{-}olv}$ values between 1200-1500K from Kalamarides (1986). Note all mineral pairs are clearly out of equilibrium.

Stage 1: TH

The Ruapehu basalt is the most primitive lava from Ruapehu and the only sample to contain olivine. Radiogenic isotopes indicate this sample share a similar petrogenetic history to the TH series as a result of contamination by meta-igneous granulite. A $\delta^{18}O_{olv}$ value of +5.50‰ corresponds to olivine in upper mantle peridotite ((+4.8 to +5.5‰; Mattey et al., 1994) suggesting this phase may have a pre-assimilation origin. Olivine phenocrysts (Fo_{90}) with forsterite contents in equilibrium with mantle compositions also support this conclusion. However, +5.50‰ is the very upper limit for mantle olivine and petrographic evidence in olivine phenocrysts (e.g. corroded anhedral crystals) indicates disequilibrium with the groundmass. Modelling illustrated in Figure 3.16 confirms that the $\delta^{18}O_{olv}$ value in the Ruapehu basalt is too high to be

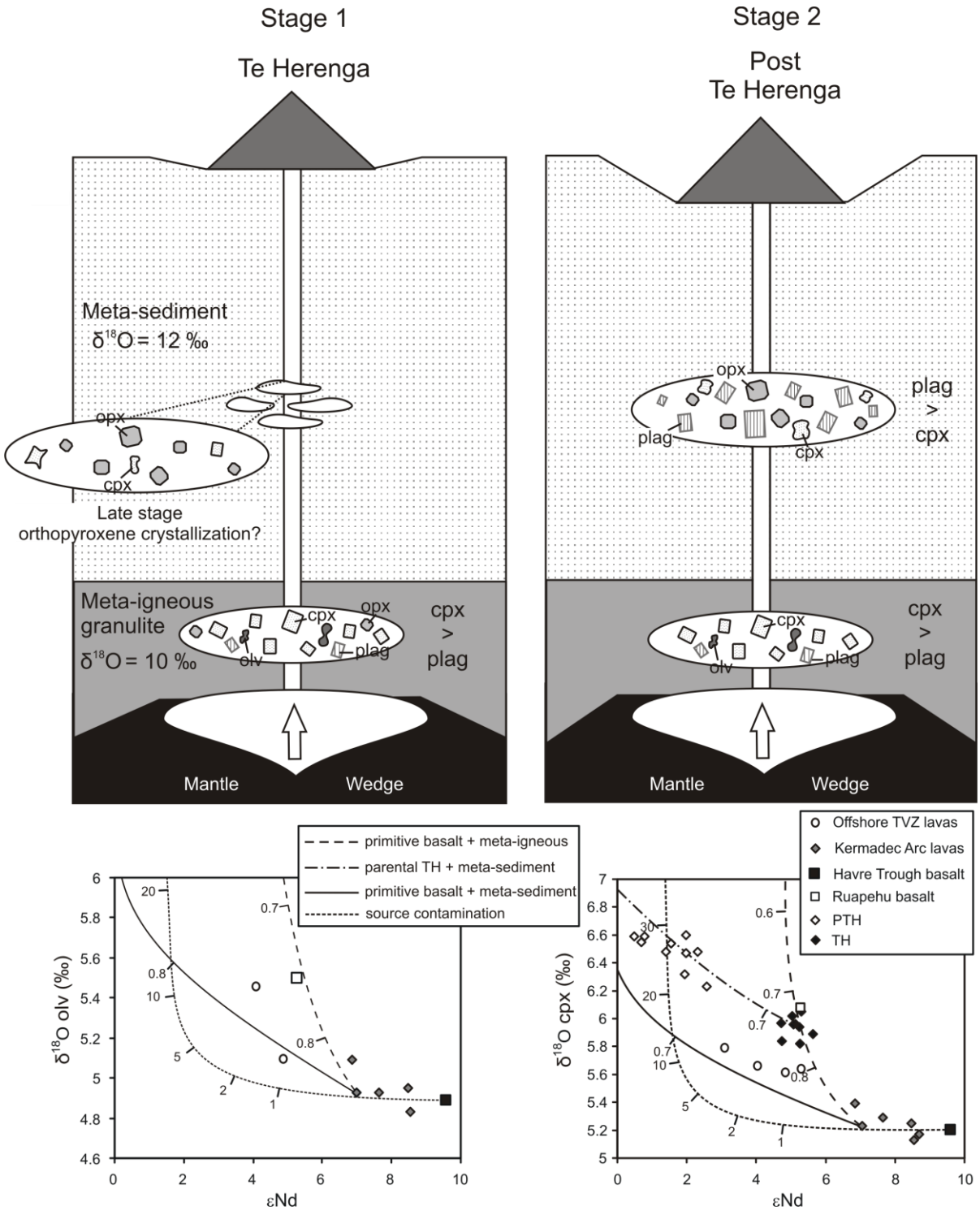

Fig. 3.16. Schematic diagram summarizing differentiation pathways for TH and PTH lavas based on evolving melt compositions as determined by $\delta^{18}O_{olv\text{-}cpx\text{-}opx}$. Stage 1 illustrates the development of a lower crustal thermal perturbation due to prolonged underplating. This facilitates assimilation of meta-igneous granulite by subsequent basalt from the mantle producing TH compositions. Stage 2 is the consequence of thermal weakening in the shallower crust. This allows further differentiation in the overlying meta-sediment producing PTH lavas. Oxygen isotope modelling uses parameters from Table 3.3. Meta-igneous granulite (+10.0) and meta-sediment (+12.0) $\delta^{18}O$ values from Graham et al. (1990) and Graham et al. (1992) respectively. Cont...

Source contamination curve and Kermadec Arc, Offshore TVZ and Havre Trough samples from Macpherson et al. (1998). Havre Trough lava represents local uncontaminated mantle. Kermadec lavas represent local source contaminated mantle. Tick marks on source contamination curve represent fraction of recycled component in source.

a result of source contamination and requires crustal contamination by meta-igneous granulite in the lower crust.

The similar radiogenic isotope composition of the RB and TH lavas is also reflected in comparable $\delta^{18}O_{cpx}$ values (TH = 5.82-6.05‰; RB = 6.08‰) indicating these clinopyroxene share a similar petrogenetic history. Modelling indicates the oxygen isotope compositions of this phase are a result of contamination by meta-igneous granulite (Fig. 3.16). However in the case of the RB, the isotopic disequilibrium between clinopyroxene and olivine (Fig. 3.15) suggests the former phase crystallised later, following more extensive granulite contamination. This is supported by petrography, where clinopyroxene overgrowths occur around olivine phenocrysts. TH $\delta^{18}O_{opx}$ values also display isotopic disequilibrium with coexisting phases ($\Delta_{opx\text{-}cpx}$ = 0.53-0.64). Orthopyroxene is commonly euhedral in TH lavas indicating equilibrium with groundmass compositions. This may suggest it crystallised shortly before eruption and consequently may have experienced the most crustal contamination of all ferromagnesian phases. Isotopic disequilibrium with clinopyroxene ($\Delta_{opx\text{-}cpx}$ 0.53-0.64) could be attributed to orthopyroxene crystallising after more extensive granulite contamination. Although radiogenic isotopes suggest TH magmas did not assimilate meta-sediment, minor degrees of late stage contamination in the upper crust, coincident with orthopyroxene crystallisation, could also account for disequilibrium with clinopyroxene. Unfortunately however, current

data is unable to confirm which crustal assimilant influences the oxygen isotope composition of orthopyroxene.

Stage 2: PTH

Isotopes and major and trace element data suggest PTH magma differentiated at relatively shallow levels where melt initially contaminated in the lower crust, experienced a further stage of crustal interaction with meta-sediment. This is demonstrated by elevated oxygen isotope ratios in clinopyroxene and orthopyroxene PTH phenocrysts ($\delta^{18}O_{cpx}$ = 6.23-6.60‰; $\delta^{18}O_{opx}$ = 6.93-7.19‰). A mean value of $\delta^{18}O_{cpx}$ and $\delta^{18}O_{opx}$ from each series reveal PTH pyroxenes are ~0.5‰ higher than respective phases in TH lavas due to assimilation of high $\delta^{18}O$ meta-sediment. This is illustrated for clinopyroxene, where PTH compositions result from mixing between average TH magma and meta-sediment. However, coexisting clinopyroxene and orthopyroxene phenocrysts in PTH lavas display isotopic disequilibrium ($\Delta_{opx\text{-}cpx}$ = 0.46-0.87). This could be explained by PTH magma hosting a crystal cargo which has crystallised at differing levels in the arc crust, i.e. clinopyroxene in the lower differentiation zone (meta-igneous granulite) and orthopyroxene in the upper differentiation zone (meta-sediment). However, orthopyroxene crystallizing after more extensive meta-sediment contamination may also be an equally valid explanation for disequilibrium with co-existing clinopyroxene. Unfortunately whole-rock radiogenic isotope data or mineral separate $\delta^{18}O$ values are unable to discern which process is responsible for pyroxene disequilibrium. Complimenting oxygen isotope data with radiogenic isotope analysis for clinopyroxene and orthopyroxene mineral separates may provide greater constraints on the contamination history of PTH lavas. In addition, recent advances in trace element and isotopic micro-sampling

within individual phenocrysts has proved particularly useful in constraining the true end-members that generate the hybrid compositions recognised in arc magmas (Davidson et al., 2005), and could be used here to improve constraints on the initial onset of meta-sediment contamination.

3.7. Summary and Conclusions

Crystal fractionation and crustal assimilation processes can account for the temporal variation in the geochemistry of lavas from Mt. Ruapehu. Major element modelling suggests the trends in TH and PTH lavas result from differing fractionating assemblages. The trends to higher Al_2O_3 and lower MgO in TH lavas with respect to the Ruapehu basalt composition are a result of clinopyroxene + olivine > plagioclase fractionation. However, in PTH lavas the steady decrease in Al_2O_3 throughout the series is produced by plagioclase > clinopyroxene + olivine/orthopyroxene fractionation. On the basis that plagioclase abundance is the primary difference in the fractionating assemblage of each series, we can infer that TH lavas fractionated at relatively deeper levels in the crust relative to the PTH series. Trace element modelling for each series supports this conclusion however strong negative residuals for LILE and HFSE in PTH calculations suggests the addition of a crustal component.

Isotopic compositions for Ruapehu lavas are displaced from local MORB (primitive Kermadec Arc lavas) with the TH and PTH series trending towards different crustal compositions. In particular, new Hf isotope data provides unequivocal evidence for progressive crustal contamination throughout the lifetime of Ruapehu. Isotopic modelling indicates TH lavas result from assimilation of mantle wedge derived basalt by ~30-50% mass of meta-igneous granulite. PTH compositions can only be resolved by contamination of a parental TH magma by 6-11% mass of

meta-sedimentary material. Mineral separate oxygen isotope analysis support radiogenic isotope modelling and permit additional constraints to be placed upon the progressive nature of meta-igneous granulite and meta-sediment contamination.

It is possible to interpret the temporal geochemical evolution of the volcano as a two-stage process, as originally proposed by Price et al. (2005). As a result of buoyancy contrasts, the earliest melts produced by the mantle wedge would probably have stalled near the Moho, underplating the lower crust. This created a deep, and long-lived, site for magma storage, similar to the MASH zones of Hildreth and Moorbath (1988) or hot zones of Annen et al. (2006). After prolonged, focussed intrusion at this depth (10,000-100,000 yrs - based on U-series estimates for arc magma residence times, Reagan et al., 2003; Zellmer et al., 2003), the crust became sufficiently hot to allow assimilation of meta-igneous granulite near its base. Subsequent batches of basaltic magma arriving in this differentiation zone generated the TH magma series. The overlying meta-sediment remained cool, limiting interaction with TH magma that was travelling to the surface. However, continued magmatic intrusion enhanced crustal heat flow sufficiently to thermally weaken the crust facilitating the development of a further differentiation zone within the meta-sediment. This changed the baseline chemistry of magma in a similar manner to that proposed for the Central Andes (Hildreth and Moorbath, 1988), by adding a further stage of crustal interaction with meta-sediment after granulite interaction in the lower crustal differentiation zone. Assimilation of meta-sediment created the heterogeneous trace element concentrations and distinctive shifts to higher Sr, Pb, O and lower Nd, Hf isotopic compositions observed in PTH lavas.

Chapter 4

Primitive basaltic andesites/andesites at the southwest termination of the Taupo Volcanic Zone

4.1. Introduction

Most primary melts generated at subduction zones are believed to be basaltic in composition (Arculus, 1981). However relatively rare andesites with high MgO contents (High-Mg Andesites) found predominantly at arcs such as Izu Bonin (e.g. Crawford et al., 1989), Setouchi Volcanic Belt (e.g. Tatsumi and Ishizaka, 1981), Aleutians (e.g. Kay, 1979) and Cascades (e.g. Baker et al., 1994), also exhibit primary characteristics, e.g. high Ni concentration and Mg# ~ 0.7. High-Mg andesites have received considerable attention due to their close chemical similarity to Archaean crust and consequently may have contributed to crustal growth early in the Earth's history (Kelemen, 1995). Various models have been proposed to explain their occurrence with hydrous partial melting of both lherzolite (Hirose, 1997) and harzburgite (Grove et al., 2002) or melt-rock interaction in the upper mantle (Kelemen et al., 1998) commonly cited as viable methods of generating high-Mg andesite. However overwhelming evidence suggests the majority of primary melts are basaltic at Phanerozoic arcs, hence other means of generating high-Mg andesite should be considered.

Some of the highest MgO contents (> 7 wt %) in lavas from the southern TVZ occur in relatively evolved basaltic andesites and andesites (52-58 SiO_2 wt %). These high-Mg andesites have been erupted from satellite vents near the southwest termination of the TVZ, peripheral to the current zone of andesite production (Fig. 4.1). This is in contrast to the central TVZ where equivalent MgO levels are only found in basalts (high-alumina basalts; Gamble et al., 1990; Graham, 1985a). The distinct geographic distribution of high-Mg andesite versus high-alumina basalt also corresponds to an abrupt increase in crustal thickness (~10 km) from north to south (Stern et al., 2006). It has been demonstrated that much of the chemical diversity in

TVZ lavas results from varying degrees and/or types of crustal differentiation (e.g. Chapter 3; Gamble et al., 1993a; Graham et al., 1995; McCulloch et al., 1994; Macpherson et al. 1998; Price et al., 2005; Sutton et al., 1995). Therefore given the overwhelming evidence for crustal-level differentiation in the TVZ, this chapter will investigate whether the North Island crust and its variable thickness (20-35 km) contribute to the generation of high Mg-andesites and their restriction to the southern TVZ.

4.2. Overview of satellite vents

Samples in this study were collected from two satellite vents of Mt. Ruapehu (Ohakune and Pukeonake Craters) in addition to the Waimarino basalt locality (SE of Lake Taupo) (Fig. 4.1). Data from Hauhungatahi volcano (16 km west of Ruapehu) collected by Graham (1985a) and Hackett (1985) are also included in this study due to its close similarity in petrography and geochemistry.

Ohakune Craters comprise four clustered monogenetic centres 17 km SW of Ruapehu where they define the most southern extent of volcanism in the TVZ. The basement comprises Miocene-Pliocene marine sediments which exist as a series of east-west trending fault-bounded blocks (Ohakune fault set; Villamor and Berryman, 2006b). The craters themselves outcrop on the southern margin of the Ohakune Fault set and comprise scoria cones consisting of alternating lava flows and highly vesicular Strombolian block and bomb deposits (Houghton and Hackett, 1984). Dating of a closely associated tuff ring (Hackett and Houghton, 1988) suggests the vents were active at approximately 25 ka.

Pukeonake is a 140 m high scoria cone approximately 15 km north of Ruapehu consisting predominantly of pyroclastic material. However several 5-10 m thick lava flows are exposed at the Mahuia Rapids stream section 1 km NW of the cone. The

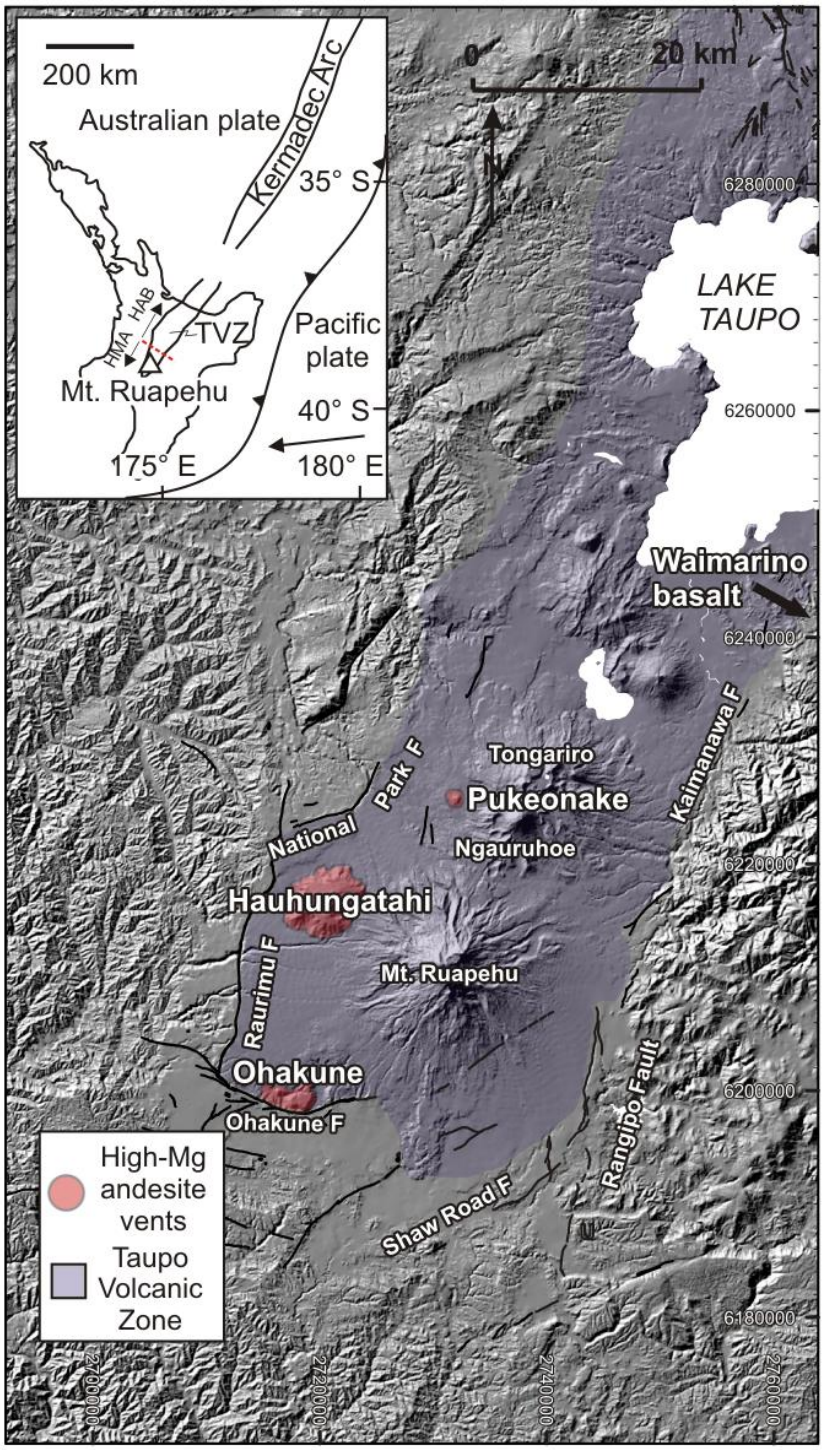

Fig. 4.1. Image of the southern TVZ (adapted from Villamor et al., 2007) showing the location of high-Mg andesite vents. Note they tend to occur relatively near faults. High alumina basalts only occur north of Lake Taupo (see inset) in the central and northern TVZ (see Gamble et al., 1993a)

lava flows and scoria cone cover approximately 55 km^2 (Topping, 1973) and are associated with a 1-2 km fissure trending N-S, east of the National Park Fault. The overlying c.22.6 ka rhyolitic Oruanui Tephra dates Pukeonake lavas at ~23 ka (Hackett, 1985).

Hauhungatahi is a low eroded cone ~12 km west of Ruapehu resting on Miocene sedimentary basement. It is comprised of lava flows at the base and summit of the cone with numerous inter-bedded pyroclastic and lahar sequences. The main graben bounding Raurimu and National Park Faults bound the W and NW slopes of the volcano. Recent $^{40}Ar/^{39}Ar$ ages (Cameron, 2004) confirm that Hauhungatahi is at least 800 ka making it the oldest preserved vent in the southern TVZ.

The Waimarino basalt sample was supplied from the Victoria University of Wellington collection. It was originally collected by W. Hackett from a remote location SE of Lake Taupo. Although distant from Ruapehu and surrounding vents, it is included within this study because it represents a potential parental magma to the high-Mg andesites of the southern TVZ. Hackett (1985) estimated an age of 13.8-19.8 ka based on the lava flow overlying the Oruanui breccia.

4.3. Petrography and Mineral Chemistry

A mineralogical and petrographical summary of all high-Mg andesites is reported below with modal analyses and mineral compositions available in Appendix A and D. Olivine phenocrysts are ubiquitous throughout all samples enabling relatively easy distinction from lavas erupted from the main Ruapehu vent.

Ohakune lavas are highly vesicular and hypocrystalline usually containing <12% phenocrysts ranging in size from 0.2-3mm. Olivine, clinopyroxene and orthopyroxene constitute the main phenocryst phases with plagioclase only occurring

in the groundmass. Olivine occurs as anhedral-euhedral crystals constituting 1-2 % modal volume and is generally subordinate to clinopyroxene. Compositions range between Fo_{88-82} and display equilibrium with bulk rock FeO/MgO (Fig. 4.2). CaO contents of this olivine are generally ≤ 0.1 wt% which may indicate a high pressure origin (Stormer, 1973). Crystal margins are often resorbed and occasionally exhibit thin orthopyroxene overgrowths. Clinopyroxene-orthopyroxene ratios are generally 0.8-0.9 (cpx/cpx+opx) with both minerals occurring in small pyroxene glomerocrysts (5 mm wide). Clinopyroxene phenocrysts usually comprise ~7% modal volume and are subhedral-euhedral. Compositions range between $Ca_{42}Mg_{49}Fe_9$ - $Ca_{38}Mg_{44}Fe_{18}$ lying in the augite and endiopside fields on the pyroxene quadrilateral (Fig. 4.3) with many crystals exhibiting normal and reverse oscillatory zoning. Orthopyroxene phenocrysts occur as subhedral-euhedral crystals constituting ~1-2% modal volume. Compositions range between $Ca_3Mg_{81}Fe_{16}$ - $Ca_3Mg_{72}Fe_{25}$ and display both normal and reverse zoning. Orthopyroxene also occurs as overgrowths on olivine and clinopyroxene phenocrysts. Plagioclase is only observed within the groundmass in addition to pyroxene and titanomagnetite.

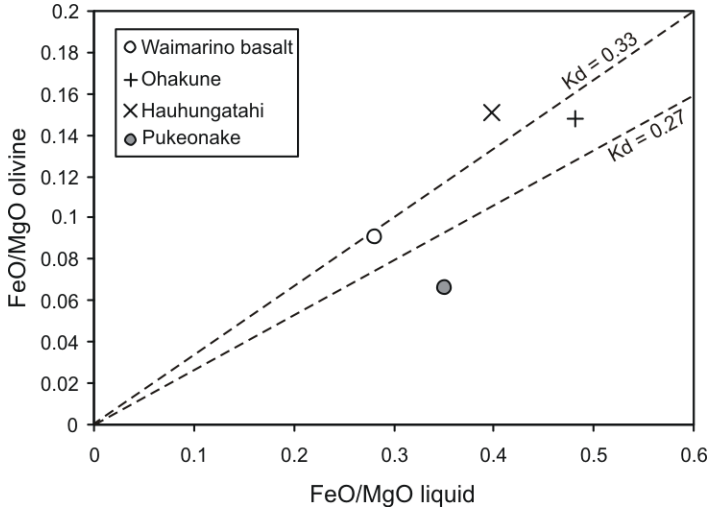

Fig. 4.2. FeO/MgO (mole %) for bulk rock and coexisting olivine phenocrysts. Hauhungatahi data from Graham (1985a). Distribution coefficients (Kd) from Roeder and Emslie (1970).

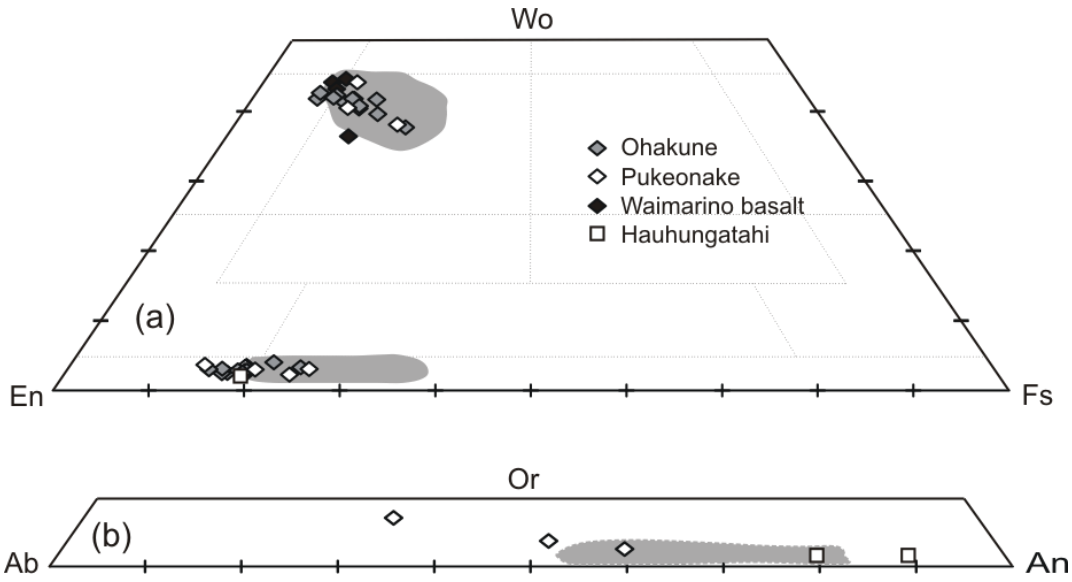

Fig. 4.3. a) Pyroxene and b) plagioclase compositions in high-Mg andesites. Grey fields represent compositions of Ruapehu phenocrysts.

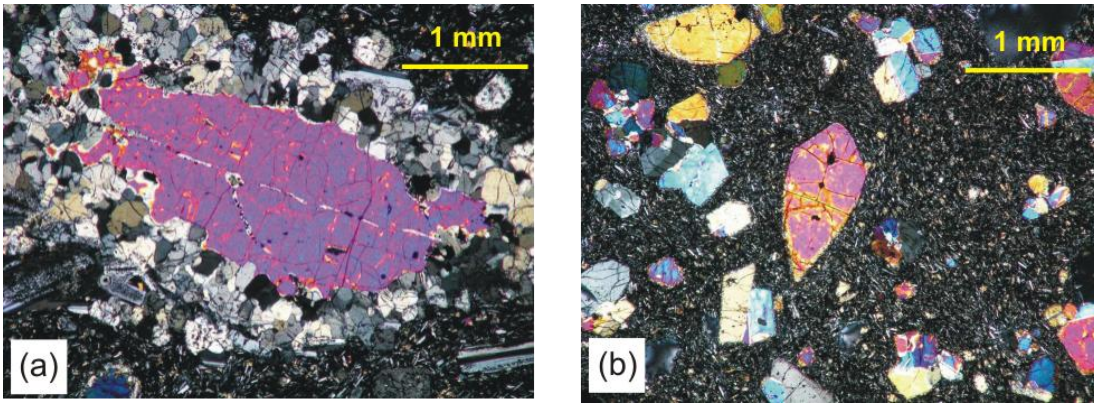

Fig. 4.4. Photographs (XPL) of a) Pukeonake olivine phenocryst with orthopyroxene corona b) euhedral olivine in the Waimarino basalt.

Pukeonake lavas are hypocrystalline and moderately to strongly porphyritic containing ~30% phenocrysts up to 6 mm wide. Olivine, clinopyroxene, orthopyroxene and plagioclase constitute the main phenocryst phases. Forsteritic olivine (Fo_{93}) occurs as large (up to 6 mm) subhedral to anhedral phenocrysts while smaller microphenocrysts (< 2mm) generally contain a higher fayalite component

(Fo_{75}). Olivine constitutes 2-5% modal volume and commonly contains chrome spinel inclusions in addition to exhibiting well developed orthopyroxene coronas (Fig. 4.4a). The poor correlation between FeO/MgO in the whole-rock and olivine phenocrysts (Fig. 4.2) composition indicates disequilibrium, suggesting this phase is xenocrystic and may represent entrained crystals from the mantle. Clinopyroxene phenocrysts comprise up to 10% modal volume and occur as subhedral-euhedral crystals. Compositions range from $Ca_{41}Mg_{49}Fe_{10}$ - $Ca_{38}Mg_{45}Fe_{17}$ and commonly display reverse zoning. Orthopyroxene are generally subhedral and constitute 1-2% modal abundance. Compositions range between $Ca_4Mg_{82}Fe_{14}$ - $Ca_2Mg_{74}Fe_{24}$ and display resorbed cores and/or heavily sieved rims. Pukeonake lavas are the only high-Mg andesite to contain plagioclase phenocrysts which generally exhibit strong disequilibrium textures: reverse zoning (Graham, 1985a; Hobden, 1997) and sieved cores/rims. An_{57-32} contents span labradorite to andesine compositions.

Hauhungatahi lavas are generally more crystalline than the other high-Mg samples containing olivine, clinopyroxene and orthopyroxene phenocrysts with plagioclase only occurring as microphenocrysts or within the groundmass. Olivine compositions range from Fo_{86-80}, clinopyroxene are generally augite and plagioclase occupy the bytownite field. On the basis of petrography and major element modelling, Graham (1985a) interpreted Hauhungatahi lavas forming by fractional crystallisation of clinopyroxene and olivine from a parental melt similar in composition to the Waimarino basalt.

The Waimarino basalt is hypocrystalline and moderately porphyritic containing ~20% phenocrysts. Olivine and clinopyroxene constitute the main phenocryst phases with little or no orthopyroxene or plagioclase present (Fig. 4.4b). Forsteritic olivine (Fo_{91}) up to 3 mm wide occurs as subhedral to euhedral phenocrysts

and constitutes about 15% modal volume. They commonly contain chrome spinel inclusions and exhibit normal zoning. Clinopyroxene phenocrysts comprise ~7% modal volume and occur as anhedral-euhedral crystals. Compositions range from $Ca_{36}Mg_{51}Fe_{13}$ - $Ca_{44}Mg_{46}Fe_{10}$ with evidence for both normal and reverse zoning. The groundmass is predominantly composed of plagioclase and pyroxene microlites.

4.4. Geochemistry

4.4.1. Major element data

Major element data are listed in Appendix B. Excluding the Waimarino basalt, the high-Mg andesites from the southern TVZ have a fairly restricted range of SiO_2 contents (55.9-57.7 wt %) ranging from basaltic andesite to andesite. With the exception of the Pukeonake lavas all samples can be classified as low-K island arc tholeiites (Peccerillo and Taylor, 1976). Major element variations are presented using MgO variation diagrams due to the relatively primitive (high MgO) compositions (Fig. 4.5a-g). Data from Ruapehu (Chapter 3) and the high-alumina basalts of the central/northern TVZ (locations: Rotokawau, Matahi, Tarawera, Johnson Road, Ongaroto, Kakuki, Tatua, Ben Lomond, K-Trig; see Gamble et al., 1993a) are also plotted for comparison. Ohakune and Hauhungatahi lavas commonly define a similar trend illustrated by CaO abundances which remain relatively constant with decreasing MgO. In contrast, CaO decreases linearly in high-alumina basalts and define a relatively steep trend over a narrow range in MgO (~5-8 wt %). Pukeonake samples however, form a distinct outlier to this trend with much lower CaO contents (7.3 wt %) at equivalent MgO. Ohakune, Hauhungatahi and Pukeonake lavas collectively define a series in which Al_2O_3 gradually increases from ~14-16 wt % as MgO

decreases. This contrasts with the high-alumina basalts which steadily decrease in Al_2O_3 from ~18-17 wt %. K_2O abundance increases with decreasing MgO in high-Mg andesites and high-alumina basalts although the former series possess elevated K_2O

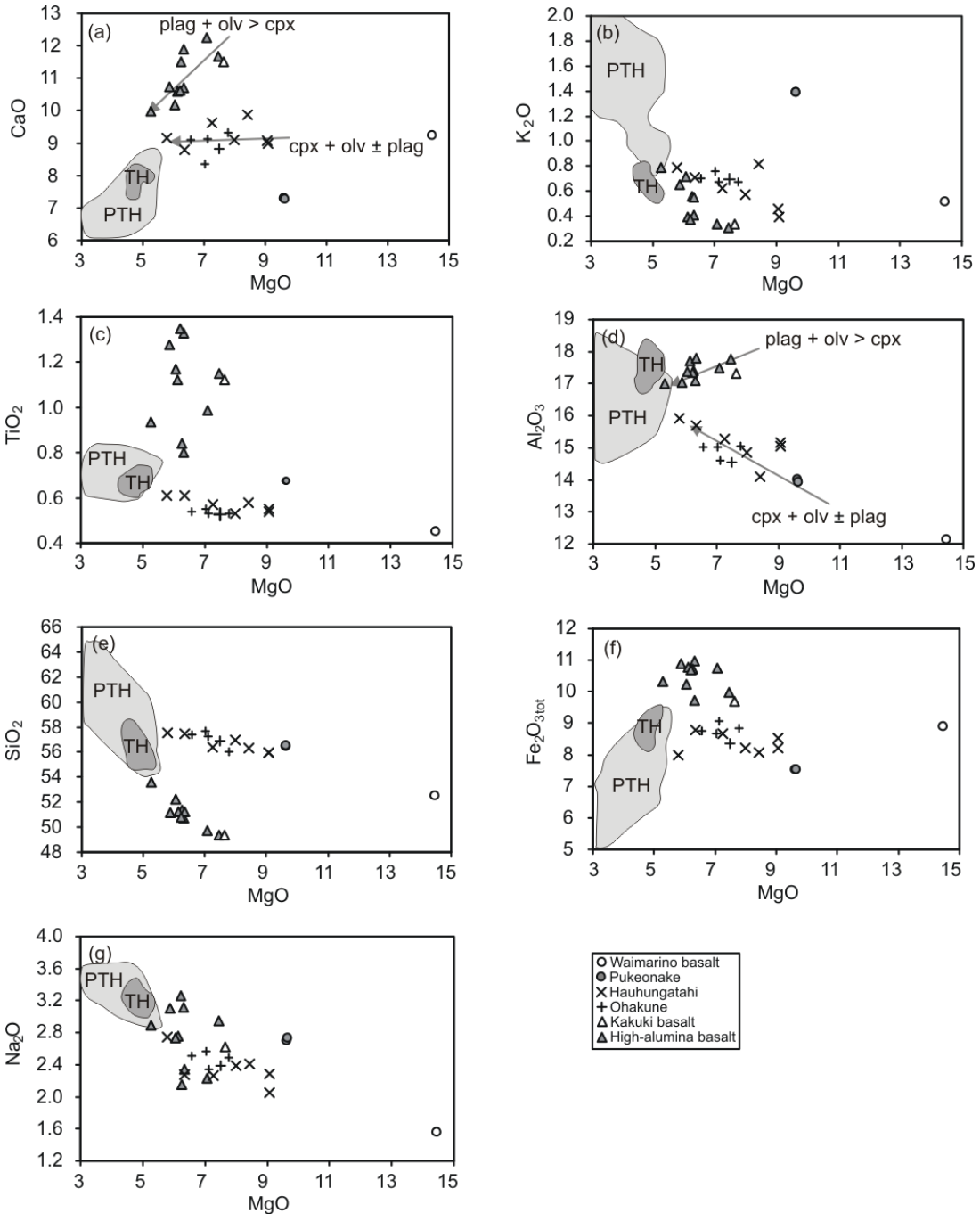

Fig. 4.5. Major element variations for high-Mg andesites and high-alumina basalts. Crystallisation vectors based on least squares major element modelling. Hauhungatahi data and smaller symbol Ohakune data are from Graham (1985a). Dark and light grey fields are TH and PTH lavas respectively (see chapter 3). High-alumina basalt data from Gamble et al. (1990).

abundance at MgO >7 wt%; both K_2O trends however converge at 5-6 wt% MgO. Fe_2O_3tot, SiO_2 and Na_2O abundances also increase with decreasing MgO contents throughout the high-Mg andesite series. Pukeonake lavas however, lie out with the general trends in K_2O, Na_2O and TiO_2 towards higher values at equivalent MgO. The Waimarino basalt is offset from trends in other lavas as a result of its high MgO content (14.5 wt %). However, trajectories of the high-Mg andesites in SiO_2, Al_2O_3 and K_2O plots suggest the Waimarino basalt may be an appropriate parental composition.

4.4.2. Trace element geochemistry

Many of the high-Mg andesites have Ni concentrations ≥ 50 ppm and define a positive correlation with MgO (Fig. 4.6a). A maximum concentration of 420 ppm is recorded in the Waimarino basalt while Pukeonake samples also have anomalously high Ni abundances (~280 ppm). Large ion lithophile element variations (LILE; Rb and Ba) and U and Th within the high-Mg andesites (Fig. 4.6b-c) mirror that of K_2O, displaying a negative correlation and possessing higher abundances than high alumina basalts at >7 wt% MgO; both series converge at MgO ~ 5-6 wt%. Sr concentrations in Ohakune and Hauhungatahi samples are ~50-500 ppm higher than Ruapehu lavas (Fig 4.6d). Ohakune lavas define a trend similar to the high-alumina basalts with moderately high Sr values (345-390 ppm) which increase with decreasing MgO. On the other hand, Hauhungatahi lavas have higher Sr concentrations (463-569 ppm) which display a weak positive correlation with MgO. High field strength elements (HFSE; e.g. Zr) in Ohakune and Hauhungatahi lavas also display similarities to K_2O variations with a negative correlation versus MgO; high-alumina basalts however,

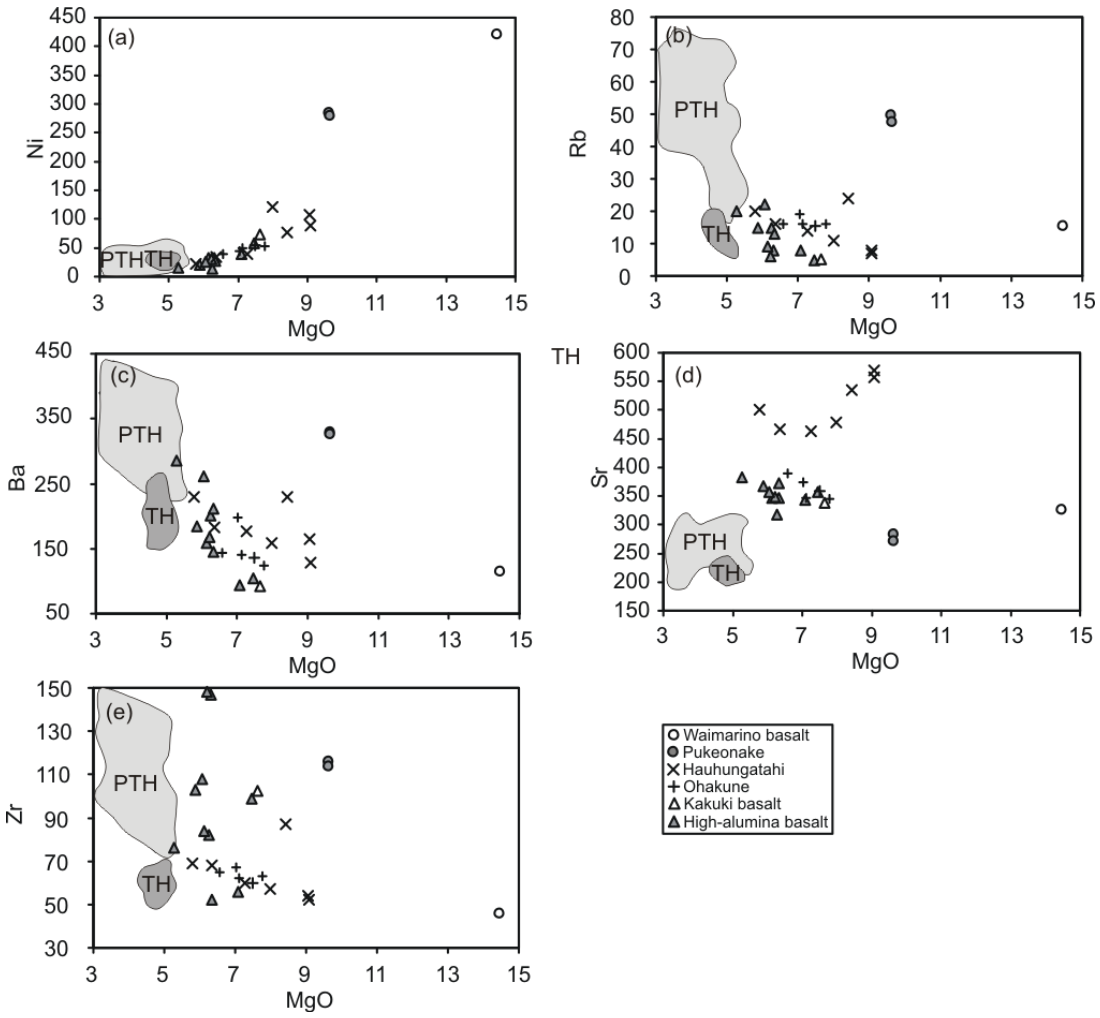

Fig. 4.6. Trace element variations for high-Mg andesites and high-alumina basalts. Hauhungatahi data and smaller symbol Ohakune data are from Graham (1985a). Dark and light grey fields are TH and PTH lavas respectively (see chapter 3). High-alumina basalt data from Graham et al. (1990).

show considerable scatter and a higher mean Zr value (~100 ppm). Pukeonake samples are unique in having anomalously high incompatible trace element concentrations comparable to PTH lavas from Ruapehu (e.g. Fig. 4.6c) while also having high compatible element abundances (e.g. Ni = 285 ppm; Cr = 558 ppm). Incompatible trace element concentrations in the Waimarino basalt are generally lower or similar to mean high-Mg andesite values.

Ohakune, Hauhungatahi and Waimarino lavas exhibit typical N-MORB

normalised trace element abundance patterns of subduction related rocks, with enrichment of LILE and LREE relative to HFSE and HREE (Fig. 4.7). The highly to moderately incompatible elements are all enriched, while many of the HFSE and MREE-HREE are depleted relative to N-MORB. Ti in particular displays the greatest

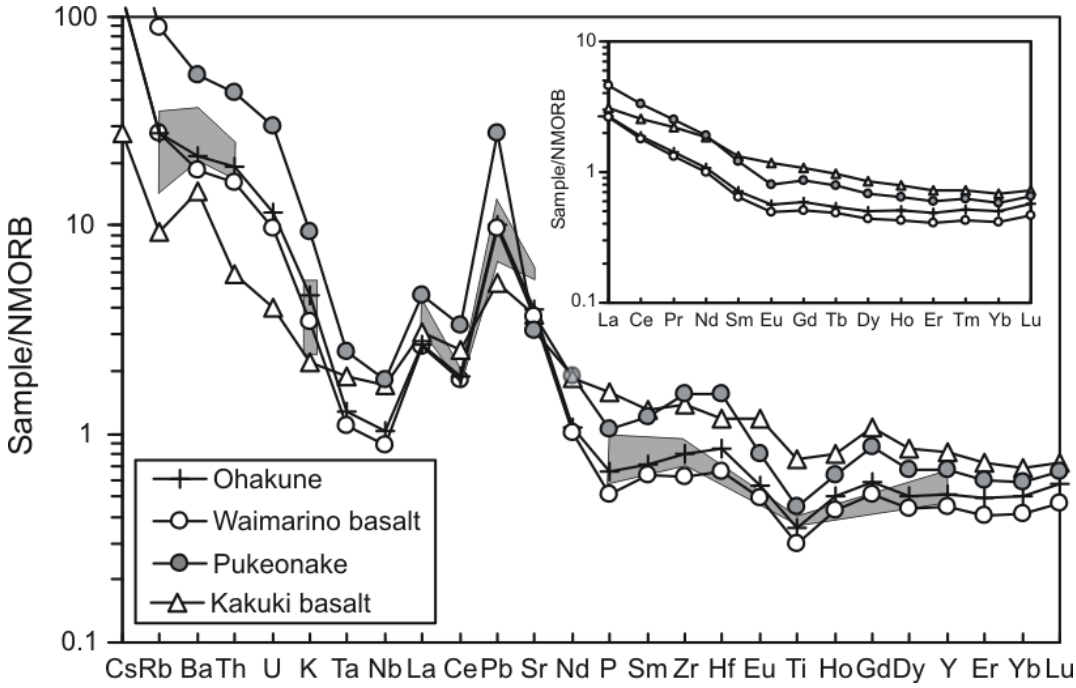

Fig. 4.7. N-MORB normalised trace element diagram for high-Mg andesites and the Kakuki basalt. The grey field represents the range in Hauhungatahi lavas (Graham, 1985a). Inset diagram displays N-MORB normalised REE variations for selected compositions. N-MORB normalisation values from Sun and McDonough, 1989.

degree of depletion with the Waimarino basalt exhibiting ~70% relative to NMORB. Other HFSE (Zr and Hf) and MREE-HREE generally display ~40-50% depletion relative to NMORB. The Kakuki basalt (most primitive high-alumina basalt) also displays a typical subduction related trace element pattern however in contrast to the high-Mg andesites is only depleted in HREE relative to N-MORB, being enriched in all REE relative to Ohakune and Waimarino samples. Pukeonake lavas display the

greatest enrichment in LILE-LREE-HFSE and like Ohakune and Hauhungatahi samples are depleted in MREE-HREE by up to 40% relative to N-MORB.

4.4.3. Radiogenic isotopes

Sr, Pb, Nd and Hf isotope data for Ohakune, Pukeonake, Waimarino and Kakuki basalt are listed in Appendix C and plotted in Fig. 4.8a-d. Only Sr and Nd isotope compositions are available for Hauhungatahi lavas (Graham, 1985a). All high-Mg

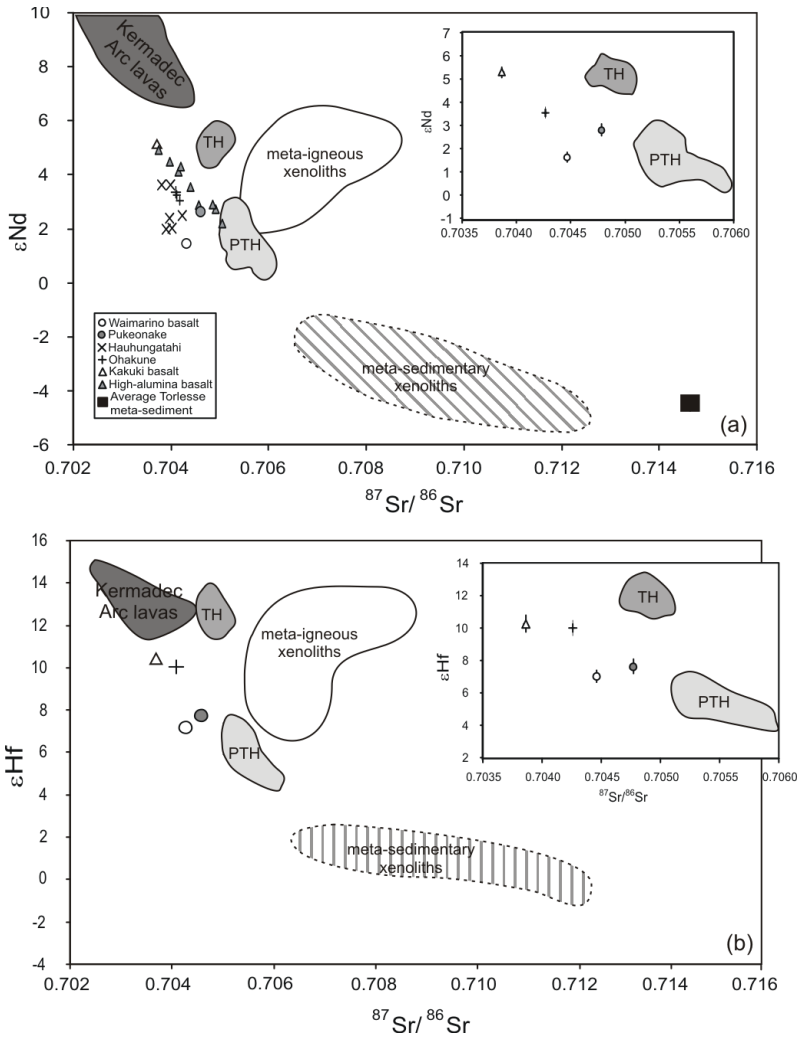

Fig. 4.8. Variation of (a) εNd vs $^{87}Sr/^{86}Sr$ and (b) εHf vs $^{87}Sr/^{86}Sr$ for high-Mg andesites and high-alumina basalts. Dark and light grey fields are TH and PTH lavas respectively (see chapter 3). Hauhungatahi data and smaller symbol Ohakune data are from Graham (1985a). High-alumina basalt data from Graham et al. (1990). Average Torlesse meta-sediment (non-xenolith) from Graham et al. (1992). Insets display external errors (2σ) for each data point however they are often smaller than the symbol.

andesites show displacement from local primitive basalt (Kermadec arc lavas). The Waimarino basalt and Ohakune and Hauhungatahi lavas illustrate a distinct trend from the Ruapehu suite and high-alumina basalts with rapidly decreasing εNd values (3.8-

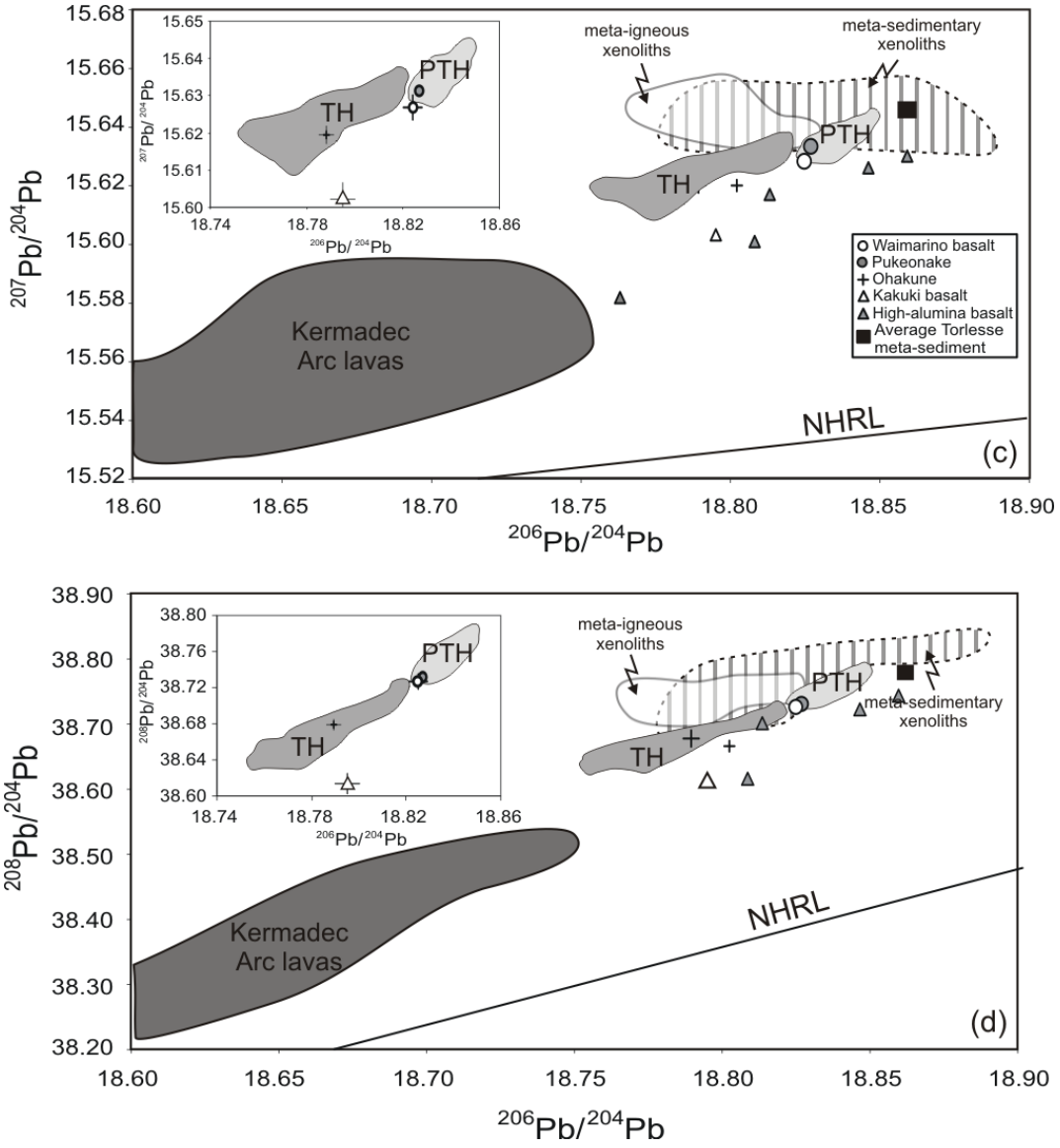

Fig. 4.8. cont. Variation of (c) $^{207}Pb/^{204}Pb$ vs $^{206}Pb/^{204}Pb$, (d) $^{208}Pb/^{204}Pb$ vs $^{206}Pb/^{204}Pb$, for high-Mg andesites and high-alumina basalts. Dark and light grey fields are TH and PTH lavas respectively (see chapter 3). Hauhungatahi data and smaller symbol Ohakune data are from Graham (1985a). High-alumina basalt data from Graham et al. (1990). Average Torlesse meta-sediment (non-xenolith) from Graham et al. (1992). NHRL (Northern Hemisphere Reference Line) from Hart (1984). Insets display external errors (2σ) for each data point however they are often smaller than the symbol.

1.7). The Ohakune samples have a more restricted range of compositions than Hauhungatahi lavas while the Waimarino basalt has a more radiogenic composition ($^{87}Sr/^{86}Sr$ = 0.704465). Although εHf values are only available for one Ohakune lava and the Waimarino basalt, a similar trend is evident in Sr-Hf isotope space (Fig. 4.8b). The Pukeonake sample ($^{87}Sr/^{86}Sr$ = 0.704781; εNd = 2.9; εHf = 7.7) has an intermediate composition in Sr-Nd-Hf isotopic space between the Ohakune-Hauhungatahi array and the PTH series. Pb isotope compositions for Ohakune-Pukeonake-Waimarino lavas define a linear array above and tangential (Δ7/4 = 9.4; Δ8/4 = 33.5; $\Delta 7/4 = [(^{207}Pb/^{204}Pb)_{sample} - (^{207}Pb/^{204}Pb)_{NHRL}] \times 100$; $\Delta 8/4 = [(^{208}Pb/^{204}Pb)_{sample} - (^{208}Pb/^{204}Pb)_{NHRL}] \times 100$; $(^{207}Pb/^{204}Pb)_{NHRL} = 0{\cdot}1084 \times (^{206}Pb/^{204}Pb)_{sample} + 13{\cdot}491$ (Hart, 1984); $(^{208}Pb/^{204}Pb)_{NHRL} = 1{\cdot}209 \times (^{206}Pb/^{204}Pb)_{sample} + 15{\cdot}627$ (Hart, 1984)) to the Northern Hemisphere Reference Line (NHRL) (Fig. 4.8c and d). The high-alumina basalts define a linear array similar to the high-Mg andesites however are displaced to lower $^{207}Pb/^{204}Pb$ and $^{208}Pb/^{204}Pb$ values (Δ7/4 = 7.6; Δ8/4 = 28.4).

4.4.4. Oxygen isotope data

Oxygen isotope data for Ohakune, Pukeonake and Waimarino lavas are listed in Table 4.1. Clinopyroxene and olivine are common ferromagnesian phenocryst phases in the high-Mg andesites and consequently were analysed in all samples. Additional oxygen isotope ratios were also measured for orthopyroxene in Ohakune and Pukeonake lavas. The range in $\delta^{18}O$ values for clinopyroxene, olivine and orthopyroxene is +5.47 to +6.57 (n = 4), +4.82 to +5.25 (n = 4) and +6.15 to +7.08 (n = 3) respectively. All $\delta^{18}O_{olv}$ values correspond to mantle olivine values (+4.8 – +5.5 ‰, Mattey et al., 1994); however, only clinopyroxene from Ohakune has a $\delta^{18}O_{cpx}$ value (+5.47)

consistent with the upper mantle (+5.35 – +5.89 ‰, Mattey et al., 1994; Ionov et al., 1994). Orthopyroxene measured in Ohakune and Pukeonake lavas both exceed the range in mantle $\delta^{18}O_{opx}$ (+5.39 – +6.10; Mattey et al., 1994). A mean $\delta^{18}O_{olv}$ value

Table 4.1. Oxygen isotope data ($\delta^{18}O$) for Waimarino, Ohakune and Pukeonake lavas

Sample	Cpx	2σ	Opx	2σ	Olv	2σ	Δcpx-olv	Δopx-cpx
Waimarino	6.16	-	-	-	5.25	-	0.91	-
Pukeonake 01	6.52	-	6.96	-	5.14	0.24	1.38	0.44
Pukeonake 02	6.57	-	7.08	-	5.12	0.07	1.45	0.51
Ohakune	5.47	-	6.15	-	4.82	0.06	0.65	0.68

from the southern Kermadec arc lavas (+5.04; Macpherson et al., 1998), which represent local source contaminated upper mantle (Macpherson et al., 1998), is also similar to average high-Mg andesite olivine (+5.08). However, with the exception of Ohakune, all $\delta^{18}O_{cpx}$ values display significant ^{18}O enrichment (~1.0‰) relative to average Kermadec arc clinopyroxene ($\delta^{18}O_{cpx}$ = 5.39; Macpherson et al., 1998). $\Delta_{cpx\text{-}olv}$ (0.65-1.45; n = 4) and $\Delta_{opx\text{-}cpx}$ (0.44-0.68; n = 3) values from coexisting mineral pairs are higher than mantle peridotite values (Mattey et al., 1994), particularly in the Pukeonake lavas (e.g. mean $\Delta_{cpx\text{-}olv}$ = 1.41), suggesting isotopic disequilibrium at typical magmatic temperatures for andesite liquids (Macpherson and Mattey, 1998; Macpherson et al., 1998). If high forsterite olivine within the high-Mg andesites represent entrained crystals from the mantle, this mineral most likely represents the phase out with of equilibrium.

4.5. Discussion

4.5.1. Magmatic differentiation

On initial inspection many high-Mg andesites from the southern TVZ have features indicative of primary magmas: Mg# ~ 0.7, modal forsteritic olivine ($Fo_{82\text{-}93}$) and ≤

20% phenocrysts. However low Ni concentrations in some samples (< 50 ppm) suggest these lavas no longer represent primary mantle liquids. Correlation of many major and trace elements with MgO (Figs. 4.5 and 4.6) indicate that processes such as fractional crystallisation, crystal accumulation, magma mixing or crustal contamination control element concentrations. The high-Mg andesites also display significant differences to the high-alumina basalt series. CaO versus MgO distinguishes between each series; high-Mg andesites display constant and lower CaO concentrations at equivalent MgO content compared to the high-alumina basalts. Al_2O_3 versus MgO also separates each group with high-Mg andesites displaying a negative correlation and lower Al_2O_3 concentration at a given MgO content relative to the high-alumina basalts (positive correlation). Crystallisation vectors (Fig. 4.5) predicting magmatic evolution from respective parental compositions suggest fractionation of a clinopyroxene + olivine ± plagioclase assemblage can replicate high-Mg andesite while high-alumina basalts require a plagioclase + olivine > clinopyroxene assemblage. Furthermore the absence of plagioclase phenocrysts in Ohakune-Hauhungatahi-Waimarino samples contrasts with the high alumina basalts where plagioclase is the dominant phenocryst phase. This suggests that the contrasting trends in major elements of high-Mg andesites and high-alumina basalts in CaO and Al_2O_3 versus MgO may be controlled by the relative proportion of plagioclase in each fractionating assemblage.

4.5.2. Fractional Crystallisation

The major element variations in high-Mg andesites and high-alumina basalts can be investigated using XLFRAC least-squares modelling (see Stormer and Nicholls, 1978) to ascertain if separate differentiation trends are the result of varying

plagioclase fraction (Table 4.2). The Waimarino and Kakuki basalt were used as parental melts in modelling of the high-Mg andesites (models 1, 2, 6) and high-alumina basalts (model 7) respectively. Intra-suite variation for Ohakune and Hauhungatahi lavas are also considered in models 3-5. Major element modelling indicates high-Mg andesite require substantial clinopyroxene and olivine fractionation accompanied by plagioclase accumulation (particularly evident for Hauhungatahi – model 2). High-alumina basalts on the other hand require substantial plagioclase fractionation. Attempts to generate high-Mg andesite from primitive high-alumina basalt (model 8) fail indicating these lavas represent two distinct evolutionary series originating from different parental compositions.

Table 4.2. Results of major element least squares modelling

Series	Model No.	Parent	Daughter	ΔMgO (wt%)	Σr^2	% removed				% Crystals
						olv	cpx	plag	chrome spinel	
High-Mg andesites	1	WB	OQ	7	0.03	9.6 (0.35)	12.9 (0.47)	**1.9 (0.07)**	4.8 (0.18)	27
	2	WB	HAU - V24485	6.5	0.04	8.7 (0.34)	12 (0.47)	**3.9 (0.15)**	4.8 (0.18)	25
	3	OQ	OQ - F4	0.38	0.01	4.2 (0.48)	**2.7 (0.31)**	4.5 (0.52)	2.1 (0.24)	7
	4	HAU - V24155	HAU - H4	2.6	0.03	3.1 (0.23)	9.9 (0.72)	0	0.7 (0.05)	14
	5	HAU - V24155	OQ - F1	1.9	0.15	3.3 (0.23)	7.4 (0.52)	3.6 (0.25)	**0.3 (0.02)**	14
	6	WB	PUKE 01	4.9	0.79	2.1 (0.08)	18.5 (0.67)	**4.9 (0.18)**	6.9 (0.25)	23
High-alumina basalts	7	KB	HAB	1.4	0.42	3.9 (0.17)	6 (0.27)	12.8 (0.56)	-	33
Between groups	8	KB	OQ	0.1	24.02	7.2 (0.12)	17.6 (0.29)	35.3 (0.59)	-	42

XLFRAC least-squares modelling based on eight oxides (4 phases in high-Mg andesites, 3 phases in high-alumina basalts). Mineral compositions taken from parental lava (see Appendix D). ΔMgO refers to the difference calculated between parent and daughter compositions. Bold font represents addition of phase. olv, olivine; cpx, clinopyroxene; plag, plagioclase. Number in brackets refers to the phase percentage of the total assemblage.

Therefore based on the relative proportion of fractionating phases in major element modelling (Table 4.2), plagioclase is the primary difference between fractionating assemblages in each series. High-Mg andesites are produced by clinopyroxene + olivine fractionation accompanied by minimal plagioclase fractionation/accumulation

from a parental melt similar to the Waimarino basalt. In contrast, high-alumina basalt require plagioclase + olivine >> clinopyroxene fractionation from a parental melt similar in composition to the Kakuki basalt

Some trace element trends in the high-Mg andesites are similar to major element variations indicating their concentrations are also influenced by fractional crystallisation. With the results from major element modelling (i.e. phase proportions and degree of crystallisation) it is possible to examine the validity of least-squares analysis using the Rayleigh fractionation equation, $C_l = C_o F^{(D-1)}$: C_o = concentration of element in parental liquid, C_l = concentration of element in daughter liquid, F = fraction of liquid remaining, D = bulk distribution coefficient (given in Appendix F). The results of modelling for high-Mg andesites and high-alumina basalts are shown in Table 4.3, with differences between calculated and measured trace element concentrations illustrated in Fig. 4.9a&b. Trace element modelling for high-Mg andesites (models 1-6) and high-alumina basalts (model 7) supports least-squares analysis suggesting each series can be derived by fractional crystallisation from a parental end-member (Waimarino and Kakuki basalt). The generation of most high-Mg andesites require clinopyroxene and olivine fractionation (models 1-6) while plagioclase accumulation also appears to be important at Hauhungatahi which may account for the elevated Sr concentrations in these lavas (Fig. 4.6d). High-alumina basalts however, demand a large amount of plagioclase fractionation relative to olivine (model 7). The high concentration of both incompatible and compatible elements in Pukeonake lavas are difficult to derive by fractional crystallisation models alone, suggesting other differentiation processes are required.

Table 4.3. Results of trace element fractional crystallisation modelling

Model no:	1	2	3	4	5	6	7
Parent	WB	WB	OQ	HAU - V24155	HAU - V24155	WB	KB
Daughter	OQ	HAU - V24485	OQ - F4	HAU - H4	OQ - F1	PUKE 01	HAB
Σr^2	0.03	0.04	0.01	0.03	0.15	0.793	0.42
olv	9.6 (0.35)	8.7 (0.34)	4.2 (0.48)	3.1 (0.23)	3.3 (0.23)	2.1 (0.08)	3.9 (0.17)
cpx	12.9 (0.47)	12 (0.47)	**2.7 (0.31)**	9.9 (0.72)	7.4 (0.52)	18.5 (0.67)	6 (0.27)
plag	**1.9 (0.07)**	**3.9 (0.15)**	4.5 (0.52)	0	3.6 (0.25)	**4.9 (0.18)**	12.8 (0.56)
cr-spinel	4.8 (0.18)	4.8 (0.18)	2.1 (0.24)	0.7 (0.05)	0.3 (0.02)	6.9 (0.25)	-
total	27	25	7	14	14	23	33
F	0.73	0.75	0.93	0.86	0.86	0.77	0.67
Calculated (ppm)							
Rb	21.2	20.6	16.6	27.8	27.7	21.5	6.7
Ba	156	152	144	265	261	158	112
La	8.76	8.55	7.13	10.29	10.26	8.86	9.66
Ce	18.22	17.76	15.03	20.67	20.65	18.34	24.16
Sr	435	425	350	612	559	439	300
Zr	61	59	64	99	99	61	129
Y	15	15	16	17	17	14	28
Ni	63	77	39	31	37	114	36
Measured (ppm)							
Rb	15.5	11.0	16.0	20.0	16.0	16.0	8.0
Ba	136	159	140	229	144	144	145
La	6.70	8.00	8.00	11.00	4.00	4.00	8.36
Ce	14.05	18.00	12.00	15.00	6.00	6.00	19.87
Sr	358	478	346	501	390	390	347
Zr	60	57	62	69	65	65	147
Y	14	14	17	18	15	15	30
Ni	55	121	49	22	39	39	33

Σr^2 values and phase proportions for each model taken from Table 4.2.

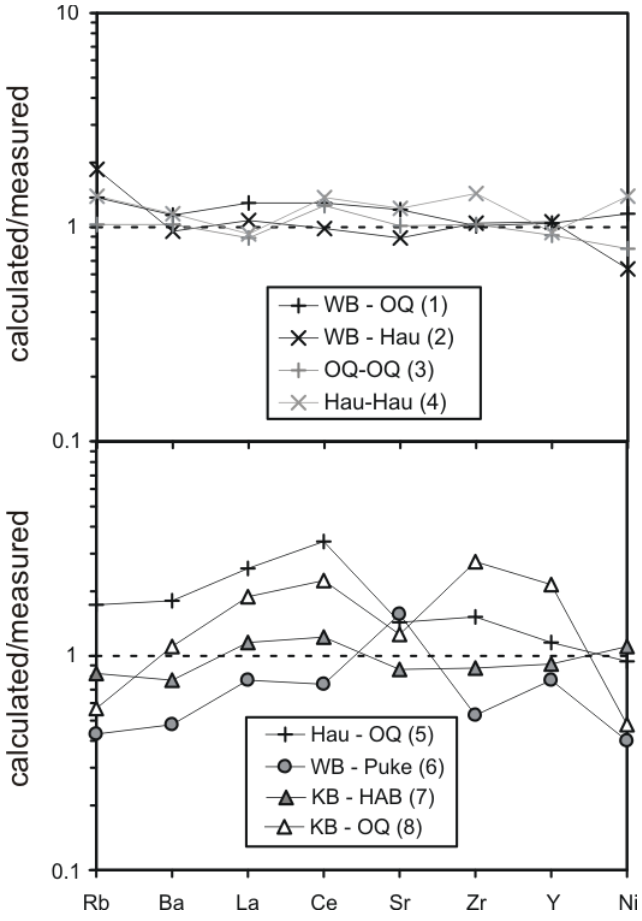

Fig. 4.9. Comparison of trace element concentrations measured in samples with results from forward modelling for high-Mg andesites and high-alumina basalts. Model numbers in brackets correspond to Table 4.3. Table 4.2 (major element least squares modelling) displays the degree of crystallisation, mineral phases and abundances used in trace element modelling. Distribution coefficients are listed in Appendix F.

4.5.3. Magma mixing and contamination by peridotite/cumulate material

Recent studies have indicated magma mixing accompanied by entrainment of small volumes of peridotite can be important in the generation of HMA (Streck et al., 2007). High concentrations of both compatible and incompatible elements in Pukeonake lavas could result from magma mixing (e.g. basalt and dacite), while high forsterite content and oxygen isotope disequilibrium (Table 4.1) in olivine suggests crystal entrainment of mafic material (peridotite or cumulates). These processes may provide an alternative to fractional crystallisation in generating HMA in the southern TVZ and are investigated using simple mixing models outlined in Table 4.4. Waimarino and Ruapehu basalts and R96/12 (andesite) and T5-14 (dacite) samples were chosen as mafic and silicic end members respectively in mixing models. Xenocrystic olivine (Fo_{92}) was either used alone in mixing models or combined with high-Mg# orthopyroxene and clinopyroxene (compositions taken from HMA) at a 3:1:1 and 3:2 ratio (cf. Bodiner and Godard, 2003) to approximate entrained lherzolite and harzburgite compositions respectively. Pukeonake compositions are most closely reproduced by mixing 53% Ruapehu basalt, 38% dacite and 9% lherzolite, although various proportions of Waimarino or Ruapehu basalt mixed with andesite/dacite and olivine/harzburgite/lherzolite also provide reasonably close alternatives. Attempts to reproduce Ohakune and Hauhungatahi lavas however yield poor results with sum of residuals consistently >2.7.

Table 4.4. Results of major element mixing models

	Basalts		Dacite/Andesite		Mantle derived component			HMA		
	RB	WB	T5-14	R96/12	Perd	Harz	Olv	P01	Hau (V14817)	OQ
SiO_2	52.65	52.51	64.34	60.60	46.94	47.06	41.52	56.49	56.93	56.93
Al_2O_3	15.47	12.14	15.06	17.40	0.54	0.66	0.00	14.03	15.55	14.56
$Fe_2O_{3\ tot}$	9.33	8.90	5.25	6.66	6.96	8.07	6.52	7.53	8.72	8.37
MgO	8.92	14.46	3.28	2.91	40.78	43.22	51.68	9.62	6.30	7.49
CaO	9.49	9.24	4.72	6.23	4.64	0.87	0.19	7.31	8.72	8.82
Na_2O	2.64	1.56	3.33	3.62	0.04	0.02	0.00	2.70	2.26	2.39
K_2O	0.59	0.52	3.01	1.65	0.00	0.00	0.00	1.39	0.70	0.69
TiO_2	0.65	0.45	0.76	0.70	0.03	0.04	0.00	0.67	0.60	0.53
MnO	0.15	0.15	0.08	0.11	0.06	0.06	0.09	0.12	0.15	0.14
P_2O_5	0.09	0.06	0.16	0.12	0.00	0.00	0.00	0.13	0.07	0.08

HMA	Mixture	$\sum R^2$
P01	53% RB, 38% T5-14, 9% Perd	0.02
P01	55% RB, 37% T5-14, 8% Harz	0.12
P01	53% RB, 40% T5-14, 7% Olv	0.21
P01	42% WB, 53% R96/12, 5% Harz	0.28
P01	42% WB, 54% R96/12, 4% Olv	0.34
Hau	60% RB, 36% T5-14, 4% Perd	3.49
OQ	68% RB, 30% T5-14, 2% Harz	2.73

RB - Ruapehu basalt, WB - Waimarino basalt, T5-14 - dacite, R96/12 - andesite, Perd - Peridotite, Olv - Olivine, Harz - Harzburgite

Peridotite contaminant (60% Fo_{92} Olivine, 20% Opx Mg#82, 20% Cpx Mg#89)

Harzburgite contaminant (60% Fo_{92} Olivine, 20% Opx Mg#82)

4.5.4. Different sources and variable crustal thickness in the generation of high-Mg andesites and high-alumina basalts

Comparison of major (Fig. 4.5) and trace (Fig. 4.6) element variations for high-Mg andesite and high-alumina basalt highlight that each magma series must be derived from a chemically distinct source. This is particularly evident in CaO and Al_2O_3 versus MgO, which highlights that the high-Mg andesite source is depleted in these elements relative to the high-alumina basalt source. NMORB trace element variations also support different sources with high-Mg andesite patterns displaying considerably greater depletions in HFSE (particularly Ti) and MREE-HREE compared to the high-alumina basalts (Fig. 4.7). Therefore on the basis of Ca, Al and Ti variations, it appears the high-Mg andesites are derived from a depleted/refractory source as oppose to the high-alumina basalts which seem to be derived from relatively fertile mantle.

Stern et al. (2006) provided a recent summary of the tectonic evolution of the TVZ based on previous geophysical studies. They concluded that the tectonic development of the TVZ could be subdivided into two stages; 1) a southern segment dominated by compression and thickened lithosphere and 2) a central-northern region characterised by extension accompanied by substantial erosion of the lithosphere (Fig. 4.10). Stage 1 occurs prior to viscous removal of the lithosphere and the onset of stage 2. The composition of sub-continental lithosphere as identified in stage 1 is most likely refractory, depleted in elements such as Ca and Al due to crustal extraction (Rollinson, 2007). Consequently, hydrous melting of lithospheric mantle in the southern TVZ could produce relatively Mg-rich melts illustrating the depleted

characteristics of high-Mg andesites. However, the increased mantle flow envisaged beneath the central-northern TVZ would replenish the mantle wedge with fertile

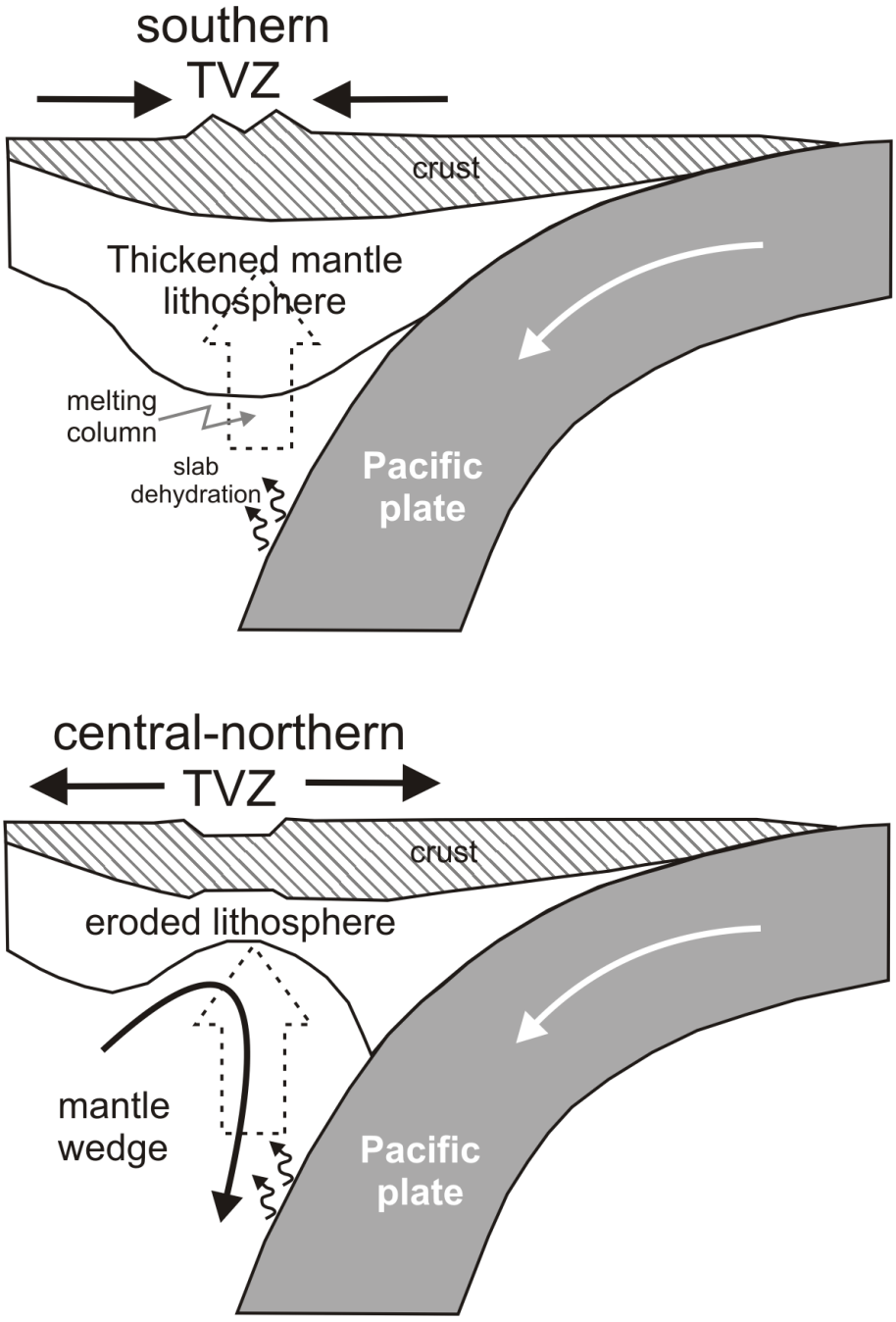

Fig. 4.10. Tectonic evolution of the TVZ (modified from Stern et al., 2006). The southern TVZ is characterised by compression and thickened lithosphere with a relatively depleted mantle. The central-northern TVZ develops following extension and significant erosion of the lithosphere caused by more vigorous mantle flow.

asthenosphere. Partial melting in this setting where mantle flow is more vigorous could generate melts like high-alumina basalts with relatively enriched compositions.

With the exception of the mixed magmas from Pukeonake, we can infer the relative fractionation depths of the high-Mg andesites and high-alumina basalts based on fractional crystallisation modelling and observed phenocryst assemblages. Lower pressures and/or lower water contents in basaltic/andesitic magma tends to induce greater plagioclase crystallisation (Grove et al., 2002), hence we interpret the relative proportion of this mineral in fractionation models as reflecting a shallower mean differentiation depth for high-alumina basalt relative to high-Mg andesite. This is consistent with seismic refraction studies that suggest thickening of the crust along the TVZ from north (20-25 km) to south (35-40 km) (e.g. Stern et al., 2006) (Fig. 4.11). Primary magma is likely to fractionate at higher pressure in the southern TVZ as a consequence of thicker crust (~35 km), thereby promoting lower degrees of plagioclase fractionation. High-alumina basalt from the central TVZ on the other hand fractionates at relatively shallower levels (~25km) inducing greater degrees of plagioclase fractionation. Therefore, the restricted distribution of high-Mg andesite (southern region) and high-alumina basalt (central region) in the TVZ appears to be a direct consequence of local variation in crustal thickness from north to south.

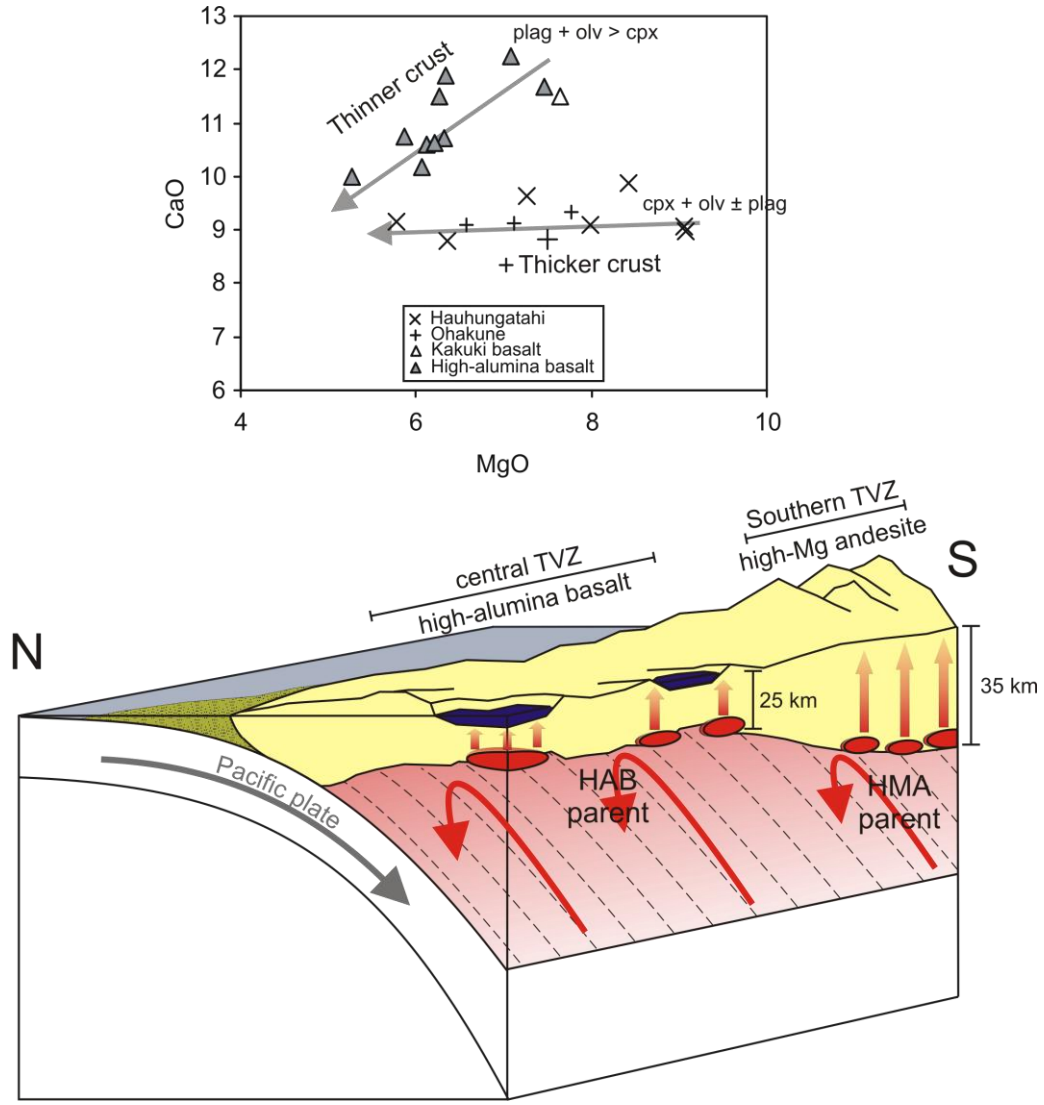

Fig. 4.11. Correspondence between CaO/MgO variations in lavas and crustal thickness/depth of differentiation. High-Mg andesites have a constant CaO abundance with decreasing MgO content due to a clinopyroxene + olivine > plagioclase ratio in its fractionating assemblage as a result of crystallizing at higher pressure. Hauhungatahi data and smaller symbol Ohakune data are from Graham (1985a).

4.5.4 Crustal Contamination of high-Mg andesites and high alumina basalts

A consequence of magma stalling and differentiating at deeper levels within crust is the increased likelihood of contamination. Isotope ratios in arc magmas that are displaced from MORB values are often attributed to contamination of primary mantle-wedge derived melts by isotopically distinct crust (Davidson, 1987, 1996; Davidson et al., 2005; Hildreth and Moorbath, 1988; Macpherson et al., 1998). Crustal material can be added to magma in the source region of the mantle wedge (source contamination) and/or during ascent through the arc lithosphere (crustal contamination). These different contamination processes can be distinguished by examining how isotope ratios vary with indices of differentiation (e.g. MgO). If the crustal isotopic signature was imparted to the magma during differentiation in the arc crust (ie. crustal contamination) isotopes would be expected to correlate with MgO. This is illustrated with Hauhungatahi lavas where correlations in εNd with MgO (Fig. 4.12) are consistent with assimilation within the arc crust, during differentiation..

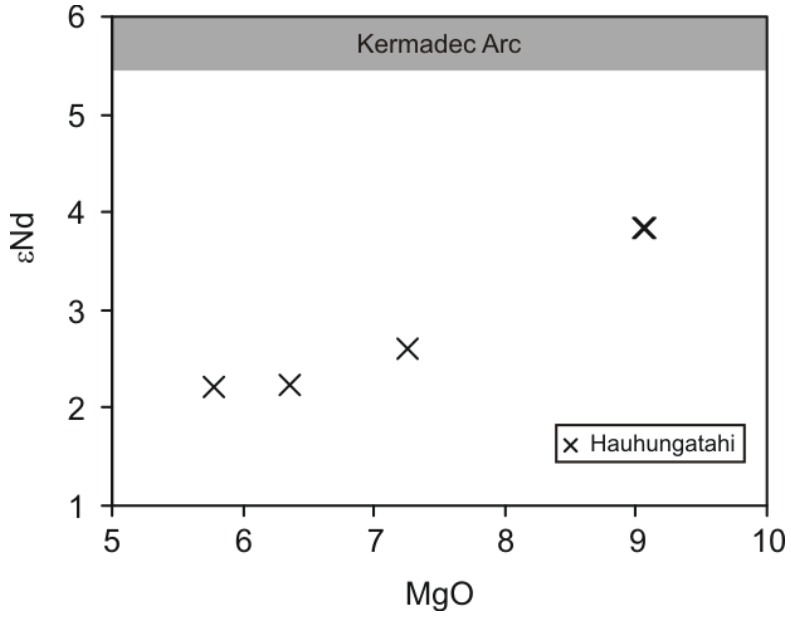

Fig. 4.12. εNd vs MgO for Hauhungatahi lavas. Hauhungatahi data from Graham (1985a).

4.5.4.1 Identification of end-member components

Crustal contaminants of Ruapehu lavas were summarized in Chapter 2. Given the close proximity of the high-Mg andesite centres to Mt. Ruapehu, it is reasonable to assume a similar basement of lower crustal meta-igneous granulite overlain by 20-25 km of meta-sediment is present beneath other vents in the southern TVZ.

Major and trace element modelling suggests the Waimarino basalt is the most appropriate end-member for generating more evolved high-Mg andesite. However it has the lowest εNd and εHf values in this series and a Pb isotope composition that overlaps with PTH and Torlesse meta-sediment fields (Fig. 4.8a-d), indicating that this sample does not represent unmodified primary mantle melt. On the basis of Hf and Pb isotope data presented in Chapter 3 the best approximation for the isotopic composition of primary melt in the southern TVZ are primitive lavas from the Ngatoro Basin/southern Kermadec Arc, the isotopic composition of which has been reconciled by <1% source contamination of mantle wedge derived melt (Macpherson et al., 1998). Given that similar subduction parameters (velocity and dip of the Pacific plate and composition of subducted sediment) exist along the strike of this section of arc, it is suggested a similar source contaminated melt composition is also suitable for modelling differentiation in southern TVZ lavas (Chapter 3). Therefore the most appropriate primitive end-member for modelling crustal contamination of high-Mg andesites likely consists of a major and trace element composition similar to the Waimarino basalt but with an isotopic composition similar to the southern Kermadec Arc lavas. Based on its primitive isotopic composition, the Kakuki basalt represents the most likely parent to the high alumina basalt series (Gamble et al., 1993a; Graham et al., 1995).

4.5.4.2. High-Mg Andesites and high-alumina basalts: constraints from isotopes

With the exception of Pukeonake lavas and more evolved high alumina basalts, both series are characterised by relatively low $^{87}Sr/^{86}Sr$ values. It is evident that meta-igneous granulite is unlikely to have contaminated either series as both sets of lavas trend to lower εNd values indicating interaction with meta-sedimentary crust. Figure 4.13a and b display Energy Constrained - Assimilation Fractional Crystallisation (EC-AFC; Bohrson and Spera, 2001) modelling between a primitive Kermadec Arc composition (with Waimarino basalt trace element concentration) and meta-sedimentary crust (Table 4.4; modelling parameters). Mixing arrays in Nd/Sr isotope space indicate that contamination of primitive Kermadec magma by ~ 1 % mass of meta-sediment can reproduce Ohakune, Hauhungatahi and Waimarino isotopic compositions. No Hf isotope data are available for Hauhungatahi lavas however, the Kermadec magma - meta-sediment mixing array in Sr/Hf isotope space also replicates Ohakune and Waimarino compositions.

Gamble et al (1993a) conducted modelling of the high-alumina basalts. They concluded that 10% meta-sediment contamination of the Kakuki basalt can account for much of the high-alumina basalt array.

The different slopes in mixing curves between this study and that produced by Gamble et al (1993a) is largely a result of different bulk partition coefficients for Sr used in modelling. Gamble et al (1993a) used a higher DSr in the parental magma (DSr = 1) to reflect that plagioclase is a major phenocryst phase in high-alumina basalts. Furthermore, EC-AFC modelling considers the DSr of meta-sediment during partial melting. As such the compatible nature of Sr during crustal melting (DSr = 2)

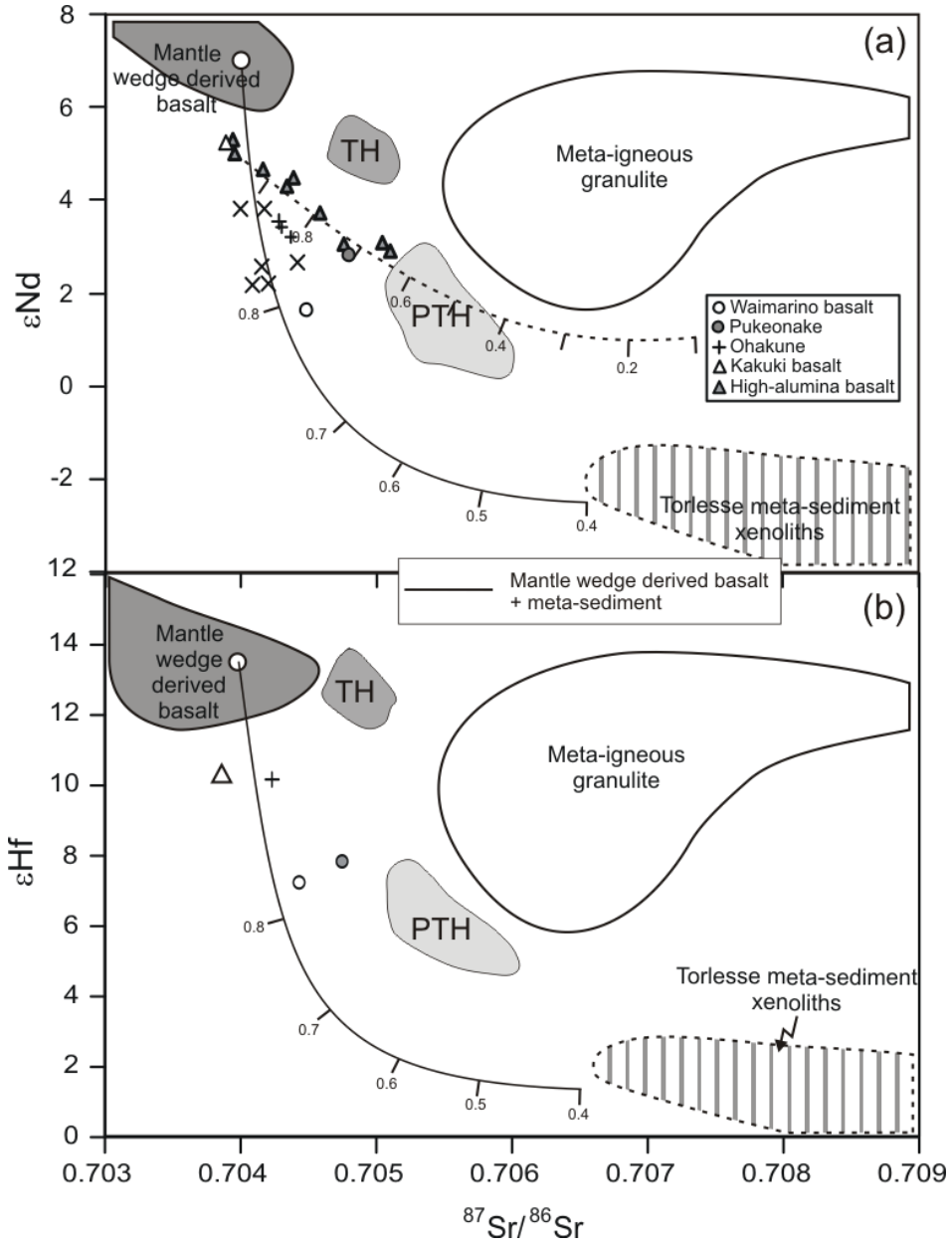

Fig. 4.13. Energy Constrained-Assimilation Fractional Crystallization (Spera and Bohrson, 2001) models using (a) $^{87}Sr/^{86}Sr$ vs εNd and (b) $^{87}Sr/^{86}Sr$ vs εHf, for a mantle wedge basalt contaminated with Torlesse meta-sediment. Dark and light grey fields are TH and PTH lavas respectively (see chapter 3). Modelling parameters listed in Table 4.5. Tick marks represent fraction of liquid remaining (F) in 0.1 increments (0.8-0.4). Kakuki basalt – Torlesse meta-sediment mixing curve from Gamble et al. (1993a). Mantle wedge basalt field is from Kermadec Arc lavas (Gamble et al., 1996; Woodhead et al., 2001). Hauhungatahi data and smaller symbol Ohakune data are from Graham (1985a). High-alumina basalt data from Gamble et al. (1990).

prevents the meta-sediment from influencing the $^{87}Sr/^{86}Sr$ composition of the magma until higher degrees of contamination.

Table 4.5. End member compositions and parameters used in EC-AFC modelling

	Sr ppm (D)	Nd ppm (D)	Hf ppm (D)	$^{87}Sr/^{86}Sr$	εNd
Mantle Wedge derived Basalt	327 (0.1)	7.3 (0.2)	1.36 (0.2)	0.704	+7.0
Meta-sediment	217 (2)	30 (0.4)	7 (0.4)	0.71459	-5.0

	εHf	$\delta^{18}O$	Initial Temp (°C)	Liquidus (°C)	Solidus (°C)
Mantle Wedge derived Basalt	+13.4	+5.23	1200	1150	-
Meta-sediment	-1	+12	650	1000	800

Bulk distribution coefficients (D) in brackets. Crustal lithology D values from Chapter 2.
Melt D values calculated from observed phase proportions in samples and Kds given in appendix F.
Mantle wedge εHf and $\delta^{18}O$ from Woodhead et al. (2001) and Macpherson et al. (1998) respectively.
Meta-sediment δ18O from Graham et al. (1992).
Initial temperature and liquidus values of parental magmas determined by comparison of experimental estimates of primitive mantle wedge melts (Baker et al., 1994; Pichavant et al., 2002; Tatsumi, 1982; Ulmer, 2001).
Initial temperature of meta-sediment are based on conservative estimates of a typical continental geotherm - 20°C/km (Brown and Musset, 1993), and relative depths of each lithology.
Solidus values of meta-sediment based on experimental studies of meta-sediments (Stevens and Clemens, 1993 and references therein).

4.5.5 Temporal melt evolution of high-Mg andesites: constraints from oxygen isotopes

Radiogenic isotope modelling has shown that Hauhungatahi, Ohakune and Waimarino compositions result from crustal contamination of primitive basalt by meta-sediment, with major element constraints indicating that this took place at relatively high pressure (clinopyroxene + olivine >> plagioclase fractionation). The Pukeonake lavas however reflect magma mixing between three end-members; RB or WB, an evolved andesite/dacite and a mantle derived component. Oxygen isotope ratios in phenocrysts from arc lavas are commonly used to calculate a $\delta^{18}O_{melt}$ value (e.g. Vroon et al., 2001) based on the assumption that the mineral phases and melt were in equilibrium at magmatic temperatures. A test for equilibrium in the high-Mg andesites can be made by comparing coexisting mineral fractionations with corresponding phases in peridotites (Mattey et al., 1994). Figure 4.14 shows mineral pair Δ values of cpx-opx and cpx-olv in relation to mantle values ($\Delta_{i\text{-}j} = \delta^{18}O_i - \delta^{18}O_j$). $\Delta_{cpx\text{-}olv}$ values in Pukeonake lavas (1.38 and 1.45) greatly exceed mantle values while Ohakune (0.65) and Waimarino (0.91) samples also exhibit disequilibrium. In addition, $\Delta_{cpx\text{-}opx}$ values

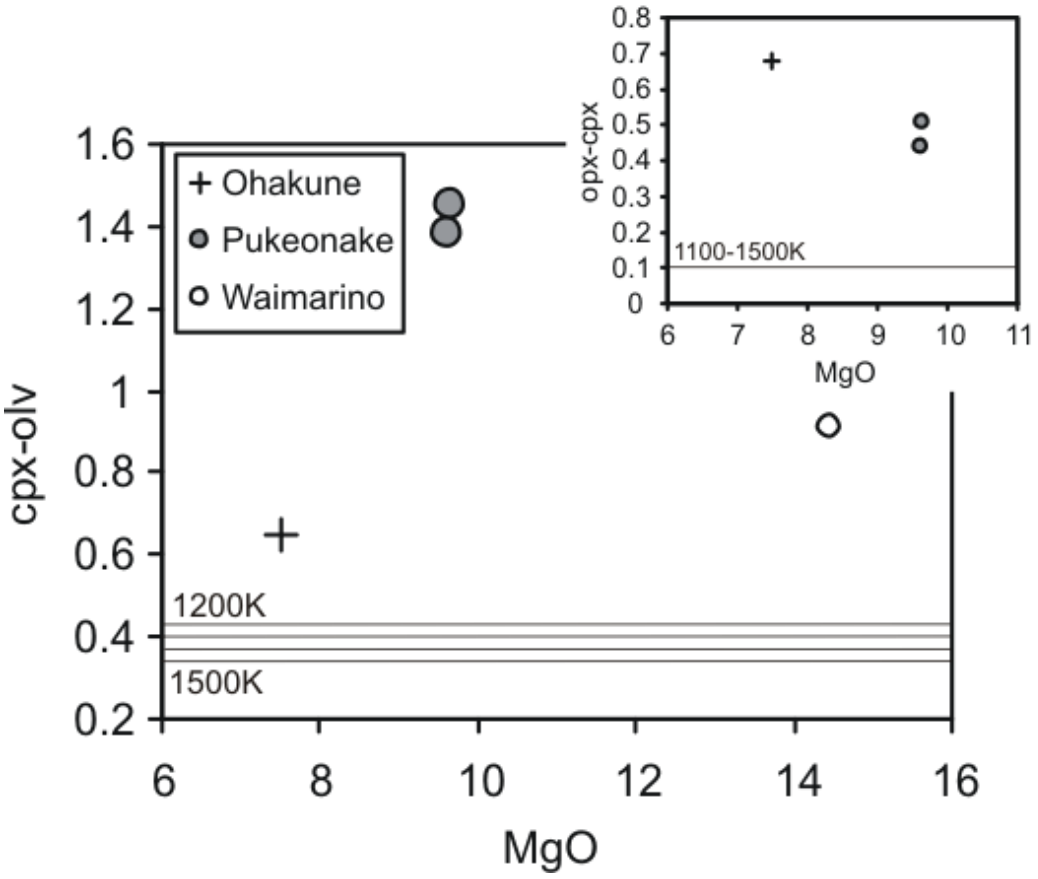

Fig. 4.14. $\Delta_{cpx\text{-}olv}$ and $\Delta_{opx\text{-}cpx}$ vs MgO. Theoretical $\Delta_{opx\text{-}cpx}$ values from Zheng (1993a). Experimental $\Delta_{cpx\text{-}olv}$ values between 1200-1500K from Kalamarides (1986). Note all mineral pairs are clearly out of equilibrium.

in Pukeonake and Ohakune also lie outside the range of mantle compositions. As oxygen isotope ratios of phenocrysts are primarily controlled by the $\delta^{18}O_{melt}$, disequilibrium in coexisting mineral pairs indicates that each phase crystallised from magma of differing isotopic composition. Evolving isotopic compositions within a batch of magma result from open system processes such as crustal contamination or magma mixing. As both these processes have been identified in this study, $\delta^{18}O$ values from phenocrysts can be used to investigate the evolution of high-Mg andesites in greater detail.

Although radiogenic isotopes and major elements indicate that high-Mg andesites have experienced crustal contamination or magma mixing, all $\delta^{18}O_{olv}$ values

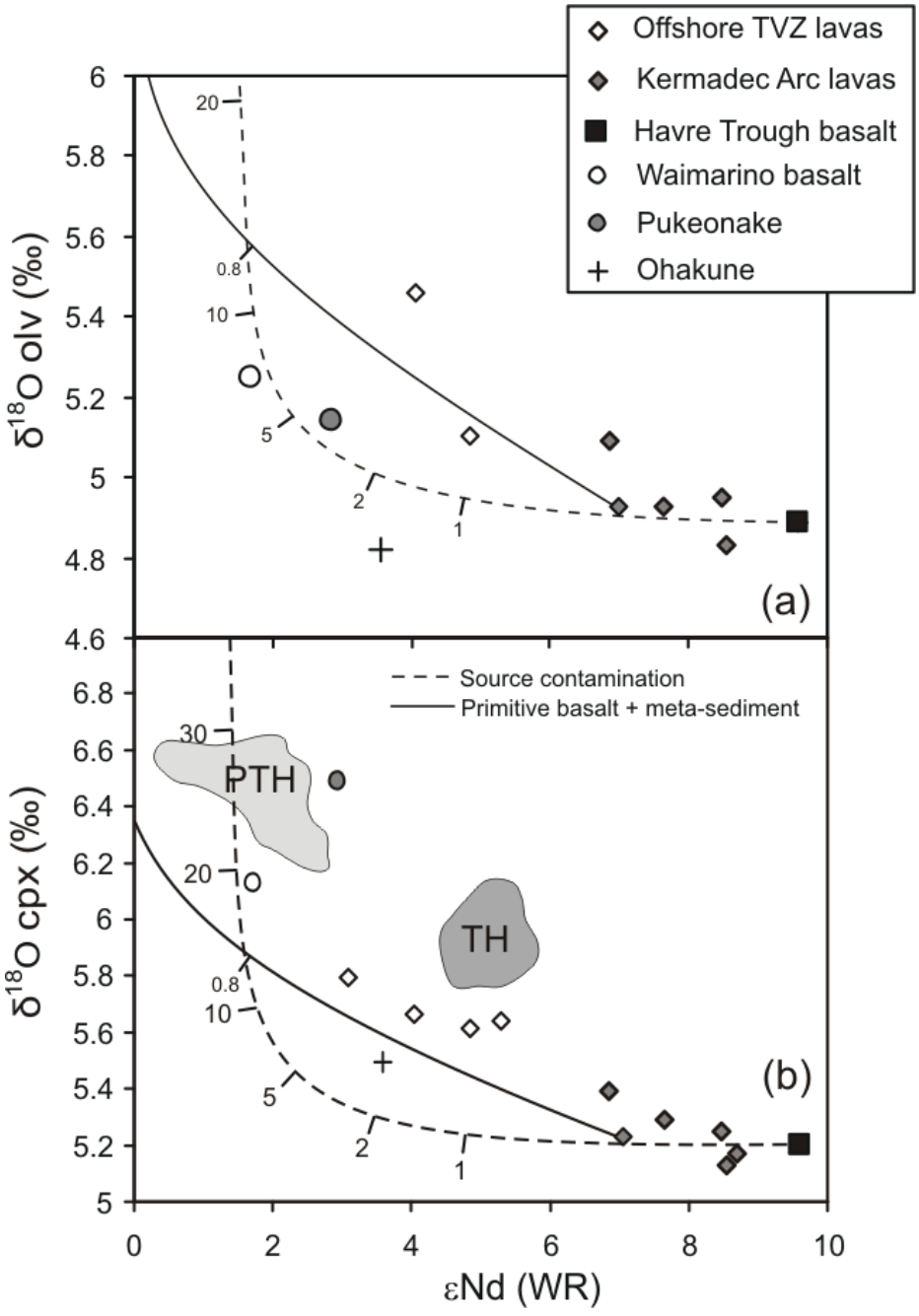

Fig. 4.15. Variations in a) $\delta^{18}O_{olv}$ vs εNd and b) $\delta^{18}O_{cpx}$ vs εNd for high-Mg andesites. Source contamination curves calculated using subduction composition and parameters from Macpherson et al. (1998). EC-AFC curves calculated using parameters from Table 4.5. Dark and light grey fields are TH and PTH lavas respectively (see chapter 3). Kermadec and Offshore TVZ data from Macpherson et al. (1998).

correspond to olivine in upper mantle peridotite (+4.8 to +5.5‰; Mattey et al., 1994) indicating this phase either represents xenocrystic mantle material or crystallised from its respective magma prior to assimilation of meta-sediment. εNd versus $\delta^{18}O_{olv}$ illustrates that Waimarino olivine lies close to the source contamination curve and well below the meta-sediment contamination curve (Fig. 4.15a). Ohakune however, has a lower $\delta^{18}O_{olv}$ value lying below the source contamination curve. This can be explained if the Ohakune magma was also derived from source contaminated mantle with a slightly lower original $\delta^{18}O$ value. $\delta^{18}O_{cpx}$ in Waimarino basalt are greater than upper mantle clinopyroxene (+5.25 to +5.89; Mattey et al., 1994) suggesting they crystallised after olivine following the onset of meta-sediment contamination. This is reasonably consistent with εNd / $\delta^{18}O_{cpx}$ modelling (Fig. 4.15b) as 20% source contamination is very high and not consistent with $\delta^{18}O_{olv}$ modelling (~7%). Ohakune clinopyroxene is consistent with average $\delta^{18}O$ mantle values and like olivine may indicate a pre-assimilation origin. However, isotopic disequilibrium between these phases in the Ohakune lava is best accounted for if the $\delta^{18}O$ clinopyroxene records low levels of meta-sediment contamination as indicated in Figure 4.15b. Ohakune $\delta^{18}O_{opx}$ values also display isotopic disequilibrium with coexisting phases (Δopx-cpx = 0.68). Orthopyroxene commonly forms overgrowths on clinopyroxene phenocrysts in Ohakune lavas; hence, this phase must have either crystallised at a later stage or formed through peritectic reaction when the magma had become increasingly silica saturated. Therefore, orthopyroxene probably crystallised after the magma had experienced more extensive meta-sediment contamination resulting in its isotopic disequilibrium with clinopyroxene.

$\delta^{18}O_{olv}$ in Pukeonake lavas also indicates source contamination, however this phase probably represents xenocrystic material derived from the mantle wedge.

$\delta^{18}O_{opx}$ and $\delta^{18}O_{cpx}$ values on the other hand overlap with PTH compositions (Fig. 4. 15b) indicating this phase is derived from the evolved andesite/dacite end-member during magma mixing.

In summary, mantle-like oxygen isotope compositions in Waimarino and Ohakune olivine result from source contamination of mantle wedge derived melt. This phase crystallised before significant degrees of crustal contamination from meta-sediment. However, the ^{18}O enrichment in clinopyroxene and orthopyroxene in these lavas indicates they crystallised during or after meta-sediment contamination. Pukeonake lavas on the other hand host a mixed crystal cargo were olivine is derived from the upper mantle while clinopyroxene and orthopyroxene are sourced from a crustal rock resembling an evolved PTH andesite.

4.6. Summary and Conclusions

Some of the most primitive lavas collected from the southern TVZ are high-Mg andesites/basaltic andesites. High-Mg andesites are commonly interpreted as primary melts due to high Ni concentrations and an Mg# ~ 0.7 (e.g. Kelemen, 1995; Hirose, 1997). However, although some high-Mg andesites from the southern TVZ exhibit primary characteristics, geochemical evidence suggests they do not represent unmodified mantle wedge melts. Rather their major and trace element concentrations suggest they are the result of hydrous partial melting of depleted mantle (lithospheric mantle?) followed by clinopyroxene + olivine >> plagioclase fractionation at relatively high pressure (presumably in the lower crust), or in the case of Pukeonake, magma mixing. In contrast, the most primitive lavas present in the central TVZ are high-alumina basalts with major element trends indicating this series is derived from relatively fertile asthenospheric mantle followed by olivine + plagioclase >

clinopyroxene fractionation. High-Mg andesites and high-alumina basalts also display distinct trends in major and trace element diagrams. This appears to be a consequence of each respective parental melt fractionating at differing levels in the crust. The distinct geographical distribution of each magma series can be directly related to local variations in crustal thickness. The high-Mg andesites are confined to the southern TVZ where the crust is demonstrably thicker (~35 km) encouraging higher pressure crystal fractionation. Further north in the central TVZ the crust has thinned by approximately 10 km due to more prolonged extension. This results in magma fractionating at relatively shallower levels producing the high-alumina basalts.

Radiogenic isotope data indicate only small degrees of meta-sediment assimilation are required to account for the low εNd and εHf values in the high-Mg andesites. However, $^{87}Sr/^{86}Sr$ appears less sensitive to crustal contamination presumably due to the relatively high Sr concentrations in the magma. Oxygen isotope measurements on phenocryst phases in high-Mg andesites on the other hand, provide greater constraints on the contamination history of these magmas. Interestingly olivine in all high-Mg andesites appears to have a pre-assimilation origin and records source contamination processes in the mantle wedge. However, clinopyroxene and orthopyroxene display ^{18}O enrichment relative to equivalent mantle phases which can be accounted for by crystallisation during or after meta-sediment contamination. Oxygen isotopes have been particularly useful in refining magma mixing models for the hybrid Pukeonake lavas. Mantle like $\delta^{18}O_{olv}$ values strongly suggest this phase represents xenocrystic material derived from the upper mantle. The strong ^{18}O enrichment in clinopyroxene and orthopyroxene however, indicate these phases were derived from the andesite/dacite end-member, very similar to an evolved PTH composition.

Finally, inferences can be made about the changing composition of primitive TVZ magma as crustal extension permeates southwards with time. High-Mg andesite is probably only produced during the earliest stages of the TVZ magmatism prior to crustal thinning, when mantle-wedge derived melts can fractionate at greater depth. This type of magmatism will most likely be accompanied by evolved andesite production seen at Mt. Ruapehu. Although caldera forming events have largely obscured older volcanics north of Lake Taupo, lavas with high-Mg andesite characteristics have been documented at Titiraupenga (1.89 Ma) and Pureora (1.6 Ma) vents on the western margin of TVZ (Graham et al., 1995). These compositions represent some of the oldest volcanics in the region, recording magmatic differentiation pathways during the initial inception of the TVZ. However, as rates of crustal extension increased, a gradual shallowing in mean differentiation depth led to the generation of high-alumina basalts (derived from a different parental magma than high-Mg andesite). Therefore, it appears that high-Mg andesite lavas in the TVZ are transient in time and space and are replaced by high-alumina basalt as the magmatic system evolves, extension rates increase and the lithosphere thins.

Chapter 5

Structural controls on changing differentiation pathways at an arc volcano, Mt. Ruapehu, New Zealand

5.1. Introduction

The mass flux of material across the Moho at convergent margins and the depth that magma differentiates in the crust have a significant impact on the evolution of arc crust. This is particularly evident at Mt. Ruapehu volcano in New Zealand where temporal adjustments in the depth of intra-crustal recycling can be related to structural movements in the arc crust. The crustal column beneath Ruapehu is composed of two main lithologies; a localised 5-10 km thick lower crustal meta-igneous granulite overlain by 20-25 km of meta-sediment. On the basis of new trace element and Hf isotope data for lavas and crustal xenoliths we have confirmed a distinct change in the likely assimilants between the oldest (Te Herenga - TH) and younger formations (Post Te Herenga - PTH). TH lavas are a product of lower crustal differentiation involving assimilation of meta-igneous granulite. PTH lavas display evidence for interaction with the same meta-igneous granulite followed by contamination with meta-sedimentary crust. This change in assimilant coincides with increased rates of extension at the southern tip of the Taupo Volcanic Zone (TVZ). We propose that the change in melt-crust interaction reflected in major geochemical changes from TH to PTH lavas is a response to adjustments in differentiation depth. Fault movement dating suggests that this can be broadly correlated with increased rates of extension within the Ruapehu crustal column.

Differentiation processes that affect primary arc magma are responsible for generating andesite at convergent margins and have contributed to the evolved composition of continental crust (Rudnick, 1995; Davidson and Arculus, 2006). Differentiation is believed to take place primarily during ascent through arc crust. In continental arcs extensive crystal fractionation and assimilation of older crustal material often produces magmas with complex evolutionary histories (e.g. Hildreth

and Moorbath, 1988). The effects of crustal assimilation have been documented in many arc settings and tend to be most tightly constrained when studies focus on single volcanic edifices and/or obtain good control on the composition of local contaminants (e.g. Baker et al., 1994; Davidson et al., 1988; Macpherson et al., 1998; Hobden et al., 1999; Price et al., 1999; Dungan et al., 2001). Isotopic analyses have proved particularly useful in this regard since there are usually significant contrasts in isotopic ratios between basalt derived from the mantle and crustal contaminants. However, there is a common assumption that the availability and composition of contaminants remains constant throughout the lifetime of magmatic systems. We test this assumption by examining isotopic variations in lavas from Mt. Ruapehu (North Island, New Zealand); a volcanic system containing two suites of distinctive crustal xenoliths.

5.2. Mt. Ruapehu

Mt. Ruapehu is an andesitic composite volcano in the Taupo Volcanic Zone where the lithosphere at the southern extremity of the Tonga-Kermadec arc is continental (Fig. 5.1). TVZ volcanism has migrated south as rifting from the Kermadec arc has propagated into North Island lithosphere. Average crustal extension rates of 8-10 mm/yr (Villamor and Berryman, 2001) decrease to 2-3 mm/yr (Villamor and Berryman, 2006a) at the young southern tip of the rift, where Ruapehu represents the most recent addition to the TVZ and provides a unique example of early stage magmatism within a continental arc.

On the basis of detailed geological mapping Graham and Hackett (1987) identified four main stratigraphic formations at Ruapehu; Te Herenga (250-180 ka),

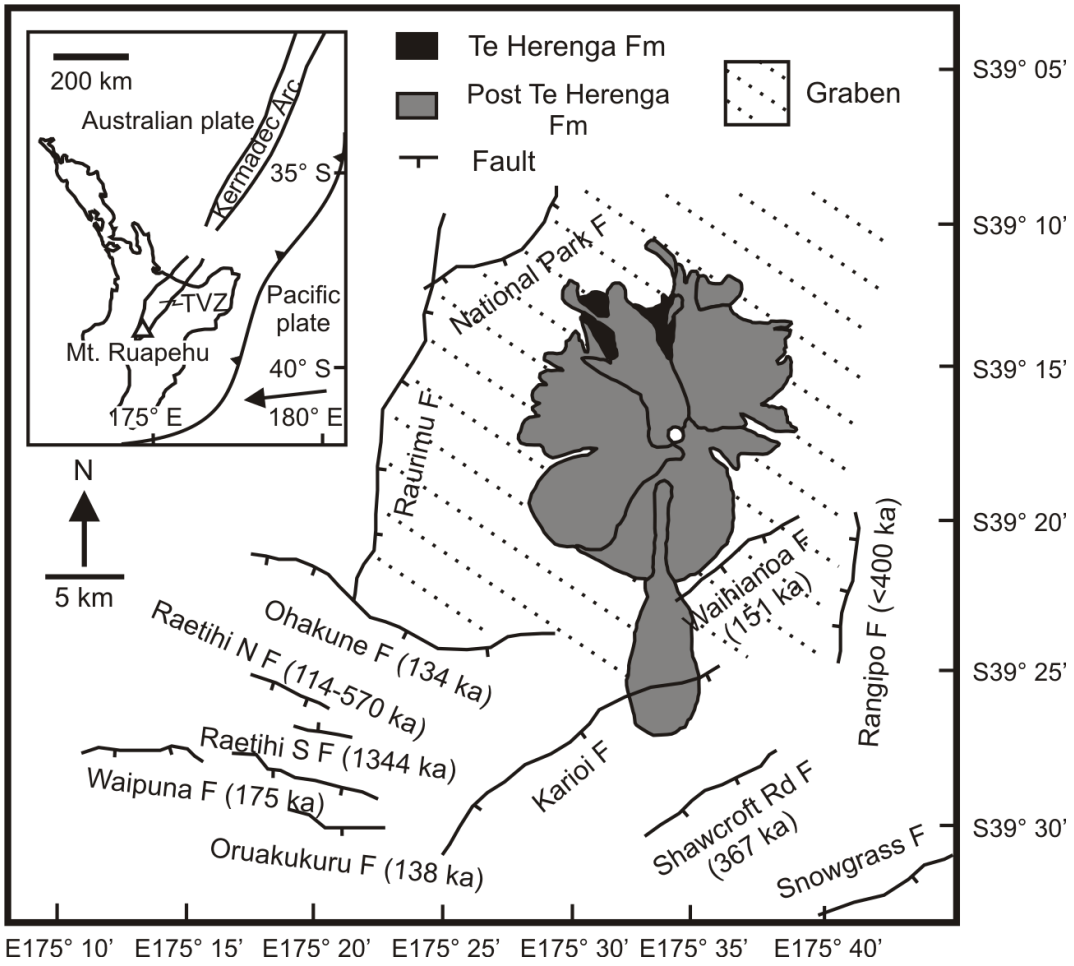

Fig 5.1. Location map (adapted from Gamble et al., 2003) showing Mt. Ruapehu positioned within the faults of the Mt. Ruapehu Graben (Villamor and Berryman, 2006b). TH lavas are exposed on the northern flanks of Ruapehu. Inset displays the location of the Taupo Volcanic Zone (TVZ) in the North Island of New Zealand at the southern end of the Tonga-Kermadec Arc.

Waihianoa (160-115 ka), Mangawhero (55-15 ka) and Whakapapa (<15 ka; Ar-Ar dates from Gamble et al., 2003). Geochemically, however, there is little distinction between the three younger formations so we classify Ruapehu products into the Te Herenga (TH; >180ka) and Post Te Herenga (PTH; <160ka) series.

Price et al. (2001, 2005) recognised the geochemical contrasts between the earliest and later Ruapehu lavas and used this to develop a two stage model involving assimilation fractional crystallisation processes operating at different levels within the

crust. We have used this general model to quantify the temporal geochemical evolution of the Ruapehu magmatic system and have related this to the structural history of the southern TVZ.

Crust beneath Ruapehu is ~30-35 km thick (Stern et al., 2006) and is penetrated by peripheral faults that form the Mt. Ruapehu Graben (Fig. 5.1). Due to the lack of exposure in the immediate vicinity, information concerning the composition of crust beneath Mt. Ruapehu is best determined from crustal xenoliths brought to the surface by lavas. These suggest that the basement is composed of two lithologies; meta-igneous granulite and meta-sediments resembling the Torlesse formation. Geobarometry suggests that these comprise a 5-10 km thick meta-igneous lower crust overlain by 20-25 km of meta-sediment (Graham, 1987; Graham et al., 1990). Seismic attenuation studies (*Qp*) conducted south of Ruapehu also identified a two-layered crustal structure with a high-*Qp* (>600) deep crustal region, below 20-30 km of low-*Qp* (300-400) crust (Eberhart-Philips et al., 2005; Reyners et al., 2007).

5.3. Temporal Evolution of Differentiation Depth

TH lavas comprise low-K basaltic andesites and andesites with high modal abundances of plagioclase (~30%) and sub-equal quantities of orthopyroxene and clinopyroxene (10-20%). A restricted range in SiO_2 (55.2–57.9 wt %) is associated with homogenous trace element compositions throughout the group. PTH lavas are generally medium-K andesites containing fewer phenocrysts (10 - 40%) than TH lavas with a lower modal abundance of plagioclase (10 - 20 %). There is greater variation in SiO_2 (54.7–62.3 wt %) and incompatible trace element concentrations compared to TH lavas. Xenoliths of meta-igneous granulite are present in both magma series whereas meta-sedimentary xenoliths tend to be restricted to PTH lavas.

Major element variations reveal different evolutionary histories in TH and PTH suites (Fig. 5.2), which we have modelled using a least squares approach (Table 5.1). From a parental magma (either Ruapehu basalt or primitive Kermadec Arc basalt) the TH array can be reproduced through fractionation of an assemblage in which cpx > plag, while PTH compositions require a plag > cpx assemblage. Plagioclase abundance is the primary difference in the fractionating assemblages; the PTH suite requiring ~ 50% (of total assemblage) compared to only ~ 30% for TH. On the basis of the modelling and phenocryst assemblages in each series, we can infer the relative fractionation depths. Lower pressures and/or lower water contents in basaltic/andesitic magma tends to induce greater plagioclase crystallisation (Grove et al., 2002), hence we interpret the relative proportion of this mineral in fractionation models as reflecting a shallower mean differentiation depth for PTH relative to TH. However, crystal fractionation cannot be the only process operating during differentiation since each series has a distinctive isotopic composition (Fig. 3) which cannot be reconciled with contamination processes operating in the mantle.

5.4. Temporal Evolution of Crustal Contaminants

Moderately primitive, homogenous isotopic compositions in the TH formation contrast with evolved and heterogeneous isotopic ratios of the PTH lavas (Fig. 5.3; see also Price et al., 2001 and 2005). In Hf/Sr isotopic space, both suites are displaced from the range of primary Kermadec Arc lavas, but they trend towards different crustal compositions (Fig. 5.3). Energy Constrained - Assimilation Fractional Crystallisation modelling (EC-AFC; Bohrson and Spera, 2001) indicates that contamination of primitive Kermadec magma by ~30-50 % mass of meta-igneous granulite is the only means of reproducing the isotopic compositions of the TH suite

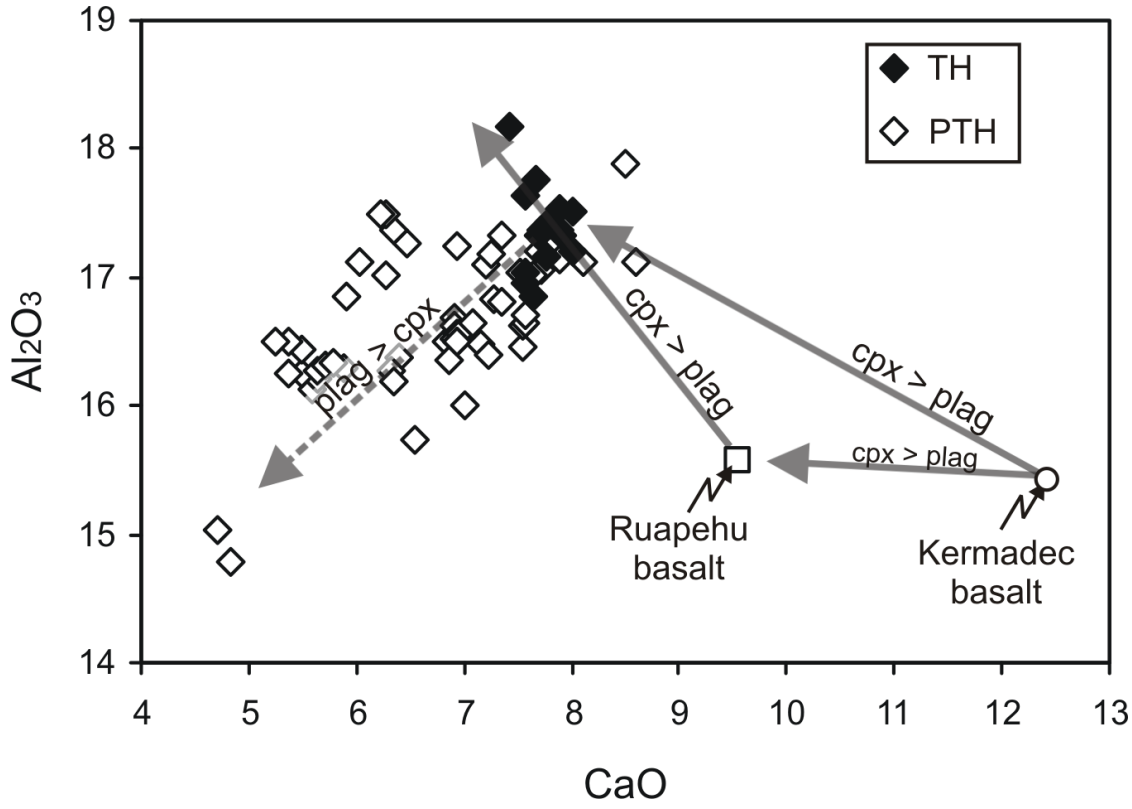

Fig 5.2. Plot of CaO vs Al_2O_3 illustrating different evolutionary pathways for TH and PTH lavas. Arrows illustrate results of least squares major element modelling from

by interaction with local crust. Higher $^{87}Sr/^{86}Sr$ and lower εHf values in the PTH lavas strongly suggests involvement of Torlesse meta-sediment, but this cannot be achieved simply by contaminating the same primitive basalt identified for TH, due to the low Sr/Hf ratio of the assimilant. An average TH composition provides a more appropriate parental magma for modelling the PTH suite with assimilation of ~6-11 % mass of meta-sediment accounting for the relatively wide isotopic array.

New Hf isotope data point unequivocally towards involvement of primitive Kermadec arc lava and meta-igneous granulite during all stages of magmatism at Mt. Ruapehu. Meta-sedimentary rocks only became involved during the PTH phase of the volcano.

Table 5.1. Results of major element least squares modelling

Series	Model No.	Parent	Daughter	ΔSiO_2 (wt%)	Σr^2	% removed					% Crystals	Modal abundance in thin section				
						olv	opx	cpx	plag	mag		olv	opx	cpx	plag	mag
TH	1	RB	WX2	2.23	0.03	7.2 (24)	-	12.7 (43)	8.8 (30)	1 (3)	29.7	-	4.2	8.1	27.4	0.6
	2	RB	W6	3.36	0.05	7.6 (23)	-	13.7 (42)	9.8 (30)	1.8 (5)	32.9	-	11.2	7.1	31.8	1.3
	3	RB	W7	2.22	0.05	6.9 (22)	-	15.6 (48)	8.2 (25)	1.5 (5)	32.2	-	6.9	7.2	33.4	1.8
	4	RB	W5	3.37	0.06	7.7 (23)	-	13.8 (40)	10.8 (31)	2 (6)	34.3	-	-	-	-	-
	5	RB	WX3	4.33	0.02	8.6 (24)	-	12.3 (34)	13.6 (37)	2.1 (5)	36.6	-	-	-	-	-
	6	168/1B	RB	2.73	0.04	0.1 (0.2)	-	20.5 (51)	17.6 (44)	2.2 (4)	40	7.2	3.5	8.7	25.4	0.4
	7	168/1B	W7	4.95	0.12	2.5 (5)	-	28.2 (55)	17 (34)	3.3 (6)	51	-	6.9	7.2	33.4	1.8
	8	RB	Avg TH	3.66	0.07	8.1 (24)	-	12.7 (37)	11.7 (34)	1.9 (5)	34.4	-	-	-	-	-
	9	WX2	W17	1.22	0.01	-	3.4 (31)	**0.2 (1)**	6.7 (61)	0.8 (7)	10.9	-	8.9	4.8	32.4	0.8
	10	WX2	W14	1.88	0.01	-	4.7 (22)	1 (4)	14.2 (65)	2.1 (9)	22	-	7.9	5.5	33.8	1.6
PTH	11	R04-03	WX9	2.69	0.24	-	4.8 (15)	2.5 (8)	22.6 (68)	3.1 (9)	33	-	7.5	2.9	18.1	0.1
	12	WX9	R96-26	0.89	0.02	-	3.2 (26)	2.2 (17)	7 (56)	0.01 (1)	12.4	-	6.4	2.2	22.7	0.6
	13	R96-26	W27	3.62	0.34	-	5.3 (17)	7 (22)	15.9 (52)	2.6 (52)	30.8	-	-	-	-	-
	14	W27	T5-14	2.56	0.37	-	**0.2 (1)**	**1.6 (11)**	13.1 (87)	1.9 (13)	15	-	3.2	3.8	17.8	0.4
	15	Avg TH	Avg PTH	2.94	0.56	-	4.2 (16)	2.8 (11)	16.5 (62)	3 (11)	26.8	-	-	-	-	-
	16	RB	Avg PTH	6.91	0.36	9.3 (21)	-	14.1 (31)	18.1 (40)	3.5 (7.8)	45	-	-	-	-	-

XLFRAC least-squares modelling based on eight oxides. Minerals compositions taken from parental lava (see Appendix D) or in the case of 168/1B, Gamble et al. (1993b). ΔSiO_2 refers to the difference calculated between parent and daughter compositions. olv, olivine; opx, orthopyroxene; cpx, cliinopyroxene; plag, plagioclase; mag, magnetite. Number in brackets refers to the phase percentage of the total assemblage. Bold font infers the addition of a phase.

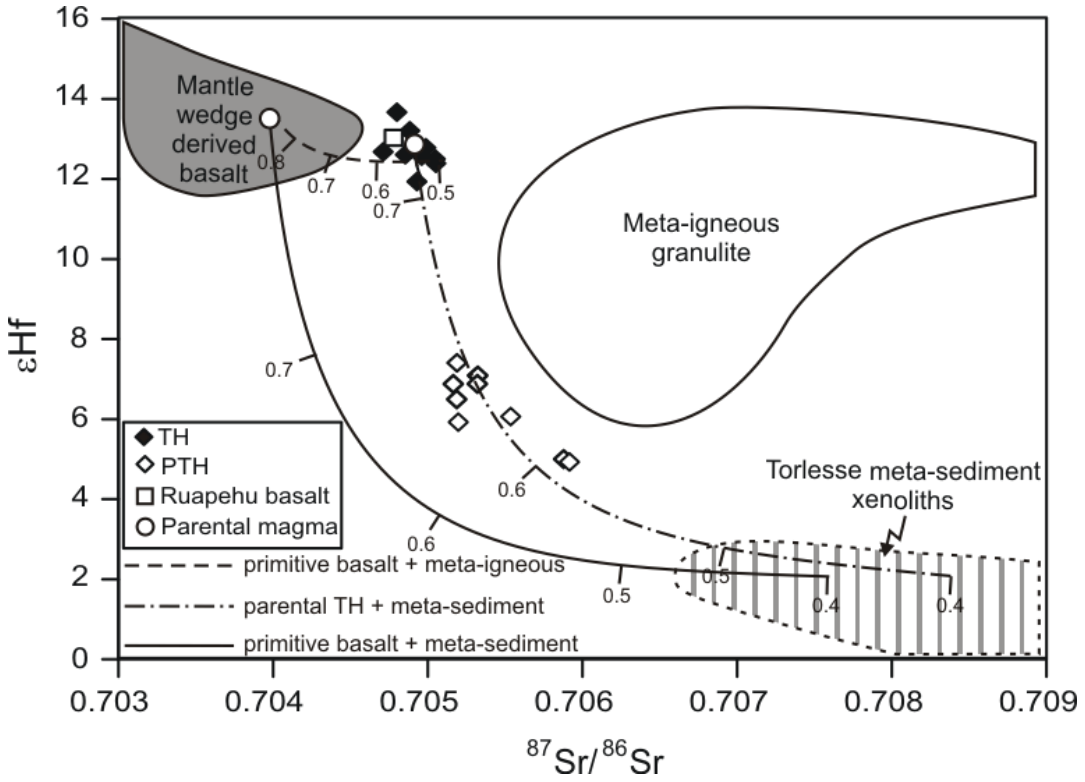

Fig. 5.3. EC-AFC models using $^{87}Sr/^{86}Sr$ and εHf compositions (Spera and Bohrson, 2001) for a mantle wedge basalt and average TH lava contaminated with meta-igneous granulite and Torlesse meta-sediment (see also Price et al., 2001; 2005). Mantle wedge field is from Kermadec Arc lavas (Gamble et al., 1996). Compositions of end members (with D values in brackets): Mantle wedge basalt - $^{87}Sr/^{86}Sr$ = 0.704, εHf = +13.4, Sr = 243 ppm (0.5-1), Hf = 1.3 ppm (0.2). TH lava - $^{87}Sr/^{86}Sr$ = 0.704909, εHf = +13.0, Sr = 220 ppm (1.0), Hf = 1.74 ppm. Meta-igneous granulite - $^{87}Sr/^{86}Sr$ = 0.707, εHf = +10.0, Sr = 323 ppm (2.0), Hf = 1.25 ppm (0.3). Torlesse meta-sediment - $^{87}Sr/^{86}Sr$ = 0.71459, εHf = -1.0, Sr = 217 ppm (2.0), Hf = 7 ppm (0.4). Tick marks represent fraction of liquid remaining (F) in 0.1 increments. EC-AFC calculations used an initial country rock temperature of 650°C (F = 0.8 - 0.4) for meta-igneous granulite and 450°C (F = 0.7 - 0.3) for Torlesse meta-sediment based on an initial geotherm of 20°C/km.

5.5. Lithospheric Control of Differentiation Pathways

Villamor and Berryman (2006a) estimated initiation times of faults forming the Mt. Ruapehu Graben by extrapolating average displacements of late Quaternary chronological markers back in time (Fig. 5.1). The earliest known faulting in the area began in the late Quaternary (e.g. Rangipo Fault ~ 400 ka; Villamor and Berryman,

2006b) and preceded initiation of Ruapehu volcanism. However, 50% of faults (n = 8) are estimated to have initiated, or accelerated their movement, between 134 and 175 ka. This coincides with the earliest PTH lavas (~160 ka; Gamble et al., 2003). Therefore, changes in melt - crust interaction recorded by the geochemistry of Ruapehu lavas could reflect the structural evolution of the TVZ lithosphere. Furthermore, accelerated fault movement in conjunction with increased magma production rate during 13.8-26.5 ka has also been reported at Ruapehu (Villamor et al., 2007), indicating structural controls on magmatic activity have been important throughout the history of the volcano.

We interpret the geochemical evolution of the volcano as a direct product of its tectonic environment. As a result of buoyancy contrasts, the earliest melts produced by the mantle wedge would probably have stalled near the Moho, underplating the lower crust. This created a deep, and long-lived, site for magma storage, similar to the MASH zones of Hildreth and Moorbath (1988) or hot zones of Annen et al. (2006). After prolonged, focussed intrusion at this depth (10,000-100,000 yrs - based on U-series estimates for arc magma residence times, Reagan et al., 2003; Zellmer et al., 2003), the crust became sufficiently hot to allow assimilation of meta-igneous granulite near its base. Subsequent batches of basaltic magma arriving in this differentiation zone generated the TH magma series (Fig. 5.4; Stage 1). The overlying meta-sediment remained cool, limiting interaction with TH magma that was travelling to the surface. However, continued magmatic intrusion enhanced crustal heat flow sufficiently to allow increased rates of extension by thermally weakening the crust. The coincidence between ages estimated for a significant number of fault initiation events and for the timing of a major transition in magma chemistry suggests increased extension rates and crustal heating facilitated additional interaction between melts and

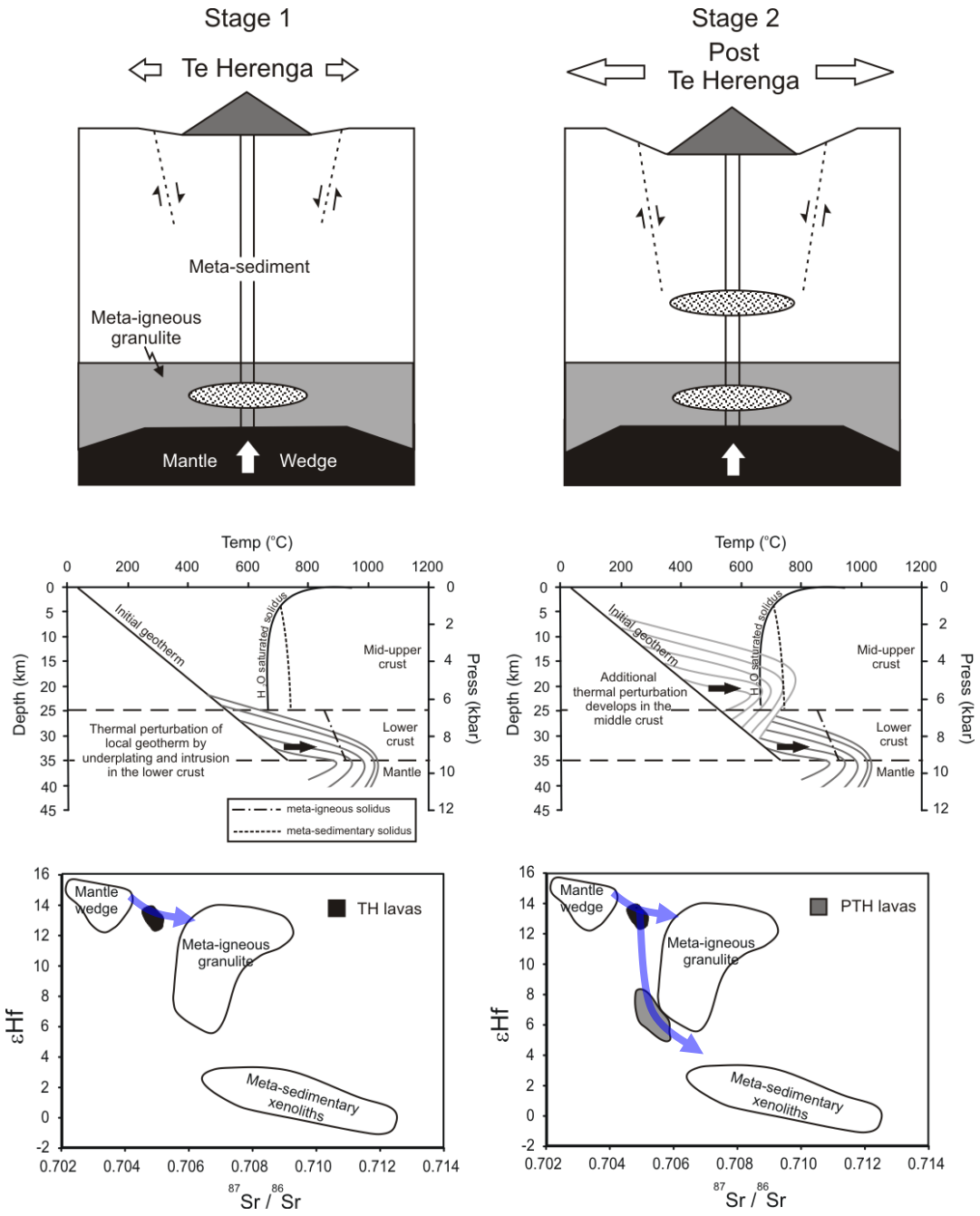

Fig. 5.4. Schematic diagram summarizing structural control on differentiation pathways for TH and PTH lavas, illustrated in $^{87}Sr/^{86}Sr$ vs εHf. Stage 1 illustrates the development of a lower crustal thermal perturbation due to prolonged underplating. This facilitates assimilation of meta-igneous granulite by subsequent basalt from the mantle producing TH compositions. Stage 2 is the consequence of thermal weakening in the shallower crust allowing increased rates of extension. This allows further differentiation in the overlying meta-sediment producing PTH lavas. Meta-igneous granulite and meta-sedimentary solidus curves based on melting experiments from meta-basalts (Beard and Lofgren, 1991) and meta-pelites (Vielzeuf and Holloway, 1988).

the meta-sedimentary rocks (Fig. 5.4; Stage 2). This changed the baseline chemistry of magma by adding a further stage of crustal interaction with meta-sediment after granulite interaction in the lower crustal differentiation zone. Assimilation of meta-sediment created the distinctive shifts to higher $^{87}Sr/^{86}Sr$ and lower εHf compositions observed in PTH lavas.

5.6. Conclusions/Implications

Differentiation in arc systems is often modelled as occurring at fixed depths without variation in the availability or composition of contaminants during the lifetime of the system. This study demonstrates that the depth of differentiation changed at Mt. Ruapehu, probably in response to the tectonic evolution of the extending arc crust. Temporal variations at Mt. Ruapehu also add an extra stage to TVZ crust evolution models in which andesite centres like Ruapehu are precursors to rhyolitic activity when extension rates increase further (Price et al., 2005).

Initial seismic studies within the central TVZ identified the Moho at ~16 km depth which, assuming an initial thickness of 30 km, equates to a stretching factor of ~2 (Stern, 1987; Stratford and Stern, 2004). However, more recent seismic refraction-reflection studies report the Moho at ~30 km depth implying no net crustal thinning, despite considerable extension (Harrison and White, 2004; 2006; Stratford and Stern, 2006; Stern et al., 2006). The discrepancy in crustal thickness is accounted for by the presence of ~15 km of underplated material forming over the past 2 Ma (Harrison and White, 2004; 2006). We attribute formation of this material to the deeper level differentiation that our data require to be active throughout the lifetime of Ruapehu (Fig. 4). This indicates that underplating within or beneath the lower crust may be an important magmatic process throughout the history of the region and suggests

continental arcs, like the TVZ, may provide localised regions where crustal growth can be greatly accelerated.

Finally the unpredictable nature and varying style of eruption at arc volcanoes presents a significant hazard at convergent margins. For example, the degree of exsolved volatile content within a melt can influence eruption intensity resulting in magmas derived from deeper levels in the crust erupting more violently than those sourced from shallower levels. Consequently, temporal adjustments in differentiation depths may be capable of varying the intensity and eruption style throughout the lifetime of an arc volcano posing significant challenges for long-term hazard assessment in these regions.

Chapter 6

Summary and Conclusions: Structural and crustal influences on differentiation pathways at Mt. Ruapehu and surrounding vents

6.1. Mt. Ruapehu Crustal Column

Arc magmas commonly display geochemical evidence for interaction with crust in the over-riding plate. However, given the strong heterogeneity in crustal compositions at arcs, constraining the nature of crust at individual arc volcanoes is fundamental in understanding magma evolution at convergent margins. The crustal column at the southern termination of the TVZ has a major influence on the geochemical composition of lavas from Mt. Ruapehu and surrounding satellite vents. Recent seismic attenuation studies (Eberhart-Philips et al., 2005; Reyners et al., 2007) support previous petrological evidence (Graham, 1987; Graham et al., 1990) that indicates the crustal column comprises two main lithological layers; a 5-10km thick meta-igneous lower crust overlain by 20-25 km Torlesse meta-sediment (Chapter 2). Most crustal-derived melts are formed by fluid absent melting reactions, usually at temperatures ≥ 800 °C during the transition from amphibolite to granulite facies (Clemens, 2006). Petrography and geochemistry of meta-sedimentary xenoliths from Ruapehu lavas illustrates this lithology is particularly susceptible to assimilation (fertile) by mantle wedge derived magmas with melting primarily controlled by mica breakdown. Geochemical evidence also suggests meta-igneous crust influences the composition of Ruapehu lavas. However, partial melting in thin section is lacking due to the anhydrous assemblage of meta-igneous xenoliths. Nevertheless, REE data (Dy/Yb) indicates partial melting of meta-igneous xenoliths in this study is controlled by amphibole breakdown (Chapter 2). Previous interpretations of the meta-igneous xenoliths based on Sr and O isotope ratios suggested an altered Jurassic oceanic crust protolith (Graham et al., 1990). However relatively similar trace element patterns (LILE-LREE enrichment and HFSE depletion relative to NMORB) between Ruapehu lavas and meta-igneous xenoliths may indicate they represent recent underplated

material (Chapter 2). The use of Re and Os isotopes in lavas from volcanic arcs has become increasingly popular (e.g. Alves et al., 1999; Chesley et al., 2002; Dreher et al., 2005; Hart et al., 2002) and may help determine the relative age of the meta-igneous xenoliths due to their unique behaviour during mantle melting.

Table 6.1. Whole rock Os isotopes and PGE data for meta-igneous xenoliths

Sample	$^{187}Os/^{188}Os$	1SE	Os (ppt)	Re (ppt)
17411	0.14589	0.00072	61.3	14.7
17430	2.20758	0.00888	8.7	464.9
17441	0.17978	0.00020	20.1	111.1
17442	0.13702	0.00011	65.8	245.3

Four meta-igneous samples were chosen for Re-Os analysis based on high but variable MgO contents (7-14 wt%). Re generally behaves as a relatively incompatible element during mantle melting while Os, being a siderophile/chalcophile element is highly compatible. Consequently, mantle melts have relatively high Re/Os ratios (100-3000; Schiano et al., 1997) and can evolve to radiogenic $^{187}Os/^{188}Os$ ratios in a matter of a few million years. Therefore, the $^{187}Os/^{188}Os$ ratio of Jurassic oceanic crust should be considerably more radiogenic than recent underplated material. With the exception of one meta-igneous xenolith, Os isotope data are considerably less radiogenic than $^{187}Os/^{188}Os$ compositions expected for Jurassic oceanic crust modelled for different Re/Os ratios (Fig. 6.1a). Similarly meta-igneous εHf values are also considerably less radiogenic than modelled Jurassic oceanic crust (Fig. 6.1a&b), with xenolith compositions falling within the range of Ruapehu lavas (Fig. 6.2). Although

the $^{187}Os/^{188}Os$ ratio of xenolith 17430 may suggest it represents Jurassic oceanic crust, it also has an extremely low Os concentration. Owing to the potentially radiogenic $^{187}Os/^{188}Os$ composition of North Island continental crust (Fig. 6.1b) sample 17430 may therefore

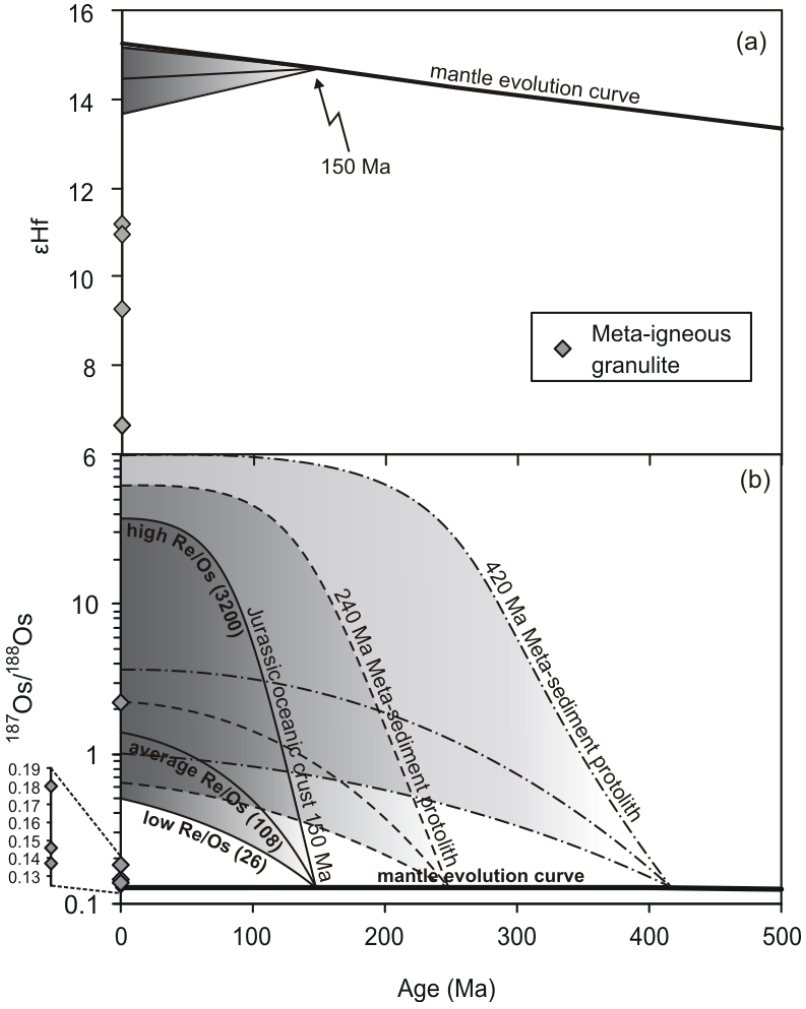

Fig. 6.1. a) $^{187}Os/^{188}Os$ evolution of melts extracted at 150 Ma with differing $^{187}Re/^{188}Os$ ratios. Meta-igneous xenoliths $^{187}Os/^{188}Os$ compositions shown for comparison. Evolution of melts extracted at 240 and 420 Ma represent igneous protoliths for Torlesse meta-sediment (ie. potential $^{187}Os/^{188}Os$ range for typical TVZ crust). $^{187}Os/^{188}Os$ mantle evolution curve calculated using $^{187}Os/^{188}Os_{initial}$, $^{187}Re/^{188}Os$ = 0.4346 and ^{187}Re decay rate = $1.666E^{-11}$ (Brandon and Walker, 2005). $^{187}Re/^{188}Os$ ratios used in melt modeling taken from range in MORB (Schiano et al. 1997). b) εHf evolution of melts extracted from the mantle at 150 Ma with differing $^{176}Lu/^{177}Hf$ ratios. Meta-igneous xenoliths εHf compositions shown for comparison. The isotopic composition of depleted mantle source at 150 Ma is calculated assuming a present-day average $^{176}Hf/^{177}Hf$ depleted mantle composition of 0.283200 and formation of the depleted reservoir from bulk silicate reservoir at 4 Ga, giving a $^{176}Lu/^{177}Lu$ ratio of 0.039. $^{176}Lu/^{177}Hf$ ratios taken from range in MORB (Workman and Hart, 2005).

record crustal contamination by Torlesse meta-sediment (Fig. 6.2, Table 2.2; modelling parameters). In fact, the remaining $^{187}Os/^{188}Os$ compositions of meta-igneous xenoliths can also be explained by minor amounts (1-4%) of contamination by Torlesse meta-sediment. Consequently, the relatively unradiogenic Re-Os isotope data suggests the meta-igneous xenoliths are unlikely to be fragments of altered Jurassic oceanic crust but probably represent recent underplated material contaminated by small quantities of Torlesse meta-sediment followed by hydrothermal isotopic exchange processes (see Chapter 2).

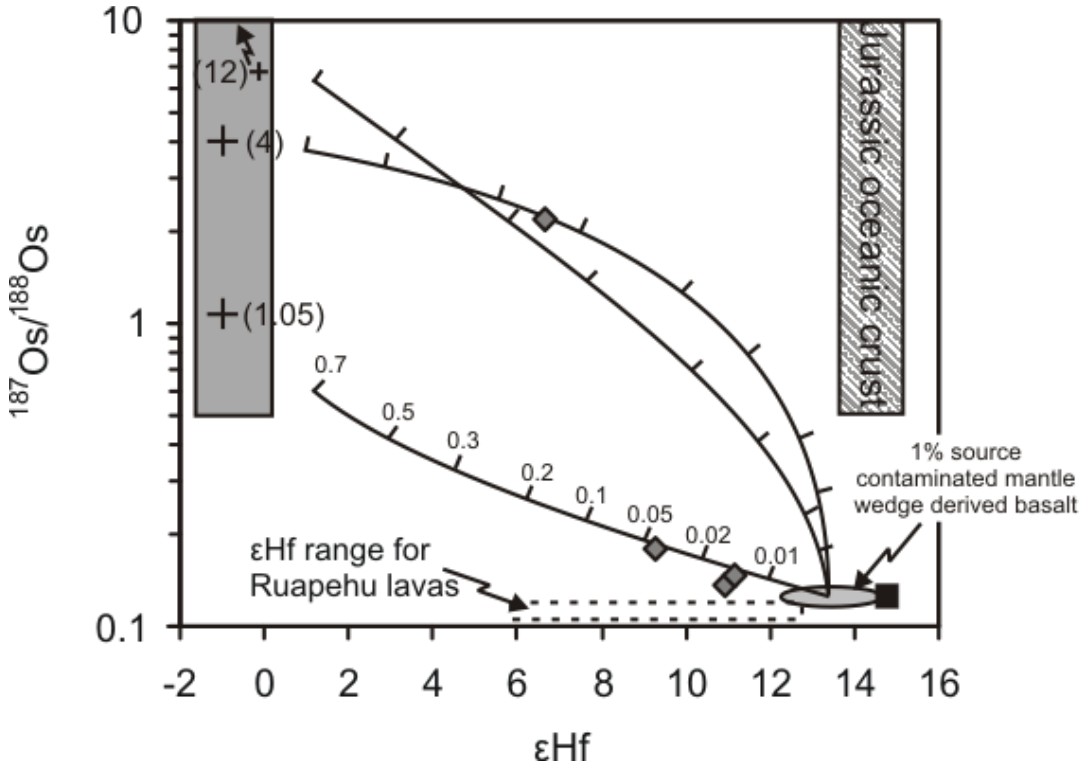

Fig. 6.2. Simple mixing models using εHf vs $^{187}Os/^{188}Os$ for a mantle wedge derived basalt contaminated by Torlesse meta-sediment. Modelling parameters listed in Table 6.1. Tick marks represent fraction of meta-sediment added to mantle wedge derived basalt (0.01-0.7). Grey area represents potential crustal compositions (crosses represent actual crustal values used in modelling); εHf values taken from meta-sedimentary xenoliths, $^{187}Os/^{188}Os$ range derived from modelling in Fig. 6.1.

Table 6.2. End-member compositions used in mixing calculations

	Os	Hf	$^{187}Os/^{188}Os$	εHf
Underplate	65	1.43	0.1248	12.3
Crust (1)	31	3.96	1.05	-1
Crust (2)	31	3.96	4	-1
Crust (3)	31	3.96	12	-1

Underplate: Os concentration from xenolith 17411 (highest value); Hf concentration from local mantle wedge basalt (Rumble IV volcano; Gamble et al., 1996); $^{187}Os/^{188}Os$ - average MORB estimate from Hart et al. (1999); εHf - 1% source contamination (Hikurangi sediment) of local mantle wedge basalt (Handler, M. pers comm).

Crust: Os concentration from average continental crust (Rudnick and Gao, 2004); $^{187}Os/^{188}Os$ - 1.05 (average continental crust Saal et al. (1998)), 4 & 12 (modelled crustal values using Torlesse sediment protolith ages from Adams et al. (1998); εHf value - lowest meta-sediment value.

6.2. Magma sources

Comparison between differentiation histories in HMA and HAB illustrates that source regions along the TVZ appear to differ in degrees of depletion (Chapter 4). HMA in southern TVZ are derived from a relatively depleted mantle wedge (low Ca, Al and Ti concentrations) whereas HAB in the central-northern region are derived from a relatively fertile source. This can be explained by considering the structure of the TVZ lithosphere outlined by Stern et al. (2006). The southern segment is dominated by compression and thickened lithosphere whereas the central-northern region is characterised by extension accompanied by substantial erosion of the lithosphere from upwelling asthenosphere. As subcontinental lithosphere is generally refractory and comprises a large proportion of the wedge beneath the southern TVZ, hydrous melting of the mantle in this region could produce relatively Mg-rich melts illustrating the depleted characteristics of high-Mg andesites. The increased mantle flow envisaged beneath the central-northern TVZ would replenish the mantle wedge with fertile

asthenosphere. Partial melting in this setting where mantle flow is more vigorous could generate melts the high-alumina basalts with relatively enriched compositions.

6.3. Differentiation Processes

Fractional crystallisation, magma mixing and crustal assimilation are important differentiation processes that influence the geochemical composition of lavas at convergent margins.

Fractional crystallisation has exerted a major influence on major and trace element abundances in Ruapehu and HMA lavas. Upwards development of the magmatic plumbing system at Ruapehu over time has been identified based on a change in fractionating assemblage at the transition from TH to PTH lavas (Chapter 3). TH lavas result from fractionation of an assemblage in which cpx > plag, while PTH compositions require a plag > cpx assemblage. Lower pressures and/or lower water contents in basaltic/andesitic magma tends to induce greater plagioclase crystallisation (Grove et al., 2002), hence we interpret the relative proportion of this mineral in fractionation models as reflecting a shallower mean differentiation depth for PTH relative to TH. Modelling of HMAs (with the exception of Pukeonake) also suggests major elements are controlled by fractional crystallisation. Clinopyroxene + olivine >> plagioclase fractionation can account for the majority of the HMA array and like the TH suite, probably differentiated at relatively high pressure in the lower crust (Chapter 4).

Magma mixing is an important process in the formation of Pukeonake lavas (Graham, 1985a) with petrographic evidence displaying unmistakable magmatic disequilibrium textures (e.g orthopyroxene coronas on olivine phenocrysts). Major element modelling indicates Pukeonake compositions can be reproduced by mixing

between basalt and andesite-dacite accompanied by entrainment xenocrystic olivine derived from the mantle wedge (Chapter 4). Mantle like $\delta^{18}O_{olv}$ values supports this conclusion (e.g. 5.14‰).

However, crystal fractionation and magma mixing are not the only processes operating during differentiation as Ruapehu magmas and HMAs have a distinct isotopic composition from local mantle wedge derived basalt. In particular, new Hf isotope data point unequivocally towards a temporal evolution of crustal contaminants between TH and PTH suites; meta-igneous granulite is involved during all stages of magmatism at Mt. Ruapehu whereas meta-sedimentary rocks only became involved during the PTH phase of the volcano (Chapter 3). $\delta^{18}O_{olv}$, $\delta^{18}O_{cpx}$ and $\delta^{18}O_{cpx}$ compositions from TH and PTH phenocrysts support radiogenic isotope modelling and illustrate complex multi-stage crystallisation in each magmatic series. Isotopic data from Mt. Ruapehu confirms that deep long-lived sites for magma storage are common features at convergent margins (MASH zones of Hildreth and Moorbath (1988); hot zones of Annen et al. (2006)) which influence magma compositions throughout the lifetime of an arc volcano.

6.4. Structural and thickness variations in arc crust: controls on differentiation pathways

Palaeoseismic studies at the southern termination of the TVZ (Villamor and Berryman, 2006a) have revealed that changes in melt - crust interaction recorded by the geochemistry of Ruapehu lavas could reflect the structural evolution of the TVZ lithosphere (Chapter 5). The earliest melts produced by the mantle wedge would have stalled near the Moho, underplating the lower crust and eventually forming meta-

igneous granulite through hydrothermal isotopic exchange with overlying meta-sediment. Subsequent batches of basaltic magma arriving at the Moho generated the TH magma series by assimilating meta-igneous granulite (Fig. 6.3; Stage 1).

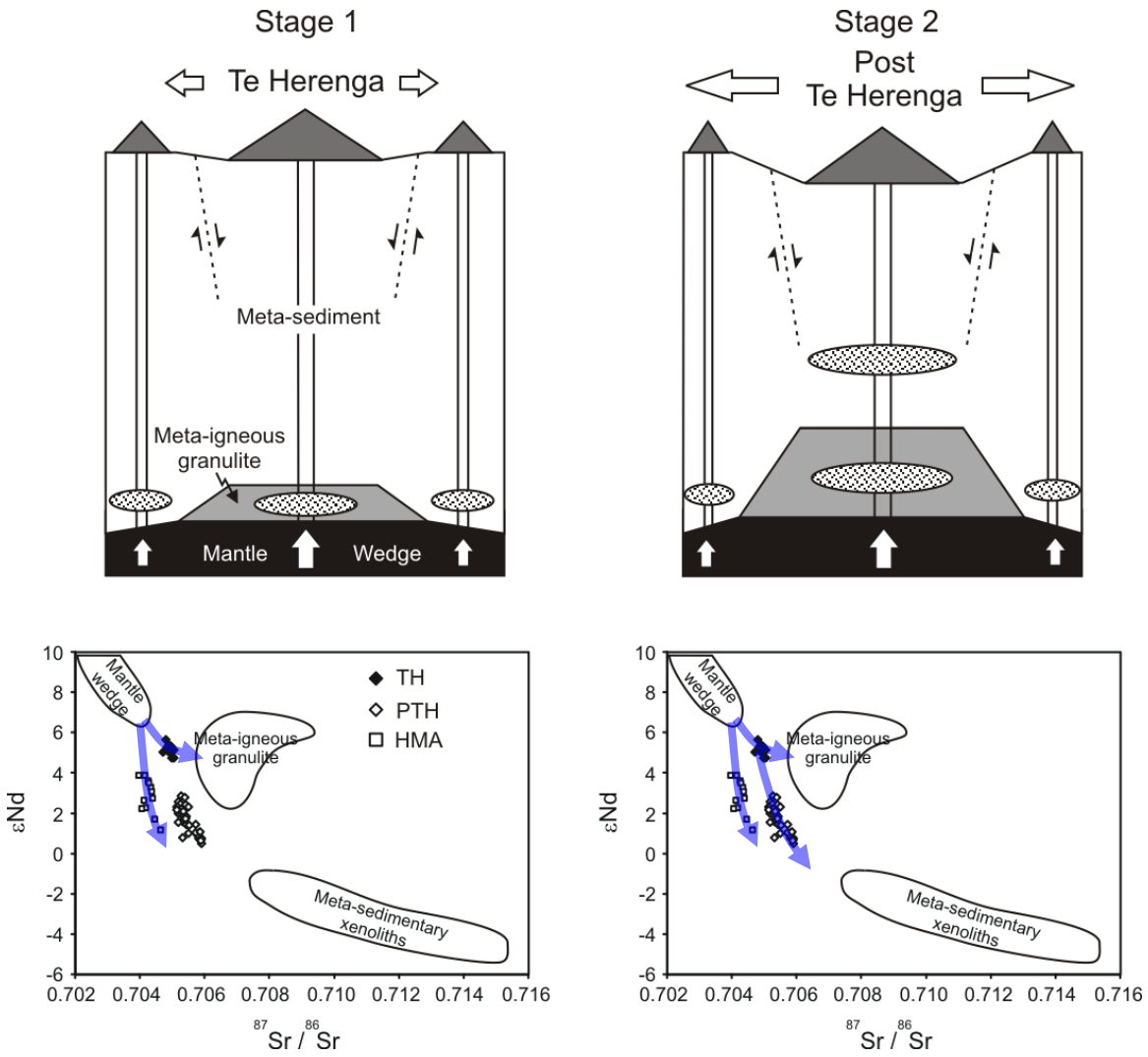

Fig. 6.3. Schematic diagram summarizing differentiation pathways for Ruapehu and HMA lavas, illustrated in $^{87}Sr/^{86}Sr$ vs εNd. Early underplate material forms meta-igneous granulite beneath the axis of the Mt. Ruapehu graben where extension is greatest. Stage 1 illustrates the development of a lower crustal thermal perturbation due to prolonged underplating. This facilitates assimilation of meta-igneous granulite by subsequent basalt from the mantle producing TH compositions. Stage 2 is the consequence of thermal weakening in the shallower crust allowing increased rates of extension. This allows further differentiation in the overlying meta-sediment producing PTH lavas. HMA magmatism is active throughout the lifetime of Ruapehu. They record no interaction with lower crustal granulite due to its absence at the margin of the graben.

Continued magmatic intrusion enhanced crustal heat flow sufficiently to allow increased rates of extension by thermally weakening the crust. The coincidence between age estimates for fault initiation events and for the timing of a major transition in magma chemistry suggests increased extension rates and crustal heating facilitated additional interaction between melts and meta-sediment generating the PTH magma series (Fig. 6.3; Stage 2). This changed the baseline chemistry of magma by adding a further stage of crustal interaction with meta-sediment following granulite interaction in the lower crustal differentiation zone.

The current restriction of HMA lavas to satellite vents near Mt. Ruapehu is a direct consequence of the appreciably thicker crust (~35km) in the southern TVZ. This has resulted in relatively high-pressure fractionation (cpx + olv > plag) compared to HAB in the central/northern TVZ (plag > cpx + olv). Given that HMAs are proposed to have fractionated at a similar depth to the TH series, it is therefore surprising that radiogenic and stable isotope data indicates crustal contamination dominated by Torlesse meta-sediment. However, this supports that meta-igneous granulite represents recent underplated material and consequently is a localised feature at depth forming only beneath the main axis of extension where the magma flux is highest, i.e. is absent at the margins of the graben (Fig. 6.3).

6.5. Implications for arc-wide geochemical research

Studies of arc andesites suggest convergent margins play an important role in the formation of continental crust due to the widespread occurrence of intra-crustal recycling (Rudnick, 1995; Davidson and Arculus, 2006). This is illustrated by isotope ratios in many arc magmas being displaced towards crustal values caused by

assimilation of lithologies in the over-riding plate (e.g. Davidson et al., 1987; Hildreth and Moorbath, 1988; Macpherson et al., 1998). Crustal compositions are most tightly constrained when focussing on single volcanic edifices where reasonable controls can be placed on the composition of local contaminants (e.g. Graham and Hackett, 1987). Due to the lack of exposure at active arcs, information concerning the composition of crust at volcanoes is best determined from crustal xenoliths brought to the surface by lavas. At Mt. Ruapehu, this reveals a crustal column composed of two contrasting lithologies that have each influenced the geochemical evolution of lavas throughout the lifetime of the volcano. This example of local variability in crustal compositions at convergent margins therefore cautions against using average crustal lithologies for modelling crustal assimilation processes at arcs.

The complex geochemical variation exhibited by Ruapehu lavas also highlights the importance of characterising the evolution of individual volcanoes prior to conducting regional arc studies. For example, changing differentiation depths and pathways at Ruapehu result in two temporally distinct magmatic series. Consequently, fixed depth differentiation models without variation in the availability or composition of contaminants maybe an oversimplification of magma evolution at arc volcanoes.

This study has illustrated that the tectonic evolution of arc crust can cause adjustments in magma differentiation depths resulting in changes in magma geochemistry. As lithospheric extension in the over-riding plate at convergent margins is relatively common (e.g. Tonga-Kermadec; Kamchatka; Andes; Cascades), it suggests local tectonics may directly influence magma evolutionary pathways at arcs in general. Therefore, further geochemical studies in sections of arcs where detailed fault activation estimates are available will provide a better understanding in the thermal evolution of subduction zone lithosphere.

6.6. Areas for future research

The effects of crustal melting are particularly evident in the geochemistry of lavas from the southern TVZ. Assessing the temporal evolution of melt-crust interactions in Mt. Ruapehu and satellite vent lavas has been aided by the collection of new whole-rock Hf and mineral separate O isotope compositions. Combining oxygen isotope values with radiogenic isotope ratios is a particularly effective method for determining processes of crustal contamination (James, 1981). However comparing radiogenic and stable isotope ratios obtained from whole-rock and mineral separates respectively may be problematic due to disequilibrium between phenocrysts and melts. Therefore, crustal contamination modelling could be improved by measuring radiogenic isotope ratios on the same individual phases used for $\delta^{18}O$ analysis. Furthermore, oxygen isotope ratios of crustal compositions at the southern TVZ may not be entirely accurate as they were determined on whole-rock samples. More precise crustal oxygen isotope compositions could be determined by analysing major phases within meta-igneous granulite and Torlesse meta-sediment xenoliths.

Modelling crustal assimilation on lavas invariably uses whole rock compositions of crustal contaminants. However, studies examining partial melts generated from crustal lithologies indicate they may not attain isotopic equilibrium with the residual assemblage. Therefore, crustal partial melts are unlikely to have the same composition as the whole rock (e.g. Knesel and Davidson, 1999). For example, $^{87}Sr/^{86}Sr$ crustal melt compositions will differ greatly depending on whether biotite (low Sr, high $^{87}Sr/^{86}Sr$) or plagioclase (high Sr, low $^{87}Sr/^{86}Sr$) is being consumed. Therefore, examination of trapped melts within Torlesse meta-sediment xenoliths using micro-sampling techniques (e.g. Davidson et al., 2007) may assist in defining more precise crustal melt compositions contaminating Ruapehu magmas.

Furthermore, this may also reveal how crustal melt compositions from the same lithology can change with time as the magmatic system thermally evolves and the contaminant becomes increasingly refractory.

Finally, new Os isotope data from meta-igneous granulite xenoliths indicates the lower crust beneath Mt. Ruapehu is composed of relatively recent underplated material. However, current interpretations are based on a limited data set and therefore more Os isotopes analyses should be conducted before a Jurassic oceanic crust origin is fully rejected. Furthermore, Os isotope data should also be determined for the Torlesse meta-sediment as appose to using average continental crustal compositions in contamination modelling.

References

Acocella, V., Spinks , K., Cole, J., Nicol A., 2003, Oblique back arc rifting of Taupo Volcanic Zone, New Zealand: Tectonics, v. 22(4), p. 1–18.

Adams, C.J., Campbell, H.J., Graham, I.J. and Mortimer, N., 1998, Torlesse, Waipapa and Caples suspect terranes of New Zealand: Integrated studies of their geological history in relation to neighbouring terranes: Episodes, v. 21, p. 235–240.

Alves, S., Schiano, P. and Alle'gre, C.J., 1999, Rhenium-osmium isotopic investigation of Java subduction zone lavas: Earth Planetary Science Letters, v. 168, p. 65–77.

Annen, C., Blundy, J.D., and Sparks, S.J., 2006, The Genesis of Intermediate and Silicic Magmas in Deep Crustal Hot Zones: Journal of Petrology, v. 47, p. 505–539.

Arculus, R.J., 1981, Island arc magmatism in relation to the evolution of the crust and mantle: Tectonophysics, v. 75, p. 113-133.

Baker, M.B., Grove, T.L., and Price, R., 1994, Primitive basalts and andesites from the Mt Shasta region, N California - products of varying melt fraction and water-content: Contributions to Mineralogy and Petrology, v. 118, p. 111–129.

Bannister, S., Reyners, M., Stuart, G., and Savage, M., 2007, Imaging the Hikurangi subduction zone, New Zealand, using teleseismic receiver functions: crustal fluids above the forearc mantle wedge: Geophysical Journal International, v. 169, p. 602–616.

Beard, J.S., and Lofgren, G.E., 1991, Dehydration melting and water-saturated melting of basaltic and andesitic greenstones and amphibolites at 1, 3 and 6.9 kbar: Journal of Petrology, v. 32, p. 365–401.

Beyer, E., 1996, Geology and geochemistry of volcanic rocks of the Tukino skifield area and middle Whangaehu gorge, east Ruapehu, New Zealand: Unpublished BSc (Honours) thesis, La Trobe University, Melbourne.

Bibby, H.M., Caldwell, T.G., Davey, F.J., and Webb, T.H., 1995, Geophysical evidence on the structure of the Taupo Volcanic Zone and its hydrothermal circulation: Journal of Volcanology and Geothermal Research, v. 68, p. 29-58.

Blichert-Toft, J., and Albarede, F., 1997, The Lu-Hf isotope geochemistry of chondrites and the evolution of the crust-mantle system: Earth and Planetary Science Letters, v. 148, p. 243–258.

Bodiner, J.-L., and Godard, M., 2003, Orogenic, ophiolitic, and, abyssal peridotites, in: R.W., Carlson, H.D., Holland, and K.K., Turekian, (Eds.), Treatise on Geochemistry, vol. 2, The mantle and the core: Elsevier, New York. pp. 103–170.

Bohrson, W.A., and Spera, F.J., 2001, Energy-constrained open system magmatic processes II: Application of energy-constrained assimilation-fractional crystallisation (EC-AFC) model to magmatic systems: Journal of Petrology, v. 42, p. 1019–1041.

Bottazzi, P., Tiepolo, M., Vanucci, R., Zanetti, A., Brumm, R., Foley, S.F., Oberti, R., 1999, Distinct site preferences for heavy and light REE in amphibole and the prediction of $^{Amph/L}D_{REE}$: Contributions to Mineralogy and Petrology, v. 137, p. 36–45.

Brandon, A.D., and Walker, R.J., 2005, The debate over core-mantle interaction: Earth and Planetary Science Letters, v. 232, p. 211–225.

Brown, G.C., and Musset, A.E., 1993, The Inaccessible Earth, second ed. Chapman and Hall, London.

Brown, M., 2006, Melt extraction from the lower continental crust of orogens: the field evidence, in: Brown, M., Rushmer, T. (Eds.), Evolution and Differentiation of the Continental Crust: Cambridge University Press, pp. 331–383.

Cameron, E., 2004, The geology, petrology and geochemistry of Hauhungatahi Volcano, Tongariro Volcanic Centre, New Zealand: Unpublished MSc thesis, Victoria University of Wellington, New Zealand.

Cesare, B., 2000, Incongruent melting of biotite to spinel in a quartz-free restite at El Joyazo (SE Spain): Textures and reaction characterization: Contribution to Mineralogy and Petrology, v. 139, p. 273–284.

Charlier, B.L.A., Ginibre, C., Morgan, D., Nowell, G.M., Pearson, D.G., Davidson, J.P., and Ottley, C.J., 2006, Methods for the microsampling and high-precision analysis of strontium and rubidium isotopes at single crystal scale for petrological and geochronological applications: Chemical Geology, v. 232, p. 114–133.

Chesley, J., Ruiz, J., Righter, K., Ferrari, L., and Gomez-Tuena, A., 2002, Source contamination versus assimilation: an example from the Trans-Mexican Volcanic arc: Earth Planetary Science Letters, v. 195, p. 211–221.

Clemens, J.D., 2006, Melting of the continental crust: fluid regimes, melting reactions, and source-rock fertility, in: Brown, M., Rushmer, T. (Eds.), Evolution and Differentiation of the Continental Crust: Cambridge University Press, pp. 298–327.

Cole, J.W., and Nairn, I.A., 1975, Part XXII, New Zealand: Catalogue of the active volcanoes of the world including solfatara fields: International Association of Volcanology, Rome, Italy, p. 156.

Cook, P.G., and Herczeq, A.L., 1999, Environmental Traces in Subsurface Hydrology, first ed. Kluwer Academic Publishers.

Crawford, A.J., Falloon, T.J., and Green, D.H., 1989, Classification, petrogenesis and tectonic setting of boninites. in: Crawford, A.J. (Eds), Boninites: Unwin Hyman, London, pp. 1– 49.

Davidson, J.P., 1987, Crustal contamination versus subduction zone enrichment: examples from the Lesser Antilles and implications for mantle source compositions of island arc volcanics: Geochimica et Cosmochimica Acta, v. 51, p. 2185–2198.

Davidson, J.P., 1996, Deciphering mantle and crustal signatures in subduction zone magmatism, in: Bebout, G.E., Scholl, D.W., Kirby, S.H., and Platt, J.P. (Eds.), Subduction: Top to Bottom. Geophysical Monograph: American Geophysical Union, v. 96, pp. 251–262.

Davidson, J.P., Dungan, M.A., Ferguson, K., and Colucci, M.A., 1987, Crust-magma interaction and the evolution of arc magmas from the San Pedro-Pellado volcanic complex, Southern Chilean Andes: Geology, v. 15, p. 443–446.

Davidson, J.P., Ferguson, K.M., Colucci, M.T., and Dungan, M.A., 1988, The origin and evolution of magmas from the San Pedro–Pellado volcanic complex, S. Chile: Multi-component sources and open system evolution: Contributions to Mineralogy and Petrology, v. 100, p. 429–445.

Davidson, J.P., Hora, J.M., Garrison, J.M., and Dungan, M.A., 2005, Crustal forensics in arc magmas: Journal of Volcanology and Geothermal Research, v. 140, p. 157–170.

Davidson, J.P., and Arculus, R.J., 2006, The significance of Phanerozoic arc magmatism in generating continental crust, in: Brown, M., Rushmer, T. (Eds.), Evolution and Differentiation of the Continental Crust: Cambridge University Press, pp. 135–172.

Davidson, J.P., Morgan, D.J., Charlier, B.L.A., Harlou, R., and Hora, J.M., 2007, Microsampling and Isotopic Analysis of Igneous Rocks: Implications for the Study of Magmatic Systems: Annual Reviews in Earth and Planetary Sciences, v. 35, p. 273–311.

DePaolo, D.J., 1981, Trace element and isotopic effects of combined wallrock assimilation and fractional crystallisation: Earth and Planetary Science Letters, v. 53, p. 189–202.

Dostal J., and Capedri S., 1979, Rare earth elements in highgrade metamorphic rocks from the western Alps: Lithos, v. 12, p. 41–49.

Dowall, D.P., Pearson, D.G., and Nowell, G.M., 2003, Chemical preconcentration procedures for high-precision analysis of Hf–Nd–Sr isotopes in geological materials by plasma ionisation multi-collector mass spectrometry (PIMMS) techniques, in: Holland, J.G. & Tanner, S.D. (Eds.), Plasma Source Mass Spectrometry: Applications and Emerging Technologies. Cambridge: Royal Society of Chemistry, pp. 321–337.

Dreher, S.T., Macpherson, C.G., Pearson, D.G., and Davidson, J.P., 2005, Re-Os isotope studies of Mindanao adakites: Implications for source metals and melts: Geology, v. 33, p. 957–960.

Dungan, M.A., Wulff, A, and Thompson, R., 2001, Eruptive stratigraphy of the Tatara–San Pedro complex, 368S, Southern volcanic zone, Chilean Andes: Reconstruction method and implications for magma evolution at long lived arc volcanic centers: Journal of Petrology, v. 42, p. 555–626.

Eberhart-Philips, D., Reyners, M., Chadwick, M., and Chiu, J., 2005, Crustal heterogeneity and subduction processes: 3-D *Vp*, *Vp/Vs* and *Q* in the southern North Island, New Zealand: Geophysical Journal International, v. 162, p. 270–288.
Environmental Chemistry: http://environmentalchemistry.com

Fujimaki, H., Tatsumoto, M., and Aoki, K., 1984, Partition coefficients of Hf, Zr and REE between phenocrysts and groundmass. Proceedings of the fourteenth lunar and planetary science conference, Part 2: Journal of Geophysical Research, v. 89, Supplement B662–B672.

Galer, S.J.G., and Abouchami, W., 1998, Oractical application of Pb triple spiking for correction of instrumental mass discrimination: Mineralogical Magazine, v. 63A, p. 491-492

Gamble, J.A., Smith, I.E.M., McCulloch, M.T., Graham, I.J., and Kokelaar, B.P., 1993a, The geochemistry and petrogenesis of basalts from the Taupo Volcanic Zone and Kermadec Island Arc, S.W. Pacific: Journal of Volcanology and Geothermal Research, v. 54, p. 265–290.

Gamble, J.A., Wright, I.C., and Baker, J.A., 1993b, Seafloor geology and petrology in the oceanic to continental transition zone of the Kermadec-Havre-Taupo Volcanic Zone arc system, New Zealand: New Zealand Journal of Geology and Geophysics, v. 36, p. 417–435.

Gamble, J.A., Woodhead, J. Wright, I.C., and Smith, I.E.M., 1996, Basalt and sediment geochemistry and magma petrogenesis in a transect from oceanic island arc to rifted continental margin arc: the Kermadec-Hikurangi margin, SW Pacific: Journal of Petrology, v. 37, p. 1523–1546.

Gamble, J.A., Wood, P., Price, R.C., Smith I.E.M., and Waight, T.E., 1999, A fifty year perspective of magmatic evolution on Ruapehu Volcano, New Zealand: Verification of open system behaviour in an arc volcano. Earth and Planetary Science Letters, v. 170, p. 301–314.

Gamble, J.A., Price, R.C., Smith, I.E.M., McIntosh, W.C., and Dunbar, N.W., 2003, $^{40}Ar/^{39}Ar$ geochronology of magmatic activity, magma flux and hazards at Ruapehu volcano, Taupo Volcanic Zone, New Zealand: Journal of Volcanology and Geothermal Research, v. 120, p. 271–287.

GERM: http://earthref.org/GERM/index.html

Gill, J.B., 1981, Orogenic Andesites and Plate Tectonics: Springer-Verlag, Berlin, pp. 392.

Graham, I.J., 1985a, Petrochemical and Sr isotopic studies of lavas and xenoliths from Tongariro Volcanic Centre - Implications for crustal contamination of calc-alkaline magmas: Unpublished PhD thesis, Victoria University of Wellington, New Zealand.

Graham, I.J., 1985b, Rb-Sr geochronology and geochemistry of Torlesse metasediments from the central North Island, New Zealand: Chemical Geology, v. 52, p. 317–331.

Graham, I.J., 1987, Petrography and origin of metasedimentary xenoliths in lavas from Tongariro Volcanic Centre: New Zealand Journal of Geology and Geophysics, v. 30, p. 139–157.

Graham, I.J., and Hackett, W.R., 1987, Petrology of calc-alkaline lavas from Ruapehu Volcano and related vents, Taupo Volcanic Zone, New Zealand: Journal of Petrology, v. 28, p. 531–567.

Graham, I.J., Grapes, R.H., and Kifle, K., 1988, Buchitic metagreywacke xenoliths from mount Ngauruhoe, Taupo Volcanic zone, New Zealand: Journal of Volcanology and Geothermal Research, v. 35, p. 205–216.

Graham, I.J., Blattner, P., and McCulloch, M.T., 1990, Meta-igneous granulite xenoliths from Mount Ruapehu, New Zealand: fragments of altered oceanic crust?: Contributions to Mineralogy and Petrology, v. 105, p. 650–661.

Graham, I.J., Gulson, B.L., Hedenquist, J.W., and Mizon, K., 1992, Petrogenesis of late Cenozoic volcanic rocks from the Taupo Volcanic Zone, New Zealand, in the light of new Pb isotope data. Geochimica et Cosmochimica Acta, v. 56, p. 2797–2819.

Graham, I.J., Cole, J.W., Briggs, R.M., Gamble, J.A., and Smith, I.E.M., 1995, Petrology and petrogenesis of volcanic rocks from the Taupo Volcanic Zone: a review: Journal of Volcanology and Geothermal Research, v. 68, p. 59-87.

Grove, T.L., Parman, S.W., Bowring, S.A., Price, R.C., and Baker, M.B., 2002, The role of an H_2O-rich fluid component in the generation of primitive basaltic andesites and andesites from Mt. Shasta region, N California: Contributions to Mineralogy Petrology, v. 142, p. 375–396.

Guerina, S., and Sawyer, E.W., 2003, Large-scale melt-depletion in granulite terranes: an example from the Archean Ashuanipi Subprovince of Quebec: Journal of Metamorphic Petrology, v. 21, p. 181–201.

Hackett, W.R., 1985, The geology and petrology of Ruapehu Volcano and related vents: Unpublished PhD thesis, Victoria University of Wellington, New Zealand.

Hackett, W.R., and Houghton, B.F., 1988, A facies model for a Quaternary andesitic composite volcano: Ruapehu, New Zealand: Bulletin of Volcanology, v. 51, p. 51–68.
Handley, H.K, Macpherson, C.G., Davidson, J.P., Berlo, K., and Lowry, D., 2007, Constraining fluid and sediment contributions to subduction-related magmatism in Indonesia: Ijen Volcanic Complex: Journal of Petrology, v. 48, p. 1155–1183.

Harrison, T.A., and White, R.S., 2004, Crustal structure of the Taupo Volcanic Zone, New Zealand: stretching and igneous intrusion: Geophysical Research Letters, v. 31, L13615, doi:10.1029/2004GL019885.

Harrison, T.A., and White, R.S., 2006, Lithospheric structure of an active backarc basin: the Taupo Volcanic Zone, New Zealand: Geophysical Journal International, v. 167, p. 968–990.

Hart, S.R., 1984, A large-scale isotope anomaly in the southern hemisphere mantle: Nature, v. 309, p. 753-757.

Hart, G.L., Johnson, C.M., Shirey, S.B., Clynne, M.A., 2002, Osmium isotope constraints on lower crustal recycling and pluton preservation at Lassen Volcanic Center, CA: Earth and Planetary Science Letters, v. 199, p. 269-285.

Hart, S.R., Blusztajn, J., Dick, H.J.B., Meyer, P.S., and Muehlenbachs, K., 1999, The fingerprint of seawater circulation in a 500-meter section of ocean crust gabbros: Geochimica et Cosmochimica Acta, v. 63, p. 4059−4080.

Heier, K.S., and Thoresen, K., 1971, Geochemistry of high grade metamorphic rocks, Lofoten-Vesterålen North Norway: Geochimica et Cosmochimica Acta, v. 35(1), p. 89−99.

Hildreth, W., and Moorbath, S., 1988, Crustal contributions to arc magmatism in the Andes of central Chile: Contributions to Mineralogy and Petrology, v. 98, p. 455–499.

Hirose, K., 1997, Melting experiments on lherzolite KLB-1 under hydrous conditions and generation of high-magnesian andesitic melts: Geology, v. 25, p. 42–44.

Hobden, B.J., 1997, Modelling magmatic trends in time and space: eruptive and magmatic history of Tongariro volcanic complex, New Zealand: Unpublished PhD thesis, University of Canterbury, New Zealand.

Hobden, B.J., Houghton, B.F., Davidson, J.P., and Weaver, S.D., 1999, Small and short-lived magma batches at composite volcanoes: time windows at Tongariro volcano, New Zealand: Journal of the Geological Society of London, v. 156, p. 865–868.

Hochstein, M.P., 1995, Crustal heat-transfer in the Taupo Volcanic Zone (New-Zealand) - comparison with other volcanic arcs and explanatory heat-source models: Journal of Volcanology and Geothermal Research, v. 68, p. 117–151.

Houghton, B.F., Hackett, W.R., 1984, Strombolian and phreatomagmatic deposits of Ohakune Craters, Ruapehu, New Zealand: a complex interaction between external water and rising basaltic magma: Journal of Volcanology and Geothermal Research, v. 21, p. 207–231.

Houghton, B.F., Latter, J.H., and Hackett, W.R., 1987, Volcanic hazard assessment for Ruapehu composite volcano, Taupo Volcanic Zone, New Zealand: Bulletin of Volcanology, v. 49, p. 737–751.

Ionov, D.A., Harmon, R.S., France-Lanord, C., Greenwood, B., and Ashchepkov, I.V., 1994, Oxygen isotope composition of garnet and spinel peridotites in the continental mantle: evidence from the Vitim xenoliths suite, southern Siberia: Geochimica et Cosmochimica Acta, v. 58, p. 1463–1470.

Ishikawa, H., Ohba, T., Fujimaki, H., 2007, Sr isotope diversity of hot spring and volcanic lake waters from Zao volcano, Japan: Journal of Volcanology and Geothermal Research, v. 166, p. 7–16.

James, D.E., 1981, The combined use of oxygen and radiogenic isotopes as indicators of crustal contamination: Annual Review Earth Sciences, v. 9, p. 311–344.

Kalamarides, R.I., 1986, High temperature oxygen isotope fractionation among the phases of Kiglapait intrusion, Labrador, Canada: Chemical Geology, v. 58, p. 303–310.

Kay, R.W, 1979, Aleutian magnesian andesites: melts from subducted Pacific ocean crust: Journal Volcanology and Geothermal Research, v. 4, p. 117–132.

Kelemen, P.B., 1995, Genesis of high Mg# andesites and the continental crust: Contributions to Mineralogy and Petrology, v. 120, p. 1 –19.

Kelemen, P.B., Hart, S.R., and Bernstein, S., 1998, Silica enrichment in the continental upper mantle via melt/rock reaction: Earth and Planetary Science Letters, v. 164, p. 387–406.

Knesel, K.M., and Davidson, J.P., 1999, Sr isotope systematics during melt generation by intrusion of basalt into continental crust: Contributions to Mineralogy and Petrology, v. 136, p. 285–295.

Le Maitre, R., Bateman, P., Dudek, A., Keller, J., Lameyre, J., Le Bas, M., Sabine, P., Schmid, R., Sorensen, H., Streckeisen, A., Woolley, A., and Zanettin, B., 1989, A classification of igneous rocks and glossary of terms: Recommendations of the International Union of Geological Sciences Subcommission on the Systematics of igneous rocks, Blackwell, Oxford.

Levander, A., Lenardic, A., and Karlstrom, K, 2006, Structure of the continental lithosphere, in: Brown, M., Rushmer, T. (Eds.), Evolution and Differentiation of the Continental Crust: Cambridge University Press, pp. 21–66.

Macpherson, C.G., and Mattey, D.P., 1998, Oxygen isotope variations in Lau Basin lavas: Chemical Geology, v. 144, p. 177–194.

Macpherson, C.G., Gamble, J.A., and Mattey, D.P., 1998, Oxygen isotope geochemistry of an oceanic to continental arc transition, Kermadec–Hikurangi margin, SW Pacific: Earth and Planetary Science Letters, v. 160, p. 609–621.

Macpherson, C.G., Hilton, D.R., Mattey, D.P., and Sinton, J.M., 2000, Evidence for an ^{18}O-depleted mantle plume from contrasting $^{18}O/^{16}O$ ratios of back-arc lavas from the Manus Basin and Mariana Trough: Earth and Planetary Science Letters, v. 176, p. 171–183.

Malpas, J, Sporli, K.B., Black, P.M., and Smith, I.E.M., 1992, Northland ophiolite, New Zealand, and implications for plate-tectonic evolution of the southwest Pacific: Geology, v. 20, p. 149–153.

Malahoff, A., Feden, R.H., and Fleming H.S., 1982, Magnetic anomalies and tecotnic fabric of marginal basins north of New Zealand: Journal of Geophysical Research, v. 87, p. 4109–4125.

Mattey, D., Lowry, D., and Macpherson, C., 1994, Oxygen isotope composition of mantle peridotite: Earth and Planetary Science Letter, v. 128, p. 231–241.

McCulloch, M.T., and Gamble, J.A., 1991, Geochemical and geodynamical constraints on subduction zone magmatism: Earth and Planetary Science Letters, v. 102, p. 358–374.

McCulloch, M.T., Kyser, T.K., Woodhead, J.D., and Kinsley, L., 1994, Pb-Sr-Nd-O isotopic constraints on the origin of rhyolites from the Taupo Volcanic Zone of New Zealand: evidence for assimilation followed by fractionation from basalt: Contributions to Mineralogy and Petrology, v. 115, p. 303–312.

Meisel, T., Walker, R.J., Irving, A.J., and Lorand, J.-P., 2001, Osmium isotopic compositions of mantle xenoliths: a global perspective: Geochimica et Cosmochimica Acta. v. 65, p. 1311-1323.

Montel, J.M., and Vielzeuf, D., 1997, Partial melting of metagreywackes, Part II. Compositions of minerals and melts: Contribution to Mineralogy and Petrology, v. 128, p. 176–196.

Nakagawa, M., Wada, K., and Wood, P.C., 2002, Mixed magmas, mush chambers and eruption triggers: evidence from zoned clinopyroxene phenocrysts in andesitic scoria from the 1995 eruptions of Ruapehu volcano, New Zealand: Journal of Petrology, v. 43, p. 2279–2303.

Newton, R.C., 1989, Metamorphic Fluids in the Deep Crust: Annual Reviews in Earth and Planetary Sciences, v. 17, p. 385–412.

Nowell, G.M., Kempton, P.D., Noble, S.R., Fitton, J.G., Saunders, A.D., Mahoney, J.J., and Taylor, R.N., 1998, High precision Hf isotope measurements of MORB and OIB by thermal ionisation mass spectrometry: Insights into the depleted mantle: Chemical Geology, v. 149, p. 211–233.

Nowell, G.M., and Parrish, R.R., 2002, Simultaneous acquisition of isotope compositions and parent/daughter ratios by non-isotope dilution solution-mode Plasma ionisation Multi-collector Mass Spectrometry (PIMMS): Plasma Source Mass Spectrometry The New Millenium, p. 298-310.

Nowell, G.M., Pearson, D.G., Ottley, C.J., Schweiters, J. and Dowall, D., 2003, Long-term performance characteristics of a plasma ionisation multi-collector mass spectrometer (PIMMS): the ThermoFinnigan Neptune. in: Holland, J.G., Tanner S.D. (Eds.) Plasma Source Mass Spectrometry. Special Publication, Royal Society of Chemistry, Cambridge, p. 307–320.

O'Hara, M.J., 1995, Trace element geochemical effects of integrated melt extraction and shaped melting regimes: Journal of Petrology, v. 34, p. 1111–1132.

Ottley, C.J., Pearson, D.G., and Irvine, G.J., 2003, A Routine Method for the Dissolution of Geological Samples for the Analysis of REE and Trace Elements via ICP-MS, in: Holland, J.G., Tanner S.D. (Eds.) Plasma Source Mass Spectrometry: Applications and Emerging Technologies. The Royal Society of Chemistry, Cambridge, pp. 221–230.

Patino-Douce, A.E., and Johnston, A.D., 1991, Phase equilibria and melt productivity in the pelitic system: implications for the origin of peraluminous granitoids and aluminous granulites, Contributions to Mineralogy and Petrology, v. 107, p. 202–218.

Patino-Douce, A.E., and Beard, J.S., 1995, Dehydration-melting of biotite gneiss and quartz amphibolite from 3 to 15 kbar: Journal of Petrology, v. 36, p. 707–738.

Pearson, D.G., and Nowell, G.M., 2005, Accuracy and precision in plasma ionisation multi-collector mass spectrometry: Constraints from neodymium and hafnium isotope measurements: Plasma Source Mass Spectrometry, Current Trends and Future Developments, p. 284–314.

Peccerillo, R., and Taylor, S.R., 1976, Geocehmistry of Eocene calc-alkaline volcanic rocks from the Kastamonu area, northern Turkey: Contributions to Mineralogy and Petrology, v. 58, p. 63–81.

Pichavant, M., Mysen, B. O., and Macdonald, R., 2002, Source and H_2O content of high-MgO magmas in island arc settings: an experimental study of a primitive calc-alkaline basalt from St. Vincent, Lesser Antilles arc: Geochimica et Cosmochimica Acta, v. 66, p. 2193–2209.

Potts, P.J., Tindle, A.G., and Webb, P.C., 1992, Geochemical Reference Material Compositions: Rocks, Minerals, Sediments, Soils, Carbonates, Refractories and Ores Used in Research and Industry. Caithness: Whittles Publishing.

Price, R.C., Waight, T.E., Chapman, J.R., Beyer, E.E., Smith, I.E.M., and Stewart, R.B., 1997, The geochemical evolution of arc magmas in a continental setting: Evidence from detailed chemo-stratigraphy at Ruapehu, New Zealand: State of the Arc '97, Island Arc 31 Magma Genesis Workshop, Adelaide, Australia, 1997. Geological Society of Australia Abstracts, v. 45, p. 115–117.

Price, R.C., Stewart, R.B., Woodhead, J.D., and Smith, I.E.M., 1999, Petrogenesis of high-K arc magmas: Evidence from Egmont Volcano, North Island, New Zealand: Journal of Petrology, v. 40, p. 167–197.

Price, R.C., Gamble, J.A., and Hobden, B.J., 2000, Guidebook for field excursions on Ruapehu and Tongariro Volcanoes: State of the Arc 2000, pp. 14.

Price, R.C., Gamble, J.A, Eggins, S.E., Smith, I.E.M, Maas, R., and Waight, T.E., 2001, Andesitic versus rhyolitic magmatic processes and magma chambers in the Taupo Volcanic Zone of North Island New Zealand: Evidence from glass matrix and inclusion data: Penrose conference of the Geological Society of America, Mammoth California, June 2001.

Price, R.C., Gamble, J.A., Smith, I.E.M., Stewart, R.B., Eggins, S., and Wright, I.C., 2005, An integrated model for the temporal evolution of andesites and rhyolites and crustal development in New Zealand's North Island: Journal of Volcanology and Geothermal Research, v. 140, p. 1–24.

Reagan, M.K., Sims, K.W.W., Erich, J., Thomas, R.B., Cheng, H., Edwards, R.L., Layne, G., and Ball, L., 2003, Time-scales of differentiation from mafic parents to rhyolite in North American continental arcs: Journal of Petrology, v. 44, p. 1703–1726.

Reyners, M., Eberhart-Phillips, D., Stuart, G., and Nishimura, Y., 2006, Imaging subduction from the trench to 300 km depth beneath the central North Island, New Zealand, with Vp and Vp/Vs: Geophysical Journal International, v. 165, p. 565–583.

Reyners, M., Eberhart-Philips, D., and Stuart, G., 2007, The role of fluids in lower-crustal earthquakes near continental rifts: Nature, v. 446, p. 1075–1078.

Roeder, P.L., and Emslie, R.F., 1970, Olivine-liquid equilibrium: Contributions to Mineralogy and Petrology, v. 29, p. 275–289.

Royse, K., Kempton, P.D., and Darbyshire, D.P.F., 1998, Procedure for the analysis for rubidium-strontium and samarium-neodymium isotopes at the NERC Isotope Geosciences Laboratory: NERC Isotope Geosciences Laboratory Report Series, v. 121.

Ringwood, A.E., 1974, The petrological evolution of island arc systems: Journal of the Geological Society, London, v. 130, p. 183–204.

Rogers J.J.W., and Adams J.A.S., 1978, Th: Abundances in common igneous rocks. in: Wedepohl, K.H., (Eds) Handbook of Geochemistry, Springer-Verlag, Berlin, p. 90-E-1–90-E-12.

Rollinson, H.R., 1993, Using Geochemical Data: Evaluation, Presentation, Interpretation, first ed. Prentice Hall, UK.

Rollinson, H.R., 2007, Early Earth Systems: a geochemical approach. Blackwell Publishing, Oxford, UK.

Rowlands, D.P., White, R.S., and Haines, A.J., 2005, Seismic tomography of the Tongariro Volcanic Centre, New Zealand: Geophysical Journal International, v. 163, p. 1180–1194.

Rudnick, R.L. 1992, Restites, Eu anomalies, and the lower continental crust: Geochimica et Cosmochimica Acta, v. 56, p. 963–970.

Rudnick, R.L., 1995, Making continental crust: Nature, v. 378, p. 571–578.

Rudnick R.L., McLennan S.M., and Taylor S.R., 1985, Large ion lithophile elements in rocks from high-pressure granulite facies terrains: Geochimica et Cosmochimica Acta, v. 49, p. 1645–1655.

Rudnick, R.L., and Fountain, D.M., 1995, Nature and composition of the continental crust: A lower crustal perspective: Reviews of Geophysics, v. 33, p. 267–309.

Rudnick, R.L., and Gao, S., 2003, The composition of the continental crust, in: Treatise on Geochemistry, v. 3, ed. H.D. Holland and K.K. Turekian, Oxford: Elsevier, pp. 1-64.

Rushmer, T., 1991, Partial melting of two amphibolites: contrasting experimental results under fluid absent conditions: Contributions of Mineralogy and Petrology, v. 107, p. 41–59.

Saal, A.E., Runick, R.L, Ravizza, G.E., and Hart, S.R. 1998, Re-Os isotope evidence for the composition, formation and age of the lower continental crust: Nature, v. 393, p. 58–61.

Sawyer, E.W., 2001, Melt segregation in the continental crust: distribution and movement of melt in anatectic rocks: Journal of Metamorphic Geology, v. 18, p. 291–309.

Schiano, P., Birck, J.-L., Allegre, C.J., 1997, Osmium-strontium-neodymium-lead isotopic covariations in mid-ocean ridgebasalt glasses and the heterogeneity of the upper mantle: Earth and Planetary Science Letters, v. 150, p. 363–381.

Schneider, J., 1995, Geology and geochemistry of volcanic rocks of the upper Whakapapaiti valley, Mt. Ruapehu, North Island, New Zealand: Unpublished BSc (Honours) thesis, La Trobe University, Melbourne.

Schnetger, B., 1994, Partial melting during the evolution of the amphibolite- to granulite-facies gneisses of the Ivrea Zone, northern Italy: Chemical Geology, v. 113, p. 71-101.

Smith, I.E.M., and Price, R.C., 2006, The Tonga–Kermadec arc and Havre–Lau back-arc system: Their role in the development of tectonic and magmatic models for the western Pacific: Journal of Volcanology and Geothermal Research, v. 156, p. 315–331.

Solar, G.S., and Brown, M., 2001, Petrogenesis of migmatites in Maine, USA: possible source of peraluminous leucogranite in plutons: Journal of Petrology, v. 42, p. 789-823.

Spooner, E.T.C., and Gale, N.H., 1982, Pb isotopic composition of ophiolitic volcanogenic sulphide deposits, Troodos Complex, Cyprus: Nature, v. 296, p. 239−242.

Stakes, D.S., and O'Neil, J.R., 1982, Mineralogy and stable isotope geochemistry of hydrothermally altered oceanic rocks: Earth and Planetary Science Letters, v. 57, p. 285−304.

Stratford, W. R., and Stern, T. A., 2004, Strong seismic reflections and melts in the mantle of a continental back-arc basin: Geophysical Research Letters, v. 31, L06622, doi:10.1029/2003GL019232.

Stratford, W.R., and Stern, T.A., 2006, Crust and upper mantle structure of continental back arc: central North Island, New Zealand: Geophysical Journal International, v. 166(1), p. 469–484.

Stern, T.A., 1987, Asymmetric back-arc spreading, heat flux and structure beneath the Central Volcanic Region of New Zealand: Earth and Planetary Science Letters, v. 85, p. 265–267.

Stern, T.A., Stratford, W.R., and Salmon, M.L., 2006, Subduction Evolution and Mantle Dynamics at a Continental Margin: Central North Island, New Zealand: Reviews of Geophysics, v. 44(4), RG4002, doi:10.1029/2005RG000171.

Steven, G., and Clemens, J.D., 1993, Fluid-absent melting and the roles of fluids in the lithosphere: a slanted summary?: Chemical Geology, v. 108, p. 1-17.

Stevens, G., Clemens, J.D., and Droop, G.T.R., 1997, Melt production during granulite-facies anatexis: experimental data from “primitive” metasedimentary protoliths: Contributions to Mineralogy and Petrology, v. 128, p. 352–370.

Stormer, J.C., Jr., 1973, Calcium zoning in olivine and its relationship to silica activity and pressure: Geochimica et Cosmochimica Acta, v. 37, p. 1815–1821.

Stormer, J.C., Jr., and Nicholls, J., 1978, XLFRAC; a program for the interactive testing of magmatic differentiation models: Computers and Geosciences, v. 4(2), p. 143–159.

Streck, M.J., Leeman, W.P., and Chesley, J., 2007, High-magnesian andesite from Mount Shasta: A product of magma mixing and contamination, not a primitive mantle melt: Geology, v. 35, p. 351–354.

Sun, S.S., and McDonough, W.M., 1989, Chemical and isotopic systematics of oceanic basalts: implications for mantle composition and processes, in: Saunders, A.D. and Norry, M.J., (eds) Magmatism in the ocean basins: Geological Society of London Special Publications, v. 42, p. 313-345.

Sutton, A.N., Blake, S., and Wilson, C.J.N., 1995, An outline geochemistry of rhyolite eruptives from Taupo volcanic centre, New Zealand: Journal of Volcanology and Geothermal Research, v. 68, p. 153–175.

Tatsumi, Y., 1982, Origin of high-magnesian andesites in the Setouchi Volcanic Belt, Southwest Japan, 2. Melting phase-relations at high pressures: Earth and Planetary Science Letters, v. 60, p. 305–317.

Tatsumi, Y., and Ishizaka, K., 1981, Existence of andesitic primary magma: an example from Southwest Japan: Earth and Planetary Science Letters, v. 53, p. 124–130.

Taylor, S.R., 1967, The origin and growth of continents: Tectonophysics, v. 4, p. 17-34.

Thirlwall, M., 1991, Long-term reproducibility of multicollector Sr and Nd isotope ratio analysis: Chemical Geology, v. 94, p. 85–104.

Topping, W.W., 1973, Tephrostratigraphy and chronology of late Quaternary eruptives from the Tongariro Volcanic Centre: New Zealand Journal of Geology and Geophysics, v. 16, p. 397–423.

Ulmer, P., 2001, Partial melting in the mantle wedge - the role of H_2O in the genesis of mantle-derived 'arc-related' magmas: Physics of the Earth and Planetary Interiors, v. 127, p. 215–232.

Valente, D.L., 1995, Geology and geochemistry of volcanic rocks of the lower Pinnacle Ridge and the upper Whakapapanui valley, Ruapehu, North Island, New Zealand: Unpublished BSc (Honours) thesis, La Trobe University, Melbourne.

Vidal, Ph. & Clauer, N., 1981, Pb and Sr isotopic systematics of some basalts and sulfides from the East Pacific Rise at 21°N (project RITA): Earth and Planetary Science Letters, v. 55, p. 237−246.

Vielzeuf, D., and Holloway, J.R., 1988, Experimental determination of the fluid-absent melting relations in the pelitic system. Consequences for crustal differentiation: Contributions to Mineralogy and Petrology, v. 98, p. 257–276.

Vielzeuf, D., and Montel, J.M., 1994, Partial melting of metagreywackes. 1. Fluid-absent experiments and phase relationships: Contributions to Mineralogy and Petrology, v. 117, p. 375–393.

Vigneresse, J.L., Barbey, P., and Cuney, M., 1996, Rheological transitions during partial melting and crystallization with application to felsic magma segregation and transfer: Journal of Petrology, v. 37, p. 1579-1600.

Villamor, P., and Berryman, K.R., 2001, A late Quaternary extension rate in the Taupo Volcanic Zone, New Zealand, derived from fault slip data: New Zealand Journal of Geology and Geophysics, v. 44, p. 243–269.

Villamor, P., and Berryman, K.R., 2006a, Late Quaternary geometry and kinematics of faults at the southern termination of the Taupo Volcanic Zone, New Zealand: New Zealand Journal of Geology and Geophysics, v. 49, p. 1–21.

Villamor, P., and Berryman, K.R., 2006b, Evolution of the southern termination of the Taupo Rift, New Zealand: New Zealand Journal of Geology and Geophysics, v. 49, p. 23–37.

Villamor, P., Van Dissen, R., Alloway, B.V., Palmer, A.S., and Litchfield, N., 2007, The Rangipo fault, Taupo Rift, New Zealand: An example of temporal slip-rate and single-event displacement variability in a volcanic environment: GSA Bulletin, v. 119, p. 529–547.

Vroon, P.Z., Lowry, D., van Bergen, M.J., Boyce, A.J., and Mattey, D.P., 2001, Oxygen isotope systematics of the Banda arc: low $\delta^{18}O$ despite involvement of subducted continental material in magma genesis: Geochimica et Cosmochimica Acta, v. 65, p. 589–609.

Waight, T.E., Price, R.C., Stewart, R.B., Smith, I.E.M., and Gamble, J.A., 1999, Stratigraphy and geochemistry of the Turoa area, with implications for andesite petrogenesis at Mt Ruapehu, Taupo Volcanic Zone, New Zealand: New Zealand Journal of Geology and Geophysics, v. 42, p. 513–532.

Wilson, C.J.N., Blake, S., Charlier, B.L.A., and Sutton, A.N., 2006, The 26.5 ka Oruanui Eruption, Taupo Volcano, New Zealand: Development, Characteristics and Evacuation of a Large Rhyolitic Magma Body: Journal of Petrology, v. 47, p. 35–69.

Wolf, M.B., and Wyllie, P.J., 1994, Dehydration-melting of amphibolite at 10 kbar - the effects of temperature and time: Contributions of Mineralogy and Petrology, v. 115, p. 369–383.

Woodhead, J.D. Hergt, J.M. Davidson, J.P. and Eggins, S.M., 2001, Hafnium isotope evidence for ‘conservative’ element mobility during subduction zone processes: Earth and Planetary Science Letters, v. 192, p. 331–346.

Workman, R.K., and Hart, S.R., 2005, Major and trace element composition of the depleted MORB mantle (DMM): Earth and Planetary Science Letters, v. 231, p. 53–72.

Zellmer, G.F., Sparks, R.S.J., Hawkesworth, C.J., and Wiedenbeck, M., 2003, Magma emplacement and remobilisation timescales beneath Montserrat: insights from Sr and Ba zonation in plagioclase phenocrysts: Journal of Petrology, v. 44, p. 1349–1374.

Zheng, Y.-F., 1993a, Calculation of oxygen isotope fractionation in anhydrous silicate minerals: Geochimica et Cosmochimica Acta, v. 57, p. 1079–1091.

Appendices

Appendices

Appendix A. Sample locations and petrography

Appendix B. Whole-rock major and trace element data

Appendix C. Whole-rock isotope data

Appendix D. Mineral data

Table A.1. Sample localities for Ruapehu lavas, satellite vents and basalts

Specimen	Grid reference	Map Sheet	Formation	Locality details	Province	Rock type	Source
W8	304159	T20	Whakapapa	Delta Corner Flow	Ruapehu	lava flow	-
WX9	301161	T20	Whakapapa	Delta Corner Flow	Ruapehu	lava flow	-
WX10	298161	S20	Whakapapa	Delta Corner Flow	Ruapehu	lava flow	-
WX18	30761565	T20	Whakapapa	Delta Corner Flow	Ruapehu	lava flow	-
WX19	30691552	T20	Whakapapa	Delta Corner Flow	Ruapehu	lava flow	-
WX22	30661379	T20	Whakapapa	Delta Corner Flow	Ruapehu	lava flow	-
WX20	29331536	S20	Whakapapa	National Downhill Flow	Ruapehu	lava flow	-
W26	28731493	S20	Whakapapa	National Downhill Flow	Ruapehu	lava flow	-
KR01	31301351	T20	Whakapapa	Knoll Ridge Flow	Ruapehu	lava flow	-
WX21	30501367	T20	Whakapapa	Knoll Ridge Flow	Ruapehu	lava flow	-
WX23	31031365	T20	Whakapapa	Knoll Ridge Flow	Ruapehu	lava flow	-
WX24	31171359	T20	Whakapapa	Knoll Ridge Flow	Ruapehu	lava flow	-
T6-75	298150	S20	Whakapapa	Knoll Ridge Flow	Ruapehu	lava flow	Valente (1995)[f]
WX30	28851565	S20	Whakapapa	Happy Valley Flow	Ruapehu	lava flow	-
WX11	296160	S20	Whakapapa	Happy Valley Flow	Ruapehu	lava flow	-
UT01	31581367	T20	Whakapapa	Upper Te Heuheu Flow	Ruapehu	lava flow	-
LT01	31521353	T20	Whakapapa	Lower Te Heuheu Flow	Ruapehu	lava flow	-
LT02	31501362	T20	Whakapapa	Lower Te Heuheu Flow	Ruapehu	lava flow	-
R96/10	298038	S20	Whakapapa	Rangataua flows- middle section. Flow 30m above the Mangaehuehu Hut	Ruapehu	lava flow	Price[a]
R96/11	297037	S20	Whakapapa	Rangataua flows- middle section. 150m SW of Mangaehuehu Hut. Overlain by 1m of soil and tephra.	Ruapehu	lava flow	Price[a]
R96/12	295040	S20	Whakapapa	Rangataua flows- middle section. 350m NW of Magaehuehu Hut. 25m N of Round Mountain Track.	Ruapehu	lava flow	Price[a]
R96/25	355184	T20	Whakapapa	Saddle Cone Flows. From easternmost breakout 200m S of the round the Mountain Track.	Ruapehu	lava flow	Price[a]
R96/26	348183	T20	Whakapapa	Saddle Cone Flows. On E edge of main flow 250m W of sample 25.	Ruapehu	lava flow	Price[a]
R96/27	344188	T20	Whakapapa	Saddle Cone Flows. On W edge of main flow. Above a significant stream and 150m S of the Round the Mountain Track.	Ruapehu	lava flow	Price[a]
W28	28241464	S20	Mangawhero	Whakapapaiti Flow	Ruapehu	lava flow	-
W29	27551469	S20	Mangawhero	Whakapapaiti Flow	Ruapehu	lava flow	-
T5-14	275136	S20	Mangawhero	Whakapapaiti Valley	Ruapehu	lava flow	Schneider (1995)[b]
T5-15	278134	S20	Mangawhero	Whakapapaiti Valley	Ruapehu	lava flow	Schneider (1995)[b]
R97/92a	341130	T20	Mangawhero	Whakapapaiti	Ruapehu	lava flow	Waight/Price[c]
R97/92b	341130	T20	Mangawhero	Whakapapaiti	Ruapehu	lava flow	Waight/Price[c]
TX9	27990742	S20	Mangawhero	Sunset Ridge	Ruapehu	lava flow	-
TX10	281073	S20	Mangawhero	Sunset Ridge	Ruapehu	lava flow	-
TX8	28400757	S20	Mangawhero	Turoa	Ruapehu	lava flow	-
TX13	278081	S20	Mangawhero	Sunset Ridge	Ruapehu	lava flow	-
TX1	286093	S20	Mangawhero	Mangaturuturu C	Ruapehu	lava flow	-
TX2	286093	S20	Mangawhero	Mangaturuturu C	Ruapehu	lava flow	-
TX3	285093	S20	Mangawhero	Mangaturuturu C	Ruapehu	lava flow	-
TX4	28430931	S20	Mangawhero	Mangaturuturu C	Ruapehu	lava flow	-
TX5	28410927	S20	Mangawhero	Mangaturuturu C	Ruapehu	lava flow	-
TX6	28370928	S20	Mangawhero	Mangaturuturu C	Ruapehu	lava flow	-
TX7	28370928	S20	Mangawhero	Mangaturuturu C	Ruapehu	lava flow	-
TX11	278081	S20	Mangawhero	Mangaturuturu B	Ruapehu	lava flow	-
TX12	279081	S20	Mangawhero	Mangaturuturu B	Ruapehu	lava flow	-
W27	28481451	S20	Mangawhero	Mangawhero	Ruapehu	lava flow	-
RB	334159	T20	Mangawhero	North side of Ruapehu - Steeply dipping flow SW of Saddle Cone at 1627m	Ruapehu	lava flow	Waight/Price[c]
R97/6	272090	S20	Mangawhero	Mangaturuturu-B	Ruapehu	lava flow	Waight/Price[c]
R97/10a	278092	S20	Mangawhero	Mangaturuturu-B	Ruapehu	lava flow	Waight/Price[c]
R97/13	281090	S20	Mangawhero	Mangaturuturu-D	Ruapehu	lava flow	Waight/Price[c]
R97/50	275092	S20	Mangawhero	Mangaturuturu-A	Ruapehu	lava flow	Price/Stewart[d]
R97/50b	275092	S20	Mangawhero	Must be near Mangaturuturu-A	Ruapehu	lava flow	Price/Stewart[d]
R/04-3	335156	T20	Mangawhero	North side of Ruapehu - At 1742m on top of ridge due S of Saddle Cone	Ruapehu	lava flow	Price/Stewart[d]

Table A.1. Sample localities for Ruapehu lavas, satellite vents and basalts continued

Specimen	Grid reference	Map Sheet	Formation	Locality details	Province	Rock type	Source
R96/7	347073	T20	Waihianoa	Waihianoa section - topmost flow in section 160-115ka	Ruapehu	lava flow	Price[a]
R96/8	346070	T20	Waihianoa	Waihianoa section - from E end of lowermost bluff. 160-115ka	Ruapehu	lava flow	Price[a]
R96/18	348094	T20	Waihianoa	Whangaehu Section. 10-15m thick flow narrowing to 3m at site sampled. Overlies 17. ~130ka	Ruapehu	lava flow	Price[a]
R96/19	347095	T20	Waihianoa	Whangaehu Section. 150m upstream from 15 at base of section. Underlies 15 but not conformable ~130ka	Ruapehu	lava flow	Price[a]
R96/22	346095	T20	Waihianoa	Whangaehu Section. At base of section underlying flow sampled 21. 130ka	Ruapehu	lava flow	Price[a]
W9-70	349108	T20	Waihianoa	Above Eloise's area onto Mangatoetoenui Glacier	Ruapehu	lava flow	Beyer (1996)[e]
W9-71	348108	T20	Waihianoa	Above Eloise's area onto Mangatoetoenui Glacier	Ruapehu	lava flow	Beyer (1996)[e]
WX3	309157	T20	Te Herenga	Te Herenga Ridge	Ruapehu	lava flow	-
W25	284151	S20	Te Herenga	Te Herenga outcrop round the mountain track	Ruapehu	lava flow	-
WX2	311155	T20	Te Herenga	Te Herenga Ridge	Ruapehu	lava flow	-
W4	308158	T20	Te Herenga	Te Herenga Ridge	Ruapehu	lava flow	-
W5	308161	T20	Te Herenga	Te Herenga Ridge	Ruapehu	lava flow	-
W6	307163	T20	Te Herenga	Te Herenga Ridge	Ruapehu	lava flow	-
W7	304162	T20	Te Herenga	Te Herenga Ridge	Ruapehu	lava flow	-
W13	30901578	T20	Te Herenga	Te Herenga Ridge	Ruapehu	lava flow	-
W14	30891578	T20	Te Herenga	Te Herenga Ridge	Ruapehu	lava flow	-
WX15	30841578	T20	Te Herenga	Te Herenga Ridge	Ruapehu	lava flow	-
W16	30801576	T20	Te Herenga	Te Herenga Ridge	Ruapehu	lava flow	-
W17	30761579	T20	Te Herenga	Te Herenga Ridge	Ruapehu	lava flow	-
T6-11	308158	T20	Te Herenga	Te Herenga Ridge/ Iwakau/ Whakapapanui valley	Ruapehu	lava flow	Valente (1995)[f]
T6-18	308161	T20	Te Herenga	Te Herenga Ridge/ Iwakau/ Whakapapanui valley	Ruapehu	lava flow	Valente (1995)[f]
T6-21	304161	T20	Te Herenga	Te Herenga Ridge/ Iwakau/ Whakapapanui valley	Ruapehu	lava flow	Valente (1995)[f]
T6-22	304161	T20	Te Herenga	Te Herenga Ridge/ Iwakau/ Whakapapanui valley	Ruapehu	lava flow	Valente (1995)[f]
T6-25	305163	T20	Te Herenga	Te Herenga Ridge/ Iwakau/ Whakapapanui valley	Ruapehu	lava flow	Valente (1995)[f]
KB	834958	U17	-	underlying ignimbrite at road cutting	Kakuki Cone	scoria	-
WB	17439	T19	-	Waimarino	Waimarino	lava flow	-
P01	297301	S20	-	Mahuia rapids	Pukeonake	lava flow	-
P02	268256	S20	-	Mahuia rapids	Pukeonake	lava flow	-
OQ	174976	S20	-	Ohakune Quarry	Ohakune Quarry	scoria	-

Price[a] - R. C. Price unpublished data
Schneider (1995)[b] - unpublished BSc (Honours) thesis, La Trobe University, Melbourne
Waight/Price[c] - T. E. Waight and R. C. Price unpublished data
Price/Stewart[d] - R. C. Price and R. B. Stewart unpublished data
Beyer (1996)[e] - unpublished BSc (Honours) thesis, La Trobe University, Melbourne
Valente (1995)[f] - unpublished BSc (Honours) thesis, La Trobe University, Melbourne

Table A.2. Modal proportions of mineral phases

	% Vol	WX9	WX10	WX18	WX19	WX23	WX30	WX11	LT02	R96/10	R96/12	R96/26
Whakapapa Fm	plag	18.1	18.3	25.6	24.2	14.3	19.5	17.3	23.4	16.3	16.1	22.7
	cpx	2.9	2.3	4.2	3.8	2.1	4.5	3.3	3.5	4.1	1.7	2.2
	opx	7.5	5.2	5.6	6.2	6.3	6.1	5.2	7.8	8.7	4.7	6.4
	olv	-	-	-	-	-	-	-	-	-	-	-
	oxid	0.1	0.2	0.4	0.7	0.4	0.5	0.8	0.9	0.6	0.9	0.6
	g/m	71.4	74.0	64.2	65.1	76.9	69.4	73.4	64.4	70.3	76.6	68.1
	phen	28.6	26.0	35.8	34.9	23.1	30.6	26.6	35.6	29.7	23.4	31.9

	% Vol	T5-14	R97/92b	TX13	TX2	TX4	TX6	R97/10a	RB
Mangawhero Fm	plag	18	15	23	15	27	22.5	8.2	25.4
	cpx	3.8	1.9	6	2.1	3.6	2.3	0.2	8.70
	opx	3	4	4	5	5.3	6.9	1.8	3.50
	olv	-	-	-	-	-	-	-	7.2
	oxid	0.4	0.1	0.7	0.1	0.5	0.1	0.6	0.4
	g/m	75	79	66	78	63.6	68.2	89.2	54.8
	phen	25.2	21.1	34.3	21.6	36.4	31.8	10.8	45.2

	% Vol	R96/8	R96/19	W9-71
Waihianoa Fm	plag	30	15	10
	cpx	4	6	4
	opx	4	7	3
	olv	-	-	-
	oxid	0.70	0.30	0.10
	g/m	62	72	84
	phen	38.3	27.9	16.0

Modal proportions based on 1000 points per sample.
plag, plagioclase; cpx, clinopyroxene; opx, orthopyroxene; olv, olivine; oxid, Fe-Ti oxide; g/m, groundmass; phen, total phenocrysts

Table A.2. Modal proportions of mineral phases continued

	% Vol	WX2	W4	W6	W7	W13	W14	WX15	W16	W17	T6-11	T6-18	T6-21	T6-22	T6-25
Te Herenga Fm	plag	27.40	30.10	31.80	33.40	29.90	33.8	33.70	28.60	32.40	34.10	33.6	26.8	29.6	32.3
	cpx	8.10	5.40	7.10	7.20	3.40	5.5	7.50	6.50	4.80	7.10	6.1	5.9	5.3	4.2
	opx	4.20	9.80	11.20	6.90	6.00	7.9	6.40	7.10	8.90	5.30	7.2	5.1	7.4	6.1
	olv	-	-	-	-	-	-	-	-	-	-	-	-	-	-
	oxid	0.60	1.20	1.30	1.80	1.70	1.6	0.70	1.50	0.80	0.60	0.4	1.6	0.7	1.1
	g/m	59.70	53.50	48.60	50.70	59.00	51.2	51.70	56.30	53.10	52.90	52.7	60.6	57	56.3
	phen	40.30	46.50	51.40	49.30	41.00	48.8	48.30	43.70	46.90	47.10	47.3	39.4	43	43.7

	% Vol	WB	P01	OQ
Satellite vents and basalts	plag	-	6.2	-
	cpx	6.90	10.20	7.50
	opx	-	6.90	1.20
	olv	15.8	5.1	2.2
	oxid	-	0.1	0.6
	g/m	77.3	71.5	88.5
	phen	22.7	28.5	11.5

Modal proportions based on 1000 points per sample.
plag, plagioclase; cpx, clinopyroxene; opx, orthopyroxene; olv, olivine; oxid, Fe-Ti oxide; g/m, groundmass; phen, total phenocrysts

Table A.3. Description of crustal xenoliths (Graham, 1985) analysed for trace elements and isotopes

Meta-sedimentary xenoliths	
Quartz-rich	
17492	Green/grey/white saccharoidal gneiss. Assemblage 1: quartz + anorthite + ferrosalite + sphene. Assemblage 2: andesine + orthopyroxene + almandine garnet + glass + ilmenite.
17485	Brown/white contorted banded gneiss. Assemblage 1: quartz + anorthite + salite + ilmenite + hematite + sphene. Assemblage 2: andesine + biotite + almandine garnet.
Feldspar and spinel rich	
17425	Grey gneiss. Finely segregated and foliated. Assemblage 1; oligoclase + sanidine + sillimanite. Assemblage 2: biotite + aluminous hypersthene + pleonaste + ilmenite.
17443	Grey, banded hornfels with 1 mm mafic segregations. Labradorite + hypersthene + pleonaste + titanomagnetite.
17423	Grey/purple gneiss. Contorted bands and lenticular masses of plagioclase + biotite + pleonaste + minor titanomagnetite + ilmenite.
17457	Grey, fine grained, heterogeneous spinel-rich schist. Bytownite-anorthite + pleonaste + hypersthene + minor biotite + olivine.
Buchitic	
17465	Grey pumice with contorted white banding. White segregations = quartz + hypersthene + silica-rich glass; dark segregations = cordierite + silica-poor glass. Also pleonaste + ilmenite + pyrite.
17469	Light grey banded pumice. Composition of banding similar to 17465.
17474	Light grey, mostly homogeneous pumice. Quartz + cordierite + silica-rich glass + pleonaste.
Meta-igneous xenoliths	
17430	Coarse grained pyroxene hornfels with strong foliation. Labradorite + hypersthene + titanomagnetite + ilmenite + apatite + glass.
17411	Coarse grained pyroxene hornfels. Plagioclase + coarsely poikiloblastic pyroxene.
17441	Coarse grained pyroxene hornfels. Labradorite + coarsely poikiloblastic hypersthene + augite + ilmenite.
17442	Coarse grained pyroxene hornfels. Bytownite + coarsely poikiloblastic bronzite + augite + chrome spinel + ilmenite. Plagioclase has a relict trachytic texture.
17449	Medium grained pyroxene hornfels. Andesine-labradorite + poikiloblastic hypersthene + augite + ilmenite + minor apatite + quartz.
17450	Grey, fine grained hornfels with relict porphyritic texture. Labradorite-anorthite + hypersthene + ilmenite.
17433	Grey, homogeneous fine-grained hornfels. Bytownite-anorthite + hypersthene + augite + ilmenite + quartz.
17432	Brown, poorly foliated fine-grained hornfels. Labradorite + hypersthene + quartz.

Table B.1. Major and trace element data for Whakapapa Fm lavas

Specimen	W8	WX9	WX10	WX18	WX19	WX22	WX20	W26
SiO_2	58.56	57.36	57.23	57.74	59.06	58.99	59.03	60.08
Al_2O_3	16.50	16.46	16.63	16.64	16.68	16.62	16.57	16.37
$Fe_2O_{3\,tot}$	6.87	7.60	7.61	7.61	6.99	6.92	6.94	6.54
MgO	4.42	5.10	5.19	5.10	4.49	4.49	4.50	4.15
CaO	6.84	7.55	7.54	7.57	6.92	6.92	6.93	6.39
Na_2O	3.26	3.13	3.13	3.18	3.32	3.35	3.31	3.39
K_2O	1.61	1.40	1.40	1.41	1.62	1.62	1.61	1.81
TiO_2	0.66	0.67	0.67	0.67	0.67	0.66	0.67	0.74
MnO	0.11	0.13	0.12	0.12	0.11	0.11	0.11	0.10
P_2O_5	0.13	0.13	0.13	0.13	0.13	0.13	0.13	0.15
Total	98.95	99.52	99.65	100.17	99.99	99.80	99.80	99.72
LOI	0.08	-0.03	0.20	-0.21	0.02	0.03	-0.09	0.01
Mg#	60	61	61	61	60	60	60	59
Sc	20	27	27	27	20	23	23	17
V	169	200	202	203	172	182	184	157
Cr	73.4	75.5	81.4	73.5	71.7	76.7	77.9	85.0
Co	22	28	29	28	23	25	24	21
Ni	38.6	47.2	48.8	47.4	39.5	40.2	42.6	44.2
Cu	46	51	59	35	41	44	45	35
Zn	60	66	65	65	61	62	63	58
Ga	17	18	18	18	17	18	17	16
Rb	56.2	49.0	48.8	48.5	56.1	60.1	58.6	65.5
Sr	266	298	297	304	269	287	266	259
Y	19	19	19	18	18	19	19	21
Zr	113	99	97	99	112	117	117	129
Nb	4.70	3.81	3.74	3.83	4.44	4.54	4.58	5.15
Cs	3.77	2.91	2.83	1.96	3.61	3.55	3.68	2.42
Ba	365	328	336	338	356	358	361	384
La	12.4	10.5	10.6	9.9	12.0	11.9	12.3	15.5
Ce	26.5	22.7	22.8	21.7	25.8	25.4	26.2	31.1
Pr	3.52	3.06	3.09	2.97	3.38	3.40	3.43	4.23
Nd	14.7	13.0	13.0	12.3	14.1	14.0	14.2	17.3
Sm	3.26	3.01	3.05	2.89	3.16	3.12	3.20	3.73
Eu	0.88	0.84	0.86	0.85	0.85	0.84	0.83	0.90
Gd	3.42	3.26	3.28	3.21	3.30	3.27	3.29	3.92
Tb	0.54	0.52	0.53	0.50	0.53	0.53	0.53	0.61
Dy	3.19	3.09	3.09	3.01	3.12	3.13	3.11	3.50
Ho	0.68	0.65	0.63	0.64	0.66	0.65	0.66	0.73
Er	1.83	1.76	1.77	1.71	1.80	1.80	1.82	1.99
Tm	0.30	0.28	0.29	0.28	0.29	0.29	0.29	0.32
Yb	1.94	1.83	1.87	1.82	1.88	1.86	1.87	2.06
Lu	0.32	0.30	0.30	0.29	0.30	0.31	0.31	0.33
Hf	3.23	2.73	2.72	2.76	3.14	3.20	3.18	3.68
Ta	0.35	0.29	0.29	0.30	0.35	0.36	0.36	0.42
Pb (total)	9.7	8.4	8.2	7.6	9.9	9.7	9.7	10.5
Th	5.55	4.45	4.44	4.46	5.43	5.46	5.50	6.39
U	1.49	1.16	1.18	1.19	1.46	1.46	1.47	1.69

Superscript font on specimens name refers to external data source listed in Table. A1

Table B.1. Major and trace element data for Whakapapa Fm lavas continued

Specimen	KR01	WX21	WX23	WX24	WX30	WX11	UT01	LT01
SiO_2	58.88	58.88	57.35	59.05	58.91	59.00	56.26	60.90
Al_2O_3	16.55	16.53	16.70	16.56	16.51	16.50	17.12	16.28
$Fe_2O_{3\,tot}$	6.96	6.94	7.59	7.01	6.98	6.96	8.34	6.43
MgO	4.53	4.48	4.94	4.54	4.57	4.53	4.75	4.02
CaO	6.97	6.92	7.58	6.95	6.94	6.93	8.11	6.33
Na_2O	3.28	3.30	3.16	3.29	3.30	3.32	3.04	3.33
K_2O	1.61	1.62	1.41	1.63	1.61	1.62	1.24	1.79
TiO_2	0.66	0.66	0.69	0.67	0.66	0.66	0.79	0.62
MnO	0.11	0.11	0.12	0.11	0.11	0.11	0.13	0.11
P_2O_5	0.13	0.13	0.13	0.13	0.13	0.13	0.13	0.13
Total	99.68	99.57	99.67	99.94	99.72	99.76	99.91	99.93
LOI	0.12	0.05	-0.21	-0.07	0.04	-0.05	-0.03	0.13
Mg#	60	60	60	60	60	60	57	59
Sc	25	23	26	23	23	23	29	20
V	202	184	202	183	185	191	243	159
Cr	87.6	78.6	73.4	75.7	80.0	80.4	36.1	65.7
Co	27	24	28	25	25	25	26	21
Ni	46.7	43.2	45.6	42.7	43.0	43.3	11.8	34.1
Cu	49	43	52	41	48	50	28	40
Zn	69	64	64	63	64	64	71	61
Ga	19	17	17	17	17	18	18	16
Rb	64.0	58.9	46.9	59.0	59.1	61.3	41.5	64.4
Sr	292	267	297	264	268	280	270	238
Y	21	19	19	19	20	20	21	19
Zr	127	117	100	115	116	120	100	116
Nb	4.88	4.48	3.93	4.48	4.54	4.69	4.18	4.85
Cs	3.99	3.68	1.73	3.65	3.71	3.76	1.14	4.32
Ba	400	360	343	362	365	375	297	356
La	13.3	12.1	11.5	12.0	12.5	12.8	11.6	12.7
Ce	28.5	25.8	24.7	25.4	26.7	27.4	24.9	27.6
Pr	3.73	3.39	3.35	3.35	3.50	3.61	3.37	3.40
Nd	15.5	14.0	14.0	13.9	14.5	15.0	14.3	13.8
Sm	3.46	3.17	3.19	3.14	3.24	3.33	3.32	3.03
Eu	0.94	0.84	0.87	0.86	0.86	0.89	0.93	0.79
Gd	3.53	3.22	3.31	3.27	3.29	3.38	3.52	3.21
Tb	0.58	0.52	0.52	0.53	0.55	0.55	0.58	0.51
Dy	3.40	3.09	3.17	3.07	3.15	3.24	3.39	2.99
Ho	0.72	0.66	0.66	0.65	0.67	0.68	0.72	0.65
Er	1.99	1.82	1.80	1.81	1.85	1.90	1.99	1.81
Tm	0.32	0.29	0.29	0.29	0.30	0.30	0.31	0.30
Yb	2.02	1.85	1.86	1.88	1.89	1.95	2.02	1.90
Lu	0.33	0.31	0.30	0.31	0.31	0.32	0.33	0.32
Hf	3.47	3.16	2.86	3.17	3.19	3.29	2.73	3.27
Ta	0.38	0.35	0.32	0.36	0.36	0.36	0.31	0.39
Pb (total)	10.5	9.7	6.7	9.3	9.7	9.8	6.7	9.8
Th	5.95	5.54	4.74	5.54	5.50	5.68	4.21	6.16
U	1.59	1.47	1.24	1.44	1.47	1.52	1.07	1.66

Superscript font on specimens name refers to external data source listed in Table. A1

Table B.1. Major and trace element data for Whakapapa Fm lavas continued

Specimen	LT02	T6-75[f]	R96/10[a]	R96/11[a]	R96/12[a]	R96/25[a]	R96/26[a]	R96/27[a]
SiO_2	60.99	58.77	59.84	60.38	60.95	57.23	58.25	58.38
Al_2O_3	16.18	16.35	17.26	17.37	17.50	16.83	16.48	16.40
$Fe_2O_{3\,tot}$	6.43	7.09	7.35	7.02	6.70	8.01	7.77	7.88
MgO	4.01	4.52	3.50	3.21	2.93	4.64	4.60	4.66
CaO	6.35	6.87	6.48	6.36	6.27	7.27	7.15	7.22
Na_2O	3.31	3.28	3.48	3.56	3.64	3.04	3.10	3.05
K_2O	1.78	1.61	1.59	1.63	1.66	1.47	1.59	1.58
TiO_2	0.62	0.67	0.74	0.72	0.70	0.72	0.71	0.72
MnO	0.11	0.12	0.12	0.12	0.11	0.13	0.13	0.13
P_2O_5	0.12	0.12	0.13	0.13	0.12	0.12	0.13	0.12
Total	99.91	100.23	101.03	100.97	101.14	100.24	100.42	100.66
LOI	0.02	-	-	-	-	-	-	-
Mg#	59	60.58	53.45	52.44	51.31	58.27	58.82	58.79
Sc	22	26	21	22	21	25	24	25
V	165	167	177	168	179	206	196	184
Cr	70.4	75.9	28.0	29.0	28.0	72.9	84.2	79.9
Co	22	-	-	-	-	-	-	-
Ni	33.3	43.4	12.0	13.0	12.0	26.9	27.4	27.1
Cu	42	49	24	25	23	36	31	41
Zn	59	62	66	67	66	65	63	61
Ga	17	17	18	19	19	17	18	18
Rb	67.4	56.7	68.0	69.1	68.6	56.0	61.9	62.2
Sr	256	267	244	247	244	237	235	236
Y	20	20	22	22	22	21	21	22
Zr	117	111	129	131	130	118	124	125
Nb	4.90	5.00	5.48	5.63	5.57	4.36	4.71	4.58
Cs	4.09		3.29	3.30	3.28	5.52	6.11	6.16
Ba	367	371	380	389	378	335	359	357
La	13.0	12.8	14.5	14.8	14.4	12.3	13.2	13.2
Ce	27.7	27.6	31.4	32.2	31.8	26.9	28.5	28.8
Pr	3.61	3.5	3.9	4.0	3.9	3.4	3.6	3.6
Nd	14.4	13.98	14.99	15.60	14.95	13.46	14.00	14.20
Sm	3.21	3.05	3.55	3.51	3.48	3.08	3.25	3.27
Eu	0.83	0.96	0.91	0.92	0.90	0.83	0.84	0.84
Gd	3.30	3.32	3.64	3.63	3.56	3.39	3.45	3.48
Tb	0.55	0.51	0.58	0.58	0.57	0.55	0.56	0.57
Dy	3.21	3.13	3.52	3.48	3.51	3.34	3.38	3.37
Ho	0.67	0.66	0.73	0.73	0.73	0.73	0.72	0.73
Er	1.84	1.89	2.02	2.09	2.01	1.96	2.00	1.96
Tm	0.30	0.27	0.32	0.32	0.32	0.30	0.32	0.33
Yb	1.92	1.91	2.10	2.17	2.14	2.11	2.18	2.19
Lu	0.32	0.31	0.34	0.34	0.34	0.34	0.34	0.34
Hf	3.24	3.15	4.21	3.92	4.11	3.63	3.91	3.59
Ta	0.41	1.13	0.76	0.68	0.72	0.58	0.66	0.55
Pb (total)	10.1	11.4	12.6	12.8	12.4	11.3	11.9	11.9
Th	6.13	4.77	5.50	5.55	5.50	4.75	5.12	5.16
U	1.67	1.43	1.62	1.62	1.62	1.46	1.55	1.57

Superscript font on specimens name refers to external data source listed in Table. A1

Table B.2. Major and trace element data for Mangawhero Fm lavas

Specimen	W28	W29	TX9	TX10	TX8	TX13	TX1	TX2
SiO_2	57.23	57.84	60.43	61.07	61.27	58.99	61.89	62.03
Al_2O_3	17.41	16.65	15.73	17.11	16.85	16.00	16.13	16.21
$Fe_2O_{3\,tot}$	7.90	7.75	6.51	6.08	6.05	7.19	5.73	5.82
MgO	4.67	4.31	4.92	2.74	2.78	4.96	3.52	3.59
CaO	7.79	7.08	6.55	6.02	5.91	7.02	5.59	5.64
Na_2O	3.25	3.09	3.16	3.58	3.54	3.06	3.32	3.30
K_2O	0.90	1.66	1.80	2.01	2.04	1.66	2.13	2.13
TiO_2	0.62	0.76	0.69	0.86	0.83	0.69	0.68	0.68
MnO	0.12	0.12	0.10	0.09	0.09	0.11	0.09	0.09
P_2O_5	0.10	0.15	0.14	0.16	0.17	0.13	0.14	0.14
Total	99.99	99.41	100.03	99.72	99.53	99.82	99.21	99.63
LOI	-0.14	0.14	0.01	0.04	-0.04	-0.11	0.08	0.11
Mg#	58	56	64	51	52	61	59	59
Sc	31	24	23	18	15	26	16	19
V	241	210	174	196	171	194	132	147
Cr	95.9	61.1	148.9	50.5	40.6	151.2	70.8	75.6
Co	33	23	23	17	16	26	16	18
Ni	48.2	21.5	49.0	17.7	17.2	54.1	29.4	30.2
Cu	58	33	31	27	30	36	20	34
Zn	80	70	61	60	57	62	56	55
Ga	20	17	17	18	18	17	17	18
Rb	32.2	60.6	69.9	79.4	73.9	66.2	81.3	85.2
Sr	264	262	283	298	281	248	254	282
Y	21	20	20	21	19	21	20	23
Zr	87	114	136	147	138	125	136	139
Nb	3.21	4.75	5.60	6.13	5.79	4.95	6.10	6.26
Cs	1.30	3.66	4.27	4.86	4.76	2.98	4.46	2.61
Ba	282	356	400	439	438	334	427	425
La	8.1	13.0	15.1	15.5	15.6	12.4	16.3	18.9
Ce	17.8	27.8	32.2	32.9	33.3	26.9	34.7	39.7
Pr	2.49	3.60	4.18	4.24	4.30	3.61	4.46	5.33
Nd	10.7	15.0	16.8	17.2	17.6	14.7	17.7	21.1
Sm	2.73	3.34	3.62	3.70	3.71	3.30	3.74	4.35
Eu	0.85	0.88	0.91	0.93	0.92	0.85	0.90	0.93
Gd	3.14	3.57	3.54	3.59	3.75	3.50	3.85	4.22
Tb	0.54	0.57	0.56	0.57	0.59	0.57	0.60	0.66
Dy	3.31	3.36	3.30	3.33	3.36	3.39	3.42	3.70
Ho	0.72	0.70	0.68	0.69	0.70	0.71	0.71	0.78
Er	2.00	1.96	1.88	1.89	1.95	1.97	1.91	2.10
Tm	0.33	0.32	0.30	0.30	0.31	0.31	0.30	0.33
Yb	2.12	2.03	1.95	1.93	1.98	2.06	1.98	2.08
Lu	0.36	0.34	0.31	0.32	0.32	0.34	0.33	0.33
Hf	2.39	3.21	3.69	3.88	3.89	3.39	3.88	3.87
Ta	0.24	0.37	0.42	0.47	0.47	0.39	0.51	0.51
Pb (total)	5.1	9.1	11.0	12.1	12.0	8.2	12.4	12.3
Th	2.79	5.61	6.70	7.00	7.13	5.93	7.90	7.84
U	0.79	1.46	1.67	1.83	1.87	1.60	2.07	2.05

Superscript font on specimens name refers to external data source listed in Table. A1

Table B.2. Major and trace element data for Mangawhero Fm lavas continued

Specimen	TX3	TX4	TX5	TX6	TX7	TX11	TX12	W27	RB
SiO_2	61.84	61.79	62.06	62.31	61.66	61.49	57.75	61.87	52.98
Al_2O_3	16.26	16.44	16.26	16.28	16.32	16.29	16.81	16.51	15.57
$Fe_2O_{3\ tot}$	5.71	5.77	5.67	5.84	5.85	5.84	7.86	6.09	9.39
MgO	3.51	3.59	3.49	3.64	3.63	3.62	4.49	2.69	8.98
CaO	5.48	5.50	5.37	5.65	5.70	5.88	7.35	5.38	9.55
Na_2O	3.26	3.33	3.33	3.32	3.29	3.33	3.09	3.85	2.66
K_2O	2.15	2.10	2.18	2.11	2.02	1.99	1.50	2.18	0.60
TiO_2	0.67	0.68	0.68	0.68	0.68	0.67	0.76	0.87	0.66
MnO	0.09	0.09	0.09	0.09	0.10	0.09	0.12	0.09	0.15
P_2O_5	0.14	0.14	0.14	0.14	0.14	0.14	0.13	0.17	0.09
Total	99.10	99.43	99.26	100.06	99.38	99.34	99.865	99.69	100.63
LOI	0.22	0.22	0.29	0.14	0.04	0.17	0.05	0	-0.32
Mg#	59	59	59	59	59	59	57	51	69
Sc	19	20	16	19	21	17	24	16	33
V	152	145	130	147	161	136	206	194	240
Cr	78.2	75.0	68.1	79.6	83.9	68.4	57.6	53.4	355.4
Co	18	18	16	18	20	17	23	17	40
Ni	32.6	30.1	28.9	30.8	35.1	28.4	18.1	22.8	146.6
Cu	38	37	28	35	32	30	24	36	73
Zn	59	59	55	60	63	55	68	60	72
Ga	17	18	17	18	19	17	17	18	15
Rb	90.4	83.9	80.2	87.5	86.5	74.4	52.3	85.1	12.3
Sr	253	267	240	276	289	263	244	251	200
Y	19	18	18	19	21	19	20	23	17
Zr	136	129	130	134	142	134	110	159	49
Nb	6.37	6.52	6.12	6.70	6.67	5.74	4.50	6.33	1.45
Cs	5.90	3.87	3.79	4.94	2.92	4.95	3.28	5.46	0.34
Ba	424	423	432	412	465	408	321	448	195
La	15.0	14.1	15.0	14.2	16.4	15.4	12.3	16.2	4.7
Ce	31.5	30.4	34.2	29.9	36.1	32.9	26.7	34.9	10.4
Pr	3.97	3.90	4.21	3.86	4.56	4.20	3.57	4.53	1.59
Nd	15.7	15.2	16.8	15.2	18.2	16.9	15.0	18.4	7.6
Sm	3.37	3.38	3.66	3.32	3.97	3.60	3.44	4.06	2.07
Eu	0.87	0.87	0.87	0.89	0.97	0.92	0.90	0.95	0.70
Gd	3.26	3.14	3.63	3.31	3.71	3.56	3.62	3.99	2.60
Tb	0.53	0.53	0.58	0.52	0.60	0.58	0.59	0.63	0.44
Dy	3.09	3.07	3.37	3.10	3.47	3.28	3.49	3.71	2.65
Ho	0.65	0.64	0.68	0.64	0.73	0.68	0.73	0.77	0.58
Er	1.76	1.78	1.87	1.73	1.98	1.87	2.04	2.10	1.62
Tm	0.29	0.29	0.30	0.28	0.33	0.30	0.32	0.33	0.26
Yb	1.85	1.87	1.97	1.87	2.04	1.96	2.08	2.13	1.67
Lu	0.30	0.30	0.31	0.31	0.33	0.31	0.34	0.35	0.27
Hf	3.77	3.60	3.86	3.69	3.91	3.84	3.15	4.30	1.46
Ta	0.51	0.52	0.52	0.50	0.53	0.48	0.35	0.49	0.10
Pb (total)	12.5	15.5	12.1	12.2	16.2	12.1	8.2	13.2	3.1
Th	7.88	7.58	8.04	7.34	7.83	7.37	5.18	7.58	1.23
U	2.05	1.87	2.08	1.84	1.93	1.93	1.34	2.01	0.34

Superscript font on specimens name refers to external data source listed in Table. A1

Table B.2. Major and trace element data for Mangawhero Fm lavas continued

Specimen	T5-14b	T5-15b	R97/92a[c]	R97/92b[c]	R97/6[c]	R97/10a[c]	R97/13[c]	R97/50[c]	R97/50b[c]	R/04-3[d]
SiO_2	64.25	64.43	58.48	58.64	58.75	62.56	61.74	56.50	60.66	54.67
Al_2O_3	15.04	14.79	17.10	17.18	17.25	16.50	16.34	17.14	17.02	17.89
$Fe_2O_{3\ tot}$	5.24	5.31	7.67	7.75	7.71	5.99	6.03	8.40	6.90	9.10
MgO	3.28	3.42	3.79	3.85	3.53	2.48	3.35	4.76	3.59	9.10
CaO	4.71	4.83	7.21	7.26	6.94	5.25	5.78	7.88	6.28	5.03
Na_2O	3.33	3.32	3.30	3.37	3.29	3.88	3.37	3.15	3.44	8.51
K_2O	3.01	2.99	1.49	1.50	1.55	2.14	2.02	0.88	1.96	2.97
TiO_2	0.76	0.75	0.72	0.72	0.72	0.80	0.69	0.70	0.81	0.79
MnO	0.08	0.08	0.14	0.14	0.14	0.11	0.12	0.16	0.11	0.69
P_2O_5	0.16	0.16	0.14	0.14	0.14	0.20	0.15	0.11	0.18	0.16
Total	100.46	100.70	100.57	100.98	100.52	100.43	100.27	100.32	101.30	100.11
LOI	-	-	-	-	-	-	-	-	-	-
Mg#	60.13	60.82	54.40	54.47	52.44	49.99	57.25	57.72	55.65	57.10
Sc	16	16	27	28	23	15	19	31	20	25
V	126	125	182	183	169	125	129	215	159	236
Cr	100.1	111.3	57.3	57.0	49.2	41.3	74.6	59.9	66.1	48.5
Co	-	-	-	-	-	-	-	-	-	-
Ni	40.5	42.0	17.3	15.2	14.1	9.7	23.7	23.1	18.5	21.5
Cu	43	31	30	34	25	25	29	51	37	54
Zn	48	50	69	71	69	59	57	68	66	78
Ga	15	15	23	23	23	23	22	22	23	18
Rb	128.5	128.3	59.8	59.9	62.7	82.9	84.4	28.6	73.6	19.1
Sr	202	202	234	233	229	302	261	235	306	229
Y	23	25	22	23	21	22	20	18	23	17
Zr	215	225	130	130	118	162	147	76	156	75
Nb	8.45	8.46	5.15	5.27	4.76	6.39	5.98	6.77	6.39	2.77
Cs	7.78	8.65	4.88	4.96	4.11	5.59	5.06	1.41	-	0.92
Ba	537	534	352	351	350	496	430	234	456	236
La	18.5	20.4	13.6	13.7	12.9	17.5	15.2	7.7	16.3	5.9
Ce	43.4	45.9	29.8	30.3	27.0	38.6	33.6	17.0	36.1	14.6
Pr	5.2	5.7	3.8	3.9	3.5	4.9	4.1	2.3	-	1.9
Nd	20.82	22.63	15.24	15.20	14.01	18.36	15.53	9.59	-	8.66
Sm	4.38	4.62	3.44	3.56	3.13	3.88	3.55	2.34	-	2.29
Eu	1.02	0.97	0.96	0.94	0.91	1.09	1.01	0.78	-	0.80
Gd	3.79	4.18	3.66	3.71	3.48	4.18	3.58	2.70	-	2.48
Tb	0.65	0.70	0.57	0.59	0.55	0.58	0.53	0.45	-	0.42
Dy	3.76	4.05	3.49	3.54	3.19	3.46	3.14	2.83	-	2.61
Ho	0.80	0.87	0.76	0.76	0.69	0.74	0.65	0.59	-	0.61
Er	2.32	2.48	2.08	2.13	1.97	1.99	1.80	1.66	-	1.73
Tm	0.34	0.36	0.32	0.33	0.32	0.29	0.27	0.26	-	0.26
Yb	2.16	2.27	2.18	2.22	1.97	2.06	1.93	1.76	-	1.70
Lu	0.33	0.35	0.34	0.34	0.33	0.31	0.28	0.28	-	0.26
Hf	5.97	6.37	3.45	3.43	3.23	4.12	3.89	2.11	-	2.15
Ta	0.62	0.76	0.42	0.54	0.76	0.68	0.62	2.01	-	0.34
Pb (total)	15.4	16.4	9.0	8.1	11.7	16.8	16.1	13.3	12.2	4.9
Th	12.06	12.32	4.82	4.77	4.83	6.54	6.62	2.42	11.60	1.96
U	3.10	3.36	1.50	1.51	1.35	1.72	1.79	0.68	1.71	0.52

Superscript font on specimens name refers to external data source listed in Table. A1

Table B.3. Major and trace element data for Waihianoa Fm lavas

Specimen	R96/7[b]	R96/8[b]	R96/18[b]	R96/19[b]	R96/22[b]	W9-70[e]	W9-71[e]
SiO_2	60.48	58.68	54.95	56.91	57.44	57.11	56.82
Al_2O_3	17.49	18.35	17.12	17.21	17.32	17.05	17.04
$Fe_2O_{3\ tot}$	6.67	7.08	9.34	8.38	8.23	8.33	8.30
MgO	2.87	3.22	5.37	4.75	4.40	4.29	4.40
CaO	6.23	6.96	8.59	7.69	7.34	7.72	7.53
Na_2O	3.55	3.53	2.96	3.23	3.32	3.05	3.06
K_2O	1.69	1.29	0.94	1.08	1.19	1.40	1.38
TiO_2	0.71	0.65	0.75	0.67	0.68	0.78	0.78
MnO	0.10	0.11	0.14	0.13	0.13	0.14	0.14
P_2O_5	0.13	0.12	0.11	0.11	0.11	0.13	0.14
Total	100.24	100.30	100.79	100.55	100.69	100.22	100.37
LOI	-	-	-	-	-	-	-
Mg#	50.93	52.31	58.10	57.75	56.32	55.39	56.07
Sc	19	20	27	26	26	26	28
V	166	165	259	215	205	222	211
Cr	26.0	15.0	74.0	74.0	54.0	37.3	50.6
Co	-	-	-	-	-	-	-
Ni	12.0	5.0	25.0	35.0	31.0	4.7	4.2
Cu	38	14	54	60	55	31	32
Zn	72	67	78	74	72	83	82
Ga	19	19	19	18	18	20	19
Rb	60.0	42.0	27.0	34.0	38.0	51.5	50.1
Sr	246	252	226	232	243	262	256
Y	23	21	19	21	20	23	20
Zr	118	100	74	79	87	120	118
Nb	5.02	4.31	3.03	3.13	2.70	5.05	5.08
Cs	1.50	0.95	2.06	1.14	3.62	3.11	3.57
Ba	379	304	237	255	300	327	324
La	16.0	12.0	7.7	9.6	9.2	13.2	10.7
Ce	31.5	25.7	17.8	19.4	20.1	30.1	24.9
Pr	4.2	3.2	2.4	2.7	2.7	4.0	3.2
Nd	16.29	12.86	10.15	11.42	10.96	14.72	11.61
Sm	3.59	3.06	2.71	2.84	2.73	3.57	2.92
Eu	0.91	0.83	0.81	0.82	0.78	1.01	1.00
Gd	3.83	3.30	3.05	3.10	3.09	3.68	2.99
Tb	0.60	0.53	0.49	0.52	0.50	0.56	0.47
Dy	3.66	3.32	3.11	3.21	3.08	3.30	2.83
Ho	0.75	0.70	0.69	0.69	0.68	0.72	0.63
Er	2.08	1.98	1.88	1.94	1.83	2.00	1.81
Tm	0.32	0.31	0.28	0.29	0.30	0.31	0.29
Yb	2.08	2.02	1.96	1.92	1.99	2.09	1.87
Lu	0.34	0.33	0.31	0.31	0.32	0.33	0.31
Hf	3.53	3.20	2.59	2.76	2.81	3.28	3.60
Ta	0.51	0.57	0.57	0.49	0.37	0.51	0.57
Pb (total)	12.6	7.2	6.1	7.7	9.6	13.0	10.6
Th	4.54	3.39	2.18	2.53	2.95	4.44	4.22
U	1.36	1.02	0.69	0.81	0.95	1.34	1.28

Superscript font on specimens name refers to external data source listed in Table. A1

Table B.4. Major and trace element data for Te Herenga Fm lavas

Specimen	WX3	W25	WX2	W5	W6	W7	W13	W14
SiO_2	57.31	56.45	55.21	56.35	56.34	55.20	57.99	57.08
Al_2O_3	17.02	17.33	17.54	17.64	17.77	18.18	17.32	16.95
$Fe_2O_{3\,tot}$	8.60	8.87	9.34	8.36	8.44	8.58	8.65	8.66
MgO	4.54	4.79	5.12	4.72	4.70	4.75	4.61	4.65
CaO	7.64	7.92	7.90	7.58	7.67	7.42	7.69	7.57
Na_2O	3.60	3.23	3.05	3.28	3.30	3.17	3.34	3.19
K_2O	0.78	0.67	0.56	0.76	0.79	0.67	0.74	0.73
TiO_2	0.65	0.65	0.71	0.63	0.65	0.66	0.67	0.65
MnO	0.14	0.14	0.15	0.13	0.14	0.14	0.14	0.14
P_2O_5	0.10	0.09	0.09	0.10	0.11	0.11	0.09	0.09
Total	100.37	100.14	99.67	99.55	99.90	98.87	101.24	99.72
LOI	-0.19	-0.11	0.42	0.31	0.23	0.68	-0.09	-0.14
Mg#	55	56	56	57	56	56	55	55
Sc	29	26	32	22	23	26	29	30
V	242	219	257	195	198	222	240	233
Cr	60.5	40.1	50.6	37.5	39.4	47.0	62.1	56.9
Co	29	28	31	27	27	31	29	29
Ni	34.0	25.9	30.3	36.5	30.7	36.9	33.7	30.9
Cu	30	34	42	52	43	60	41	21
Zn	76	70	78	71	73	79	77	75
Ga	18	17	17	16	17	17	18	17
Rb	18.3	14.1	8.5	16.2	17.9	10.8	16.9	17.6
Sr	230	207	211	216	225	222	226	228
Y	20	19	19	17	17	19	19	19
Zr	64	53	58	58	59	63	64	61
Nb	1.97	1.66	1.80	1.84	1.95	2.12	1.93	1.80
Cs	0.45	0.36	0.78	0.55	0.97	0.63	0.95	0.40
Ba	204	169	180	207	242	251	200	188
La	5.8	4.9	4.6	5.6	6.1	6.5	4.9	5.0
Ce	12.0	10.9	10.5	11.9	13.1	14.1	11.3	11.4
Pr	1.82	1.75	1.57	1.77	1.90	2.03	1.67	1.74
Nd	8.5	8.4	7.5	8.3	8.9	9.3	7.8	8.2
Sm	2.29	2.30	2.13	2.19	2.25	2.37	2.20	2.23
Eu	0.74	0.77	0.72	0.73	0.75	0.75	0.73	0.73
Gd	2.86	3.02	2.72	2.68	2.77	2.84	2.72	2.84
Tb	0.49	0.50	0.48	0.45	0.46	0.48	0.47	0.47
Dy	3.01	3.10	2.93	2.72	2.81	2.90	2.94	3.00
Ho	0.66	0.69	0.66	0.60	0.61	0.63	0.65	0.65
Er	1.85	1.92	1.84	1.70	1.74	1.78	1.81	1.84
Tm	0.30	0.31	0.30	0.27	0.28	0.28	0.29	0.29
Yb	1.95	2.01	1.90	1.79	1.84	1.86	1.95	1.90
Lu	0.32	0.33	0.32	0.30	0.30	0.32	0.32	0.32
Hf	1.83	1.61	1.70	1.75	1.79	1.76	1.87	1.76
Ta	0.13	0.12	0.13	0.14	0.14	0.14	0.13	0.13
Pb (total)	3.4	2.8	5.8	3.8	4.9	6.1	4.2	3.5
Th	1.47	1.20	1.34	1.44	1.94	1.89	1.50	1.43
U	0.46	0.39	0.38	0.46	0.57	0.56	0.46	0.45

Superscript font on specimens name refers to external data source listed in Table. A1

Table B.4. Major and trace element data for Te Henrega Fm lavas continued

Specimen	WX15	W16	W17	T6-11[f]	T6-18[f]	T6-21[f]	T6-22[f]	T6-25[f]
SiO_2	57.59	57.03	56.42	57.37	56.75	56.72	56.11	56.46
Al_2O_3	17.03	17.42	17.52	16.85	17.37	17.17	17.21	17.37
$Fe_2O_{3\,tot}$	8.52	8.95	9.12	8.76	8.48	8.80	9.17	8.59
MgO	4.51	4.62	4.75	4.62	4.73	4.70	5.03	4.68
CaO	7.58	7.78	8.01	7.65	7.89	7.76	8.02	7.72
Na_2O	3.30	3.27	3.24	3.30	3.37	3.24	3.19	3.40
K_2O	0.76	0.66	0.67	0.73	0.75	0.68	0.64	0.79
TiO_2	0.66	0.68	0.70	0.66	0.65	0.64	0.67	0.66
MnO	0.14	0.14	0.15	0.14	0.14	0.15	0.15	0.14
P_2O_5	0.09	0.09	0.10	0.08	0.09	0.07	0.08	0.10
Total	100.18	100.65	100.68	100.42	100.35	100.31	100.58	100.19
LOI	-0.21	0.02	-0.13	-	-	-	-	-
Mg#	55	54	55	55.98	57.35	56.30	56.95	56.77
Sc	27	30	30	26	26	32	32	29
V	227	246	247	196	180	207	215	191
Cr	54.2	34.4	42.8	232.8	44.0	56.3	54.6	45.9
Co	27	30	29	-	-	-	-	-
Ni	30.4	24.5	26.5	22.5	25.3	24.9	24.2	29.0
Cu	33	29	30	34	29	17	47	45
Zn	73	76	77	63	66	73	74	73
Ga	17	18	17	16	18	15	16	16
Rb	17.9	14.8	13.8	15.5	16.4	15.5	10.0	17.8
Sr	219	226	211	217	234	212	213	230
Y	18	19	20	19	18	18	21	18
Zr	61	57	58	60	55	52	67	56
Nb	1.86	1.74	1.91	2.13	1.90	2.20	2.12	2.30
Cs	0.52	0.36	0.58	0.53	-	-	0.83	-
Ba	196	163	172	194	238	181	211	244
La	5.2	4.2	5.1	5.3	7.4	5.3	5.7	4.6
Ce	11.6	10.0	11.3	11.8	17.1	5.1	13.0	8.6
Pr	1.72	1.55	1.73	1.7	-	-	1.8	-
Nd	8.0	7.4	8.2	7.68	-	-	8.32	-
Sm	2.24	2.17	2.25	2.14	-	-	2.28	-
Eu	0.72	0.73	0.76	0.79	-	-	0.79	-
Gd	2.68	2.77	2.92	2.61	-	-	2.70	-
Tb	0.47	0.48	0.50	0.47	-	-	0.46	-
Dy	2.86	3.05	3.05	2.72	-	-	3.06	-
Ho	0.64	0.66	0.68	0.65	-	-	0.66	-
Er	1.79	1.86	1.91	1.67	-	-	1.86	-
Tm	0.29	0.30	0.30	0.26	-	-	0.28	-
Yb	1.87	1.96	1.97	1.73	-	-	1.89	-
Lu	0.32	0.32	0.33	0.26	-	-	0.29	-
Hf	1.74	1.69	1.71	1.66	-	-	2.23	-
Ta	0.14	0.12	0.13	0.45	-	-	0.60	-
Pb (total)	8.2	3.1	3.6	3.7	2.0	2.9	4.0	4.2
Th	1.49	1.20	1.42	2.01	1.67	1.78	1.34	3.41
U	0.46	0.38	0.40	0.46	0.57	1.67	0.46	2.06

Superscript font on specimens name refers to external data source listed in Table. A1

Table B.4. Major and trace element data for satellite vents and basalts

Specimen	KB	WB	P01	P02	OQ
SiO_2	49.37	52.49	56.49	56.50	56.92
Al_2O_3	17.31	12.14	14.03	13.93	14.56
$Fe_2O_{3\,tot}$	9.70	8.90	7.53	7.52	8.37
MgO	7.64	14.46	9.62	9.64	7.49
CaO	11.51	9.24	7.31	7.28	8.82
Na_2O	2.62	1.56	2.70	2.73	2.39
K_2O	0.33	0.52	1.39	1.39	0.69
TiO_2	1.12	0.45	0.67	0.67	0.53
MnO	0.16	0.15	0.12	0.12	0.14
P_2O_5	0.19	0.06	0.13	0.13	0.08
Total	99.96	99.97	99.99	99.91	99.98
LOI	-0.02	-0.08	-0.04	-0.08	0.04
Mg#	65	79	75	75	67
Sc	34	33	26	26	30
V	240	202	198	188	208
Cr	90.2	868.1	558.3	540.3	223.8
Co	42	56	41	40	34
Ni	73.0	420.2	285.5	280.3	55.0
Cu	50	90	89	93	85
Zn	71	62	61	60	60
Ga	16	13	16	15	15
Rb	5.2	15.6	49.8	47.7	15.5
Sr	338	327	283	272	359
Y	23	13	19	18	14
Zr	103	46	116	114	60
Nb	3.99	2.05	4.27	4.15	2.39
Cs	0.19	0.87	2.79	2.74	0.89
Ba	92	115	330	326	136
La	7.7	6.6	11.5	11.3	6.7
Ce	19.1	13.5	24.9	24.4	14.0
Pr	2.90	1.76	3.32	3.22	1.88
Nd	13.6	7.3	13.9	13.5	7.9
Sm	3.45	1.68	3.18	3.06	1.87
Eu	1.20	0.51	0.81	0.78	0.58
Gd	3.96	1.89	3.20	3.19	2.17
Tb	0.66	0.33	0.53	0.51	0.36
Dy	3.85	1.99	3.09	2.99	2.30
Ho	0.80	0.43	0.65	0.62	0.51
Er	2.16	1.21	1.77	1.70	1.45
Tm	0.33	0.20	0.29	0.27	0.24
Yb	2.08	1.26	1.78	1.75	1.53
Lu	0.33	0.21	0.30	0.29	0.26
Hf	2.42	1.36	3.19	3.14	1.73
Ta	0.25	0.14	0.33	0.32	0.17
Pb (total)	1.6	2.9	8.3	8.2	3.0
Th	0.71	1.94	5.16	5.05	2.31
U	0.19	0.46	1.40	1.37	0.55

Table B.5. Trace element data for meta-igneous xenoliths

Specimen	17430	17441	17411	17442	17449	17433	17432	17450
Sc	50	38	36	32	34	29	22	22
V	289	257	205	201	227	220	200	204
Cr	307.1	489.3	1073.7	836.3	552.2	104.7	22.3	17.4
Co	59	76	109	66	59	44	29	67
Ni	100.1	161.4	465.8	352.2	60.5	47.4	10.3	12.1
Cu	67	22	27	24	19	34	29	6
Zn	76	81	78	78	75	71	75	77
Ga	20	16	14	14	16	18	19	18
Rb	6.5	7.3	4.0	9.8	7.5	2.1	52.0	6.1
Sr	377	256	195	303	378	197	795	255
Y	23	15	15	15	19	17	14	18
Zr	64	33	52	44	15	15	31	19
Nb	6.17	1.83	2.04	1.84	3.53	1.57	2.81	3.04
Cs	0.39	0.40	0.63	5.82	0.52	0.36	5.54	0.97
Ba	104	97	146	120	150	53	346	96
La	5.4	4.7	4.5	4.8	10.5	3.4	5.4	7.8
Ce	13.1	10.1	10.2	11.1	22.6	7.9	11.9	17.3
Pr	2.05	1.55	1.55	1.66	3.07	1.22	1.69	2.45
Nd	9.7	7.1	7.0	7.4	12.0	5.7	7.2	10.3
Sm	2.85	2.02	1.95	1.90	2.84	1.75	1.84	2.54
Eu	0.96	0.75	0.63	0.59	0.74	0.63	0.68	0.73
Gd	3.64	2.40	2.36	2.21	2.92	2.34	2.16	2.85
Tb	0.62	0.41	0.40	0.37	0.49	0.42	0.36	0.48
Dy	3.80	2.51	2.50	2.34	3.04	2.63	2.25	2.94
Ho	0.79	0.53	0.52	0.49	0.64	0.56	0.49	0.62
Er	2.20	1.50	1.52	1.42	1.86	1.63	1.43	1.76
Tm	0.33	0.24	0.25	0.22	0.31	0.27	0.23	0.28
Yb	2.09	1.51	1.54	1.43	1.94	1.72	1.54	1.77
Lu	0.34	0.25	0.25	0.24	0.31	0.29	0.26	0.28
Hf	1.87	0.98	1.50	1.30	0.68	0.65	0.94	0.64
Ta	0.60	0.52	0.84	0.37	0.82	0.30	0.43	0.80
Pb (total)	3.0	3.8	3.7	6.4	6.4	7.2	10.6	8.1
Th	0.94	0.71	1.32	1.56	4.61	1.03	1.62	3.29
U	0.28	0.20	0.34	0.47	1.06	0.36	0.43	0.67

Specimen	17423	17457
Sc	48	65
V	366	385
Cr	487.4	857.9
Co	59	95
Ni	118	97.0
Cu	134	437
Zn	185	202
Ga	28	29
Rb	168.8	17.8
Sr	287	241
Y	17	29
Zr	48	74
Nb	3.27	4.54
Cs	8.91	1.56
Ba	903	163
La	3.0	5.8
Ce	7.6	10.3
Pr	1.53	2.12
Nd	8.1	10.9
Sm	2.67	3.37
Eu	0.87	0.86
Gd	3.37	4.42
Tb	0.57	0.77
Dy	3.45	4.95
Ho	0.70	1.11
Er	1.92	3.26
Tm	0.31	0.54
Yb	2.07	3.59
Lu	0.33	0.59
Hf	1.39	2.43
Ta	0.22	0.64
Pb (total)	29.3	5.1
Th	0.19	0.72
U	0.11	0.28

Trace element data for meta-sedimentary xenoliths

Specimen	17492	17485	17425	17443	17469	17465	17474
Sc	10	11	17	21	8	15	8
V	61	71	147	201	65	119	65
Cr	30.8	30.7	52.1	87.3	33.3	53.1	32.7
Co	134	156	24	116	74	56	76
Ni	7.2	10.2	30.6	34.7	15.6	10.3	12.9
Cu	33	52	28	72	147	39	54
Zn	41	50	121	175	71	82	58
Ga	14	14	38	39	18	23	16
Rb	0.8	42.0	134.4	17.0	117.4	171.5	109.2
Sr	611	272	689	549	161	137	148
Y	20	14	26	27	20	27	18
Zr	21	11	23	60	66	156	78
Nb	8.68	7.20	15.99	18.70	8.63	12.93	7.92
Cs	0.06	1.72	4.26	0.88	7.32	8.21	7.23
Ba	46	190	1717	900	596	768	465
La	24.8	21.1	47.4	45.8	31.4	38.5	25.9
Ce	48.6	44.0	94.3	90.4	65.1	81.2	54.2
Pr	6.27	5.58	11.65	11.06	8.03	10.34	6.86
Nd	23.5	20.7	42.8	40.6	28.9	38.6	25.5
Sm	4.41	4.01	7.79	7.29	5.23	7.45	4.81
Eu	1.07	0.87	1.94	2.14	1.19	1.60	0.99
Gd	3.67	3.27	6.25	6.15	4.20	6.09	4.05
Tb	0.57	0.48	0.92	0.88	0.63	0.93	0.60
Dy	3.31	2.62	5.00	4.80	3.56	5.09	3.39
Ho	0.67	0.50	0.94	0.94	0.70	0.98	0.66
Er	1.83	1.30	2.47	2.46	1.89	2.65	1.77
Tm	0.29	0.20	0.37	0.38	0.29	0.41	0.28
Yb	1.83	1.20	2.18	2.33	1.79	2.56	1.71
Lu	0.28	0.17	0.31	0.37	0.28	0.41	0.27
Hf	0.75	0.32	0.81	2.13	1.97	4.37	2.11
Ta	3.18	3.26	1.29	2.61	0.91	1.86	0.86
Pb (total)	3.8	9.6	23.3	16.3	22.9	24.6	24.2
Th	9.26	8.74	21.41	15.27	10.99	15.24	10.09
U	1.92	1.07	4.17	2.50	1.94	3.00	1.87

Table C.1. Whole rock Sr, Pb, Nd and Hf isotope data for lavas from Ruapehu, satellite vents and basalts

Specimen	$^{87}Sr/^{86}Sr$	2σ	$^{143}Nd/^{144}Nd$	2σ	εNd	$^{176}Hf/^{177}Hf$	2σ	εHf
W8	0.705311[b]	0.000013	0.512741[b]	0.000013	2.0	-	-	-
WX10	0.705140[b]	0.000015	0.512757[b]	0.000010	2.3	-	-	-
WX18	0.705182[a]	0.000024	0.512770[a]	0.000011	2.6	0.282978[a]	0.000011	7.4
WX22	0.705310[b]	0.000012	0.512741[b]	0.000010	2.0	-	-	-
WX20	0.705310[b]	0.000015	0.512735[b]	0.000010	1.9	-	-	-
W26	0.705263[a]	0.000019	0.512763[a]	0.000009	2.4	-	-	-
KR01	0.705311[b]	0.000012	0.512746[b]	0.000012	2.1	-	-	-
WX24	0.705303[b]	0.000013	0.512739[b]	0.000011	2.0	0.282969[a]	0.000011	7.1
WX30	0.705317[b]	0.000014	0.512678[b]	0.000010	0.8	0.282969[a]	0.000011	7.1
WX11	0.705306[b]	0.000013	0.512737[b]	0.000010	1.9	0.282967[b]	0.000012	7.0
UT01	0.705158[b]	0.000014	0.512756[b]	0.000010	2.3	0.282963[a]	0.000012	6.9
LT02	0.705278[a]	0.000018	0.512784[a]	0.000014	2.8	-	-	-
T6-75[f]	0.705331	-	0.512740	-	2.0	-	-	-
R96/10[a]	0.705826	-	0.512692	-	1.1	-	-	-
R96/11[a]	0.705813	-	0.512677	-	0.8	-	-	-
R96/12[a]	0.705762	-	0.512686	-	0.9	-	-	-
R96/25[a]	0.705226	-	0.512743	-	2.0	-	-	-
R96/26[a]	0.705321	-	0.512719	-	1.6	-	-	-
R96/27[a]	0.705269	-	0.512750	-	2.2	-	-	-
W29	0.705181[a]	0.000025	0.512739[a]	0.000011	2.0	0.282952[b]	0.000016	6.5
TX10	0.705192[a]	0.000025	0.512717[a]	0.000013	1.5	0.282936[a]	0.000011	5.9
TX8	0.705530[b]	0.000014	0.512710[b]	0.000010	1.4	0.282940[a]	0.000010	6.0
TX13	0.705175[b]	0.000013	0.512746[b]	0.000011	2.1			
TX1	0.705903[a]	0.000017	0.512676[a]	0.000010	0.7			
TX4	0.705872[b]	0.000013	0.512673[b]	0.000009	0.7	0.282910[a]	0.000010	5.0
TX7	0.705910[b]	0.000013	0.512663[b]	0.000010	0.5	0.282908[a]	0.000011	4.9
RB	0.704774[a]	0.000021	0.512909[a]	0.000010	5.3	0.283137[a]	0.000018	13.0
T5-14[b]	0.705425	-	0.512732	-	1.8	-	-	-
T5-15[b]	0.705354	-	0.512724	-	1.7	-	-	-
R97/92a[c]	0.705429	-	0.512711	-	1.4	-	-	-
R97/92b[c]	0.705414	-	0.512727	-	1.7	-	-	-
R97/6[c]	0.705717	-	0.512691	-	1.0	-	-	-
R97/10a[c]	0.705494	-	0.512689	-	1.0	-	-	-
R97/13[c]	0.705879	-	0.512671	-	0.6	-	-	-
R97/50[c]	0.705148	-	0.512749	-	2.2	-	-	-
R/04-3[d]	0.705115	-	-	-		-	-	-
R96/7[b]	0.705728	-	0.512712	-	1.4	-	-	-
R96/8[b]	0.705858	-	0.512694	-	1.1	-	-	-
R96/18[b]	0.705384	-	0.512780	-	2.8	-	-	-
R96/19[b]	0.705403	-	0.512762	-	2.4	-	-	-
R96/22[b]	0.705490	-	0.512756	-	2.3	-	-	-
W9-70[e]	0.705352	-	0.512746	-	2.1	-	-	-
W9-71[e]	0.705419	-	0.512726	-	1.7	-	-	-
W25	0.704871[b]	0.000015	0.512918[b]	0.000011	5.5	0.283141[a]	0.000012	13.1
WX2	0.704849[a]	0.000018	0.512908[a]	0.000010	5.3	0.283125[a]	0.000011	12.6
W4	0.704954[c]	0.000013	0.512910[c]	0.000020	5.3	0.283124[a]	0.000010	12.5
W5	0.704897[a]	0.000019	0.512914[a]	0.000014	5.4	0.283130[a]	0.000012	12.8
W6	0.705046[c]	0.000012	0.512901[c]	0.000017	5.1	0.283119[a]	0.000011	12.4
W7	0.705042[b]	0.000015	0.512880[b]	0.000011	4.7	0.283122[a]	0.000014	12.5
W13	0.704706[a]	0.000058	0.512896[a]	0.000012	5.0	0.283127[a]	0.000011	12.7
W14	0.704923[c]	0.000012	0.512907[c]	0.000015	5.2	0.283106[a]	0.000011	11.9
WX15	0.704982[a]	0.000022	0.512881[a]	0.000011	4.7	0.283130[a]	0.000011	12.8
W16	0.704794[c]	0.000012	0.512927[c]	0.000017	5.6	0.283155[a]	0.000012	13.6
W17	0.704877[a]	0.000022	0.512898[a]	0.000014	5.1	0.283142[a]	0.000034	13.2
T6-22[f]	0.704971	-	0.512894	-	5.0	-	-	-
KB	0.703867[a]	0.000017	0.512909[a]	0.000011	5.3	0.283060[a]	0.000015	10.3
WB	0.704465[a]	0.000017	0.512724[a]	0.000010	1.7	0.282969[a]	0.000011	7.1
P01	0.704782[b]	0.000016	0.512784[b]	0.000010	2.9	0.282986[a]	0.000013	7.7
OQ	0.704265[b]	0.000013	0.512821[b]	0.000013	3.57	0.283052[a]	0.000014	10.0

Superscript font refers to the respective analytical session for which standard data is presented in Table E.6, Appendix E
2σ uncertainty = quadratic addtion of sample internal precision and standard reproducibility
Superscript font on specimens name refers to external data source listed in Table. A1
εHf values calculated using a $^{176}Hf/^{177}Hf$ ratio for CHUR of 0.282769 (Blichert-Toft & Albarede, 1997)

Table C.1. Whole rock Sr, Pb, Nd and Hf isotope data for lavas from Ruapehu, satellite vents and basalts continued

Specimen	$^{206}Pb/^{204}Pb$	2σ	$^{207}Pb/^{204}Pb$	2σ	$^{208}Pb/^{204}Pb$	2σ
W8	18.8366[b]	0.0016	15.6364[b]	0.0013	38.7551[b]	0.0039
WX10	18.8364[b]	0.0014	15.6369[b]	0.0012	38.7570[b]	0.0033
WX18	18.8252[a]	0.0026	15.6313[a]	0.0023	38.7329[a]	0.0061
WX22	18.8342[b]	0.0025	15.6353[b]	0.0021	38.7508[b]	0.0054
WX20	18.8282[b]	0.0019	15.6350[b]	0.0014	38.7445[b]	0.0037
W26	18.8290[a]	0.0016	15.6308[a]	0.0016	38.7360[a]	0.0043
KR01	18.8364[b]	0.0016	15.6374[b]	0.0014	38.7573[b]	0.0038
WX24	18.8326[b]	0.0014	15.6382[b]	0.0012	38.7559[b]	0.0032
WX30	18.8397[b]	0.0013	15.6396[b]	0.0011	38.7657[b]	0.0032
WX11	18.8352[b]	0.0011	15.6351[b]	0.0009	38.7507[b]	0.0026
UT01	18.8436[b]	0.0035	15.6378[b]	0.0028	38.7622[b]	0.0073
LT02	18.8329[a]	0.0017	15.6318[a]	0.0017	38.7430[a]	0.0042
T6-75[f]	18.8150	-	15.6077	-	38.6549	-
R96/10[a]	-	-	-	-	-	-
R96/11[a]	-	-	-	-	-	-
R96/12[a]	-	-	-	-	-	-
R96/25[a]	-	-	-	-	-	-
R96/26[a]	-	-	-	-	-	-
R96/27[a]	-	-	-	-	-	-
W29	18.8334[a]	0.0025	15.6301[a]	0.0023	38.7395[a]	0.0058
TX10	18.8371[a]	0.0016	15.6332[a]	0.0016	38.7475[a]	0.0042
TX8	18.8372[b]	0.0014	15.6369[b]	0.0010	38.7568[b]	0.0031
TX13	18.8400[b]	0.0017	15.6367[b]	0.0015	38.7598[b]	0.0042
TX1	18.8370[a]	0.0017	15.6335[a]	0.0016	38.7499[a]	0.0042
TX4	18.8433[b]	0.0010	15.6400[b]	0.0008	38.7714[b]	0.0025
TX7	18.8473[b]	0.0017	15.6436[b]	0.0014	38.7825[b]	0.0038
RB	18.7700[a]	0.0045	15.6170[a]	0.0038	38.6475[a]	0.0093
T5-14[b]	-	-	-	-	-	-
T5-15[b]	-	-	-	-	-	-
R97/92a[c]	-	-	-	-	-	-
R97/92b[c]	-	-	-	-	-	-
R97/6[c]	-	-	-	-	-	-
R97/10a[c]	-	-	-	-	-	-
R97/13[c]	-	-	-	-	-	-
R97/50[c]	-	-	-	-	-	-
R/04-3[d]	-	-	-	-	-	-
R96/7[b]	-	-	-	-	-	-
R96/8[b]	-	-	-	-	-	-
R96/18[b]	-	-	-	-	-	-
R96/19[b]	-	-	-	-	-	-
R96/22[b]	-	-	-	-	-	-
W9-70[e]	-	-	-	-	-	-
W9-71[e]	-	-	-	-	-	-
W25	18.7629[b]	0.0040	15.6241[b]	0.0026	38.6544[b]	0.0072
WX2	18.7568[a]	0.0026	15.6200[a]	0.0024	38.6399[a]	0.0059
W4	18.7970[b]	0.0024	15.6280[b]	0.0020	38.6917[b]	0.0053
W5	18.7740[a]	0.0047	15.6117[a]	0.0038	38.6419[a]	0.0099
W6	18.8140[b]	0.0026	15.6300[b]	0.0020	38.7078[b]	0.0057
W7	18.8182[b]	0.0030	15.6351[b]	0.0024	38.7212[b]	0.0062
W13	18.7833[a]	0.0043	15.6181[a]	0.0036	38.6567[a]	0.0091
W14	18.7879[b]	0.0028	15.6259[b]	0.0025	38.6771[b]	0.0060
WX15	18.7908[a]	0.0016	15.6231[a]	0.0016	38.6776[a]	0.0042
W16	18.7799[b]	0.0031	15.6249[b]	0.0025	38.6741[b]	0.0066
W17	18.7689[a]	0.0047	15.6161[a]	0.0041	38.6468[a]	0.0100
T6-22[f]	-	-	-	-	-	-
KB	18.7950[a]	0.0053	15.6022[a]	0.0045	38.6133[a]	0.0113
WB	18.8246[a]	0.0038	15.6272[a]	0.0033	38.7315[a]	0.0081
P01	18.8265[b]	0.0015	15.6322[b]	0.0013	38.7364[b]	0.0037
OQ	18.7891[b]	0.0031	15.6198[b]	0.0025	38.6834[b]	0.0063

Superscript font refers to the respective analytical session for which standard data is presented in Table E.6, Appendix E
2σ uncertainty = quadratic addtion of sample internal precision and standard reproducibility
Superscript font on specimens name refers to external data source listed in Table. A1
εHf values calculated using a $^{176}Hf/^{177}Hf$ ratio for CHUR of 0.282769 (Blichert-Toft & Albarede, 1997)

Table C.2. Whole rock Sr, Pb, Nd and Hf isotope data for meta-igneous and meta-sedimentary xenoliths

Specimen	$^{87}Sr/^{86}Sr$	2σ	$^{143}Nd/^{144}Nd$	2σ	` ` `	$^{176}Hf/^{177}Hf$	2σ	` ` `	$^{206}Pb/^{204}Pb$	2σ
17430	0.706739[d]	0.000016	0.512838[d]	0.000012	4.1	0.282957[b]	0.000010	6.6	18.8259[c]	0.0041
17441	0.705941[c]	0.000012	0.512756[c]	0.000016	2.8	0.283031[a]	0.000013	9.3	18.5300[b]	0.0033
17411	0.706404[c]	0.000012	0.512871[c]	0.000021	4.5	0.283085[a]	0.000025	11.2	18.7919[b]	0.0025
17442	0.705774[c]	0.000011	0.512882[c]	0.000017	4.9	0.283079[a]	0.000028	11.0	18.7993[b]	0.0017
17449	0.705678[d]	0.000015	0.512750[d]	0.000014	2.8	0.282996[b]	0.000013	8.0	18.8253[c]	0.0024
17433	0.706916[d]	0.000016	0.512957[d]	0.000014	6.3	0.283148[b]	0.000017	13.4	18.7712[c]	0.0020
17432	0.708698[d]	0.000014	0.512913[d]	0.000012	5.5	0.283119[b]	0.000010	12.4	18.8042[d]	0.0036
17450	0.706905[d]	0.000014	0.512793[d]	0.000013	3.4	0.283015[b]	0.000015	8.7	18.7687[d]	0.0037
17423	0.709969[d]	0.000015	0.513072[d]	0.000019	8.5	0.283107[d]	0.000012	11.9	18.7813[d]	0.0036
17457	0.706993[d]	0.000015	0.512964[d]	0.000012	6.4	0.283129[b]	0.000012	12.7	18.8087[c]	0.0030
17492	0.707111[d]	0.000014	0.512558[d]	0.000014	-1.6	0.282836[b]	0.000027	-0.9	18.8633[c]	0.0027
17485	0.708924[d]	0.000014	0.512527[d]	0.000012	-2.2	0.282835[b]	0.000024	-0.9	18.7978[d]	0.0036
17425	0.706723[d]	0.000014	0.512532[d]	0.000013	-2.1	0.282839[b]	0.000015	-0.7	18.8839[d]	0.0036
17443	0.708072[d]	0.000015	0.512457[d]	0.000012	-3.5	0.282784[b]	0.000009	-2.7	18.8371[d]	0.0036
17469	0.712072[d]	0.000015	0.512380[d]	0.000012	-5.0	0.282764[b]	0.000011	-3.4	18.8203[d]	0.0036
17465	0.711939[d]	0.000015	0.512422[d]	0.000012	-4.2	0.282735[b]	0.000010	-4.4	18.8213[d]	0.0036
17474	0.711733[d]	0.000015	0.512378[d]	0.000012	-5.1	0.282736[b]	0.000011	-4.4	18.7944[d]	0.0036

Specimen	$^{207}Pb/^{204}Pb$	2σ	$^{208}Pb/^{204}Pb$	2σ
17430	15.6379[c]	0.0032	38.7439[c]	0.0091
17441	15.6240[b]	0.0027	38.4317[b]	0.0074
17411	15.6370[b]	0.0022	38.7045[b]	0.0055
17442	15.6545[b]	0.0014	38.7614[b]	0.0039
17449	15.6365[c]	0.0019	38.7652[c]	0.0058
17433	15.6484[c]	0.0014	38.7207[c]	0.0051
17432	15.6468[d]	0.0013	38.7660[d]	0.0069
17450	15.6479[d]	0.0014	38.7501[d]	0.0071
17423	15.6349[d]	0.0013	38.6965[d]	0.0068
17457	15.6382[c]	0.0023	38.7354[c]	0.0070
17492	15.6533[c]	0.0020	38.8220[c]	0.0065
17485	15.6479[d]	0.0013	38.7849[d]	0.0069
17425	15.6354[d]	0.0013	38.8242[d]	0.0069
17443	15.6360[d]	0.0013	38.7510[d]	0.0068
17469	15.6453[d]	0.0013	38.7689[d]	0.0069
17465	15.6434[d]	0.0014	38.7147[d]	0.0069
17474	15.6527[d]	0.0012	38.7836[d]	0.0068

Superscript font refers to the respective analytical session for which standard data is presented in Table E.6, Appendix E
2σ uncertainty = quadratic addtion of sample internal precision and standard reproducibility
εHf values calculated using a $^{176}Hf/^{177}Hf$ ratio for CHUR of 0.282769 (Blichert-Toft & Albarede, 1997)

Table C.3. Whole rock Os isotopes and PGE data for meta-igneous xenoliths

Sample	$^{187}Os/^{188}Os$	1SE	Os (ppt)	Re (ppt)	Ir (ppt)	Pt (ppt)
17411	0.14589	0.00072	61.3	14.7	80.1	1498.6
17430	2.20758	0.00888	8.7	464.9	3.1	123.8
17441	0.17978	0.00020	20.1	111.1	28.2	1289.8
17442	0.13702	0.00011	65.8	245.3	110.1	2024.9

Table C.4. Oxygen isotope data ($\delta^{18}O$) for lavas from Ruapehu, satellite vents and basalts

		Cpx	2σ						
Post Te Herenga	WX18	6.23							
	WX24	6.47		6.93					0.46
	WX30	6.59							
	WX11	6.32		7.19					0.87
	UT01	6.48							
	W29	6.6							
	TX10	6.54							
	TX8	6.48							
	TX4	6.55							
	TX7	6.59		7.18					0.59
Te Herenga	W25	5.82							
	WX2	6.05		6.58					0.53
	W5	5.97							
	W6	5.97							
	W7	6.02		6.66					0.64
	W13	5.94							
	W14	5.84							
	WX15	5.89	0.21						
	W16	5.96							
Satellite vents and basalts	WB	6.16				5.25		0.91	
	RB	6.08				5.50		0.58	
	P01	6.52		6.96		5.14	0.24	1.38	0.44
	P02	6.57		7.08		5.12	0.07	1.45	0.51
	OQ	5.47		6.15		4.82	0.06	0.65	0.68

Table C.5. Comparison of xenolith Sr and Nd isotope values with Graham (1985)

	Graham (1985)			Graham (1985)		
Specimen	$^{87}Sr/^{86}Sr$	$^{87}Sr/^{86}Sr$	2σ	$^{143}Nd/^{144}Nd$	$^{143}Nd/^{144}Nd$	2σ
17430	0.7067	0.706739	0.000016	0.512850	0.512838	0.000012
17441	0.70593	0.705941	0.000012	0.512780	0.512756	0.000016
17411	0.70642	0.706404	0.000012	0.512890	0.512871	0.000021
17442	0.7057	0.705774	0.000011		0.512882	0.000017
17449	0.7056	0.705678	0.000015	0.512780	0.512750	0.000014
17433	0.70689	0.706916	0.000016	0.512960	0.512957	0.000014
17432	0.70872	0.708698	0.000014	0.512920	0.512913	0.000012
17450	0.70679	0.706905	0.000014	0.512810	0.512793	0.000013
17423	0.7100	0.709969	0.000015	-	0.513072	0.000019
17457	0.70701	0.706993	0.000015	-	0.512964	0.000012
17492	0.7070	0.707111	0.000014	-	0.512558	0.000014
17485	0.7089	0.708924	0.000014	-	0.512527	0.000012
17425	0.70662	0.706723	0.000014	-	0.512532	0.000013
17443	0.7080	0.708072	0.000015	-	0.512457	0.000012
17469	0.7120	0.712072	0.000015	-	0.512380	0.000012
17465	0.7119	0.711939	0.000015	-	0.512422	0.000012
17474	0.71058	0.711733	0.000015	-	0.512378	0.000012

2σ uncertainty = quadratic addtion of sample internal precision and standard reproducibility

Table D.1. Ruapehu lavas - Plagioclase mineral data

Sample	WX2	WX2	WX2	WX2	WX2	WX2	WX2	WX2
Grain	P1	P1	P2	P2	P2	P3	P3	P3
Position	core	rim	core 1	core 2	rim	inner core	outer core	rim
SiO_2	50.75	54.32	53.50	50.22	52.78	50.29	53.52	50.08
TiO_2	0.00	0.03	0.00	0.00	0.11	0.09	0.14	0.14
Al_2O_3	31.12	28.51	29.01	31.19	29.51	30.98	29.14	31.22
Fe_2O_3	0.60	0.54	0.55	0.64	0.72	0.65	0.52	0.64
MnO	0.04	0.03	0.02	0.00	0.01	0.03	0.06	0.00
MgO	0.04	0.06	0.06	0.07	0.06	0.08	0.08	0.07
CaO	13.98	11.36	12.01	14.88	12.77	14.44	12.18	14.70
Na_2O	3.32	4.80	4.29	3.05	4.25	3.25	4.61	3.26
K_2O	0.21	0.32	0.26	0.13	0.17	0.14	0.24	0.17
total	100.06	99.96	99.70	100.18	100.37	99.94	100.48	100.27
Si	2.31	2.46	2.43	2.29	2.39	2.30	2.42	2.28
Ti	0.00	0.00	0.00	0.00	0.00	0.00	0.00	0.00
Al	1.67	1.52	1.55	1.68	1.57	1.67	1.55	1.68
Fe(iii)	0.02	0.02	0.02	0.02	0.02	0.02	0.02	0.02
Mn	0.00	0.00	0.00	0.00	0.00	0.00	0.00	0.00
Mg	0.00	0.00	0.00	0.00	0.00	0.01	0.01	0.01
Ca	0.68	0.55	0.58	0.73	0.62	0.71	0.59	0.72
Na	0.29	0.42	0.38	0.27	0.37	0.29	0.40	0.29
K	0.01	0.02	0.02	0.01	0.01	0.01	0.01	0.01
total	5.00	4.99	4.98	5.00	5.00	5.00	5.00	5.01
An	69.2	55.8	60.0	72.6	62.0	70.7	58.9	70.9
Ab	29.6	42.3	38.5	26.7	37.1	28.5	39.8	28.2
Or	1.2	1.9	1.5	0.7	1.0	0.8	1.4	1.0

Sample	R96/26	R96/26	R96/26	R96/26	R96/26	R96/26	R96/26	WX9
Grain	P1	P1	P2	P2	P3	P3	P3	P1
Position	core	rim	core	rim	inner core	outer core	rim	core
SiO_2	54.70	52.82	54.06	54.62	53.83	52.83	54.61	54.70
TiO_2	0.18	0.08	0.10	0.02	0.07	0.11	0.00	0.00
Al_2O_3	28.26	29.37	28.64	27.85	28.49	29.74	28.81	28.69
Fe_2O_3	0.62	0.71	0.65	0.63	0.57	0.53	0.56	0.63
MnO	0.00	0.01	0.02	0.03	0.01	0.00	0.00	0.00
MgO	0.06	0.06	0.06	0.04	0.06	0.07	0.06	0.07
CaO	11.44	12.56	11.65	10.82	11.71	12.97	11.60	12.05
Na_2O	4.95	4.29	4.65	5.08	4.75	4.16	4.67	4.63
K_2O	0.29	0.27	0.32	0.34	0.31	0.26	0.35	0.38
total	100.50	100.17	100.15	99.43	99.80	100.67	100.67	101.14
Si	2.46	2.40	2.44	2.48	2.44	2.39	2.45	2.45
Ti	0.01	0.00	0.00	0.00	0.00	0.00	0.00	0.00
Al	1.50	1.57	1.53	1.49	1.52	1.58	1.53	1.51
Fe(iii)	0.02	0.02	0.02	0.02	0.02	0.02	0.02	0.02
Mn	0.00	0.00	0.00	0.00	0.00	0.00	0.00	0.00
Mg	0.00	0.00	0.00	0.00	0.00	0.00	0.00	0.00
Ca	0.55	0.61	0.56	0.53	0.57	0.63	0.56	0.58
Na	0.43	0.38	0.41	0.45	0.42	0.36	0.41	0.40
K	0.02	0.02	0.02	0.02	0.02	0.02	0.02	0.02
total	4.99	5.00	4.99	4.99	5.00	5.00	4.99	4.99
An	55.3	61.0	57.2	53.2	56.8	62.5	56.8	57.9
Ab	43.0	37.4	41.0	44.8	41.4	36.0	41.1	39.9
Or	1.7	1.6	1.8	2.0	1.8	1.5	2.0	2.1

Grain: P = phenocryst; INC = inclusion; OVG = overgrowth; GLOM = glomerocryst

An = Anorthite; Ab = Albite; Or = Orthoclase

Table D.1 Ruapehu lavas - Plagioclase mineral data continued

Sample	WX9	WX9	WX9	WX9	WX9	WX9	WX9	RB
Grain	P1	P2	P2	P3	P3	P4	P4	P1
Position	rim	core	rim	core	rim	core	rim	core
SiO_2	51.98	51.44	51.46	54.58	53.81	53.14	52.71	48.22
TiO_2	0.00	0.00	0.01	0.00	0.01	0.03	0.00	0.04
Al_2O_3	30.04	30.75	29.89	28.37	28.97	28.97	28.90	32.53
Fe_2O_3	0.75	0.86	0.84	0.59	0.55	0.72	0.80	0.88
MnO	0.01	0.04	0.05	0.00	0.00	0.02	0.01	0.04
MgO	0.08	0.11	0.10	0.05	0.07	0.10	0.11	0.11
CaO	13.71	14.42	14.05	11.76	12.16	12.13	12.47	16.53
Na_2O	3.70	3.41	3.54	4.91	4.44	4.36	4.26	2.17
K_2O	0.18	0.16	0.20	0.29	0.26	0.26	0.27	0.01
total	100.44	101.18	100.15	100.55	100.26	99.74	99.52	100.52
Si	2.36	2.32	2.35	2.46	2.43	2.42	2.41	2.20
Ti	0.00	0.00	0.00	0.00	0.00	0.00	0.00	0.00
Al	1.61	1.64	1.61	1.51	1.54	1.55	1.55	1.75
Fe(iii)	0.03	0.03	0.03	0.02	0.02	0.02	0.03	0.03
Mn	0.00	0.00	0.00	0.00	0.00	0.00	0.00	0.00
Mg	0.01	0.01	0.01	0.00	0.00	0.01	0.01	0.01
Ca	0.67	0.70	0.69	0.57	0.59	0.59	0.61	0.81
Na	0.33	0.30	0.31	0.43	0.39	0.38	0.38	0.19
K	0.01	0.01	0.01	0.02	0.02	0.02	0.02	0.00
total	5.00	5.00	5.00	5.00	4.99	4.99	5.00	5.00
An	66.7	69.7	68.2	56.1	59.5	60.0	61.1	80.9
Ab	32.3	29.4	30.7	42.2	39.0	38.5	37.3	19.0
Or	1.0	0.9	1.1	1.6	1.5	1.5	1.5	0.0

Sample	RB	RB	RB	RB	RB	RB	RB	RB
Grain	P1	P2	P2	P3	P3	P3	P4	P4
Position	rim	core	rim	core 1	core 2	rim	core	rim
SiO_2	48.36	50.50	52.74	48.76	48.67	52.47	49.14	53.12
TiO_2	0.02	0.04	0.04	0.00	0.02	0.08	0.01	0.05
Al_2O_3	32.42	31.23	29.61	32.26	32.53	28.96	31.86	29.13
Fe_2O_3	0.84	0.74	1.10	0.75	0.83	1.00	0.86	1.00
MnO	0.00	0.05	0.05	0.11	0.03	0.04	0.10	0.08
MgO	0.12	0.13	0.16	0.13	0.09	0.20	0.09	0.24
CaO	16.85	15.07	13.27	16.32	16.62	13.16	15.86	12.99
Na_2O	2.20	3.13	4.06	2.54	2.36	4.23	2.74	4.28
K_2O	0.06	0.08	0.14	0.05	0.03	0.15	0.07	0.14
total	100.86	100.98	101.15	100.93	101.19	100.29	100.73	101.03
Si	2.21	2.29	2.38	2.22	2.21	2.38	2.24	2.39
Ti	0.00	0.00	0.00	0.00	0.00	0.00	0.00	0.00
Al	1.74	1.67	1.57	1.73	1.74	1.55	1.71	1.55
Fe(iii)	0.03	0.03	0.04	0.03	0.03	0.03	0.03	0.03
Mn	0.00	0.00	0.00	0.00	0.00	0.00	0.00	0.00
Mg	0.01	0.01	0.01	0.01	0.01	0.01	0.01	0.02
Ca	0.82	0.73	0.64	0.80	0.81	0.64	0.77	0.63
Na	0.19	0.28	0.35	0.22	0.21	0.37	0.24	0.37
K	0.00	0.00	0.01	0.00	0.00	0.01	0.00	0.01
total	5.01	5.00	5.00	5.01	5.01	5.01	5.01	5.00
An	80.8	72.6	64.3	78.0	79.6	63.2	76.1	62.9
Ab	18.9	26.9	34.9	21.7	20.3	36.0	23.5	36.3
Or	0.3	0.4	0.8	0.3	0.2	0.8	0.4	0.8

Grain: P = phenocryst; INC = inclusion; OVG = overgrowth; GLOM = glomerocryst

An = Anorthite; Ab = Albite; Or = Orthoclase

Table D.2. Ruapehu lavas - Clinopyroxene mineral data

Sample	WX2	WX2	WX2	WX2	WX2	WX2	WX2	WX2
Grain	P1	P1	P1	P1	P1	P2	P2	P2
Position	core 1	core 2	core 3	outer core	rim	core 1	core 2	rim
SiO_2	50.58	50.39	52.71	50.83	51.09	52.40	50.70	51.81
TiO_2	0.58	0.60	0.12	0.45	0.57	0.13	0.45	0.53
Al_2O_3	2.47	2.62	1.78	1.95	2.08	2.49	2.50	1.74
Cr_2O_3	0.21	0.14	0.79	0.00	0.00	0.76	0.58	0.02
Fe_2O_3	2.02	2.68	1.61	2.48	2.83	1.38	3.12	1.79
FeO	8.09	8.04	3.42	8.35	6.91	5.11	7.32	7.78
MnO	0.09	0.27	0.14	0.31	0.25	0.15	0.30	0.34
MgO	14.49	14.54	17.61	13.93	14.99	16.71	14.24	14.90
CaO	19.62	19.34	21.01	20.37	20.65	20.46	20.17	20.59
Na_2O	0.40	0.39	0.27	0.34	0.28	0.33	0.47	0.30
total	98.56	99.00	99.45	99.01	99.64	99.90	99.85	99.82
Si	1.91	1.90	1.93	1.92	1.91	1.92	1.90	1.93
Ti	0.02	0.02	0.00	0.01	0.02	0.00	0.01	0.01
Al	0.11	0.12	0.08	0.09	0.09	0.11	0.11	0.08
Cr	0.01	0.00	0.02	0.00	0.00	0.02	0.02	0.00
Fe(ii)	0.06	0.08	0.04	0.07	0.08	0.04	0.09	0.05
Fe(iii)	0.26	0.25	0.10	0.26	0.22	0.16	0.23	0.24
Mn	0.00	0.01	0.00	0.01	0.01	0.00	0.01	0.01
Mg	0.82	0.82	0.96	0.79	0.83	0.91	0.79	0.83
Ca	0.79	0.78	0.83	0.82	0.83	0.81	0.81	0.82
Na	0.03	0.03	0.02	0.02	0.02	0.02	0.03	0.02
total	4.00	4.00	4.00	4.00	4.00	4.00	4.00	4.00
Wo	41.23	40.35	42.51	42.20	42.08	41.95	41.91	42.09
En	42.36	42.20	49.58	40.17	42.49	47.66	41.17	42.37
Fs	16.40	17.45	7.91	17.63	15.44	10.39	16.92	15.54

Sample	WX2	WX9	WX9	WX9	WX9	WX9	WX9	WX9
Grain	INC	P1	P1	P1	GLOM	GLOM	P2	P2
Position	(in opx P1)	inner core	outer core	rim	-	-	core	rim
SiO_2	52.24	50.90	50.41	52.05	50.04	50.82	51.64	50.95
TiO_2	0.46	0.46	0.64	0.29	0.38	0.38	0.47	0.55
Al_2O_3	1.74	2.39	3.00	3.62	4.68	4.53	2.40	2.24
Cr_2O_3	0.20	0.03	0.00	0.43	0.05	0.16	0.03	0.00
Fe_2O_3	2.49	2.01	1.29	0.60	2.15	2.37	1.59	2.13
FeO	5.30	9.75	9.82	5.19	4.77	5.24	7.73	8.10
MnO	0.16	0.35	0.30	0.15	0.19	0.17	0.25	0.30
MgO	15.84	13.49	13.46	16.26	15.35	15.72	14.50	14.57
CaO	21.45	19.56	19.08	21.01	20.49	20.27	20.87	19.89
Na_2O	0.37	0.44	0.49	0.28	0.35	0.36	0.34	0.34
total	100.24	99.39	98.48	99.86	98.46	100.01	99.84	99.07
Si	1.93	1.92	1.91	1.91	1.87	1.87	1.92	1.92
Ti	0.01	0.01	0.02	0.01	0.01	0.01	0.01	0.02
Al	0.08	0.11	0.13	0.16	0.21	0.20	0.11	0.10
Cr	0.01	0.00	0.00	0.01	0.00	0.00	0.00	0.00
Fe(ii)	0.07	0.06	0.04	0.02	0.06	0.07	0.04	0.06
Fe(iii)	0.16	0.31	0.31	0.16	0.15	0.16	0.24	0.25
Mn	0.00	0.01	0.01	0.00	0.01	0.01	0.01	0.01
Mg	0.87	0.76	0.76	0.89	0.85	0.86	0.81	0.82
Ca	0.85	0.79	0.78	0.83	0.82	0.80	0.83	0.80
Na	0.03	0.03	0.04	0.02	0.02	0.03	0.02	0.02
total	4.00	4.00	4.00	4.00	4.00	4.00	4.00	4.00
Wo	43.32	41.07	40.93	43.57	43.38	42.20	43.12	41.25
En	44.54	39.41	40.19	46.92	45.21	45.54	41.69	42.04
Fs	12.13	19.52	18.89	9.50	11.40	12.26	15.19	16.71

Grain: P = phenocryst; INC = inclusion; OVG = overgrowth; GLOM = glomerocryst
Wo = wollastonite; En = enstatite; Fs = ferrosilite

Table D.2. Ruapehu lavas - Clinopyroxene mineral data continued

Sample	WX9	WX9	RB	RB	RB	RB
Grain	P3	P3	P1	P1	P1	P1
Position	core	rim	inner core	outer core	inner rim	outer rim
SiO_2	51.75	52.91	50.58	49.99	51.08	51.24
TiO_2	0.50	0.22	0.49	0.48	0.34	0.32
Al_2O_3	2.10	1.98	2.82	2.98	3.95	4.05
Cr_2O_3	0.01	0.19	0.01	0.04	0.48	0.34
Fe_2O_3	1.66	1.02	2.61	3.15	2.43	1.86
FeO	9.12	6.00	9.21	9.46	5.18	5.57
MnO	0.34	0.14	0.30	0.38	0.26	0.21
MgO	13.94	17.73	14.30	14.06	16.22	16.01
CaO	20.26	19.21	19.05	18.27	19.98	20.10
Na_2O	0.44	0.24	0.33	0.41	0.31	0.32
total	100.12	99.64	99.69	99.22	100.23	100.00
Si	1.93	1.94	1.90	1.89	1.88	1.88
Ti	0.01	0.01	0.01	0.01	0.01	0.01
Al	0.09	0.09	0.12	0.13	0.17	0.18
Cr	0.00	0.01	0.00	0.00	0.01	0.01
Fe(ii)	0.05	0.03	0.07	0.09	0.07	0.05
Fe(iii)	0.28	0.18	0.29	0.30	0.16	0.17
Mn	0.01	0.00	0.01	0.01	0.01	0.01
Mg	0.78	0.97	0.80	0.79	0.89	0.88
Ca	0.81	0.76	0.77	0.74	0.79	0.79
Na	0.03	0.02	0.02	0.03	0.02	0.02
total	4.00	4.00	4.00	4.00	4.00	4.00
Wo	42.02	38.89	39.52	38.27	41.19	41.70
En	40.23	49.95	41.27	41.00	46.53	46.22
Fs	17.75	11.16	19.21	20.73	12.28	12.08

Sample	RB	RB	RB	RB	RB	RB
Grain	P2	P2	OVG	OVG	P3	P3
Position	outer core	rim	(on opx P2)	(on olv)	core	rim
SiO_2	52.66	51.36	52.00	51.88	51.47	51.38
TiO_2	0.26	0.56	0.22	0.25	0.50	0.32
Al_2O_3	2.05	2.23	2.83	2.77	1.97	3.71
Cr_2O_3	0.33	0.00	0.80	0.64	0.00	0.34
Fe_2O_3	1.25	2.64	1.56	1.35	1.71	1.83
FeO	6.87	8.68	3.74	5.53	10.43	5.39
MnO	0.30	0.37	0.13	0.33	0.40	0.26
MgO	16.97	16.18	16.46	16.43	14.44	15.97
CaO	19.17	17.52	21.78	20.18	18.65	20.39
Na_2O	0.27	0.34	0.27	0.27	0.33	0.32
total	100.12	99.88	99.80	99.61	99.90	99.90
Si	1.94	1.91	1.91	1.91	1.93	1.89
Ti	0.01	0.02	0.01	0.01	0.01	0.01
Al	0.09	0.10	0.12	0.12	0.09	0.16
Cr	0.01	0.00	0.02	0.02	0.00	0.01
Fe(ii)	0.03	0.07	0.04	0.04	0.05	0.05
Fe(iii)	0.21	0.27	0.11	0.17	0.33	0.17
Mn	0.01	0.01	0.00	0.01	0.01	0.01
Mg	0.93	0.90	0.90	0.90	0.81	0.88
Ca	0.75	0.70	0.86	0.80	0.75	0.80
Na	0.02	0.02	0.02	0.02	0.02	0.02
total	4.00	4.00	4.00	4.00	4.00	4.00
Wo	38.92	35.78	44.62	41.56	38.53	42.20
En	47.93	45.98	46.93	47.07	41.51	46.00
Fs	13.15	18.23	8.44	11.37	19.96	11.80

Grain: P = phenocryst; INC = inclusion; OVG = overgrowth; GLOM = glomerocryst
Wo = wollastonite; En = enstatite; Fs = ferrosilite

Table D.3. Ruapehu lavas - Orthopyroxene mineral data

Sample	WX2	WX2	WX2	WX2	WX2	R96/26	R96/26	R96/26
Grain	P1	P1	P1	P2	P2	P1	P1	P2
Position	inner core	outer core	rim	core	rim	core	rim	core
SiO_2	53.59	51.35	52.72	51.50	52.76	56.08	51.97	52.37
TiO_2	0.20	0.23	0.26	0.18	0.28	0.06	0.25	0.23
Al_2O_3	1.42	1.63	1.14	1.58	1.70	1.08	0.97	0.90
Cr_2O_3	0.06	0.17	0.00	0.13	0.11	0.27	0.05	0.00
Fe_2O_3	1.27	1.59	0.92	2.10	1.11	0.00	1.12	0.68
FeO	15.13	20.16	18.44	20.13	16.01	8.40	20.47	21.71
MnO	0.35	0.52	0.44	0.60	0.45	0.22	0.64	0.57
MgO	26.33	21.60	23.64	21.70	25.19	31.45	22.06	21.45
CaO	1.30	1.60	1.58	1.65	1.54	1.57	1.52	1.48
Na_2O	0.04	0.07	0.05	0.05	0.01	0.02	0.05	0.08
total	99.68	98.92	99.19	99.62	99.15	99.16	99.09	99.46
Si	1.95	1.94	1.96	1.93	1.94	1.98	1.95	1.97
Ti	0.01	0.01	0.01	0.00	0.01	0.00	0.01	0.01
Al	0.06	0.07	0.05	0.07	0.07	0.04	0.04	0.04
Cr	0.00	0.00	0.00	0.00	0.00	0.01	0.00	0.00
Fe(ii)	0.03	0.05	0.03	0.06	0.03	0.00	0.03	0.02
Fe(iii)	0.46	0.64	0.57	0.63	0.49	0.25	0.64	0.68
Mn	0.01	0.02	0.01	0.02	0.01	0.01	0.02	0.02
Mg	1.43	1.21	1.31	1.21	1.38	1.65	1.24	1.20
Ca	0.05	0.06	0.06	0.07	0.06	0.06	0.06	0.06
Na	0.00	0.01	0.00	0.00	0.00	0.00	0.00	0.01
total	4.00	4.00	4.00	4.00	4.00	4.00	4.00	4.00
Wo	2.55	3.27	3.17	3.33	3.06	3.02	3.08	3.02
En	71.97	61.43	65.98	60.99	69.81	84.05	62.04	60.67
Fs	25.49	35.30	30.85	35.67	27.13	12.93	34.89	36.32

Sample	R96/26	WX9	WX9	WX9	RB	RB
Grain	P2	P1	P1	P2	P1	P2
Position	rim	core	rim	core	core	core
SiO_2	52.48	53.56	52.81	52.24	55.29	52.88
TiO_2	0.22	0.19	0.36	0.24	0.04	0.18
Al_2O_3	3.32	1.03	1.69	1.63	0.89	1.29
Cr_2O_3	0.04	0.00	0.00	0.00	0.01	0.02
Fe_2O_3	1.13	0.12	0.52	0.22	0.00	0.00
FeO	13.50	18.08	17.92	20.34	14.06	20.48
MnO	0.36	0.43	0.38	0.47	0.41	0.43
MgO	26.36	24.41	23.82	22.27	27.47	22.28
CaO	1.53	1.56	1.87	1.57	2.00	1.96
Na_2O	0.03	0.04	0.07	0.04	0.03	0.05
total	98.98	99.41	99.43	99.02	100.21	99.57
Si	1.91	1.97	1.95	1.96	1.98	1.97
Ti	0.01	0.01	0.01	0.01	0.00	0.00
Al	0.14	0.04	0.07	0.07	0.04	0.06
Cr	0.00	0.00	0.00	0.00	0.00	0.00
Fe(ii)	0.03	0.00	0.01	0.01	0.00	0.00
Fe(iii)	0.41	0.56	0.55	0.64	0.42	0.64
Mn	0.01	0.01	0.01	0.02	0.01	0.01
Mg	1.43	1.34	1.31	1.24	1.47	1.24
Ca	0.06	0.06	0.07	0.06	0.08	0.08
Na	0.00	0.00	0.00	0.00	0.00	0.00
total	4.00	4.00	4.00	4.00	4.00	4.00
Wo	3.07	3.11	3.76	3.20	3.87	3.97
En	73.61	67.85	66.75	63.29	74.19	62.91
Fs	23.31	29.03	29.49	33.51	21.93	33.12

Grain: P = phenocryst; INC = inclusion; OVG = overgrowth; GLOM = glomerocryst
Wo = wollastonite; En = enstatite; Fs = ferrosilite

Table D.4. Ruapehu lavas - Olivine mineral data

Sample	RB	RB	RB	RB	RB	RB	RB	RB
Grain	P1	P1	P2	P2	P2	P3	P3	P3
Position	core	rim	inner core	outer core	rim	inner core	outer core	rim
SiO_2	41.10	39.36	40.67	40.05	38.22	40.80	40.33	51.44
TiO_2	0.00	0.00	0.00	0.00	0.02	0.00	0.00	0.35
Al_2O_3	0.03	0.05	0.03	0.03	0.04	0.04	0.03	3.04
FeO	9.69	17.60	10.15	15.33	24.47	9.96	13.78	6.90
MnO	0.17	0.36	0.21	0.29	0.49	0.19	0.24	0.20
MgO	48.82	42.08	47.83	43.97	36.84	48.44	45.24	16.02
CaO	0.14	0.16	0.13	0.16	0.19	0.10	0.13	20.26
NiO	0.42	0.26	0.33	0.28	0.13	0.43	0.38	0.05
total	100.37	99.86	99.35	100.09	100.39	99.96	100.12	98.27
Si	1.00	1.00	1.01	1.01	1.00	1.00	1.01	1.28
Ti	0.00	0.00	0.00	0.00	0.00	0.00	0.00	0.01
Al	0.00	0.00	0.00	0.00	0.00	0.00	0.00	0.09
Fe (ii)	0.20	0.38	0.21	0.32	0.54	0.20	0.29	0.14
Mn	0.00	0.01	0.00	0.01	0.01	0.00	0.01	0.00
Mg	1.78	1.60	1.76	1.65	1.44	1.77	1.68	0.60
Ca	0.00	0.00	0.00	0.00	0.01	0.00	0.00	0.54
Ni	0.01	0.01	0.01	0.01	0.00	0.01	0.01	0.00
total	3.00	3.00	2.99	2.99	3.00	3.00	2.99	2.67
Fo	89.8	80.7	89.2	83.4	72.5	89.5	85.2	80.1
Fa	10.2	19.3	10.8	16.6	27.5	10.5	14.8	19.9

Grain: P = phenocryst; INC = inclusion; OVG = overgrowth; GLOM = glomerocryst
Fo = forsterite; Fa = fayalite

Table D.5. Satellite vents and basalts - Plagioclase mineral data

Sample	P01	P01	P01	P01
Grain	P1	P1	P2	P2
Position	core	rim	core	rim
SiO_2	54.17	55.43	54.02	60.23
TiO_2	0.00	0.00	0.04	0.06
Al_2O_3	28.72	27.21	28.90	24.21
Fe_2O_3	0.58	0.54	0.55	0.83
MnO	0.00	0.00	0.00	0.00
MgO	0.11	0.09	0.11	0.04
CaO	11.62	10.23	11.82	6.62
Na_2O	4.59	5.29	4.41	6.94
K_2O	0.52	0.66	0.45	1.26
total	100.31	99.45	100.29	100.19
Si	2.45	2.52	2.44	2.69
Ti	0.00	0.00	0.00	0.00
Al	1.53	1.46	1.54	1.28
Fe(iii)	0.02	0.02	0.02	0.03
Mn	0.00	0.00	0.00	0.00
Mg	0.01	0.01	0.01	0.00
Ca	0.56	0.50	0.57	0.32
Na	0.40	0.47	0.39	0.60
K	0.03	0.04	0.03	0.07
total	5.00	5.00	4.99	4.99
An	56.8	50.0	58.4	32.2
Ab	40.1	46.2	39.0	60.6
Or	3.0	3.8	2.6	7.2

Grain: P = phenocryst; INC = inclusion; OVG = overgrowth; GLOM = glomerocryst
An = Anorthite; Ab = Albite; Or = Orthoclase

Table D.6. Satellite vents and basalt - Clinopyroxene mineral data

Sample	P01	P01	P01	WB	WB	WB	WB	WB
Grain	OVG	P1	P1	P1	P1	P2	P2	P3
Position	(olv)	core	rim	core	rim	core	rim	core
SiO_2	52.27	51.88	51.68	51.40	51.41	53.13	52.34	53.06
TiO_2	0.40	0.62	0.32	0.43	0.37	0.14	0.24	0.22
Al_2O_3	3.11	2.40	4.02	3.59	3.58	1.67	2.80	1.94
Cr_2O_3	0.32	0.10	0.42	0.72	0.30	0.61	0.75	0.41
Fe_2O_3	1.61	0.09	1.25	1.91	1.62	1.47	1.55	2.04
FeO	4.34	10.02	5.15	4.23	6.33	3.13	4.56	3.16
MnO	0.18	0.28	0.21	0.16	0.16	0.15	0.21	0.20
MgO	17.10	15.38	16.82	16.20	17.85	17.51	17.35	17.58
CaO	20.46	18.17	19.37	21.62	17.79	22.12	20.43	21.70
Na_2O	0.35	0.34	0.41	0.20	0.16	0.18	0.20	0.24
total	100.14	99.29	99.65	100.46	99.56	100.10	100.44	100.57
Si	1.91	1.94	1.90	1.88	1.89	1.94	1.91	1.93
Ti	0.01	0.02	0.01	0.01	0.01	0.00	0.01	0.01
Al	0.13	0.11	0.17	0.15	0.15	0.07	0.12	0.08
Cr	0.01	0.00	0.01	0.02	0.01	0.02	0.02	0.01
Fe(ii)	0.04	0.00	0.03	0.05	0.04	0.04	0.04	0.06
Fe(iii)	0.13	0.31	0.16	0.13	0.19	0.10	0.14	0.10
Mn	0.01	0.01	0.01	0.00	0.00	0.00	0.01	0.01
Mg	0.93	0.86	0.92	0.88	0.98	0.95	0.94	0.95
Ca	0.80	0.73	0.76	0.85	0.70	0.86	0.80	0.84
Na	0.02	0.02	0.03	0.01	0.01	0.01	0.01	0.02
total	4.00	4.00	4.00	4.00	4.00	4.00	4.00	4.00
Wo	41.83	38.11	40.48	44.18	36.43	44.18	41.36	43.20
En	48.65	44.90	48.92	46.07	50.87	48.65	48.89	48.71
Fs	9.52	16.99	10.60	9.75	12.71	7.17	9.75	8.09

Sample	WB	OQ	OQ	OQ	OQ	OQ	OQ	OQ
Grain	P3	P1	P1	P1	OVG 1	OVG 2	P2	P2
Position	rim	core 1	core 2	rim	(on opx P1)	(on olv P2)	-	-
SiO_2	52.35	54.56	54.09	50.59	51.38	52.19	52.93	53.75
TiO_2	0.24	0.07	0.09	0.39	0.31	0.21	0.20	0.10
Al_2O_3	2.51	1.05	1.19	3.73	1.67	3.34	2.38	1.66
Cr_2O_3	0.97	0.75	0.33	0.04	0.10	0.28	0.28	0.75
Fe_2O_3	1.92	0.00	0.00	2.50	1.56	0.50	0.40	0.00
FeO	3.42	4.20	5.23	6.33	9.50	6.69	6.16	5.15
MnO	0.16	0.08	0.19	0.23	0.29	0.14	0.14	0.15
MgO	16.75	18.26	17.52	16.13	15.43	16.54	16.73	17.64
CaO	22.16	20.66	21.03	19.24	18.29	19.47	20.46	20.75
Na_2O	0.21	0.17	0.14	0.19	0.21	0.28	0.24	0.22
total	100.70	99.80	99.81	99.36	98.73	99.65	99.92	100.17
Si	1.91	1.98	1.98	1.88	1.94	1.92	1.94	1.96
Ti	0.01	0.00	0.00	0.01	0.01	0.01	0.01	0.00
Al	0.11	0.04	0.05	0.16	0.07	0.14	0.10	0.07
Cr	0.03	0.02	0.01	0.00	0.00	0.01	0.01	0.02
Fe(ii)	0.05	0.00	0.00	0.07	0.04	0.01	0.01	0.00
Fe(iii)	0.10	0.13	0.16	0.20	0.30	0.21	0.19	0.16
Mn	0.00	0.00	0.01	0.01	0.01	0.00	0.00	0.00
Mg	0.91	0.99	0.96	0.89	0.87	0.91	0.92	0.96
Ca	0.86	0.80	0.82	0.77	0.74	0.77	0.80	0.81
Na	0.02	0.01	0.01	0.01	0.02	0.02	0.02	0.02
total	4.00	3.99	3.99	4.00	4.00	4.00	4.00	4.00
Wo	44.67	41.81	42.35	39.62	37.71	40.42	41.80	41.97
En	46.98	51.42	49.12	46.23	44.26	47.77	47.58	49.65
Fs	8.35	6.76	8.54	14.16	18.03	11.80	10.62	8.38

Grain: P = phenocryst; INC = inclusion; OVG = overgrowth; GLOM = glomerocryst
Wo = wollastonite; En = enstatite; Fs = ferrosilite

Table D.6. Satellite vents and basalt - Clinopyroxene mineral data continued

Sample	OQ	OQ	OQ	OQ
Grain	P3	P3	P3	P3
Position	core 1	core 2	outer core	rim
SiO_2	51.84	52.65	53.99	50.52
TiO_2	0.19	0.26	0.04	0.52
Al_2O_3	2.22	2.69	1.08	3.94
Cr_2O_3	0.23	0.13	0.69	0.18
Fe_2O_3	1.75	0.37	0.51	2.90
FeO	4.92	6.83	3.76	5.34
MnO	0.07	0.14	0.06	0.18
MgO	16.79	16.67	18.27	15.85
CaO	20.48	19.89	21.38	20.32
Na_2O	0.21	0.22	0.17	0.23
total	98.69	99.84	99.95	99.97
Si	1.93	1.94	1.96	1.87
Ti	0.01	0.01	0.00	0.01
Al	0.10	0.12	0.05	0.17
Cr	0.01	0.00	0.02	0.01
Fe(ii)	0.05	0.01	0.01	0.08
Fe(iii)	0.15	0.21	0.11	0.17
Mn	0.00	0.00	0.00	0.01
Mg	0.93	0.91	0.99	0.87
Ca	0.82	0.78	0.83	0.80
Na	0.02	0.02	0.01	0.02
total	4.00	4.00	4.00	4.00
Wo	41.83	40.76	42.64	41.70
En	47.72	47.55	50.70	45.26
Fs	10.45	11.69	6.66	13.04

Grain: P = phenocryst; INC = inclusion; OVG = overgrowth; GLOM = glomerocryst
Wo = wollastonite; En = enstatite; Fs = ferrosilite

Table D.7. Satellite vents and basalts - Orthopyroxene mineral data

Sample	P01	P01	P01	P01	P01	P01	OQ
Grain	OVG 1	OVG 2	OVG 3	P1	P1	OVG 4	INC 1
Position	(olv)	(olv)	(olv)	core	rim	(on opx P1)	(in cpx P1)
SiO_2	55.36	53.81	54.19	54.71	53.15	54.16	55.22
TiO_2	0.09	0.37	0.23	0.20	0.14	0.23	0.05
Al_2O_3	1.66	1.77	1.67	1.49	2.04	2.61	1.62
Cr_2O_3	0.08	0.18	0.52	0.39	0.67	0.31	0.18
Fe_2O_3	0.08	0.33	1.14	0.00	0.00	0.00	0.10
FeO	8.98	14.69	10.95	12.60	15.64	11.65	11.91
MnO	0.26	0.32	0.22	0.23	0.35	0.26	0.28
MgO	30.54	26.97	28.82	28.32	25.46	28.34	29.34
CaO	1.89	1.15	1.82	1.52	1.52	1.72	1.24
Na_2O	0.04	0.03	0.02	0.03	0.03	0.02	0.00
total	98.97	99.62	99.59	99.48	98.99	99.30	99.92
Si	1.96	1.95	1.94	1.96	1.95	1.94	1.96
Ti	0.00	0.01	0.01	0.01	0.00	0.01	0.00
Al	0.07	0.08	0.07	0.06	0.09	0.11	0.07
Cr	0.00	0.01	0.01	0.01	0.02	0.01	0.00
Fe(ii)	0.00	0.01	0.03	0.00	0.00	0.00	0.00
Fe(iii)	0.27	0.44	0.33	0.38	0.48	0.35	0.35
Mn	0.01	0.01	0.01	0.01	0.01	0.01	0.01
Mg	1.61	1.45	1.54	1.51	1.39	1.51	1.55
Ca	0.07	0.04	0.07	0.06	0.06	0.07	0.05
Na	0.00	0.00	0.00	0.00	0.00	0.00	0.00
total	4.00	4.00	4.00	4.00	4.00	4.00	4.00
Wo	3.66	2.27	3.53	2.98	3.07	3.41	2.40
En	82.27	74.13	77.96	77.36	71.67	78.16	79.04
Fs	14.07	23.60	18.51	19.67	25.26	18.43	18.56

Sample	OQ	OQ	OQ	OQ	OQ	OQ	OQ
Grain	INC 2	P1	P1	P1	OVG 1	OVG 2	OVG 3
Position	(in cpx P1)	core	outer core	rim	(on olv P1)	(on olv P1)	(on olv P1)
SiO_2	55.61	55.77	55.57	53.67	54.93	55.62	55.27
TiO_2	0.06	0.07	0.04	0.13	0.05	0.02	0.00
Al_2O_3	1.50	1.54	1.49	2.32	2.32	1.38	1.89
Cr_2O_3	0.27	0.26	0.31	0.13	0.12	0.34	0.21
Fe_2O_3	0.00	0.00	0.00	1.05	0.41	0.60	0.00
FeO	11.08	12.20	10.65	12.54	11.30	10.09	12.07
MnO	0.18	0.28	0.17	0.25	0.18	0.19	0.22
MgO	29.92	28.94	29.95	27.40	29.36	30.32	28.95
CaO	1.31	1.30	1.28	2.06	1.48	1.63	1.45
Na_2O	0.00	0.00	0.00	0.00	0.00	0.02	0.02
total	99.92	100.37	99.46	99.56	100.16	100.21	100.08
Si	1.97	1.97	1.97	1.93	1.94	1.96	1.96
Ti	0.00	0.00	0.00	0.00	0.00	0.00	0.00
Al	0.06	0.06	0.06	0.10	0.10	0.06	0.08
Cr	0.01	0.01	0.01	0.00	0.00	0.01	0.01
Fe(ii)	0.00	0.00	0.00	0.03	0.01	0.02	0.00
Fe(iii)	0.33	0.36	0.32	0.38	0.33	0.30	0.36
Mn	0.01	0.01	0.01	0.01	0.01	0.01	0.01
Mg	1.58	1.53	1.58	1.47	1.55	1.59	1.53
Ca	0.05	0.05	0.05	0.08	0.06	0.06	0.06
Na	0.00	0.00	0.00	0.00	0.00	0.00	0.00
total	4.00	3.99	3.99	4.00	4.00	4.00	4.00
Wo	2.54	2.54	2.49	4.04	2.88	3.12	2.83
En	80.48	78.47	81.08	74.88	79.19	80.71	78.48
Fs	16.99	18.99	16.43	21.08	17.93	16.17	18.69

Grain: P = phenocryst; INC = inclusion; OVG = overgrowth; GLOM = glomerocryst
Wo = wollastonite; En = enstatite; Fs = ferrosilite

Table D.7. Satellite vents and basalts - Orthopyroxene mineral data continued

Sample	OQ	OQ	OQ	OQ
Grain	OVG 4	INC 3	INC 4	INC 5
Position	(on olv P2)	(in cpx P2)	(in cpx P2)	(in cpx P2)
SiO_2	54.72	52.42	54.80	56.43
TiO_2	0.10	0.16	0.05	0.05
Al_2O_3	2.57	3.91	1.64	1.30
Cr_2O_3	0.04	0.09	0.15	0.36
Fe_2O_3	0.00	0.92	0.37	0.00
FeO	12.02	14.24	11.71	9.73
MnO	0.21	0.32	0.18	0.10
MgO	28.48	25.80	29.13	30.55
CaO	1.43	1.65	1.31	1.57
Na_2O	0.01	0.03	0.01	0.01
total	99.58	99.52	99.36	100.08
Si	1.95	1.90	1.96	1.98
Ti	0.00	0.00	0.00	0.00
Al	0.11	0.17	0.07	0.05
Cr	0.00	0.00	0.00	0.01
Fe(ii)	0.00	0.02	0.01	0.00
Fe(iii)	0.36	0.43	0.35	0.29
Mn	0.01	0.01	0.01	0.00
Mg	1.51	1.39	1.55	1.60
Ca	0.05	0.06	0.05	0.06
Na	0.00	0.00	0.00	0.00
total	3.99	4.00	4.00	3.99
Wo	2.83	3.33	2.54	3.04
En	78.31	72.43	78.90	82.14
Fs	18.86	24.24	18.56	14.82

Grain: P = phenocryst; INC = inclusion; OVG = overgrowth; GLOM = glomerocryst
Wo = wollastonite; En = enstatite; Fs = ferrosilite

Table D.8. Satellite vents and basalts - Olivine mineral data

Sample	P01	P01	P01	P01	WB	WB	WB	WB
Grain	P1	P1	P2	P2	P1	P1	P1	P2
Position	core	rim	core	rim	inner core	outer core	rim	core
SiO_2	40.85	41.05	37.98	37.76	39.93	40.94	39.78	40.42
TiO_2	0.00	0.00	0.00	0.00	0.00	0.00	0.02	0.00
Al_2O_3	0.01	0.00	0.00	0.00	0.00	0.00	0.00	0.00
FeO	8.53	6.44	22.74	21.96	13.52	9.24	15.11	12.75
MnO	0.06	0.09	0.25	0.20	0.23	0.16	0.27	0.23
MgO	49.10	51.09	37.97	38.30	45.73	48.76	43.80	46.31
CaO	0.17	0.19	0.15	0.13	0.03	0.16	0.18	0.19
NiO	0.49	0.65	0.53	0.44	0.22	0.32	0.06	0.12
total	99.22	99.51	99.63	98.77	99.65	99.58	99.22	100.00
Si	1.00	1.00	1.00	1.00	1.00	1.01	1.01	1.00
Ti	0.00	0.00	0.00	0.00	0.00	0.00	0.00	0.00
Al	0.00	0.00	0.00	0.00	0.00	0.00	0.00	0.00
Fe (ii)	0.18	0.13	0.50	0.48	0.28	0.19	0.32	0.26
Mn	0.00	0.00	0.01	0.00	0.00	0.00	0.01	0.00
Mg	1.80	1.85	1.49	1.51	1.71	1.79	1.65	1.72
Ca	0.00	0.00	0.00	0.00	0.00	0.00	0.00	0.00
Ni	0.01	0.01	0.01	0.01	0.00	0.01	0.00	0.00
total	3.00	3.00	3.00	3.00	3.00	2.99	2.99	3.00
Fo	91.1	93.3	74.6	75.5	85.6	90.2	83.5	86.4
Fa	8.9	6.7	25.4	24.5	14.4	9.8	16.5	13.6

Sample	WB	WB	WB	OQ	OQ	OQ	OQ	OQ
Grain	P2	P3	P3	P1	OVG	P2	OVG	OVG
Position	rim	core	rim	core	(on olv P1)	core	(on olv P2)	(on olv P2)
SiO_2	39.39	41.11	39.64	39.69	39.77	40.12	39.55	40.18
TiO_2	0.00	0.01	0.00	0.00	0.01	0.00	0.00	0.00
Al_2O_3	0.00	0.00	0.00	0.00	0.01	0.00	0.03	0.00
FeO	16.54	8.43	14.46	11.60	13.35	11.89	16.17	16.39
MnO	0.21	0.17	0.25	0.31	0.27	0.18	0.27	0.14
MgO	42.68	49.40	44.70	47.62	46.32	47.60	43.45	43.16
CaO	0.15	0.13	0.15	0.04	0.05	0.09	0.10	0.11
NiO	0.13	0.31	0.11	0.06	0.04	0.22	0.22	0.05
total	99.11	99.57	99.31	99.32	99.82	100.10	99.78	100.04
Si	1.01	1.01	1.00	0.99	0.99	0.99	1.00	1.01
Ti	0.00	0.00	0.00	0.00	0.00	0.00	0.00	0.00
Al	0.00	0.00	0.00	0.00	0.00	0.00	0.00	0.00
Fe (ii)	0.35	0.17	0.31	0.24	0.28	0.25	0.34	0.35
Mn	0.00	0.00	0.01	0.01	0.01	0.00	0.01	0.00
Mg	1.62	1.80	1.68	1.77	1.73	1.76	1.64	1.62
Ca	0.00	0.00	0.00	0.00	0.00	0.00	0.00	0.00
Ni	0.00	0.01	0.00	0.00	0.00	0.00	0.00	0.00
total	2.99	2.99	3.00	3.01	3.01	3.01	3.00	2.99
Fo	81.9	91.1	84.4	87.7	85.8	87.5	82.5	82.3
Fa	18.1	8.9	15.6	12.3	14.2	12.5	17.5	17.7

Grain: P = phenocryst; INC = inclusion; OVG = overgrowth; GLOM = glomerocryst
Fo = forsterite; Fa = fayalite

Table D.9. Xenoliths - Plagioclase mineral data

Sample	MIX	MIX	MIX	MIX	WX9 xeno	WX9 xeno	WX9 xeno	WX9 xeno
Grain	1	2	2	4	1	2	3	4
Position	-	-	-	-	-	-	-	-
SiO_2	48.34	46.71	45.74	45.69	57.54	56.55	54.33	55.28
TiO_2	0.00	0.00	0.00	0.00	0.00	0.00	0.00	0.00
Al_2O_3	32.87	34.29	34.90	34.92	27.12	26.81	28.44	27.62
Fe_2O_3	0.41	0.31	0.18	0.26	0.19	0.45	0.79	0.41
MnO	0.00	0.00	0.00	0.00	0.04	0.04	0.03	0.00
MgO	0.02	0.02	0.00	0.01	0.04	0.04	0.06	0.04
CaO	16.74	18.36	18.73	18.52	8.87	9.26	11.27	10.93
Na_2O	2.04	1.14	0.87	0.90	5.95	6.04	4.93	5.06
K_2O	0.11	0.04	0.06	0.03	0.85	1.03	0.62	0.38
total	100.51	100.87	100.48	100.33	100.61	100.23	100.47	99.73
Si	2.21	2.13	2.10	2.10	2.57	2.55	2.45	2.50
Ti	0.00	0.00	0.00	0.00	0.00	0.00	0.00	0.00
Al	1.77	1.84	1.89	1.89	1.43	1.42	1.51	1.47
Fe(iii)	0.01	0.01	0.01	0.01	0.01	0.02	0.03	0.01
Mn	0.00	0.00	0.00	0.00	0.00	0.00	0.00	0.00
Mg	0.00	0.00	0.00	0.00	0.00	0.00	0.00	0.00
Ca	0.82	0.90	0.92	0.91	0.42	0.45	0.55	0.53
Na	0.18	0.10	0.08	0.08	0.52	0.53	0.43	0.44
K	0.01	0.00	0.00	0.00	0.05	0.06	0.04	0.02
total	5.00	4.99	4.99	4.99	5.00	5.03	5.01	4.99
An	81.5	89.7	91.9	91.7	43.2	43.5	54.1	53.4
Ab	17.9	10.1	7.7	8.1	51.9	50.8	42.4	44.5
Or	0.6	0.3	0.4	0.2	4.9	5.7	3.5	2.2

Sample	R96/26 xeno	R96/26 xeno
Grain	1	2
Position	-	-
SiO_2	50.37	50.92
TiO_2	0.00	0.00
Al_2O_3	31.30	31.31
Fe_2O_3	0.36	0.34
MnO	0.00	0.01
MgO	0.06	0.01
CaO	14.51	14.46
Na_2O	3.20	3.26
K_2O	0.20	0.21
total	100.00	100.51
Si	2.298	2.309
Ti	0.000	0.000
Al	1.683	1.674
Fe(iii)	0.012	0.012
Mn	0.000	0.000
Mg	0.004	0.001
Ca	0.710	0.703
Na	0.283	0.286
K	0.012	0.012
total	5.001	4.997
An	70.77	70.24
Ab	28.09	28.58
Or	1.14	1.18

An = Anorthite; Ab = Albite; Or = Orthoclase

Table D.10. Xenoliths - Clinopyroxene and Orthopyroxene mineral data

Sample	MIX	MIX	MIX	MIX	MIX	MIX	WX9 xeno	WX9 xeno
Mineral	Cpx	Cpx	Cpx	Subcalcic	Subcalcic	Subcalcic	Opx	Opx
Position	-	-	-	-	-	-	-	-
SiO_2	51.04	50.74	50.89	50.46	50.01	50.99	50.82	48.87
TiO_2	0.29	0.18	0.49	0.35	0.16	0.19	0.25	3.97
Al_2O_3	1.04	0.74	1.16	0.81	0.44	0.48	3.37	1.89
Cr_2O_3	0.09	0.01	0.08	0.06	0.05	0.00	0.02	0.03
Fe_2O_3	0.00	0.44	0.14	0.55	0.00	0.00	0.00	0.00
FeO	17.98	16.67	16.29	27.52	28.48	26.86	23.60	33.05
MnO	0.78	0.72	0.75	1.16	1.07	0.83	0.54	0.65
MgO	10.28	9.59	11.77	13.95	13.69	14.76	20.29	13.70
CaO	18.13	20.13	17.35	5.34	3.98	4.85	0.26	0.20
Na_2O	0.18	0.12	0.22	0.06	0.04	0.11	0.01	0.02
total	99.80	99.35	99.15	100.25	97.93	99.07	99.15	102.37
Si	1.97	1.98	1.96	1.96	1.99	1.99	1.92	1.88
Ti	0.01	0.01	0.01	0.01	0.00	0.01	0.01	0.11
Al	0.05	0.03	0.05	0.04	0.02	0.02	0.15	0.09
Cr	0.00	0.00	0.00	0.00	0.00	0.00	0.00	0.00
Fe(ii)	0.00	0.01	0.00	0.02	0.00	0.00	0.00	0.00
Fe(iii)	0.58	0.54	0.53	0.90	0.95	0.88	0.75	1.06
Mn	0.03	0.02	0.02	0.04	0.04	0.03	0.02	0.02
Mg	0.59	0.56	0.68	0.81	0.81	0.86	1.14	0.79
Ca	0.75	0.84	0.72	0.22	0.17	0.20	0.01	0.01
Na	0.01	0.01	0.02	0.00	0.00	0.01	0.00	0.00
total	4.00	4.00	4.00	4.00	3.99	4.00	4.00	3.96
Wo	38.50	42.50	36.81	11.23	8.64	10.31	0.54	0.44
En	30.37	28.18	34.75	40.84	41.32	43.69	59.65	41.83
Fs	31.12	29.33	28.44	47.92	50.04	45.99	39.81	57.73

Sample	WX9 xeno
Mineral	Opx
Position	-
SiO_2	51.53
TiO_2	0.14
Al_2O_3	0.58
Cr_2O_3	0.06
Fe_2O_3	0.00
FeO	27.40
MnO	0.44
MgO	17.22
CaO	1.63
Na_2O	0.02
total	99.02
Si	1.99
Ti	0.00
Al	0.03
Cr	0.00
Fe(ii)	0.00
Fe(iii)	0.89
Mn	0.01
Mg	0.99
Ca	0.07
Na	0.00
total	3.99
Wo	3.44
En	50.64
Fs	45.92

Wo = wollastonite; En = enstatite; Fs = ferrosilite

Table D.11. Xenoliths - Glass data

Sample	WX9 xeno	WX9 xeno	WX9 xeno	WX9 xeno	WX9 xeno	WX9 xeno
Grain	glass 1	glass 2	glass 3	glass 4	glass 5	glass 7
Position	-	-	-	-	-	-
SiO_2	65.82	64.53	61.27	61.62	67.46	68.85
TiO_2	1.04	1.03	0.95	1.01	0.88	0.80
Al_2O_3	19.78	19.47	20.23	17.65	12.80	13.85
Fe_2O_3	2.55	2.43	7.08	5.81	4.68	4.42
MnO	0.14	0.18	0.12	0.08	0.11	0.07
MgO	1.31	1.02	2.83	4.45	0.88	0.75
CaO	0.10	0.20	0.13	0.12	0.99	1.10
Na_2O	1.35	2.33	2.31	3.58	4.55	4.30
K_2O	4.36	4.99	5.06	5.79	5.75	5.92
total	96.44	96.18	99.96	100.09	98.11	100.06

Sample	WX9 xeno	WX9 xeno	WX9 xeno	WB xeno	WB xeno	WB xeno
Grain	glass 8	glass 9	glass 10	glass1	glass 2	glass 3
Position	-	-	-	-	-	-
SiO_2	67.85	66.89	68.32	70.46	71.94	72.53
TiO_2	1.07	1.36	1.00	0.68	0.75	0.62
Al_2O_3	13.87	14.03	13.50	11.30	12.77	11.77
Fe_2O_3	5.23	5.56	4.97	7.57	5.69	5.92
MnO	0.12	0.10	0.06	0.11	0.01	0.09
MgO	0.92	0.69	0.90	0.64	0.25	0.42
CaO	1.37	1.01	1.47	2.96	3.51	2.37
Na_2O	3.99	4.03	3.65	1.23	2.34	1.42
K_2O	5.75	6.19	5.62	3.65	1.40	2.79
total	100.18	99.85	99.50	98.59	98.65	97.93

Sample	MIX	MIX	MIX	R96/26	R96/26	R96/26
Grain	glass 1	glass 2	glass 3	glass 1	glass 2	glass 3
Position	-	-	-	-	-	-
SiO_2	74.82	73.56	74.25	74.02	73.15	74.07
TiO_2	0.89	0.80	0.89	0.96	0.96	0.86
Al_2O_3	11.90	11.44	12.10	11.55	11.38	11.52
Fe_2O_3	3.58	4.97	4.17	3.05	2.94	3.07
MnO	0.01	0.03	0.01	0.06	0.03	0.09
MgO	0.14	0.51	0.07	0.35	0.31	0.30
CaO	0.71	1.67	0.62	0.99	1.02	0.93
Na_2O	0.81	1.10	1.30	2.86	2.75	3.21
K_2O	3.85	3.94	3.74	4.90	4.72	4.85
total	96.72	98.01	97.15	98.73	97.28	98.89

Sample	R96/26	R96/26
Grain	glass 4	glass 5
Position	-	-
SiO_2	73.89	72.38
TiO_2	0.98	0.89
Al_2O_3	11.55	11.37
Fe_2O_3	3.14	2.87
MnO	0.08	0.08
MgO	0.32	0.27
CaO	0.97	0.93
Na_2O	3.28	3.09
K_2O	4.73	4.84
total	98.94	96.73

Table D.12. Xenoliths - Other mineral data

Sample	WX9 xeno	WX9 xeno
Mineral	Biotite	Cordierite
Position	-	-
SiO_2	35.97	48.22
TiO_2	5.63	-
Al_2O_3	17.19	33.56
FeO	12.21	5.87
MnO	0.05	0.18
MgO	14.35	10.20
CaO	0.14	0.04
Na_2O	1.07	-
K_2O	8.79	-
H_2O	4.07	-
total	99.46	98.08
Si	5.302	4.83
Ti	0.625	-
Al	2.986	4.09
Fe (ii)	1.505	0.5
Mn	0.007	-
Mg	3.153	1.43
Ca	0.021	-
Na	0.306	0.04
K	1.653	0.03
OH	4.000	-
total	19.559	10.92
Mg#	67.59	-

Appendix E. Analytical Techniques

E.1. Sample collection and preparation for whole-rock analysis

Samples between 1-3 kg were collected from Mt. Ruapehu volcano and nearby Ohakune and Pukeonake satellite vents. The Kakuki basalt was collected from the central TVZ while samples of the Waimarino basalt and Ruapehu basalt were provided by Victoria University of Wellington and R. Price respectively. All analyses for meta-sedimentary and meta-igneous xenoliths were performed on rock powders provided by I. J. Graham.

All samples were trimmed of weathered surfaces using a rock saw with any blade marks on cut surfaces removed using corundum paper and then cleaned with de-ionised water. A Fritsch stainless steel jaw crusher was used to produce a coarse crush of the sample (particle size < 1 cm^3) which was then halved using the "cone and quartering" technique. Half the coarse crush was reserved for mineral picking while the remaining sample was ground to powder using an agate ball mill. The powders were then ready for use in whole rock chemistry procedures.

E.2. Major Element analysis

Major element contents on lavas were determined on glass discs produced from the flux fusion method - details provided below. Analyses were performed using the Automated Philips PW2404 X-ray fluorescence spectrometer at the University of Edinburgh.

Approximately 5g of rock powder from each sample was placed in an oven at 110°C for ~ 24 hours to remove moisture. 0.8-0.9g of dried sample was then placed in a pre-weighed platinum crucible and the combined weight recorded. The crucible was then covered with a platinum lid and placed in a furnace at 1100°C for 20 minutes to

ignite the sample. The crucible was then reweighed to calculate the loss on ignition, following which spectroflux 105 was added at five times the weight of the ignited sample plus an additional 0.03g to balance any volatile loss from the flux. The sample - flux combination was then fused at 1100°C for 20 minutes, immediately followed by swirling of the crucible to ensure the sample-flux mixture had completely dissolved and then allowed to cool. An additional amount of flux was then added to achieve a 5:1 flux-sample ratio (±0.0003g). This final sample-flux combination was placed over a burner for approximately 5 minutes, interspersed with swirling of the crucible to ensure dissolution, then immediately poured into a cast iron mould on a hot plate set at 220°C and placed under a glass cover. Once the sample had completely annealed the glass disc was removed from the hotplate and allowed to cool. The disc was then trimmed of any surplus glass, labelled on its underlying surface, placed in a sealed polythene bag and transferred to a dessicator. In house standards and international reference material (BHVO-1) were used for machine calibration and ensuring data quality throughout each analytical session.

E.3. Mineral analysis

Mineral analyses were performed on carbon coated polished thin section using a Cameca SX 50 electron microprobe at the School of Earth and Environment, University of Leeds. The accelerating voltage was 15kV and the beam current was 15nA. Detection limits for Mg, Al, Ca, K and Ti are 0.01 or less, Si, Na, Ni and Cr are ~0.03, while Fe is ~0.08. Element precision is mineral dependent but was ~5% for K, Na, Mn and Cr, ~2% for Fe, 3% for Ni and ~1% for Mg, Si, Al, Ca and Ti.

E.4. Trace Element analysis

Trace element concentrations were determined using ICP-MS on the Elan 6000 Perkin Elmer Sciex quadrupole at Durham University. The following is a brief summary of the analytical procedure and instrument operating conditions, outlined in full by Ottley et al. (2003).

Samples were processed in batches of 20-30 samples which included 3-4 blanks and 6 international rock standards. 0.1g ± 0.001 of rock powder was placed in a Teflon vial. 1 ml of 16N HNO_3 and 4 ml of 29N HF was then added and the vial sealed and placed on a hotplate (130-150°C) for a minimum of 48 hours to ensure dissolution. The solution was then allowed to evaporate, followed by the addition and dry down of 1 ml of 16N HNO_3 which was repeated twice to the remove silica as SiF_4. 2.5 ml of 16N HNO_3 was then added to the vial in addition to 10-15 ml of MilliQ H_2O. The solution was then spiked with a 1 ppm Re / 1 ppm Rh internal standard and further MilliQ H_2O added to dilute the sample to 50 ml in 3.5% HNO_3. Prior to analysis this solution was further diluted at a 1:10 ratio with 3.5% HNO_3 giving an overall sample dilution of 1:5000.

The solution from each sample was introduced to the plasma at an uptake rate of ~ 1 ml min^{-1} via a cross-flow nebuliser and Scott double-pass spray chamber with a 50 second wash-in time prior to analysis. Analysis time was approximately 3 minutes with data acquired by peak hopping with 10-60 ms dwell times depending on specific isotope detection limits. Each reading was replicated twice and based on 25 sweeps of the mass spectrum.

The Elan 6000 was calibrated during each session using in-house standards, international reference materials (W2, BHVO-1, AGV1, BE-N, BIR1 and NBS688) and procedural blanks. Any calibration drift in the instrument was monitored by

Table E.1. Accepted element abundances of international rock standards compared to those measured in this study

	W2			BIR1			BHVO-1			AGV1		
PPM	Accepted Value	(n = 17) AVG	1SD	Accepted Value	(n = 8) AVG	1SD	Accepted Value	(n = 8) AVG	1SD	Accepted Value	(n = 8) AVG	1SD
Sc	35	35.83	2.12	44	42.71	1.81	31.80	31.32	1.13	12.10	12.16	1.02
V	262	266.57	6.81	313	323.58	10.01	317.00	316.39	4.77	123.00	120.23	1.93
Cr	93	90.39	2.56	382	396.61	13.97	289.00	292.42	4.19	12.00	8.42	0.38
Co	44	45.19	1.30	51.4	53.60	1.27	45.00	45.55	0.68	15.10	15.46	0.20
Ni	70	80.80	2.00	166	194.65	6.11	121.00	134.03	0.83	17.00	18.82	2.00
Cu	103	104.44	2.69	126	118.84	2.57	136.00	137.64	1.93	60.00	57.39	0.82
Zn	77	74.30	1.63	71	67.31	1.87	105.00	109.16	1.23	88.00	84.46	1.42
Ga	20	17.51	0.49	16	15.18	0.41	21.00	21.05	0.38	20.00	20.24	0.19
Rb	20	19.80	0.43	0.27	0.22	0.02	11.00	9.31	0.18	67.00	66.81	0.61
Sr	194	199.73	5.84	108	110.28	3.44	403.00	395.02	13.45	662.00	661.91	11.72
Y	24	22.54	0.42	16	16.34	0.40	27.60	27.40	0.15	21.00	20.06	0.29
Zr	94	87.63	1.57	22	14.71	0.34	179.00	172.78	1.77	225.00	230.10	2.42
Nb	7.9	7.57	0.09	2	0.64	0.01	19.00	19.22	0.09	15.00	14.78	0.11
Cs	0.99	0.88	0.03	0.45	0.01	0.01	0.13	0.09	0.01	1.26	1.25	0.04
Ba	182	172.14	3.43	7.7	7.10	0.73	139.00	134.96	3.10	1221.00	1231.07	16.80
La	11.4	10.46	0.23	0.88	0.63	0.04	15.80	15.42	0.36	38.00	38.41	0.78
Ce	24	22.56	0.44	2.5	1.91	0.08	39.00	37.34	0.85	66.00	67.87	1.20
Pr	5.9	3.13	0.07	0.5	0.39	0.02	5.70	5.68	0.15	6.50	8.88	0.25
Nd	14	13.60	0.26	2.5	2.51	0.06	25.20	26.18	0.58	34.00	33.56	0.47
Sm	3.25	3.36	0.07	1.08	1.12	0.03	6.20	6.30	0.11	5.90	5.94	0.12
Eu	1.1	1.12	0.02	0.54	0.53	0.02	2.06	2.11	0.04	1.66	1.65	0.05
Gd	3.6	3.90	0.06	1.9	2.00	0.05	6.40	6.56	0.08	5.20	4.91	0.09
Tb	0.63	0.65	0.01	0.41	0.39	0.01	0.96	0.99	0.02	0.71	0.68	0.01
Dy	3.8	3.85	0.06	2.4	2.56	0.07	5.20	5.32	0.07	3.80	3.56	0.07
Ho	0.76	0.80	0.01	0.5	0.58	0.01	0.99	1.00	0.01	0.73	0.68	0.01
Er	2.5	2.14	0.03	1.8	1.65	0.03	2.40	2.42	0.03	1.61	1.76	0.03
Tm	0.38	0.33	0.01	0.27	0.26	0.01	0.33	0.34	0.00	0.32	0.27	0.01
Yb	2.05	2.07	0.03	1.7	1.67	0.02	2.02	2.02	0.02	1.67	1.67	0.02
Lu	0.33	0.33	0.00	0.26	0.27	0.01	0.29	0.30	0.00	0.28	0.27	0.00
Hf	2.56	2.35	0.03	0.58	0.59	0.01	4.38	4.44	0.04	5.10	5.14	0.05
Ta	0.5	0.49	0.01	0.0062	0.05	0.00	1.23	1.25	0.01	0.92	0.91	0.01
Pb (total)	9.3	7.65	0.08	3.2	2.94	0.14	2.60	2.27	0.14	36.00	35.88	0.37
Th	2.2	2.16	0.03	0.0031	0.04	0.00	1.08	1.24	0.02	6.50	6.40	0.05
U	0.53	0.48	0.01	0.01	0.01	0.00	0.42	0.41	0.01	1.89	1.89	0.01

	BE-N			NBS688			detection limit	detection limit	maximum blank measured
PPM	Accepted Value	(n = 11) AVG	1SD	Accepted Value	(n = 8) AVG	1SD	solid ng g^{-1}	soln pg ml^{-1}	(n = 40, ppm)
Sc	22.00	22.38	0.88	38.00	36.15	1.62	212.00	42.00	1.67
V	235.00	232.34	5.16	242.00	247.61	6.28	273.00	55.00	0.17
Cr	360.00	358.20	10.96	332.00	320.23	10.36	532.00	106.00	1.95
Co	61.00	61.74	1.50	49.00	48.40	1.06	19.50	3.90	0.05
Ni	267.00	292.61	11.20	158.00	176.29	5.41	897.00	179.00	0.80
Cu	72.00	72.22	1.41	96.00	88.80	3.35	128.00	26.00	0.26
Zn	120.00	121.91	2.85	84.00	71.46	1.78			15.54
Ga	17.00	17.76	0.38	17.00	15.86	0.46	34.30	6.90	0.09
Rb	47.00	47.55	0.81	1.91	1.93	0.05	13.40	2.70	0.03
Sr	1370.00	1462.73	124.80	169.20	168.60	5.50	43.00	0.64	0.09
Y	30.00	30.41	0.57	17.00	20.88	0.50	20.90	4.20	0.07
Zr	265.00	272.22	3.13	61.00	55.06	0.81	25.20	5.00	0.29
Nb	100.00	118.28	0.91	5.00	4.65	0.06	9.72	1.90	0.08
Cs	0.80	0.74	0.02	0.24	0.04	0.01	3.79	0.80	0.02
Ba	1025.00	1043.49	20.91	200.00	173.19	5.00	111.00	22.00	0.11
La	82.00	81.98	1.83	5.30	5.19	0.21	3.73	0.75	0.01
Ce	152.00	148.19	3.45	13.00	11.80	0.42	12.20	2.40	0.03
Pr	16.90	18.14	0.60	2.40	1.82	0.08	2.57	0.51	0.00
Nd	70.00	69.69	1.65	9.60	8.83	0.27	13.20	2.60	0.01
Sm	12.00	12.42	0.26	2.50	2.44	0.08	2.84	0.57	0.00
Eu	3.60	3.71	0.11	1.01	1.00	0.04	1.78	0.36	0.00
Gd	9.00	10.10	0.25	3.20	3.21	0.10	3.01	0.60	0.00
Tb	1.30	1.32	0.03	0.52	0.55	0.01	0.30	0.06	0.00
Dy	6.29	6.37	0.11	3.40	3.41	0.08	2.12	0.42	0.00
Ho	1.03	1.09	0.01	0.81	0.74	0.02	0.40	0.08	0.01
Er	2.48	2.44	0.06	2.10	2.07	0.05	0.23	0.05	0.00
Tm	0.37	0.33	0.01	0.29	0.33	0.00	0.40	0.08	0.00
Yb	1.80	1.84	0.03	2.05	2.10	0.03	0.44	0.09	0.00
Lu	0.24	0.27	0.01	0.35	0.34	0.00	0.12	0.02	0.00
Hf	5.40	5.73	0.06	1.55	1.50	0.03	4.46	0.89	0.01
Ta	5.50	6.10	0.10	0.31	0.31	0.03	0.68	0.14	0.00
Pb (total)	4.00	4.02	0.05	3.30	2.84	0.18	25.40	5.10	0.17
Th	11.00	10.71	0.13	0.33	0.33	0.02	2.73	0.55	0.00
U	2.40	2.40	0.02	0.31	0.33	0.04	0.78	0.16	0.00

Accepted standard values taken from Potts et al. (1992)

Table E.2. Comparison of trace element concentrations of internal standards (lavas)

PPM	WX22	WX22	WX22	AVERAGE	1SD	RSD	TX13	TX13	TX13	AVERAGE	1SD	RSD	WB	WB	WB	AVERAGE	1SD	RSD	TX10	TX10
Sc	23.09	23.25	23.38	23.24	0.1	0.6	26.11	26.65	24.60	25.79	1.1	4.1	33.35	32.17	32.04	32.52	0.7	2.2	17.30	17.91
V	182.01	183.89	181.54	182.48	1.2	0.7	192.99	195.02	193.26	193.76	1.1	0.6	208.13	201.96	196.65	202.25	5.7	2.8	190.78	200.86
Cr	77.27	76.32	76.61	76.73	0.5	0.6	151.89	152.10	149.60	151.20	1.4	0.9	960.72	881.89	761.73	868.11	100.2	11.5	53.13	47.87
Co	24.53	24.85	24.57	24.65	0.2	0.7	25.46	25.58	25.90	25.65	0.2	0.9	57.51	55.70	54.46	55.89	1.5	2.7	16.72	17.72
Ni	40.08	40.70	39.80	40.20	0.5	1.1	54.46	52.82	54.96	54.08	1.1	2.1	429.57	424.35	406.62	420.18	12.0	2.9	17.18	18.14
Cu	44.34	44.37	44.59	44.43	0.1	0.3	35.95	35.83	37.12	36.30	0.7	2.0	94.30	89.65	87.35	90.43	3.5	3.9	26.94	27.34
Zn	61.90	62.84	61.33	62.02	0.8	1.2	63.11	61.88	62.43	62.47	0.6	1.0	64.76	62.18	60.23	62.39	2.3	3.6	58.34	62.19
Ga	17.75	17.68	17.49	17.64	0.1	0.8	17.23	17.05	17.24	17.17	0.1	0.6	13.03	12.50	12.21	12.58	0.4	3.3	18.06	18.63
Rb	60.08	60.27	59.84	60.06	0.2	0.4	66.10	65.52	67.00	66.21	0.7	1.1	16.13	15.45	15.18	15.58	0.5	3.1	77.87	80.92
Sr	286.98	288.37	285.83	287.06	1.3	0.4	245.19	245.89	251.49	247.52	3.5	1.4	336.76	326.29	316.69	326.58	10.0	3.1	290.68	305.12
Y	19.35	19.38	19.21	19.31	0.1	0.5	21.20	21.23	21.55	21.32	0.2	0.9	12.93	12.70	12.25	12.62	0.3	2.8	20.37	21.57
Zr	116.98	116.50	117.59	117.02	0.5	0.5	125.95	123.67	125.32	124.98	1.2	0.9	47.31	45.79	44.50	45.87	1.4	3.1	143.99	150.17
Nb	4.55	4.52	4.57	4.54	0.0	0.5	4.90	4.97	4.97	4.95	0.0	0.8	2.16	2.02	1.97	2.05	0.1	4.7	5.95	6.31
Cs	3.55	3.51	3.58	3.55	0.0	1.1	2.97	2.98	3.00	2.98	0.0	0.6	0.90	0.87	0.84	0.87	0.0	3.9	4.72	5.00
Ba	359.94	354.78	358.35	357.69	2.6	0.7	330.50	332.53	338.46	333.83	4.1	1.2	117.51	115.15	112.80	115.15	2.4	2.0	430.64	447.67
La	12.02	11.79	11.76	11.85	0.1	1.2	12.29	12.43	12.56	12.43	0.1	1.1	6.72	6.60	6.43	6.58	0.1	2.3	15.24	15.85
Ce	25.46	25.39	25.42	25.42	0.0	0.2	26.59	26.95	27.25	26.93	0.3	1.2	13.86	13.53	13.18	13.53	0.3	2.5	32.35	33.47
Pr	3.41	3.39	3.42	3.40	0.0	0.5	3.57	3.60	3.66	3.61	0.0	1.2	1.80	1.75	1.72	1.76	0.0	2.5	4.15	4.32
Nd	14.03	14.00	14.00	14.01	0.0	0.2	14.60	14.78	14.71	14.70	0.1	0.6	7.53	7.36	7.13	7.34	0.2	2.7	16.87	17.46
Sm	3.12	3.12	3.12	3.12	0.0	0.1	3.28	3.30	3.31	3.30	0.0	0.4	1.73	1.68	1.64	1.68	0.0	2.9	3.63	3.77
Eu	0.85	0.85	0.83	0.84	0.0	1.3	0.84	0.84	0.88	0.85	0.0	2.5	0.52	0.50	0.49	0.51	0.0	2.8	0.91	0.94
Gd	3.36	3.26	3.20	3.27	0.1	2.5	3.49	3.48	3.53	3.50	0.0	0.7	1.92	1.90	1.84	1.89	0.0	2.4	3.52	3.67
Tb	0.53	0.54	0.53	0.53	0.0	1.0	0.57	0.56	0.58	0.57	0.0	1.6	0.34	0.33	0.32	0.33	0.0	3.5	0.56	0.58
Dy	3.14	3.13	3.13	3.13	0.0	0.2	3.35	3.40	3.42	3.39	0.0	1.0	2.03	2.01	1.94	1.99	0.0	2.5	3.28	3.39
Ho	0.66	0.65	0.64	0.65	0.0	1.5	0.72	0.71	0.72	0.71	0.0	0.1	0.44	0.43	0.43	0.43	0.0	2.1	0.68	0.70
Er	1.80	1.83	1.79	1.80	0.0	1.3	1.96	1.98	1.97	1.97	0.0	0.4	1.24	1.21	1.18	1.21	0.0	2.6	1.84	1.94
Tm	0.29	0.28	0.29	0.29	0.0	2.0	0.31	0.32	0.32	0.31	0.0	1.2	0.20	0.20	0.19	0.20	0.0	3.2	0.29	0.30
Yb	1.86	1.88	1.85	1.86	0.0	0.7	2.06	2.08	2.05	2.06	0.0	0.6	1.30	1.25	1.23	1.26	0.0	2.8	1.89	1.97
Lu	0.31	0.31	0.30	0.31	0.0	2.5	0.34	0.34	0.34	0.34	0.0	0.9	0.22	0.21	0.21	0.21	0.0	2.0	0.32	0.32
Hf	3.24	3.24	3.14	3.20	0.1	1.7	3.40	3.37	3.41	3.39	0.0	0.7	1.38	1.36	1.33	1.36	0.0	1.5	3.79	3.96
Ta	0.36	0.36	0.37	0.36	0.0	0.5	0.39	0.40	0.39	0.39	0.0	1.3	0.16	0.14	0.14	0.14	0.0	7.3	0.47	0.48
Pb	9.66	9.65	9.67	9.66	0.0	0.1	8.21	8.19	8.22	8.21	0.0	0.2	2.98	2.93	2.81	2.91	0.1	2.9	11.82	12.32
Th	5.46	5.44	5.47	5.46	0.0	0.3	5.91	5.95	5.93	5.93	0.0	0.3	1.99	1.95	1.89	1.94	0.1	2.6	6.85	7.16
U	1.46	1.47	1.45	1.46	0.0	0.7	1.59	1.60	1.60	1.60	0.0	0.6	0.47	0.46	0.45	0.46	0.0	2.1	1.79	1.87

Table E.2. Comparison of trace element concentrations of internal standards (lavas) continued

PPM	AVERAGE	1SD	RSD	RB	RB	RB	AVERAGE	1SD	RSD	WX19	WX19	WX19	AVERAGE	1SD	RSD	17469	17469	AVERAGE	1SD	RSD
Sc	17.61	0.4	2.5	33.23	32.96	32.88	33.02	0.2	0.6	20.56	20.46	20.35	20.46	0.1	0.5	8.505	8.245	8.38	0.2	2.2
V	195.82	7.1	3.6	240.57	238.15	240.01	239.58	1.3	0.5	172.23	171.98	171.37	171.86	0.4	0.3	66.426	64.423	65.42	1.4	2.2
Cr	50.50	3.7	7.4	359.77	351.70	354.62	355.36	4.1	1.2	72.25	71.46	71.26	71.66	0.5	0.7	33.9055	32.6755	33.29	0.9	2.6
Co	17.22	0.7	4.1	40.84	40.53	40.08	40.48	0.4	0.9	22.54	22.93	22.58	22.68	0.2	0.9	74.098	73.583	73.84	0.4	0.5
Ni	17.66	0.7	3.9	148.72	146.37	144.77	146.62	2.0	1.4	39.60	39.40	39.45	39.49	0.1	0.3	15.71	15.515	15.61	0.1	0.9
Cu	27.14	0.3	1.0	73.28	72.42	72.02	72.57	0.6	0.9	40.52	40.82	40.25	40.53	0.3	0.7	126.686	167.455	147.07	28.8	19.6
Zn	60.26	2.7	4.5	72.72	71.95	72.34	72.34	0.4	0.5	61.24	61.71	61.29	61.41	0.3	0.4	70.75	70.43	70.59	0.2	0.3
Ga	18.35	0.4	2.2	15.37	15.30	15.36	15.34	0.0	0.2	16.86	17.03	16.86	16.92	0.1	0.6	17.955	18.105	18.03	0.1	0.6
Rb	79.40	2.2	2.7	12.38	12.23	12.22	12.27	0.1	0.7	56.31	55.59	56.27	56.06	0.4	0.7	117.237	117.544	117.39	0.2	0.2
Sr	297.90	10.2	3.4	201.61	200.53	198.33	200.16	1.7	0.8	270.97	267.17	267.94	268.69	2.0	0.7	162.194	160.499	161.35	1.2	0.7
Y	20.97	0.8	4.0	16.66	16.53	16.37	16.52	0.1	0.9	18.39	18.14	18.20	18.24	0.1	0.7	20.285	20.038	20.16	0.2	0.9
Zr	147.08	4.4	3.0	49.89	49.26	48.68	49.27	0.6	1.2	113.28	111.74	112.15	112.39	0.8	0.7	65.643	66.807	66.23	0.8	1.2
Nb	6.13	0.3	4.1	1.48	1.43	1.45	1.45	0.0	1.5	4.43	4.45	4.44	4.44	0.0	0.2	8.655	8.6	8.63	0.0	0.5
Cs	4.86	0.2	4.2	0.34	0.34	0.34	0.34	0.0	1.2	3.60	3.64	3.59	3.61	0.0	0.6	7.371	7.265	7.32	0.1	1.0
Ba	439.16	12.0	2.7	196.46	195.77	193.41	195.21	1.6	0.8	360.06	357.76	350.72	356.18	4.9	1.4	595.916	595.33	595.62	0.4	0.1
La	15.55	0.4	2.8	4.71	4.71	4.65	4.69	0.0	0.7	12.04	12.10	11.82	11.99	0.2	1.3	31.513	31.355	31.43	0.1	0.4
Ce	32.91	0.8	2.4	10.49	10.41	10.41	10.44	0.0	0.5	26.11	25.96	25.38	25.82	0.4	1.5	65.403	64.706	65.05	0.5	0.8
Pr	4.24	0.1	2.7	1.61	1.57	1.59	1.59	0.0	1.0	3.40	3.44	3.31	3.38	0.1	1.9	8.026	8.041	8.03	0.0	0.1
Nd	17.16	0.4	2.4	7.71	7.59	7.61	7.64	0.1	0.8	14.33	14.27	13.80	14.13	0.3	2.0	28.718	29.052	28.89	0.2	0.8
Sm	3.70	0.1	2.5	2.07	2.07	2.08	2.07	0.0	0.3	3.21	3.15	3.13	3.16	0.0	1.3	5.2185	5.248	5.23	0.0	0.4
Eu	0.93	0.0	2.7	0.70	0.70	0.69	0.70	0.0	0.7	0.86	0.86	0.83	0.85	0.0	2.0	1.206	1.181	1.19	0.0	1.5
Gd	3.59	0.1	3.1	2.58	2.62	2.60	2.60	0.0	0.8	3.32	3.33	3.25	3.30	0.0	1.4	4.2	4.192	4.20	0.0	0.1
Tb	0.57	0.0	2.7	0.44	0.44	0.44	0.44	0.0	0.3	0.54	0.53	0.52	0.53	0.0	1.9	0.634	0.632	0.63	0.0	0.2
Dy	3.33	0.1	2.4	2.65	2.67	2.63	2.65	0.0	0.8	3.16	3.12	3.08	3.12	0.0	1.2	3.5655	3.559	3.56	0.0	0.1
Ho	0.69	0.0	1.8	0.59	0.58	0.58	0.58	0.0	1.4	0.66	0.66	0.65	0.66	0.0	0.5	0.694	0.701	0.70	0.0	0.7
Er	1.89	0.1	3.6	1.63	1.62	1.62	1.62	0.0	0.3	1.80	1.80	1.80	1.80	0.0	0.2	1.8855	1.9015	1.89	0.0	0.6
Tm	0.30	0.0	2.6	0.26	0.25	0.26	0.26	0.0	2.0	0.29	0.29	0.29	0.29	0.0	1.7	0.292	0.292	0.29	0.0	0.0
Yb	1.93	0.1	2.9	1.69	1.66	1.66	1.67	0.0	1.1	1.89	1.90	1.86	1.88	0.0	1.0	1.7755	1.804	1.79	0.0	1.1
Lu	0.32	0.0	1.3	0.28	0.27	0.27	0.27	0.0	1.8	0.30	0.31	0.30	0.30	0.0	1.7	0.281	0.272	0.28	0.0	2.3
Hf	3.88	0.1	3.2	1.47	1.48	1.44	1.46	0.0	1.5	3.16	3.15	3.12	3.14	0.0	0.7	1.957	1.977	1.97	0.0	0.7
Ta	0.47	0.0	1.6	0.10	0.10	0.10	0.10	0.0	2.9	0.35	0.36	0.35	0.35	0.0	2.0	0.904	0.911	0.91	0.0	0.5
Pb	12.07	0.4	2.9	3.12	3.09	3.15	3.12	0.0	0.9	10.01	10.03	9.70	9.91	0.2	1.8	23.076	22.725	22.90	0.2	1.1
Th	7.00	0.2	3.1	1.23	1.23	1.23	1.23	0.0	0.2	5.49	5.46	5.33	5.43	0.1	1.6	11.205	10.784	10.99	0.3	2.7
U	1.83	0.1	3.1	0.34	0.34	0.34	0.34	0.0	0.8	1.48	1.47	1.44	1.46	0.0	1.5	1.947	1.929	1.94	0.0	0.7

running blanks and standards prior to, during (every 10 samples) and following each run. Table E.1 displays the high level of accuracy from the analytical method by the good comparison between analyses and international standard values, in addition to the low total procedural blanks obtained throughout the study. Table E.2 displays replicate analyses of 6 lavas and 1 xenolith prepared from multiple separate dissolutions ran in the same session, with RSD values generally < 3% indicating good sample reproducibility. A comparison between ICP-MS (authors data) and XRF (Graham, 1985) data for Zr concentrations in lava samples and crustal xenoliths are displayed in Fig. E.1. Lavas show excellent agreement in Zr concentrations obtained from both analytical procedures supporting petrographical evidence that no zircon is present in these samples. However most of the meta-igneous and meta-sedimentary xenoliths display varying levels of Zr depletion in the ICP-MS data indicating digestion of accessory phases like zircon may not have been successful during sample preparation.

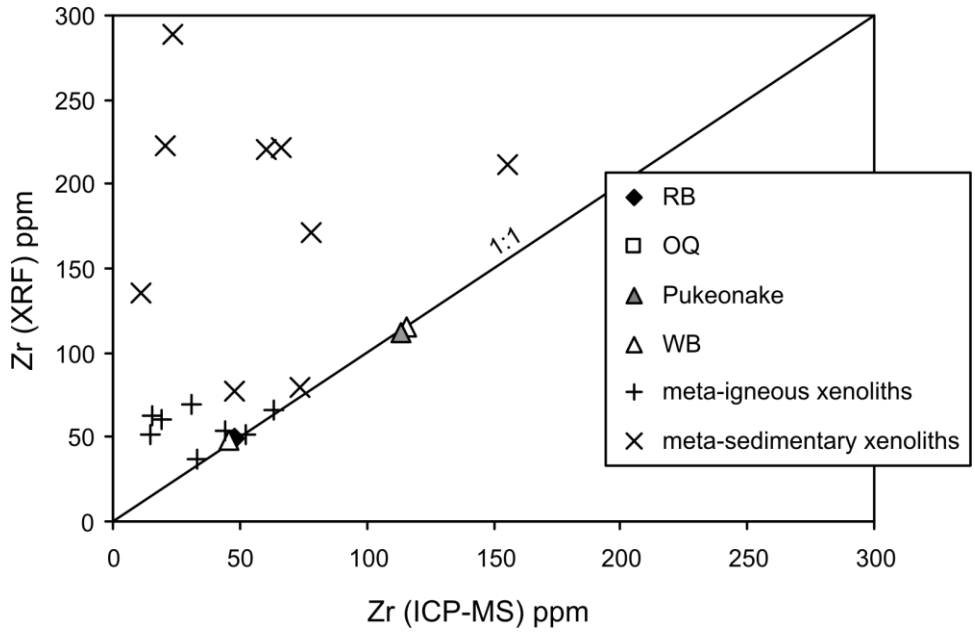

Fig. E.1. Comparsion of Zr concentrations from lavas and xenoliths using ICP-MS and XRF analysis. XRF data from Graham (1985).

E.5. Radiogenic Isotope analysis

E.5.1. Sample dissolution for Sr, Pb, Nd and Hf

Sample preparation for all radiogenic isotope analysis was carried out at Durham University in the Arthur Holmes Isotope Geology Laboratory (AHIGL). The following is a brief summary of the dissolution procedure, outlined in full by Dowall et al. (2003).

Samples were processed in batches of 20 samples which included 1 blank and 2 international rock standards (BHVO-1 and BIR1). Between 100-150 mg of rock powder was placed in a Teflon vial. 1 ml of 16N HNO_3 and 3 ml of 29N HF was then added and the vial sealed and placed on a hotplate (120°C) for 48 hours to ensure dissolution. The solution was then allowed to evaporate in a clean air extraction hood until the solute formed a viscous paste at which point 1 ml of 16N HNO_3 was added and the beaker sealed and returned to the hotplate for ~ 12 hours. The HNO_3 was then allowed to evaporate followed by repeating the HNO_3 addition and dry down step to ensure the removal of all HF. 1 ml of 12N HCl was then added to the vial and heated to dissolve the sample before drying down. Finally 1 ml of 1N HCl was added and the vial sealed and returned on the hot plate for 30 minutes prior to being transferred to centrifuge tubes (pre-cleaned with 6N HCl and MilliQ H_2O). The tubes were then centrifuged for approximately 12 minutes to separate the supernatant acid solution and insoluble fluoride precipitate. A 200 µl aliquot of this solution was then placed in a clean beaker, dried down and taken up in 150 µl of 3N HNO_3 for Sr-Pb chemistry. The remaining 800 µl was stored in the centrifuge tube for Nd-Hf chemistry.

E.5.2. Sr and Pb separation

Sr and Pb were separated using a single Sr-Spec resin column method presented in full by Charlier et al. (2006). An outline is provided in Table E.3 with additional details below.

Table E.3. Procedure for cleaning and pre-conditioning of Sr spec. resin and the collection of Sr and Pb fractions

	Reagent	Volume (ml)	Action	Purpose
Column setup	6N HCl	1 CV	Elute	Removes residual Sr
	18.2MΩ H_2O	2 CV		Removes HCl
	3N HNO_3	200 µl		Pre-conditions column
	3N HNO_3	200 µl		
Load sample (in 150µl on 3N HNO_3) and elute to waste. Clean beakers (0.5ml 6N HCl) on hotplate.				
Running the columns	3N HNO3	50 µl	Elute	Releases bulk sample from resin
		100 µl		
		150 µl		
		200 µl		
	18.2MΩ H_2O	100 µl	Collect	Releases Sr
	18.2MΩ H_2O	200 µl		
	2.5N HCl	100 µl	Elute	
	2.5N HCl	100 µl		
	8N HCl	50 µl	Collect	Releases Pb
		150 µl		
		200 µl		
		200 µl		
		200 µl		
		200 µl		

CV = column volume

The Sr-Spec resin was loaded on to the micro-column and then ~ 1-2 cm height of MilliQ H_2O passed through while gently agitating with a plastic pipette to ensure fluid flow. The resin was then cleaned and pre-conditioned following the steps outlined in Table E.3. Using a clean pipette tip, the samples were then carefully loaded on to the resin. The vials were then washed with MilliQ H_2O and then 0.5 ml of 6N HCl added and sealed before placing on a hotplate at 80°C. The bulk of the sample was then released from the column and discarded. The vials were then removed from the hotplate and thoroughly rinsed with MilliQ H_2O before being placed under the

column to collect the Sr cut. Once the Sr had been collected the sample was dried down on a hot plate and taken up in 0.5 ml 3% HNO_3 and placed in pre-cleaned micro-centrifuge tubes. 8N HCl was used to release the Pb from the column which was collected in a clean set of vials. This solution was then allowed to dry-down on a hot plate prior and similarly taken up in 0.5 ml of 3% HNO_3 and placed in pre-cleaned micro-centrifuge tubes.

E.5.3. Nd and Hf separation

Nd and Hf were separated using a two stage ion exchange method presented in full by Dowall et al. (2003). An outline is provided in Tables E.4 and E.5 with additional details below.

Once the Nd cut had been collected from the first stage cation column it was dried down and taken up in 1ml of 3% HNO_3 and then transferred into pre-cleaned (6 HCl and MilliQ H_2O) micro-centrifuge tubes. The Hf cut collected from the first stage cation column was dried down on the hotplate and 1ml 0.52N H_2SO_4 - 5% H_2O_2 added to each sample. This solution was then loaded on to the second stage cation column. Once the Hf cut was collected from the second stage column the samples were dried down at 220°C for approximately 48 hours to evaporate the concentrated H_2SO_4. As some of the second stage columns leaked small amounts of resin in to the samples, this material was removed by adding H_2O_2, converting the resin to CO_2 and H_2O. Finally the Hf cut was taken up in 0.5 ml of 3% HNO_3 and 10µl of 29N HF added before being transferred into pre-cleaned micro-centrifuge tubes.

Table E.4. Procedure for cleaning and pre-conditioning of Bio-Rad AG50W-X8 cation-exchange resin and the collection of the Nd fraction

	Reagent	Volume (ml)	Action	Purpose
Column setup	29N HF	5	Elute	Cleans column
	18.2MΩ H_2O	10		
	6N HCl	10		
	18.2MΩ H_2O	10		Pre-conditions column
	1N HCl	10		
Load sample (in 1N HCl) and collect.				
Running the columns	1N HF-1N HCl	3	Collect	Releases HFSE (Hf) and Period 1 transition elements
	1N HF-1N HCl	13	Elute	Releases bulk sample plus Rb
	2.5N HCl	14	Elute	Releases alkaline earth elements
	2N HNO_3	10	Elute	Releases Ba
	6N HCl	12	Collect	Releases Nd and other REE

Modified from Dowall et al. (2003)

Table E.5. Procedure for cleaning and pre-conditioning of Bio-Rad AG1-X8 anion-exchange resin and the collection of the Hf fraction

	Reagent	Volume (ml)	Action	Purpose
Column setup	29N HF	5	Elute	Cleans column
	18.2MΩ H_2O	10		
	12N H_2SO_4	4		
	18.2MΩ H_2O	10		
	0.52N H_2SO_4 - 5% H_2O_2	6		Pre-conditions column
Load sample (in 0.52N H_2SO_4 - 5% H_2O_2) and elute.				
Running the columns	0.52N H_2SO_4 - 5% H_2O_2	5-10	Elute	Releases Ti and other Period 1 transition elements
	1N HF-2N HCl	4	Elute	Releases Hf, Zr and other HFSE

Modified from Dowall et al. (2003)

E.5.4. Sr, Pb, Nd and Hf analysis

Sr, Pb, Nd and Hf fractions were measured for isotope ratios using the AHIGL ThermoElectron Neptune Multi-collector Plasma Mass Spectrometer (MC-ICP-MS). Detailed instrument operating condition including cup configurations and interference corrections are presented in Nowell et al. (2003) and Dowall et al. (2003). The basic analytical method used for each element on the Neptune comprises a static multi-collection routine of 1 block of 50 cycles with an integration time of 4 seconds per cycle; total analysis time 3.5 minutes.

After chemistry the Sr samples (in 1ml of 3% HNO_3) were introduced into the Neptune using an ESI PFA50 nebuliser and a dual cyclonic–Scott Double Pass spray chamber. With this sample introduction set up, and the normal H skimmer cone, the sensitivity for Sr on the Neptune is typically ~ 60V total Sr ppm^{-1} at an uptake rate of 90µl min^{-1}. Prior to analysis a small aliquot was first tested to establish the Sr concentration of each sample by monitoring the size of the ^{84}Sr beam (^{88}Sr was too high in non-diluted aliquot to measure directly) from which a dilution factor was calculated to yield a beam of approximately 20V ^{88}Sr. Instrumental mass bias was corrected for using a $^{88}Sr/^{86}Sr$ ratio of 8.375209 (the reciprocal of the $^{86}Sr/^{88}Sr$ ratio of 0.1194) and an exponential law.

Pb samples were taken up in 1ml of 3% HNO_3. Prior to analysis each sample was tested on the Neptune to determine its Pb concentration and thereby calculate the appropriate amount of Tl spike to add in order to obtain a Pb/Tl ratio of ~12. After spiking with Tl each sample was introduced into the Neptune using an ESI PFA50 nebuliser and a dual cyclonic–Scott Double Pass spraychamber. With this set up, and the normal H skimmer cone, the sensitivity for Pb on the Neptune is typically ~100V total Pb ppm^{-1} at an uptake rate of 90µl min^{-1}. Pb mass bias was corrected for externally using the $^{205}Tl/^{203}Tl$ ratio of the admixed Tl spike and an exponential law. The $^{205}Tl/^{203}Tl$ used for correcting the Pb ratios is determined for each analytical session by minimising the difference in offset between the session average Pb ratios (all ratios) and the Galer and Abouchami (1998) values. It is the ratio that gives the best fit of all the Pb ratios to the values of Galer and Abouchami (1998) simultaneously.

The REE cuts containing the Nd fraction (in 1ml of 3% HNO_3) were introduced into the Neptune using an ESI PFA50 nebuliser and a dual cyclonic–Scott

Double Pass spray chamber. With this sample introduction set up, and the normal H skimmer cone, the sensitivity for Nd on the Neptune is 60-80V total Nd ppm^{-1} at an uptake rate of 90µl min^{-1}. Instrumental mass bias was corrected for using a $^{146}Nd/^{145}Nd$ ratio of 2.079143 (equivalent to the more commonly used $^{146}Nd/^{144}Nd$ ratio of 0.7219) and an exponential law. The $^{146}Nd/^{145}Nd$ ratio is used for correcting mass bias since at Durham Nd isotopes are measured on a total REE-cut from the 1st stage cation columns and this is the only Ce and Sm-free stable Nd isotope ratio. This approach requires a correction for isobaric interferences from Sm on ^{144}Nd, ^{148}Nd and ^{150}Nd (see Nowell and Parrish, 2002).

Hf samples (in 0.5 ml 3% HNO_3 - 1N HF) were introduced using an ESI PFA50 nebuliser together with a Cetac Aridus desolvator. With this sample introduction set up, and the high sensitivity X skimmer cone, the sensitivity for Hf on the Neptune was 400-460V total Hf ppm^{-1} at an uptake rate of 90µl min^{-1}. Instrumental mass bias was corrected for using a $^{179}Hf/^{177}Hf$ ratio of 0.7325 and an exponential law. Corrections for isobaric interferences from Yb and Lu on ^{176}Hf were made by monitoring $^{172\text{-}173}Yb$ and ^{175}Lu and using the approach of Nowell and Parrish (2002).

E.5.5. Accuracy, precision, reproducibility and repeatability of data

Samples were analysed over several sessions with data quality being monitored by regular analysis (every 5 samples) of standard reference materials throughout each run. Details of individual standards from each run are displayed in Table E.6 and a summary of all standard data presented in Table E.7. $^{87}Sr^{86}Sr$, $^{143}Nd/^{144}Nd$ and $^{176}Hf/^{177}Hf$ reproducibility for respective standard solutions are all better than 31 ppm with most being less than 20 ppm (Table E.6).

Table E.6. Reproducibility and accuracy of Sr, Nd, Pb and Hf isotope ratios for standard solutions measured in individual runs

$^{87}Sr/^{86}Sr$	30/03/2006 (a)	05/08/2006 (b)	05/10/2006 (c)	19/09/2006 (d)
n =	13	9	9	11
NBS 987	0.710248	0.710265	0.710261	0.710280
2SD abs	0.000014	0.000009	0.000007	0.000011
2SD ppm	20.4	12.3	10.1	15.4
$^{143}Nd/^{144}Nd$	29/11/2005 (a)	10/04/2006 (b)	12/06/2006 (c)	20/09/2006 (d)
n =	12	12	16	13
J&M all	0.511109	0.511112	0.511111	0.511103
2SD abs	0.000007	0.000007	0.000008	0.000010
2SD ppm	13.7	13.8	16.2	19.7
n =	6	6	9	7
J&M - pure	0.511107	0.51111	0.511109	0.511101
2SD abs	0.000006	0.000006	0.000007	0.000011
2SD ppm	11.1	12.1	12.7	21.0
n =	6	6	7	6
J&M - Sm doped	0.511111	0.511114	0.511113	0.511106
2SD abs	0.000007	0.000006	0.000009	0.000007
2SD ppm	13.7	12.3	18.0	13.7
$^{206}Pb/^{204}Pb$	04/11/2006 (a)	05/11/2006 (b)	21/09/2006 (c)	25/09/2006 (d)
n =	10	12	8	8
NBS 981	16.9405	16.9405	16.9409	16.9405
2SD abs	0.0011	0.0006	0.0016	0.0035
2SD ppm	64.7	33.7	94.7	207.8
ΔGaler et al ppm	[illegible]	[illegible]	[illegible]	[illegible]
$^{207}Pb/^{204}Pb$	04/11/2006 (a)	05/11/2006 (b)	21/09/2006 (c)	25/09/2006 (d)
n =	10	12	8	8
NBS 981	15.4969	15.4966	15.4971	15.4961
2SD abs	0.0012	0.0005	0.0011	0.0011
2SD ppm	77.8	33.6	69.4	70.7
ΔGaler et al ppm	[illegible]	[illegible]	[illegible]	[illegible]
$^{208}Pb/^{204}Pb$	04/11/2006 (a)	05/11/2006 (b)	21/09/2006 (c)	25/09/2006 (d)
n =	10	12	8	8
NBS 981	36.7155	36.7143	36.7165	36.7138
2SD abs	0.0031	0.0017	0.0044	0.0066
2SD ppm	84.0	45.8	120.4	179.5
ΔGaler et al ppm	[illegible]	[illegible]	[illegible]	[illegible]
$^{176}Hf/^{177}Hf$	16/06/2006 (a)	22/09/2006 (b)		
n =	12	9		
JMC 475	0.282148	0.282142		
2SD abs	0.000009	0.000008		
2SD ppm	30.4	27.3		

Letters in parentheses refer to corresponding analytical session of sample data

$^{206}Pb/^{204}Pb$, $^{207}Pb/^{204}Pb$ and $^{208}Pb/^{204}Pb$ reproducibility for respective standard solutions for NBS 981 is better than 208 ppm in all cases, with most being better than 100 ppm. The average standard isotope ratios are within error of respective accepted values. The good agreement between pure Nd and Sm doped Nd isotopic standard ratios illustrates the accuracy of the interference element corrections performed on the total REE Nd cut. All Sr, Pb, Nd and Hf isotope data within this thesis are plotted relative to NBS 987 ($^{87}Sr^{86}Sr$ = 0.71024; Thirlwall, 1991), NBS 981 ($^{206}Pb/^{204}Pb$ = 16.9405, $^{207}Pb/^{204}Pb$ = 15.4963, $^{208}Pb/^{204}Pb$ = 36.7219; (Galer and Abouchami, 1998), J&M ($^{143}Nd/^{144}Nd$ = 0.51111; Royse et al., 1998) and JMC ($^{176}Hf/^{177}Hf$ = 0.282160; Nowell et al., 1998).

Table E.7. Average reproducibility and accuracy of Sr, Nd, Pb and Hf isotope ratios for standard solutions measured during this study

Element and Standard	Ratio	Accepted or reported value	Number of standards run	Mean measured value	Error (± 2SD absolute)	Error (± 2SD ppm)
Sr (NBS 987)	$^{87}Sr/^{86}Sr$	0.71024i	42	0.710263	0.000027	37.8
Nd (J&M - pure)	$^{143}Nd/^{144}Nd$	0.51111ii	28	0.511107	0.000010	20.0
Nd (J&M - Sm doped)	$^{143}Nd/^{144}Nd$	0.51111ii	25	0.511111	0.000009	18.5
Nd (J&M all)	$^{143}Nd/^{144}Nd$	0.51111ii	53	0.511109	0.000010	20.5
Pb (NBS 981)	$^{206}Pb/^{204}Pb$	16.9405iii	38	16.9406	0.00182	107.6
Pb (NBS 981)	$^{207}Pb/^{204}Pb$	15.4963iii	38	15.4967	0.00118	76.4
Pb (NBS 981)	$^{208}Pb/^{204}Pb$	36.7219iii	38	36.7150	0.00440	119.8
Hf (JMC 475 - Aridus X - Cone)	$^{176}Hf/^{177}Hf$	0.28216iiii	21	0.282146	0.000008	27.3

References: i, Thirwall, 1991; ii, Royse et al., 1998; iii, Galer & Abouchami, 1998; iiii, Nowell et al., 1998. Aridus and X-cone long-term average at Durham = 0.282145, 2RSD=26 ppm, n = 79 (Nowell et al., 2003; Pearson and Nowell, 2005)

Nd and Hf isotope ratios throughout this thesis are plotted using the epsilon notation defined relative to Chondritic Uniform Reservoir (CHUR; $^{143}Nd/^{144}Nd$ = 0.512638, $^{176}Hf/^{177}Hf$ = 0.28286) as follows:

$$\varepsilon Nd = \left[\frac{^{143}Nd/^{144}Nd_{sample}}{^{143}Nd/^{144}Nd_{CHUR}} - 1 \right] \times 10000$$

$$\varepsilon Hf = \left[\frac{^{176}Hf/^{177}Hf_{sample}}{^{176}Hf/^{177}Hf_{CHUR}} - 1 \right] \times 10000$$

Total procedural blanks (TPB) for Sr, Pb, Nd and Hf were determined using ICP-MS on the Thermo Finigan ELEMENT 2 at Durham University. Throughout the course of this study TPB were below 107pg for Sr, 377pg for Pb, 96pg for Nd and 210pg for Hf. These values are considered insignificant in relation to Sr (~200µg/g), Pb (~8µg/g), Nd (~12µg/g) and Hf (~3µg/g) in volcanic rocks and crustal xenoliths analysed in this study.

E.6. Os isotopes and PGEs

E.6.1. Sample dissolution for determining Os isotopes and PGE concentrations

1g of rock powder was weighed and transferred to a clean 90 ml quartz Asher reaction vessel for digestion. This method has the advantage that all the PGEs (in this case only Os, Ir, Pt) including Re can be retrieved from the same dissolution. Each sample was spiked with 65 µl of "basalt" spike solution enriched in ^{194}Pt, ^{191}Ir, ^{190}Os, ^{185}Re, ^{106}Pd and ^{99}Ru (used to recalculate element concentrations during analysis). The amount of spike is also weighed and factored into the calculation process of the data. High temperature "inverse" aqua regia digestion was used for dissolution in Re-Os isotope determination. Aqua regia consists of 2.5 ml of chilled conc. HCl and 5 ml of sparged-chilled conc. HNO_3. This was added to the rock powder and "basalt" spike in each reaction vessel. The high pressure Asher ((HPA) Anton Paar-Perkin-Elmer)

digestion technique is outlined in full by Meisel et al. (2001). During HPA digestion the samples are subjected to high pressures and temperatures (130 kbar and 300°C) for 5 hours which satisfactorily dissolves silicates. Once digestion is complete the vessels are removed from the Asher and opened immediately in a fume cupboard to proceed with Os extraction.

E.6.2. Os chemistry

After opening each vessel 7.5 ml of MilliQ H_2O was gently added to each sample and gently agitated with the reverse aqua regia supernatant using a transfer pipette prior to being transferred to a clean 50 ml centrifuge tube. 1 ml of chilled CCl_4 was then added to each asher vessel, shaken gently and then pipetted off the sample and added to the 50 ml centrifuge tube. An additional 2 ml of CCl_4 was then added to the centrifuge tube before being transferred to a shaker plate. The samples were then shaked for 5 minutes following which the CCl_4 was removed with a pipette and placed in a clean 20 ml Teflon vial containing 4 ml of chilled conc. HBr. The CCl_4/shaker table step was repeated twice resulting in 7 ml of CCl_4 and 4 ml HBr in the 20 ml Teflon vials. The vials were then returned to the shaker table to agitate overnight and removed the following morning allowing the HBr and CCl_4 to separate. The Os cut could then be separated using Os back extraction, i.e. removing the HBr with a pipette and placing it in a clean 20 ml Teflon vial. These vials were then placed on a hotplate and allowed to dry down before being re-hydrated with 40 µl of 12N H_2SO_4. The remaining CCl_4 in the centrifuge tube was discarded.

Os micro-distillation was then used to collect the Os cut (OsO_4) as follows. 20 µl of conc. HBr was pipetted into the apex of a 7 ml Teflon "rocket" vial. With the lid rocket vial facing upwards 20 µl of the 12N H_2SO_4 sample solution was pipetted into

the centre of lid followed by the addition of 20 µl of CrO_3 which converts the Os to OsO_4. The 7 ml rocket vial (containing the HBr) was now inverted and the lid (containing the 12N H_2SO_4 sample solution and CrO_4) carefully screwed back on using Teflon tape around the thread of the vial to ensure a tight seal. With the vial remaining inverted, it was enclosed with aluminium foil leaving only the conical base uncovered and placed on a hotplate (90°C) for 2 hours. This procedure encourages the OsO_4 vapour to condense around the HBr droplet in the conical base of the vial. Keeping the vials inverted, they were now removed from the hotplate and the foil discarded before removing the lid of the vial. The base of the vial was then turned upright and dried down on the hotplate. The lids were cleaned with MilliQ H_2O and returned to the vials when the samples had dried down.

E.6.3. PGE Chemistry

The remaining aqua regia - MilliQ H_2O solution in the 50 ml centrifuge tubes contains the highly siderophile elements (minus Os). This solution was transferred to a clean 30 ml Teflon vial and placed on a hotplate to dry down following which 1 ml of conc. HCl was added and the vial sealed before returning to the hotplate for 1 hour. The vial lid was then removed and the sample allowed to dry down again before the addition of 10 ml 0.5N HCl. The vial was then resealed before it was returned to the hotplate for 1 hour and then allowed to cool. The samples were now ready for PGE column procedure which is outlined in Table E.8. Following the collection of the Re, Ir, Pt and Ru cut in clean beakers the samples were dried down at 90°C and taken up in 1 ml of 0.5N HCl. The solution was then transferred to clean 2ml centrifuge tubes for analysis.

Table E.8. Procedure for pre-conditioning of Bio-Rad AGI-X8 100-200# resin and the collection of the PGE cut

	Reagent	Volume (ml)	Action	Purpose
Load 1 cm^3 of clean Bio-Rad AGI-X8 100-200# resin				
Column setup	6N HCl	6	Elute	Pre-conditions column
	18.2MΩ H_2O	10		
	0.5 N HCl	5		
Load 10 ml of sample (in 0.5N HCl) and collect.				
Running the columns	1N HF-1N HCl	10	Elute	Releases Hf, Zr and Y oxides
	0.8N HNO_3	10	Elute	Converts column to nitrates
	13.5N HNO_3	12	Collect	Re, Ir, Pt and Ru

Note: Pd cut was not collected

E.6.4. Os analysis

Prior to analysis the micro-distilled Os sample in the rocket vial was taken up in 0.5 µl of 9N HBr before being dried onto 99.999% pure ESPI^{TM} Pt filament ribbon using a hot lamp. The Pt filament was then finished with a mixed $Ba(OH)_2$/NaOH activator which was dried on top of the sample before being loaded into a 21 carousel magazine and inserted into the negative ion source of the AHIGL Triton (TIMS). During analysis a small oxygen bleed was used to aid ionisation while filaments had ~15mA/min current applied for 1-2 hours. Samples were measured in peak hopping mode on the secondary electron multiplier using ion counting with the following integration times; ^{188}Os (4 sec), ^{187}Os (8 sec), ^{186}Os (4 sec). Os was measured as OsO^{4-} and online corrections applied for any ReO^{4-} interference. Analyses generally lasted approximately 180 minutes. The external reproducibility based on the average value from the UMCP Johnson Matthey standard during March 2007-August 2007 (Triton in negative ion mode) is 0.113803 (2SD = 0.000241).

E.6.5. PGE analysis

PGE (Ir & Pt) and Re abundances were measured using ICP-MS on the Thermo ELEMENT 2 at Durham University. The solution from each sample was introduced to the plasma at an uptake rate of ~100 μl min^{-1} via a microflow nebuliser fitted to a cyclone Scott double-pass spray chamber with ~ 20 second wash-in time prior to analysis. Analysis time was approximately 3 minutes with data acquired by peak hopping with 10-60 ms dwell times depending on specific isotope detection limits. Each reading was replicated twice and based on 25 sweeps of the mass spectrum.

The Thermo ELEMENT 2 was calibrated using in-house standards, international reference materials and procedural blanks. Any calibration drift in the instrument was monitored by running blanks and standards prior to, during (every 5 samples) and following each run.

E.7. Stable isotope analysis

Oxygen isotope analysis of lavas was determined by laser-fluorination at Royal Hollaway University of London (RHUL) using procedures documented by Macpherson et al. (2000). 10-20mg of fresh clinopyroxene, orthopyroxene and olivine were hand picked from lightly crushed hand specimens using a binocular microscope. These mineral separates were then washed with distilled water in an ultrasonic bath, rinsed in acetone and then air dried. 1.7 ± 0.06 mg of each mineral separate was then weighed out ready for analysis.

In house standard values of San Carlos Olivine II and Jagersfontein Garnet Megacryst for the duration of the study were +5.24‰ ± 0.02 (2σ, n = 4) and +5.40‰ ± 0.05 (2 σ, n = 7); within ≤ 0.02‰ of their accepted values. Oxygen yields were >95% for olivine (n = 8), 93-97% for orthopyroxene (n = 8) and 92-95% for

clinopyroxene (n = 25). These values remained constant over the four sessions. Replicate analyses for olivine and clinopyroxene were within 0.05% and 0.12% respectively. All results are reported as per mille deviations relative to the standard mean ocean water standard (SMOW = 0.002005) as follows:

$$\delta^{18}O\,(‰) = \left[\frac{^{18}O/^{16}O_{sample}}{^{18}O/^{16}O_{SMOW}} - 1 \right] \times 1000$$

Table F.1. Partition coefficients used in gechemical modelling

	basalt - basaltic andesite					andesite - dacite				
	olv	opx	cpx	plag	mag	olv	opx	cpx	plag	mag
Cs	0.01	0.01	0.01	0.03	0.39	0.01	0.01	0.01	0.03	0.39
Rb	0.01	0.01	0.031	0.071	-	0.021	0.022	0.033	0.113	0.15
Ba	0.01	0.011	0.026	0.23	-	0.044	0.011	0.038	0.44	0.183
Th	-	-	0.03	0.01	-	0.26	0.048	0.035	0.059	0.235
U	0.002	-	0.04	0.01	-	0.083		0.016	0.112	0.11
K	0.01	0.01	0.038	0.17	-	0.013	0.017	0.01	0.178	0.045
Ta	-	-	0.013	-	4	0.059	0.079	0.123	0.057	1.113
Nb	0.01	0.15	0.005	0.01	0.4	0.027	0.351	0.168	0.275	0.837
La	0.0067		0.056	0.19	1.5	0.087	0.068	0.13	0.183	0.15
Ce	0.01	0.024	0.11	0.12	2	0.01	0.024	0.11	0.12	2
Pb	-	-	-	0.3	-	-	-	-	0.7	-
Sr	0.01	0.013	0.12	1.83	-	0.048	0.048	0.139	2.512	0.11
Nd	0.0066	0.03	0.31	0.081	2	0.0066	0.03	0.31	0.081	2
P	-	-	-	-	-	0.03	0.009	0.0065	0.02	0
Sm	0.01	0.054	0.4	0.067	1.6	0.01	0.054	0.4	0.067	1.6
Zr	0.01	0.01	0.25	0.03	0.1	0.03	0.061	0.197	0.098	0.727
Hf	0.013		0.263	0.051	3	0.37	0.101	0.297	0.031	0.353
Eu	0.0068	0.05	0.51	0.34	0.8	0.0068	0.05	0.51	0.34	0.8
Ti	0.02	0.1	0.4	0.04	7.5	0.034	0.423	0.35	0.052	9.5
Ho	-	-	-	-	-	0.0179	0.051	0.5025	0.6197	0.0125
Gd	0.0077	0.09	0.61	0.063	-	0.0077	0.09	0.61	0.063	-
Dy	0.0096	0.15	0.68	0.055	-	0.0096	0.15	0.68	0.055	-
Y	0.01	0.01	0.9	0.06	0.2	0.028	0.343	0.86	0.076	0.322
Er	0.011	0.23	0.65	0.063	-	0.011	0.23	0.65	0.063	-
Yb	0.01	0.34	0.5	0.067	1.4	0.283	0.423	0.661	0.052	0.218
Lu	0.016	0.42	0.56	0.06	-	0.016	0.42	0.56	0.06	-

Distribution coefficients taken from Rollinson (1993) and the GERM database (http://earthref.org/GERM/index.html).

Appendix G. Energy Constrained Assimilation Fractional Crystallisation (EC-AFC)

EC-AFC modelling (Spera and Bohrson, 2001) is designed to incorporate thermal parameters (energy conservation) and wallrock partial melting into traditional geochemical based AFC modelling (e.g. DePaolo, 1981; O'Hara 1995). Consequently, changes in energy, mass, isotopes and trace elements can be modelled as a magmatic system cools and crystallizes (fractional crystallisation) while assimilating surrounding wallrock.

In addition to inputting the geochemical composition and bulk partition coefficients for the magma and wallrock, the following thermal parameters are required:

Tlm = liquidus of magma
Tmo = initial temperature of magma
Tla = liquidus of assimilant
Tao = initial temperature of assimilant
Ts = solidus, required to be the same for magma and assimilant
Cpm = specific heat, magma (calculated as a weighted average for the mixture of major oxides using specific isobaric heat capacities listed in Spera and Bohrson, (2001))
Cpa = specific heat, assimilant (calculated as a weighted average for the mixture of major oxides using specific isobaric heat capacities listed in Spera and Bohrson, (2001))
Hcry = heat of crystallization (calculated as a weighted average for the mixture of phases in magma using fusion enthalpies listed in Spera and Bohrson, (2001))
Hfus = heat of fusion (calculated as a weighted average for the mixture of phases in assimilant using fusion enthalpies listed in Spera and Bohrson, (2001))

The mathematical model used to calculate EC-AFC comprises two sections:

(1) an integral calculation defining the relationship between the equilibration temperature and the mass of wallrock brought to equilibration temperature for the thermal parameters defined by the user.

(2) path dependent differential equations defining the goechemical and thermal evolution of the contaminated magma.

Full details of these calculations are given in Spera and Bohrson (2001).

A key difference between EC-AFC and traditional AFC modelling is the value of R (mass of assimilant/mass of cumulates). In traditional models R is assumed to be constant often ~0.2. However in EC-AFC models this value will vary throughout reflecting energy conservation within the system.

The spreadsheet used for EC-AFC modelling thoughout this thesis was downloaded from the Institue for Crustal Studies and Department of Geological Sciences, University of Carolina (http://magma.geol.ucsb.edu/).